



HAL
open science

Design and optimisation the composite material structures for naval applications: effects of slamming

Omar Hashim Hassoon Al-Dodoe

► **To cite this version:**

Omar Hashim Hassoon Al-Dodoe. Design and optimisation the composite material structures for naval applications: effects of slamming. Fluid mechanics [physics.class-ph]. Université de Bretagne occidentale - Brest, 2017. English. NNT: 2017BRES0050 . tel-01617095

HAL Id: tel-01617095

<https://theses.hal.science/tel-01617095>

Submitted on 16 Oct 2017

HAL is a multi-disciplinary open access archive for the deposit and dissemination of scientific research documents, whether they are published or not. The documents may come from teaching and research institutions in France or abroad, or from public or private research centers.

L'archive ouverte pluridisciplinaire **HAL**, est destinée au dépôt et à la diffusion de documents scientifiques de niveau recherche, publiés ou non, émanant des établissements d'enseignement et de recherche français ou étrangers, des laboratoires publics ou privés.

**THÈSE / UNIVERSITÉ DE BRETAGNE
OCCIDENTALE**

sous le sceau de l'Université Bretagne Loire

pour obtenir le titre de

DOCTEUR DE L'UNIVERSITÉ DE BRETAGNE OCCIDENTALE

*Mention : Génie Mécanique - mécanique des fluides et
énergétique*

École Doctorale des Sciences de la Mer

Présentée par

**Omar Hashim Hassoon
AL-DODOEE**

Préparée à l'Institut de Recherche Dupuy de
Lôme, CNRS FRE- 3744, ENSTA Bretagne.

**Conception et Optimisation
des Matériaux et Structures
Composites pour des
Applications Navales : Effet du
slamming**

**Design and Optimisation the
Composite Material structures
for Naval Applications: Effect
of slamming**

Thèse soutenue le 28 juin 2017

Devant le jury composé de :

Abdelkhalak El Hami

Professeur, INSA Rouen, Normandy University / *Rapporteur*

Mhamed SOULI

Professeur, Université des Sciences et Technologies de Lille 1 / *Rapporteur*

Alexis RUSINEK

Professeur, Ecole Nationale d'Ingénieurs de Metz / *Examineur*

François COLLOMBET

Professeur, Clément Ader Institute, Toulouse / *Examineur*

Fouad ERCHIQUI

Professeur - Université du Québec, Canada / *Examineur*

Fodil MERAGHNI

Professeur, Ecole Nationale Supérieure d'Arts et Métiers Metz / *Examineur*

Nourreddine LATTRACHE

MC, Université Européenne de Bretagne/ *Examineur*

Mostapha TARFAOUI

Enseignant Chercheur - HDR, ENSTA Bretagne / *Directeur*

Aboulghit EL MALKI ALAOUI

Enseignant-Chercheur / ENSTA Bretagne / *Co-Directeur*

Bruno MORTAIGNE

DGA-DS-MRIS, RDS Matériaux Chimie Energie / *Invité*

Acknowledgements

Since my arrival to France, I have looked toward my family who have been a light guiding me on my way. Without their support and the innocent smiles of my children work would never have been a success. Thanks you to all my family. I am particularly grateful to my wife, Shaymaa, who has succeeded in helping me to overcome all the difficulties that my pursuit of a doctoral degree.

I am grateful to my supervisor Prof. M. Tarfaoui, who supported me through his advice and guided me on the right path, with ongoing monitoring and diligent efforts to complete this work. In addition, I would like to thank Dr. A. El Malki for his excellent efforts in achieving the experimental part of this work.

I would like to thank Mr. Abdelkhalak El Hami, Professor of INSA Rouen, Normandy University, and Mhamed SOULI, Professor at University of Science and Technology, Lille 1, for having honoured me to their acceptance to be as scientific reviewers of this dissertation. I am also very grateful to Mr. Francis COLLOMBET , Professor of University Institute of Technology, Toulouse for having agreed to preside my jury of doctorate thesis. In addition, I wish to thank the members of examiners Committee, Alexis RUSINEK, Fouad ERCHIQUI, Fodil MERAGHNI, Nourreddine LATTRACHE for their suggestions and discussions. I thank Also Mr. Bruno MORTAIGNE, for his participated in my jury.

I thank my parents, my brother, all my sisters and all the people who supported me during this period. My friends in our group, especially Ahmed, Hamza, Owaisur and Mahrez, thank you for everything, I will never forget our time together over the past few years. Thank you to my Iraqi friends, Muntather and Omar. I would like to present my thanks and my respects to everybody at ENSTA Bretagne. Finally, I would like to thank my country Iraq and University of Technology, Baghdad who gave me the opportunity to achieve this research project in France.

Omar Hashim Hassoon Al-Dodoe

Contents

GENERAL INTRODUCTION

Introduction	1
Thesis objectives	3
Thesis organisation	4
References	7

CHAPTER ONE : THE SLAMMING IMPACT PHENOMENON IN NAVAL APPLICATIONS

1.1 Introduction	10
1.2 Slamming of the rigid body	11
1.2.1 The analytical model for pressure distributions based on Von Kármán	12
1.2.2 Analytical model based on pressure distributions using Wagner's slamming impact theory	14
1.3 Experimental investigations on rigid bodies under the slamming impact	21
1.4 Experimental studies of the deformable slamming impact	23
1.5 Numerical modelling of fluid-structure interaction on slamming impact	26
1.5.1 The multiple material Lagrangian-Eulerian ALE model	26
1.5.2 The Smoothed Particle Hydrodynamics (SPH) model	29
1.5.3 Computational Fluid Dynamics (CFD)	31
1.6 Hydroelasticity effect on the slamming phenomenon	33
1.7 Effect of the air cushioning on the slamming	35
1.8 Conclusions	36
References	37

CHAPTER TWO : SLAMMING NUMERICAL SIMULATION

2.1 Introduction	44
2.2 The two dimensional numerical slamming model	44
2.2.1 Effect of the hourglass control	47
2.2.2 Effect of the penalty stiffness factor (PFAC)	49
2.2.2 Effect of the element mesh size	51
2.2.3 Effect of the deadrise angles on hydrodynamic pressure	52
2.2.4 Effect of the impact velocity	55
2.2.5 Effect of body shape on the slamming	59
2.3 Numerical simulation based on the CEL model	60

2.3.1 Mesh convergence	62
2.3.2 Effect of the fluid domain	64
2.4 Beam theory for a deformable structure	66
2.5 Slamming and sandwich design	70
2.6 Effect of the stacking sequence	74
2.7 Three dimensional numerical slamming model.....	75
2.8 Conclusions	79
References	81
CHAPTER THREE : DAMAGE AND FAILURE MECHANISMS IN COMPOSITE MATERIALS	
3.1 Introduction	84
3.2 Composite materials	85
3.2.1 Composite laminates.....	86
3.2.2 Sandwich structure.....	87
3.3 Composite material levels	89
3.4 Defects in composite materials.....	90
3.5 Composite materials Failure Modes	91
3.5.1 Intralaminar failure based Continuum Damage Mechanics (CDM).....	92
3.5.1.2 Failure initiation models	93
3.5.1.3 Damage evolution	96
3.5.2 Interlaminar failure (Delamination).....	98
3.5.2.1 Constitutive model of the cohesive elements.....	102
3.5.2.2 Delamination propagation.....	103
3.6 Effect of the stacking sequence	104
3.7 Effect of velocity impact	106
3.8 Conclusions	107
CHAPTER FOUR : DAMAGE MODELLING AND SIMULATION RESULTS	
4.1 Introduction	118
4.2 Constitutive progressive degradation of composite material	118
4.2.1 Intralaminar failure criteria	120
4.2.2 Damage evolution	121
4.3 Validation of the intralaminar model	125
4.3.1 Single element model.....	125
4.3.1.1 Effect of damage propagation energy	126

4.3.1.2 Tension and compression in the longitudinal direction	127
4.3.1.3 Tension and compression in the transversal direction	129
4.3.1.4 Mesh convergence.....	131
4.3.2 High velocity impact test	132
4.4 Conclusions	139
References	140
CHAPTER FIVE : SLAMMING-EXPERIMENTAL RESULTS	
5.1 Introduction	144
5.2 Experiment setup configuration.....	145
5.2.1 Servo-test Machine	145
5.2.3 Machine Instruments.....	146
5.3 Composite Panels and fixture	147
5.4 Machines parameters calibration	148
5.5 Composite panel test results	150
5.5.1 Flexible panels (thickness =8mm)	151
5.5.2 Semi-flexible panels (thickness =13 mm)	154
5.5.3 Effect of the slamming impact along panel width	157
5.6 Comparison of different impact velocities	158
5.6.1 Hydrodynamic force	158
5.6.2 Deformation response	159
5.7 PVC Sandwich material results	162
5.7.1 Dynamic response.....	163
a) Sandwich panels, thickness=27mm.....	163
b) Sandwich panels, thickness=37mm.....	165
5.7.2 Damage assessment	167
5.8 General discussions	170
5.9 Conclusions	172
References	174
CHAPTER SIX : NUMERICAL VALIDATION WITH EXPERIMENTAL RESULTS	
6.1 Three dimensional numerical slamming model of deformable composite panels	178
6.1.1 Hydroelastic effects along the water-structure interaction	181
6.1.2 Hydroelastic effects and structural response	187
6.1.3 Hydroelastic influence	189
6.2 Composite panel	190

6.2.1 Force response	190
6.2.2 Deformation response	193
6.2.3 Damage assessment	195
6.3 Sandwich panel.....	200
6.3.1 Force response	200
6.3.2 Deformation response	201
6.3.3 Damage comparison of sandwich panels.....	203
6.4 Discussion, non-dimensional slamming force.....	206
6.5 Conclusions	209
References	211
Conclusions	213
Perspectives and future works	216
Future aspects of the slamming phenomenon.....	216
Future aspects of the structural behaviour	216
Appendix A	219
Natural frequency analysis of Fixture system and panels.....	219
Appendix B.....	223
Manufacture and specifications of composite materials.....	223
Manufacture of Sandwich panels.....	225
Appendix C.....	227
Smooth Particle Hydrodynamic method SPH	227
References	232

List of Figures

Figure 1. Slamming impact	1
Figure 2. Failure due to slamming impact.....	2
Figure 3. Effect of the structure flexibility [4]	3
Figure 4. Research methodology of the study.....	7
Figure 1. 1. High speed vessel with slamming impact.....	10
Figure 1. 2. The slamming impact categories [4].....	11
Figure 1. 3. Analogy between constant and variable impact velocity for the wedge.....	12
Figure 1. 4. Schematic of rigid wedge, Von Kármán method [6]	13
Figure 1.5. Slamming impact of the wedge body	14
Figure 1. 6. Slamming model description for inner, outer and jet flow domains	17
Figure 1. 7. Slamming impact of axisymmetric bodies [19].....	21
Figure 1. 8. Slamming impact with constant velocity, $\beta=15^\circ$ [21, 22]	22
Figure 1. 9. Schematic of the experimental set-up [23]	23
Figure 1. 10. Experimental setup [5].....	24
Figure 1. 11. Water entry problem [28]	25
Figure 1. 12. Servo-hydraulic slam testing system (SSTS) [31].....	25
Figure 1. 13. Force with different flexible panels at $\beta=10^\circ$ [30].....	26
Figure 1. 14. Parametric numerical results for ALE in wedge slamming [34]	27
Figure 1. 15. Initial boundary conditions for the fluid and body domain	29
Figure 1.16. Pressure distribution of SPH results ($\beta=30^\circ$) compared with the analytical and experimental approach carried out by Zhao [40]	30
Figure 1.17. Aluminium wedge impact results ($\beta=15^\circ$), 2 mm, $V = 5$ m/s [42].....	31
Figure 1.18. Simulation procedure.....	31
Figure 1.19. CFD model [43]	32
Figure 1.20. Flowchart of the iteration method [44]	33
Figure 1.21. Analysis of the hydroelastic problem [46].....	34
Figure 2. 1. Boundary conditions and mesh regions for the slamming of a two dimensional wedge model	46
Figure 2. 2. Hourglass behaviour for a single first-order reduced-integration element with no strain	47
Figure 2. 3. Comparison of the energy histories for combine hourglass	48
Figure 2. 4. Loading on the wedge surface with penalty contact method and deadrise angle 10° , $V=8$ m/s	49
Figure 2. 5. Penalty coupling method for the nodes of fluid-structure interface [5].....	50
Figure 2. 6. Loading on the wedge surface with different stiffness scale factors of penalty contact method, deadrise angle 10° - $V=8$ m/s	51
Figure 2. 7. Pressure distribution along the wedge with different mesh sizes, deadrise angle 30° and $V=13$ m/s.....	52

Figure 2. 8. Nondimensional coefficient pressure C_{pmax} according to the deadrise angles..	53
Figure 2. 9. Pressure coefficient distribution for deadrise angle, $V=13\text{m/s}$	54
Figure 2. 10. Pressure coefficient distribution for different deadrise angles for wedge entering water [9]	55
Figure 2. 11. Maximum values of pressures for different impact velocities and deadrise angles	56
Figure 2. 12. Free water surface and pressure histories for angle at 10° , $V=8\text{m/s}$	57
Figure 2. 13. Total vertical force for the wedge for the range of deadrise angles, $V=8\text{m/s}$	58
Figure 2. 14. Coefficient force ($C_f = F (\tan \beta)^2 / (L \rho V^3 t)$) versus the deadrise angle	58
Figure 2. 15. Points position on the free surface of the water	59
Figure 2. 16. Pressure histories for different points on the wedge, $\beta = 30^\circ$	59
Figure 2. 17. Points position on the free surface of the water for circular section.....	60
Figure 2. 18. Pressure histories for different points on the body with circular section.....	60
Figure 2. 19. Volume of Fluid method (VOF)	61
Figure 2. 20. Boundary conditions of CEL water entry model	62
Figure 2. 21. Mesh convergence for the fluid domain	63
Figure 2. 22. Mesh convergence for fluid domain, $\beta = 30^\circ$ and $V=13\text{m/s}$	64
Figure 2. 23. Different domain length of fluid	65
Figure 2. 24. The effect of the fluid domain length	66
Figure 2. 25. Hydrodynamic force comparison between ALE and CEL models, $\beta = 10^\circ$ and $V=8\text{m/s}$	66
Figure 2. 26. Boundary conditions of supported plates.....	67
Figure 2. 27. Deflection of the PVC sandwich with different boundary conditions.....	68
Figure 2. 28. Pressure histories for different boundary conditions of the deformable body, $\beta=10^\circ$ and $V=4\text{m/s}$	69
Figure 2. 29. Max deflection for three different panel materials, $V=4\text{m/s}$	73
Figure 2. 30. Max deflection corresponding to stacking sequence and ply orientation with Boundary condition (CC)	74
Figure 2. 31. Numerical slamming model.....	76
Figure 2. 32. Panel instrumentation and setup	76
Figure 2. 33. Comparison of the panel deformation between the numerical results and experimental data, $V=2\text{ m/s}$	77
Figure 2. 34. Comparison of the panel deformation between the numerical results and experimental data, $V=4\text{ m/s}$	77
Figure 2. 35. Comparison of the hydrodynamic force between the numerical results and experimental data	78
Figure 2. 36. Distribution of stresses and water jet after impact.....	78
Figure 2. 37. Numerical results of pressure peak time histories	79
Figure 2. 38. Numerical results of deformation time histories.....	79
Figure 3. 1. Damage in a naval application [1]	84
Figure 3. 2. Damage in the ship (local, panel, global scale) [2].....	85
Figure 3. 3. Stress-strain curves for brittle composite material	86

Figure 3. 4. Material mechanical properties [3]	87
Figure 3. 5. Failure modes of sandwich structures	88
Figure 3. 6. Hierarchical composite material levels	89
Figure 3. 7. Failure in composite materials [9]	91
Figure 3. 8. Failure criteria classification [10]	92
Figure 3. 9. Damage mechanism and evolution	92
Figure 3. 10. Puck Matrix failure modes: failure with crack inclination parallel to principle fibre axis	94
Figure 3. 11. Failure degradation models	97
Figure 3. 12. Modified crack closure method [26]	99
Figure 3. 13. Cohesive element model approach [37]	101
Figure 3. 14. Interface behaviour laws for cohesive elements [39]	102
Figure 3. 15. Mixed Mode softening law behaviour [40]	102
Figure 3. 16. Three modes to determine the energy release rate (a) Mode I (b) Mode II (c) Mode III [43]	104
Figure 3. 17. Effect of the fibre orientation angle and the stacking thickness of the laminate [47]	105
Figure 3. 18. Effect of the stacking sequence on delamination [48]	105
Figure 3. 19. Influence of the thickness of lamina on low velocity impacts, $[\pm 45^\circ]_n$ CFRP composites [49]	105
Figure 3. 20. Structure response [52]	106
Figure 4. 1. Effective stress and nominal stress	119
Figure 4. 2. Typical behaviour of material stiffness degradation	122
Figure 4. 3. Flowchart VUMAT subroutine intralaminar damage model	124
Figure 4.4. Orthotropic composite ply subjected to longitudinal loading (fibres oriented to 0°)	125
Figure 4.5. Evolution of dynamic response of orthotropic ply under longitudinal tension ...	127
Figure 4. 6. Evolution of dynamic response of orthotropic ply under longitudinal compression	128
Figure 4. 7. Test of one element, longitudinal direction	128
Figure 4.8. Evolution of dynamic response of orthotropic ply under transverse tension	129
Figure 4. 9. Evolution of dynamic response of orthotropic ply under transverse compression	130
Figure 4. 10. Test of one element, transversal direction	130
Figure 4. 11. Effect of ultimate tensile strengths for one element under tensile test, longitudinal direction	131
Figure 4. 12. Mesh size effect	132
Figure 4. 13. Influence of mesh density on the energy dissipation	132
Figure 4. 14. Typical finite element model under high velocity impact	133
Figure 4. 15. Correlation between the VUMAT and experimental results	134
Figure 4. 16. Effect of stacking sequence under impact velocity 250 m/s 4.3.4.2 Interlaminar (delamination) failure effect with high velocity impact	135

Figure 4.17. Time histories for damaged laminate under impact velocity of 250 m/s.....	137
Figure 4. 18. Influence of the delamination on the projectile residual velocity	137
Figure 4. 19. Effect of the stacking sequence on the structure strength.....	138
Figure 4. 20. Damage matrix tension and delamination with different stacking sequence....	138
Figure 5. 1. Experimental setup and Schematic representation	145
Figure 5. 2. Measurement Instruments.....	146
Figure 5. 3. Diagram of Panels and positioning of strain gauges, dimensions in mm.....	147
Figure 5. 4. Mode shapes of the dry panels.....	148
Figure 5. 5. Calibration of the machine with flexible composite panel, $V=6\text{m/s}$	149
Figure 5. 6. Structure response with flexible composite panel, $V=6\text{m/s}$	150
Figure 5. 7. Repeatability of tests for flexible wedge	151
Figure 5. 8. Deformation measured by strain gauges.....	152
Figure 5. 9. Mode shape histories from strain gauges along wet panel	153
Figure 5. 10. Camera images, $V= 4 \text{ m/s}$	154
Figure 5. 11. Camera images, $V= 6 \text{ m/s}$	154
Figure 5. 12. Repeatability of semi-flexible wedge tests	155
Figure 5. 13. Deformation in strain gauge	156
Figure 5. 14. Mode shapes histories from strain gauges along wet panel, $t=13\text{mm}$	157
Figure 5. 15. Three dimensional effect, $t=13\text{mm}$ and $V=8\text{m/s}$	158
Figure 5. 16. Hydrodynamic load for different rigidity and impact velocities	159
Figure 5. 17. Damage in the flexible composite panel.....	159
Figure 5. 18. Maximum experimental strain for different gauges in (FP) and (SFP) panels. 160	
Figure 5. 19. Comparison of the deformation between flexible and semi-flexible panels, $V=6\text{m/s}$	161
Figure 5. 20. Sandwich experiment set up configuration.....	162
Figure 5. 21. The repeatability of tests on PVC sandwich, $t=27\text{mm}$	163
Figure 5. 22. Deformation in the strain gauges, $t=27\text{mm}$	164
Figure 5. 23. Mode shapes histories from strain gauges along wet sandwich panel, $t=27\text{mm}$	165
Figure 5. 24. The repeatability of the tests on PVC sandwich, $t=37\text{mm}$	166
Figure 5. 25. Deformation in strain gauges of PVC sandwich, $t=37\text{mm}$	167
Figure 5. 26. Damage history in sandwich PVC $t=27\text{mm}$	168
Figure 5. 27. Damage modes in sandwich panel.....	169
Figure 5. 28. Damage in PVC sandwich $t=27$ velocity= 10 m/s	169
Figure 5. 29. Hydrodynamic loads for different structural stiffnesses.....	170
Figure 5. 30. Non-dimensional hydroelasticity relative to impact velocity and different rigidities.....	172
Figure 6. 1. Schematic representation of numerical slamming model.....	179
Figure 6. 2. Model configuration: model boundary conditions, panel dimensions and strain gauge location	180

Figure 6. 3. Analytical Quasi-Static maximum deflection (B-CC) vs. impact velocity, $\beta=10^\circ$	181
Figure 6. 4. Histories of kinematic effect of semi-flexible panel, $V= 6 \text{ m/s}$	182
Figure 6. 5. Histories of kinematic effect of flexible panel, $V= 6 \text{ m/s}$	182
Figure 6. 6. Strain at different positions along span of the panel and max deflection for flexible composite material	183
Figure 6. 7. Strain at different positions along span panel and max deflection for semi-flexible composite material	184
Figure 6. 8. Pressure time histories, $V=4 \text{ m/s}$	185
Figure 6. 9. Pressure time histories, $V=6\text{m/s}$	185
Figure 6. 10. Pressure distribution during a virtual slamming test, $V= 6 \text{ m/s}$	186
Figure 6. 11. Maximum pressure close to the chine compared to theoretical approaches	187
Figure 6. 12. Stress concentration close to the chine edge, $t=12 \text{ ms}$	188
Figure 6. 13. Slamming force of wedge	189
Figure 6. 14. Deflection design limit and strain versus impact velocity for composite material	190
Figure 6. 15. Comparison of hydrodynamic force between numerical and experimental results (FP)	191
Figure 6. 16. Comparison of hydrodynamic force between numerical and experimental results (SFP)	191
Figure 6. 17. Experimental impact velocities	192
Figure 6. 18. Time histories of water jet elevation in the flexible panel, $V=4\text{m/s}$	193
Figure 6. 19. Dynamic deformation for flexible panel (FP)	194
Figure 6. 20. Dynamic deformation for semi-flexible panel (SFP)	194
Figure 6. 21. Total signal	195
Figure 6. 22. Damage in the matrix tension and compression for semi-flexible laminate	196
Figure 6. 23. Damage in the matrix tension and compression for flexible laminate	196
Figure 6. 24. Stress concentration distribution in semi-flexible panel, $V=10\text{m/s}$	197
Figure 6. 25. Damage in semi-flexible panel, $V=10\text{m/s}$	198
Figure 6. 26. Signature of the slamming problem: impacted zone by composite panels and formation of the water jet	198
Figure 6. 27. The capture of damaged panels under slamming impact and formation of the fluid jet flow	199
Figure 6. 28. Comparison of hydrodynamic force between numerical and experiment results, $t= 27 \text{ mm}$	200
Figure 6. 29. Comparison of hydrodynamic force for sandwich panel, $t= 37 \text{ mm}$	201
Figure 6. 30. Comparison of gauges deformation between numerical and experimental results, $t=27\text{mm}$	202
Figure 6. 31. Comparison of gauge deformation between numerical and experimental results, $t=37\text{mm}$	203
Figure 6. 32. Comparison of damaged zone between numerical and experimental results, $V=10 \text{ m/s}$	204
Figure 6. 33. Damage of core and debonding sandwich panels after test	205

Figure 6. 34. Comparative hydrodynamic force between experimental and numerical results	205
Figure 6. 35. Failure modes comparison of numerical vs. experimental (debonding and core shear) results.....	206
Figure 6. 36. Comparison of hydrodynamic force for different panel stiffness, V=6 m/s	207
Figure 6. 37. Comparison of the non-dimensional slamming force ($\beta=10^\circ$) with different materials and velocities	209
Figure A. 1. Fixture System with angle of 10°	219
Figure A. 2. Fixture System with angle of 15°	220
Figure A. 3. Natural frequency analysis of composite panel, thickness =13 mm	221
Figure A. 4. Natural frequency analysis of composite panel, thickness =8 mm	222
Figure A. 5. Mode shape of composite panel, thickness =8 mm	222
Figure B. 1. Preparation of the stacking sequence and cut of panels	223
Figure B. 2. Vacuum bag and infusion of the resin.....	224
Figure B. 3. Manufacture of sandwich panels.....	225
Figure C. 1. Sandwich panel, t= 27 mm.....	229
Figure C. 2. Sandwich panel, t= 37 mm.....	230
Figure C. 3. Comparison of hydrodynamic force for sandwich panel, t= 27 mm.	231
Figure C. 4. Comparison of hydrodynamic force for sandwich panel, t= 37 mm	231
Figure C. 5. Water flow elevation for sandwich panel, t= 37 mm and V=6 m/s	231

List of Tables

Table 1. 1. Analytical and numerical methods of impact slamming for rigid body.....	20
Table 2. 1. Parameters of the water in the model	46
Table 2. 2. Comparison of the energy histories of hourglass element controls	48
Table 2. 3. Mesh convergence and CPU time	64
Table 2. 4. Material properties of the PVC panels	67
Table 2. 5. Maximum deflection for different boundary conditions	68
Table 2. 6. Sandwich stiffness and strength relative to geometric variables [17].....	70
Table 2. 7. Boundary conditions and loading [18]	73
Table 2. 8. Material properties of the panels.....	73
Table 2. 9. Skin stacking sequence and ply orientation	74
Table 3. 1 Mechanical and physical properties of sandwich structures with different core thicknesses.....	88
Table 3. 2. Failure criteria models.....	95
Table 4. 1. Hashin Failure criteria [3]	121
Table 4. 2. Equivalent displacement and equivalent stress for each mode [6]	123
Table 4. 3. Mechanical properties of orthotropic layer (glass/epoxy)	126
Table 4. 4. Fracture energy for damage evolution	126
Table 4. 5. Carbon fibre-epoxy material properties [8].....	133
Table 4. 6. Compare simulation results with experiment results	134
Table 4. 7. Cohesive properties [11]	136
Table 5. 1. Properties of two composite panels with different thicknesses (8 mm and 13 mm)	148
Table 5. 2. Sandwich panel mechanical properties [11, 12]	162
Table 5. 3. Hydrodynamic force for different panel stiffnesses and different velocities.....	171
Table 6. 1. PVC sandwich and composite panel properties considered [2, 3].....	180
Table 6. 2. Cohesive properties of the skin/core interface sandwich [4]	180
Table 6. 3. Summary of experimental and numerical results.....	208
Table A. 1. Fixture system analysis	221

Introduction

Introduction

Generally, when marine vessels encounter the water surface on entry and subsequently re-enter the water at high speed, this can subject the bottom section of the vessels to high hydrodynamic loads, especially over very short durations, as shown in Figure 1. This phenomenon can be defined according to the concepts of marine structure designers as vertical or bottom slamming. This phenomenon generates high hydrodynamic loads, which can cause a catastrophic failure in the structure [1]. When considering the design requirements and the slamming event, ship designers usually estimate and characterise the structural response by applying uniform pressure distribution, although in reality, the hydrodynamic pressure generated by the slamming event is not uniform and local hydrodynamic loads always occur [2].



Figure 1. Slamming impact

The appearance of the composite structures in the last decades has encouraged the exploitation of these structures in major construction projects for lightweight marine and aerospace applications. This is due to the nature of their mechanical properties which as they have a high stiffness-to-weight ratio. Furthermore, in comparison to heavy metal materials, composite materials possess good characteristics for particular applications such as:

General Introduction

- Minimum weight,
- Aesthetics (especially through formability),
- Longevity,
- Maintainability and reparability,
- Corrosion and environmental resistance,
- Signature performance (stealth, magnetic, acoustic, thermal, electromagnetic),
- Specific strength characteristics.

On the other hand, these structures are always subject to different and complex damage mechanisms under dynamic loading, Figure 2. Consequently, the complex behaviour of the damage during initiation and propagation in these structures needs to be clarified in order to overcome this problem and incorporate these findings into the design phase. Therefore, further researches have needed to investigate and analyse these failure modes under dynamic slamming loads.



Figure 2. Failure due to slamming impact

In addition, limited research has taken into account the influence of flexibility on these structures when interactive with the fluid. They have concentrated their efforts on the slamming impact of rigid bodies, whereas the structure flexibility has an effect on the hydrodynamic loads, as their vibration can change the fluid flow along the fluid-structure

General Introduction

interaction. Therefore, it is not sufficient to use the maximum loads determined from rigid bodies. In the slamming event, the interaction effects lead to a modification in the hydrodynamic loads acting on the structure, as a result of the inertia and kinematic effects of both fluid and structure, Figure 3. This leads to the introduction a phenomenon called hydroelastic influence. Therefore, it is important to integrate these effects into the design phase for a more reliable estimation of the vessel performance [3].

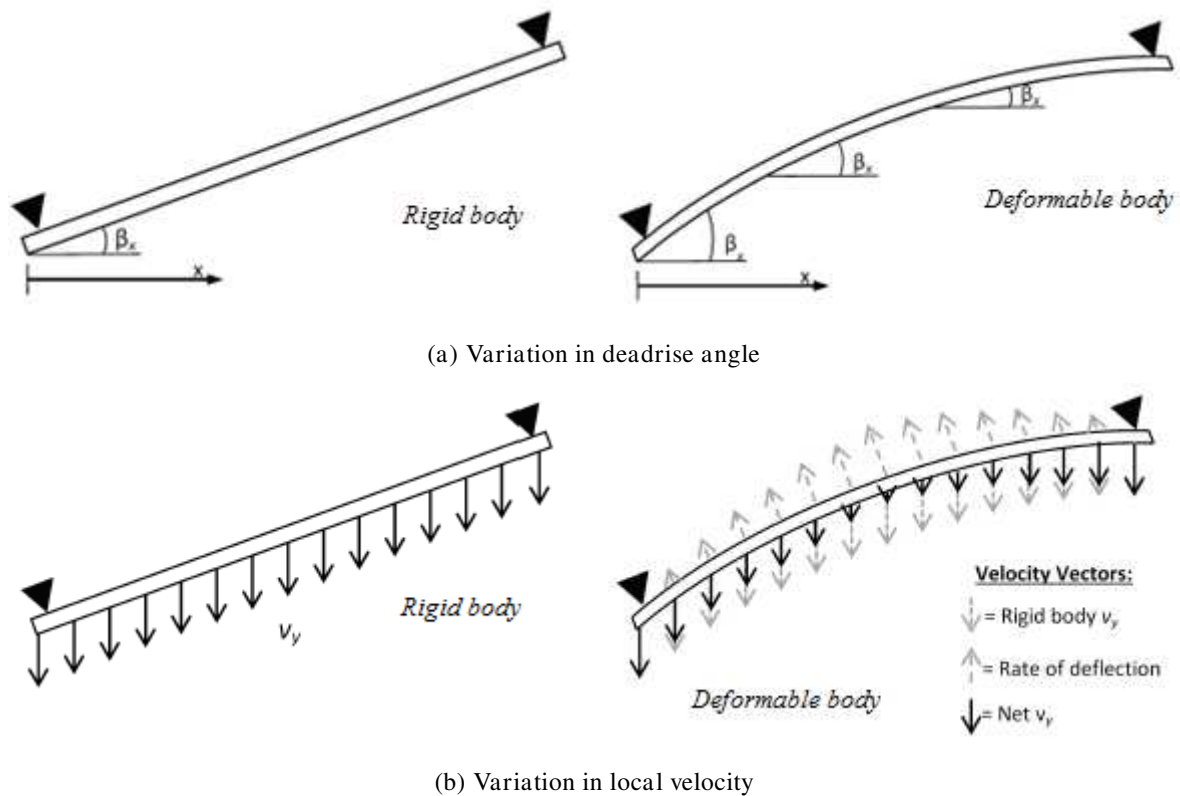


Figure 3. Effect of the structure flexibility [4]

Thesis objectives

The motivation of this work is to quantify the structural response of deformable composite (laminated and sandwich) due to the hydroelastic influence along the water-structure interface during the slamming event, which can have a great influence on hydrodynamic loads and the failure mechanism. These effects are significantly very low in rigid bodies. Consequently, the kinematic and dynamic boundary conditions of the fluid along the interface always remain unchanged. Therefore, an experimental campaign was performed for various impact velocities and various stiffness wedges composed of laminated panels and sandwich panels.

General Introduction

On the other hand, for more true-to-life simulation of the failure modes of composites used on vessels which are subjected to repeated slamming impacts over their service time, we have incorporated these modes in the numerical model. This model is capable of predicting both interlaminar and intralaminar failure for composite structures.

The second objective of this work is to model an appropriate numerical model to estimate the hydrodynamic loads for different flexibility of composite structures subjected to slamming impacts. Consequently, it can provide the validation of the simulation of the water entry problem after validation by experimental studies, as the experimental test is expensive to perform.

Thesis organisation

The adopted methodology of this work is summarised schematically in Figure 4. This thesis consists of six chapters as follows:

Chapter one gives an overview of literature reviews that deals with slamming phenomenon which were solved using analytical, experimental and numerical methods for both rigid and deformable structures. For deformable structures, the hydroelastic effects were addressed briefly in previous works which handled both the laminated and sandwich structures. The effect of the air cushioning is briefly reviewed in order to illustrate its influence on the slamming event.

Chapter two deals with the implementation of numerical methods, that began with the slamming impact of rigid bodies in two dimensional configuration using the Arbitrary Eulerian Lagrangian method (ALE) and investigated the parameters which influence on results accuracy of this method, including the contact methods, mesh density, deadrise angle, impact velocity and the body shape. This chapter includes the Coupled Eulerian Lagrangian (CEL) approach which was employed to deal with deformable structures. Finally, the model was created and validated against previous experimental works (results from the literature) evaluating the slamming water impact. Integrating these models into our work increased its authenticity.

Chapter three is devoted to a state of the art concerning the damage modes and failure mechanisms in composite materials and sandwich structures. Moreover, some of the

General Introduction

parameters were briefly addressed such as the stacking sequence and impact velocity which have an influence on the failure mechanism of these structures.

Chapter four introduced the details and the procedure of the intralaminar damage model using the VUMAT subroutine and interlaminar damage using the cohesive zone model. The model was implemented for various loadings beginning with a single element and extending to include high velocity impact.

Chapter five, presents the experimental investigation of the flexible laminate and sandwich panels (panels with different stiffness) and different velocities of impact were implemented to characterise the response of structures subjected to slamming impacts. This was done by using the high velocity shock machine which is capable of keeping approximately constant velocity through impact duration. In general, the experimental data impressively demonstrate that flexible panels have a high hydrodynamic force and significantly more dynamic noise than higher stiffness panels, which indicates that the water-structure interaction has an influence on the hydrodynamic loads. The maximum force and deformation which occurred close to the chine had enough capacity to cause damage to the structure, leading to catastrophic failure.

Subsequently in **Chapter six**, besides the experimental data was obtained in the previous chapter, the numerical results based on the CEL approach were validated by comparison with experimental data. The research extends to the assessment of the different modes of failure in both composite and sandwich panels by incorporating the interlaminar and intralaminar compositions which discussed in Chapter three. The hydrodynamic force and the structural deformation were confirmed with experimental data. However, the accurate numerical results showed good agreement with the experimental data, but exhibited some differences in the time and the peak force. This was due to variations in the experimental velocity of the impact duration which was not constant as in the numerical model and maybe other possible types of damage occurred.

Finally, the main conclusions of the experimental results and the numerical investigations and the contribution of this work for the estimation of the slamming loads and structural response in naval applications were discussed. Some suggestions have been made to improve and identify possible perspectives for future work, in order to achieve better solutions for the present study. This thesis has led to the following publications:

- **Articles in international Journals**

1. **Hassoon OH**, Tarfaoui M, El Moumen A. Progressive damage modeling in laminate composites under slamming impact water for naval applications. *Composite Structures* 2017; 167: 178-190.
2. **Hassoon OH**, Tarfaoui M, A. El Malki Alaoui, El Moumen A. Experimental and numerical investigation on the dynamic response of sandwich composite panels under hydrodynamic slamming loads. *Composite Structures* (<http://dx.doi.org/10.1016/j.compstruct.2017.07.0140263-8223/>© 2017).
3. **Hassoon OH**, Tarfaoui M, A. El Malki Alaoui. Numerical simulation of fiber bragg grating spectrum for mode-i delamination detection. *International Journal of Mechanical, Aerospace, Industrial, Mechatronic and Manufacturing Engineering* Vol:9, No:1, 2015.
4. **Hassoon OH**, Tarfaoui M, A. El Malki Alaoui. An experimental investigation on dynamic response of composite panels subjected to hydroelastic impact loading at constant velocities. *Engineering structures*. ENGSTRUCT_2016_447R1 (Revised version).
5. **Hassoon OH**, Tarfaoui M, A. El Malki Alaoui, El Moumen A. Mechanical behavior of composite structures subjected to constant slamming impact velocity: Experimental and numerical investigation. *International journal of Mechanical sciences* (Under review).

- **International conferences:**

1. **Hassoon OH**, Tarfaoui M, A. El Malki Alaoui. Slamming Impact Water Entry Problem for Deformable Composite Materials: numerical investigation. ICCES'15, Reno, NV, USA, 2015.
2. **Hassoon OH**, Tarfaoui M, A. El Malki Alaoui. ICCM International Conference on Composite Materials, Paris, 2015.
3. **Hassoon OH**, Tarfaoui M, A. El Malki Alaoui, Mahrez Ait M. Damages Modeling in Composite Materials: Effect of Laminate Stacking Sequences. Italy, Turin, 2016.
4. **Hassoon OH**, Tarfaoui M, A. El Malki. Slamming impact simulation of 2d water entry for rigid structures. ECCOMAS, VII European Congress on Computational Methods in Applied Sciences and Engineering , Crete Island, Greece, 2016.
5. **Hassoon OH**, Tarfaoui M, A. El Malki Alaoui, Benyahia Hamza. Dynamic Behavior and Damage Modeling for Sandwich Composite Structure under Slamming Impact Water. 2nd International Conference on Mechanics of Composites, Porto, Portugal, 2016.
6. Mahrez Ait M, Tarfaoui M, **Hassoon OH**. Numerical Investigation of the Damage in Composite Materials Under Dynamic Loads Using a Combination of Intralaminare and Interlaminare Model. American Society for Composites 31st Technical Conference and ASTM Committee D30 Meeting, USA, 2016.
7. **Hassoon OH**, Tarfaoui M, A. El Malki. The effect of Composite structure flexibility on slamming impact loads: experimental study. ECCOMAS, Marine, Nantes, France, 2017.

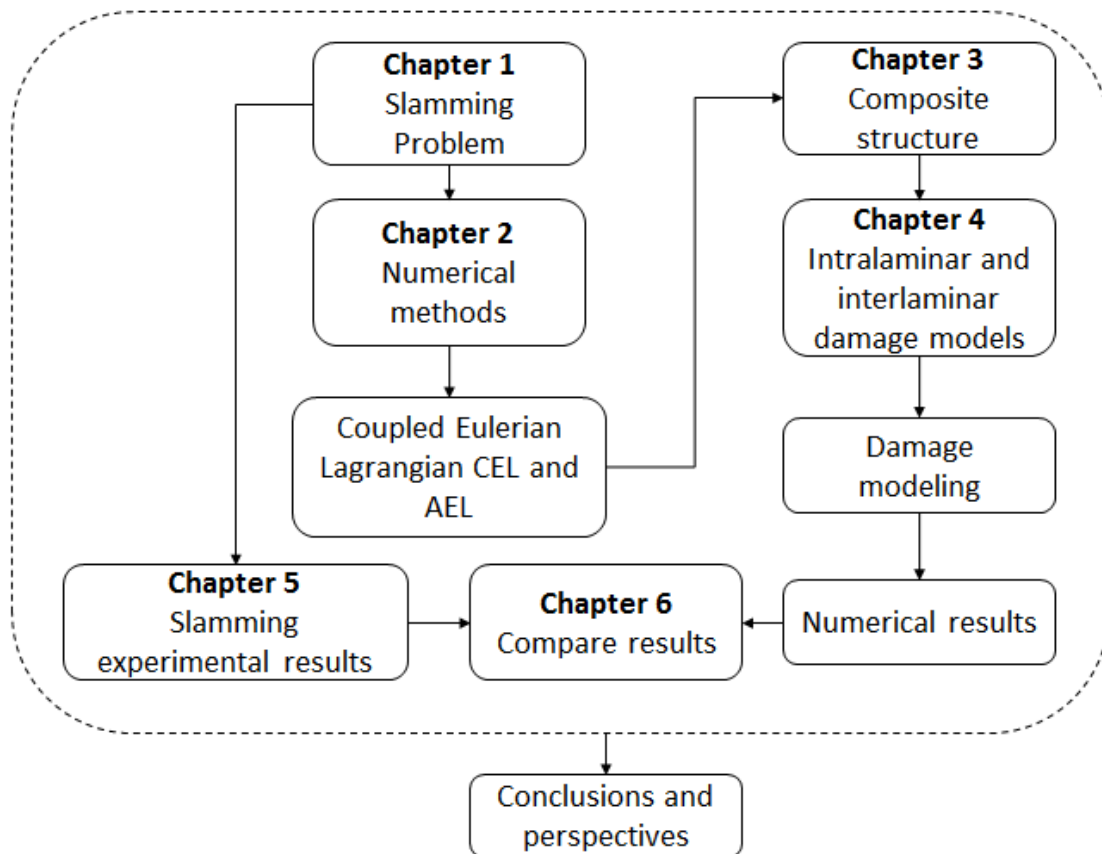


Figure 4. Research methodology of the study

References

- [1] R. E. D. Bishop, W. G. Price, "Ship response," Hydroelasticity of ships, London, New York, Melbourne, Cambridge university press, 1979, pp. 1-10.
- [2] R. Sheno, J. Wellicome , "Response of sandwich structures to slamming and impact loads," Composite materials in maritim structures, Cambridge university press, 1993, pp. 161-176.
- [3] J. P. Dominic, "A hydroelastic method for the analysis of global ship response due to slamming events," Phd thesis, The University of Michigan, 2013.
- [4] T. Allen, "Mechanics of flexible composite hull panels subjected to water impacts," Ph.D. thesis, The University of Auckland, New Zealand, 2013.

CHAPTER 1

Slamming Impact Phenomenon in Naval Application

Contents

1.1 Introduction	10
1.2 Slamming of the rigid body	11
1.2.1 The analytical model for pressure distributions based on Von Kármán.....	12
1.2.2 Analytical model based on pressure distributions using Wagner's slamming impact theory	14
1.3 Experimental investigations on rigid bodies under the slamming impact.....	21
1.4 Experimental studies of the deformable slamming impact	23
1.5 Numerical modelling of fluid-structure interaction on slamming impact	26
1.5.1 The multiple material Lagrangian-Eulerian ALE model	26
1.5.2 The Smoothed Particle Hydrodynamics (SPH) model	29
1.5.3 Computational Fluid Dynamics (CFD).....	31
1.6 Hydroelasticity effect on the slamming phenomenon	33
1.7 Effect of the air cushioning on the slamming.....	35
1.8 Conclusions	36
References	37

1.1 Introduction

Slamming is the water impact loads against the hull bottom which has important influence on the structural ship design. These loads can cause both local and global effects and generate unwanted vibrations in the structure, Figure 1. 1. The global effect is often called whipping. The hydrodynamic effect is important parameter for the global slamming event. On the other hand, local slamming can cause a high pressure impulse which happens in small time [1, 2]. Loads that occur during the slamming of the body into a water surface are strongly relevant in defining vessels design requirements. Unfortunately, the analysis of this scenario are challenging for several reasons. During impact, free surface was characterized by a thin jet with velocities that are much larger comparing with the body velocity. This means that free-surface undergoes stretching and its topology becomes extremely complex, especially with elastic bodies that may require a more in-depth investigation about the pressure changing distribution, local and global stresses [3]. The slamming impact could be categorized into four groups as bottom, wet-deck, bow stem and bow-flare slamming, Figure 1. 2 [4].



Figure 1. 1. High speed vessel with slamming impact

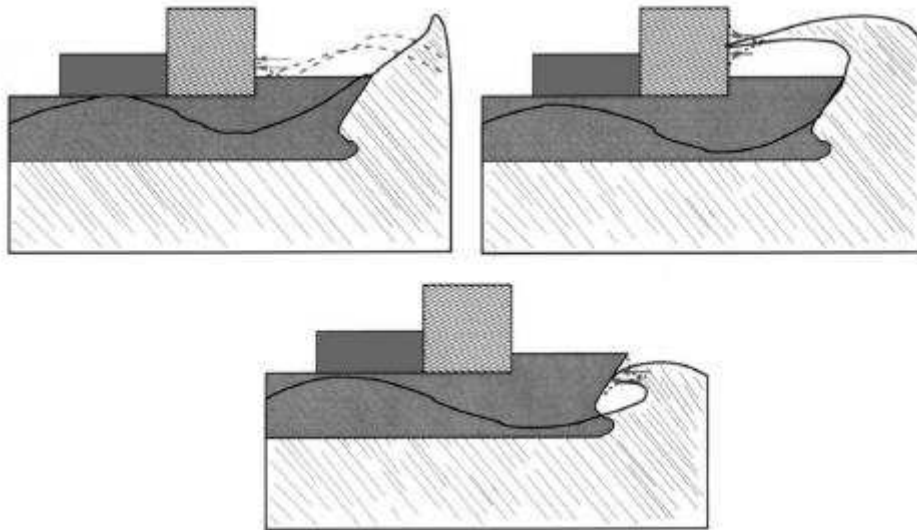


Figure 1. 2. The slamming impact categories [4]

1.2 Slamming of the rigid body

The major interest of ship engineers is to find the analytical solution capable of estimating the hydrodynamic loads and the impact pressure distribution when the slamming event occurs, as these loads can be used for structural analysis during the design process [5]. The slamming pressure distribution can be used in the static structure analysis to find the local impact induced stresses, when the local deadrise angle between the fluid and the structure is not very small at the impact position, while the hydrodynamic calculations can be assumed for a rigid body [1]. Several assumptions were established to calculate the pressure for the rigid body which assumes the fluid is incompressible and the flow is irrotational. Von Karman who is the first author attempting for determining analytically the slamming loads using the mass conservation with disregarding the effect of free jet flow [6]. More adapted method based on Wagner theory that taken into account the effect of jet flow of free surface, which assume the impact of the blunt body for small deadrise angles [7]. Dobrovol'skaya [8] introduced a similar solution for the symmetric wedge with a constant entry velocity, which calculated analytically by integrating the solution numerically. This method is suitable for a variety of deadrise angles. In contrast, the drawback of this method is that it is incapable of solving the flow for arbitrary buoys. Zaho and Faltinsen [9] presented numerical results of water entry problem with constant velocity using the new similarity solution without flow separation. This method was applied to two dimensional arbitrary cross-section for a wide range of deadrise angles using a Boundary Element Method (BEM). The jet flow was cut off

to give more stable numerical results in small deadrise angles. This gave a good estimate compared with other approaches. An extension of this method for asymmetric bodies was performed to include the flow separation from the Knuckles. The flow separation was estimated using the Kutta condition. The results of this method were compared with drop test experiments to validate wedge and flare sectional for shapes of vessel [10]. Yettou et al. [11] developed a new analytical solution for rigid symmetrical wedges entering the water by extending the approach of Mei [12], taking into account the effect of impact velocity reduction on the hydrodynamic pressure and force, Figure 1. 3. They explained that the pressure coefficient reduction over time depends on the body mass and the initial impact velocity. Scolan and Korobkin [13] used inverse Wagner theory for the three dimensional bodies of water entry problem, by assuming that the velocity of the fluid and the projection plane of the wetted surface were given at any time instance during impact duration.

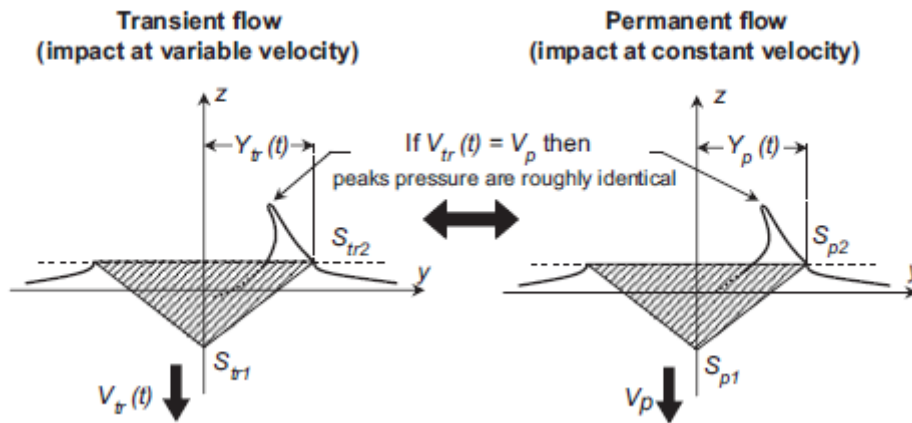


Figure 1. 3. Analogy between constant and variable impact velocity for the wedge

1.2.1 The analytical model for pressure distributions based on Von Kármán

The slamming theory was initially studied by Von Kármán in order to analyse the slam induced loads on the bottoms of seaplanes during landing, by simplifying the slamming problem of a wedge [6]. He studied the theoretical solution a deadrise angle of around 20° for the wedge based on the conservation of added mass. Knowing that the angle between the horizontal plane of water surface and the body is β , and the wetting half width in calm water is x , see Figure 1. 4. The calculation of the force applied to the structure was obtained by the use of the conservation of momentum and given by Equation (1. 1):

$$M * V_0 = (M_{add} + M) * V, \tag{1. 1}$$

where, $M_{add} = \frac{1}{2} x^2 \rho \pi$

$$V(M_{add} + M) = M * V_0 \quad (1.2)$$

$$V = \frac{dy}{dt} = \tan \beta \frac{dx}{dt} \quad (1.3)$$

Where M_{add} , is the unit added mass of the wedge, M the total added mass of the wedge, V_0 is the initial velocity of the wedge and V represents the impact velocity of the first contact.

By combining Equations (1.2) and (1.3), we will have:

$$\frac{dx}{dt} = \frac{V_0 \cot \beta}{1 + \frac{x^2 \rho g \pi}{2M}} \quad (1.4)$$

Then the acceleration of the fluid can be calculated by derivative of Equation (1.4). Therefore the impact force can be calculated using Newton's second law ($F = Ma$) and the pressure defined as:

$$P = \frac{F}{2x} = \frac{\rho V_0^2}{2} \frac{\pi \cot \beta}{\left(1 + \frac{x^2 \rho g \pi}{2M}\right)^3} \quad (1.5)$$

According to Von Kármán, the maximum pressure occurs in the middle of the plate and the first contact can be determined as:

$$P_{max} = \frac{\rho V_0^2 \pi \cot \beta}{2} \quad (1.6)$$

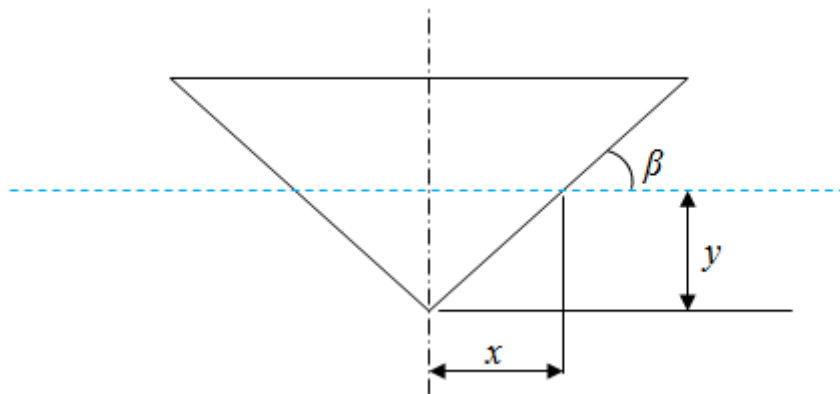


Figure 1. 4. Schematic of rigid wedge, Von Kármán method [6]

The jet flow of the fluid along the interface is not taken into consideration in this method. Therefore, slamming pressure distribution cannot be determined depending on the conservation of the momentum, therefore fluid mechanics was applied to the slamming phenomena.

1.2.2 Analytical model based on pressure distributions using Wagner's slamming impact theory

Wagner extended the Von Karman's method which takes into account the jet flow effect [7]. This theory assumed that the fluid is ideal and incompressible. It is also ignore the air cushion effect gravity can be neglected as the acceleration of the fluid was assumed to be higher than gravity. Figure 1.5 shows the impacting symmetric body and the free surface in the outer flow domain. The water entry velocity V is constant, the Vt represents the submergence of the lowest point of the body from the free water surface. There is an up-rise water caused by the impact; the volume of the water above $z = 0$ is equal to the volume of the water bellow $z=0$ for the body's displacements for $z \leq 0$.

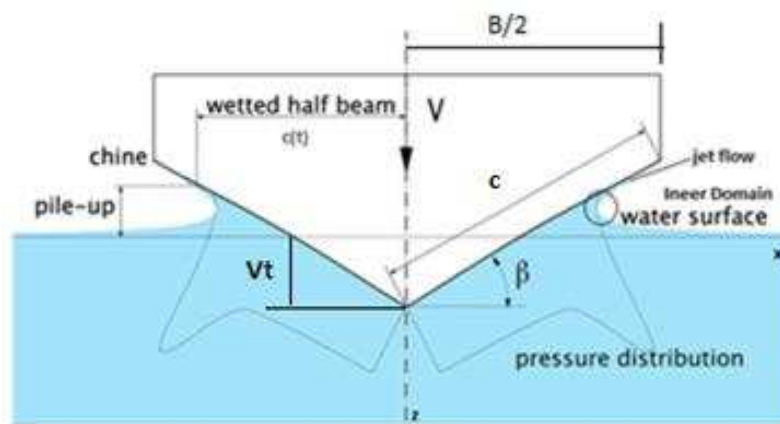


Figure 1.5. Slamming impact of the wedge body

By examining Euler's equations which are the basis when deriving Bernoulli's equation:

$$\frac{dv}{dt} + v \cdot \nabla v = -\frac{\nabla p}{\rho} - gK \quad (1.7)$$

Where v , p , g , K represent respectively, the fluid velocity, the pressure, the gravity and the unit vector along the z axis. Assuming that both $v \cdot \nabla v$ and gK are small relative to dv/dt then:

$$\rho \frac{dv}{dt} = -\nabla p \quad (1.8)$$

Assuming that the water surface is calm and has irrotational flow, then $v = \nabla\phi$ represents the potential velocity of the fluid relative to the z axis and x axes that is approximately equal to the total potential velocity relative with time:

$$\nabla \left(\rho \frac{d\phi}{dt} + p \right) = 0 \quad (1.9)$$

Assuming that there is no surface tension and atmospheric pressure p_a on the free surface, this means that $\rho \frac{d\phi}{dt} + p$ is a constant, which gives:

$$p - p_a = -\rho \frac{d\phi}{dt} \quad (1.10)$$

On the free water surface $p = p_a$, therefore $\frac{d\phi}{dt} = 0$. The water particles move at initial time with $\phi=0$.

The free surface moves when the $\frac{d\phi}{dt} \neq 0$. According to the boundary condition on the wetted body surface, then:

$$\frac{d\phi}{dz} = -V, \quad |x| \leq c_t, \quad z = 0, \quad (1.11)$$

Where V represents the vertical velocity of the structure

Integral the both side of the equation above. Therefore, the velocity potential on the body surface can be formulated as follows:

$$\phi = -V\sqrt{c^2 - x^2(t)}, |x| \leq c_t \quad (1.12)$$

To determine the hydrodynamic pressure, V will be time-dependent, suppose that the vertical distance of the lowest point on the keel is $\int_0^t v(t)dt$ relative to the calm water surface, which gives:

$$p - p_a = \rho V \frac{c}{\sqrt{(c^2 - x^2)}} \frac{dc}{dt} + \rho \sqrt{(c^2 - x^2)} \frac{dV}{dt} - \frac{1}{2} \rho V^2 \frac{x^2}{c^2 - x^2} \quad (1.13)$$

The first term in Equation (1.13) was denoted as the slamming pressure. It is associated with the rate of change of wetted surface which is approximately $2dc/dt$. The second term is called the added mass pressure, which equals to infinite pressure at $x = \pm c$, this state is unphysical.

From boundary conditions where $\frac{d\phi}{dz} = \frac{V_x}{(x^2-c^2)^{1/2}}$, $x \leq c_t, z = 0$, the elevation of free water surface is:

$$\eta(t) = \int_0^t \frac{d\phi}{dz} dt \quad (1.14)$$

If the fluid particles rise to the free water surface and the same position on the x-axis of the body surface, then $\eta(t)=\eta_b$, and assuming that $V(t) = V \frac{dt}{dc}$ then:

$$\eta(t) = \eta_b(x) = \int \frac{V(c)x}{\sqrt{(x^2 - c^2)}} dc \quad (1.15)$$

For the wedge, the curve shape is $\beta_b=x \tan\beta$, therefore, the half wetting width $c(t)$ at any instant time is equal:

$$c(t) = \frac{\pi}{2 \tan \beta} \int_0^t V(t)dt \quad (1.16)$$

By deriving both sides of Equation (1.16) as a function of the time we obtain:

$$\frac{dc}{dt} = \frac{\pi}{2 \tan \beta} V * t \quad (1.17)$$

When the impact velocity is constant during the penetration period, then the second right term of the equation (1.13) is equal to zero, and thus the pressure coefficient C_p has been obtained:

$$C_p = \frac{p - p_a}{\frac{1}{2} \rho V^2} = \frac{\pi c}{\tan \beta \sqrt{(c^2 - x^2)}} - \frac{x^2}{c^2 - x^2} \quad (1.18)$$

Where the maximum peak value of the pressure according to Wagner's theory is:

$$C_{p \max} = 1 + \frac{\pi^2}{4 \tan^2 \beta} \quad (1.19)$$

To determine the slamming force along the body surface, we integrate Equation (1.13) as follows:

$$F = \int_{-c}^c p \, dx = \rho V c \frac{dc}{dt} \int_{-c}^c \frac{dx}{\sqrt{c^2 - x^2}} + \rho \frac{dV}{dt} \int_{-c}^c \sqrt{c^2 - x^2} \, dx \quad (1.20)$$

Thus

$$F = \rho \pi V c \frac{dc}{dt} + \rho \frac{\pi}{2} c^2 \frac{dV}{dt} \quad (1.21)$$

For the wedge, the vertical force coefficient of a unit length with constant velocity as follows:

$$C_F = \frac{F}{\rho V^3 t} \tan^2 \beta \quad (1.22)$$

The vertical force coefficient equals $3\pi/4$ according to Wagner's theory, while in Von Karman's theory this coefficient equals π because it ignores the free water surface elevation.

As illustrated in Figure 1. 6, based on the asymptotic method the slamming impact event could be decomposed into three regions [14]:

1. The outer domain: where the flow is similar that obtained around a flat plate.
2. The inner domain: the spray source domain near the contact line where the flow overturns to create a jet.
3. The jet domain.

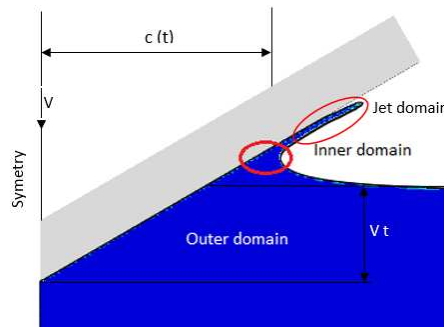


Figure 1. 6. Slamming model description for inner, outer and jet flow domains

A- The outer domain

This problem reduces to Taylor series at the first-order of the conservation equations in the neighbourhood of zero. Boundary conditions are projected onto the plane $z = 0$. Assuming that the fluid is initially calm and irrotational, then:

$$\vec{v} = \nabla\phi \tag{1.23}$$

By using the mass conservation equation, the velocity potential satisfies the Laplace equation:

$$\nabla^2\phi = 0 \tag{1.24}$$

By submitting Eq. (1.7) in equation below, $\vec{f}_f = -\rho gK$, where \vec{f}_f is the gravitational forces of the fluid, g is the acceleration of gravity, then we obtain the pressure in terms of the velocity potential.

$$\frac{d\phi}{dt} + \frac{1}{2} (\nabla\phi)^2 + \frac{p}{\rho} + gK = 0 \tag{1.25}$$

For the free surface boundary condition there is no pressure $p=0$, and if the gratify effect are neglected, and thus the pressure is determined by the potential rate and quadratic terms of the velocity potential.

$$\frac{d\phi}{dt} + \frac{1}{2} (\nabla\phi)^2 = 0 \tag{1.26}$$

Assuming that atmospheric pressure $p_a=0$ in Equation (1.10), the water particles start at initial time with $\phi=0$ at $t=0$ and $z = 0$, then we obtain the pressure:

$$p = -\rho \frac{d\phi}{dt} \tag{1.27}$$

The problem could be solved analytically by determining of free-surface elevation and the velocity potential:

$$z(x, t) = -Vt + V \int_0^t \frac{x}{x^2 - d^2(t)} dt \tag{1.28}$$

And,

$$\phi = -v\sqrt{c^2 - x^2(t)} \quad (1.29)$$

Where c represents the projection of the wetted line on the water surface $z=0$, thus the pressure for the outer domain is:

$$p_e(x, t) = \rho \frac{V c(t)}{\sqrt{c^2(t) - x^2}} \cdot \frac{dc}{dt}, \quad \text{for } x < c(t), \quad \text{where } c(t) = \frac{\pi \cdot V}{2 \tan(\beta)} \cdot t \quad (1.30)$$

B- The Inner domain.

For the inner domain based on the Taylor expansion, where $x=c$, the jet flow thickness is equal to:

$$\delta(t) = \frac{\pi V^2 c(t)}{8} \cdot \left(\frac{dc}{dt}\right)^2 \quad (1.31)$$

The inner pressure could be determined as follow:

$$p_{in}(x, t) = \frac{2\rho u}{(1+u)^2} \cdot \left(\frac{dc}{dt}\right)^2 \quad (1.32)$$

Where u related to x as follow:

$$x - c(t) = \frac{\delta(t)}{\pi} (-2 \ln u - 4u - u^2 + 5) \quad (1.33)$$

The maximum p_{in} occurs when:

- $0 < u < 1$ for $x > c(t)$
- $u = 1$ for $x = c(t)$
- $u > 1$ for $x < c(t)$

The common pressure between the inner and outer domain becomes:

$$p_{com} = \rho \frac{V c(t)}{\sqrt{2c(t)(c(t) - x)}} \cdot \frac{dc}{dt} \quad \text{for } x < c(t) \quad (1.34)$$

Any moment of impact can determine the hydrodynamic pressure can determine the hydrodynamic pressure by summation of the outer and inner pressure domains and subtracting the common values of both, assuming the velocity is constant [9].

The pressure for the rigid body equals:

$$p = p_{in} + p_{out} - p_{com} \tag{1.35}$$

Considering that the velocity is not constant over the time, this should be considered to take the wetted surface calculation, therefore the outer pressure is given by:

$$p_e(x, t) = \rho \frac{V c(t)}{\sqrt{c^2(t) - x^2}} \cdot \frac{dc}{dt} + \rho \sqrt{c^2(t) - x^2} \frac{dV}{dt}, \quad \text{for } x < c(t) \tag{1.36}$$

According to the analytical methods mentioned above, the predicted of slamming loads results have limited usefulness, as they are limited to simple geometrical shapes and just the initial stage of the impact [15]. Table 1. 1 illustrates some the analytical and numerical methods of impact slamming for a rigid body.

Approaches	Theory base	Free surface	C_F	P_{max}
Von Kármán (1929)	Momentum theory	Negligible deformation of free surface	π	$P_{max} = \frac{\rho V_0^2 \pi \cot \beta}{2}$
Wagner (1932)	Potential flow theory	The free surface (pile- up) taken into account	$3\pi/4$	$P_{max} = \frac{\rho V_0^2}{2} \left[1 + \frac{\pi^2 \cot^2 \beta}{4} \right]$
Zaho and Faltinsen (1993,1996)	Potential theory Non-linear BEM	The free surface (pile- up) and flow separation take into account	$\frac{F}{\rho V^3 t} \tan^2 \beta$	$P_{max} = 0.5 \rho V^2 \frac{\pi^2}{\tan^2 \beta}$

Table 1. 1. Analytical and numerical methods of impact slamming for rigid body

1.3 Experimental investigations on rigid bodies under the slamming impact

There are several experimental attempts which have studied the slamming phenomenon to further the understanding of influence of hydrodynamic loads against ship structures. However, these attempts have concentrated on rigid bodies and most of these have been achieved using drop test impact. Chuang [16] performed a series of experimental tests for a wedge-shaped steel body with deadrise angles less than 15° to determine the effect of trapped air, which has an important influence on the slamming phenomenon with deadrise angles β such that $(0^\circ < \beta < 15^\circ)$. Wu et al. [17] analysed the hydrodynamic problem numerically and experimentally for symmetric wedges with different weights, entering velocities and deadrise angles by means of the drop test. They noted that the comparisons between the numerical and experimental results were in good agreement, and that the divergence became increasingly apparent for the deadrise angle less than 45° . They explicated this discrepancy by the air cushion, which leads to a change in the acceleration before and after the wedge enters the water. B. Peseux et al. [18] solved three dimensional Wagner's theory numerically using the finite element method for rigid and deformable structures and performed a series of the experimental tests with different deadrise angles and thicknesses, and analysed the distribution and evolution of the pressure. Backer et al. [19] performed a series of drop tests for hemispheres and conical shapes with different deadrise angles. Pressure distribution and elevation of the water flow were compared with a three dimensional asymptotic theory with constant velocity. They found that this method overestimated the experimental results by 25-50 %, Figure 1. 7a. This difference may be attributed to the separation of the water jet from the body which was not considered in the analytical method, Figure 1. 7b.

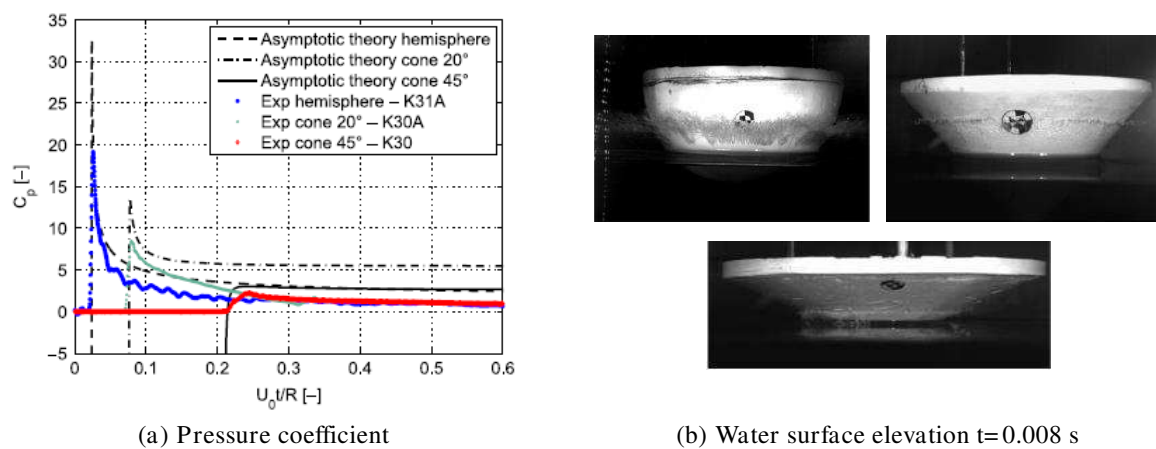
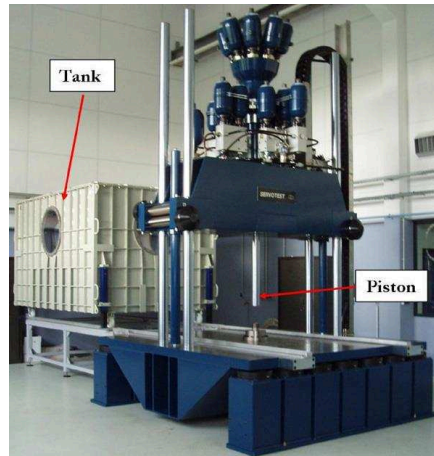
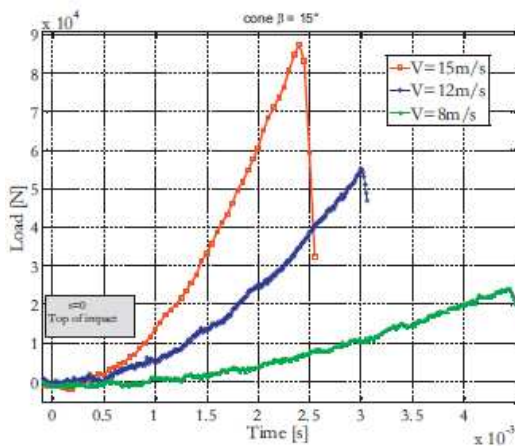


Figure 1. 7. Slamming impact of axisymmetric bodies [19]

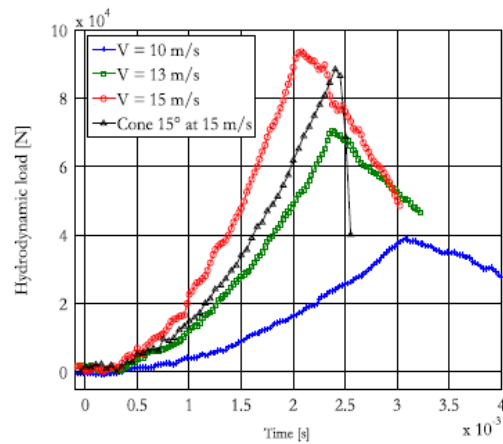
Constant impact velocity has been used widely to enhance results of analytical methods. Tveitnes et al [20] studied the water entry problem for wedge-shaped section with constant velocity to further the understanding of planning and slamming of marine vessels. El Malki Alaoui et al. [21, 22] performed experimental studies for both axisymmetric and pyramid rigid bodies under constant impact velocity up to 20 m/s using a high-speed shock machine, Figure 1. 8.



(a) High speed shock machine



(b) Hydrodynamic loads, Cone



(c) Hydrodynamic loads, Pyramid

Figure 1. 8. Slamming impact with constant velocity, $\beta=15^\circ$ [21, 22]

Nuffel et al [23] studied the local hydrodynamic pressure of a large set of slamming drop experimental tests for quasi-rigid cylinders, Figure 1. 9. They found that test results for deadrise angles larger than 4.25° gave a good estimation of impact pressure comparing with the Wagner's theory. On the other hand, the results diverge from the Wagner results when the deadrise angle is less than 4.25° . They attributed this to the compressibility of water not being included in Wagner's theory as compressibility can play a significant role in slamming impact.

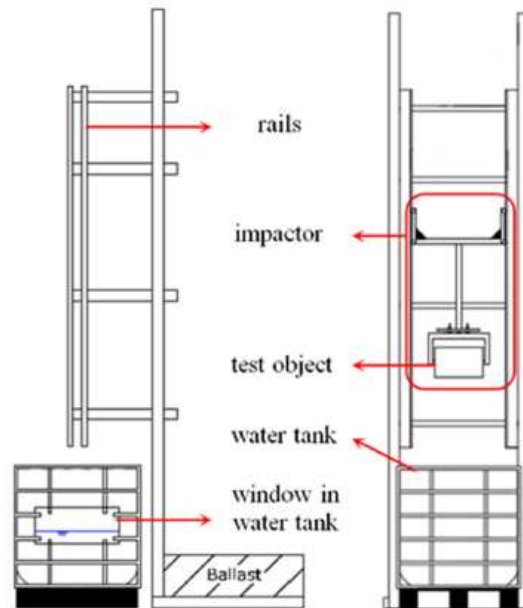


Figure 1. 9. Schematic of the experimental set-up [23]

1.4 Experimental studies of the deformable slamming impact

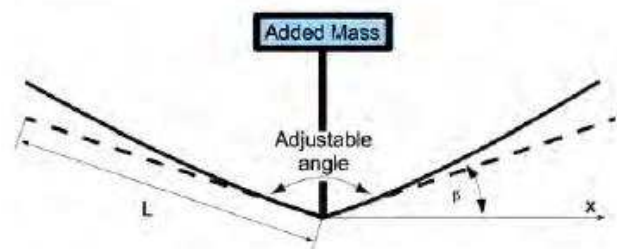
The slamming impact could be categorized as a longitudinal and transverse strength loading by water surface that hits the structure severely. However, the force generated from this phenomenon can be combination of both longitudinal and traverse loading, and as a result causes global and local effects on the structure. Besides that, the vessel speed has become an important aspect in marine design. Therefore, design requirements have been optimized in relation to the structural weight. For this reason, composite materials and sandwich panels are widely used in the construction of vessel structure. Consequently, analysis of the hull response to static and dynamic loadings should be a prerequisite in ship design. However, the structural responses were dominated by local loads rather than global loads.

In deformable structures, the hydrodynamic and hydroelastic influence are considered simultaneously. Thus, the interaction of these influences happening in some manner cause the water flow to change due to structural elastic vibrations, and the difference in hydrodynamic pressure in the particular locations [24]. This flexibility can change the fluid-structure interaction, which can be observed in high-speed vessels under slamming impact. This situation has been observed by other researchers, who have pointed out that the loads on elastic plates differ from those experienced by rigid plates [25]. Stenius et al. [26] used numerical simulations and experimental tests to estimate the hydroelastic problem related to

the panel-water impacts for high-speed craft. Experimentally, deflections and strains were compared with the corresponding data of non-hydroelastic reference solutions. The finite element simulation was determined for the quasi-static references of rigid bodies, which indicated that the hydroelastic effects were located close to the panel supports for the very flexible panels and sandwich constructions. Panciroli et al. [5, 27] investigated the water impact problem for the deformable wedge, using experimental and numerical approaches, Figure 1. 10. Their results showed that under different boundary conditions, the hydroelastic influence depended highly on the ratio (R) between the first natural frequency of the structure and the wetting time. Therefore, they used a variant of the panel's stiffness and cantilever boundary condition to obtain a large deformation which made the hydroelastic effects easy to measure and investigate. From these results, they supposed that the hydroelastic influence was important for values of R less than 1, and that the same hydrodynamic pressure was produced when comparing with rigid bodies.



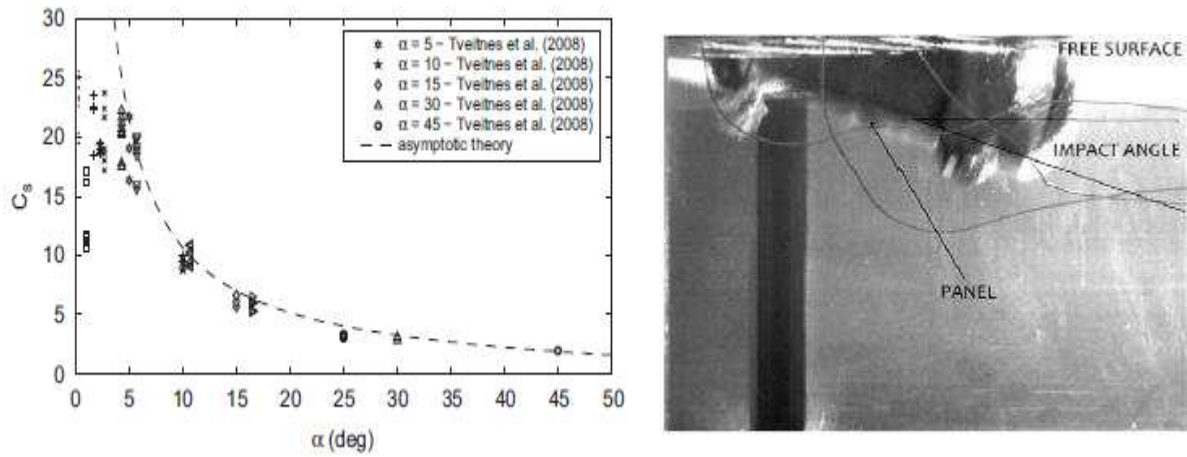
(a) Al panel setup



(b) Boundary condition

Figure 1. 10. Experimental setup [5]

Huera and Gharib [28] experimentally investigated the water entry problem of flat sandwich panels at impact velocities over of 5 m/s. They reported that the loads predicted by the asymptotic theory were in good agreement with the experimental data for deadrise angles greater than 5° . For rigid bodies with small angles, the cushioning effect produced by trapped air appearance in the initial impact duration, Figure 1. 11.



(a) Slamming coefficient with the angle (b) Panel impact with trapped air

Figure 1. 11. Water entry problem [28]

The centre for Advanced Composite Materials, of the University of Auckland [26, 29, 30] conducted experiments in order to investigate the hydroelastic effects due to fluid-structure interaction of the flexible composite panels in high speed marine craft. They characterized the variations in the pressure and the response of these panels using the servo-hydraulic slam testing system (SSTS) for over 6 m/s impact velocity and deadrise angle of 10° , Figure 1. 12. It was observed that panel flexibility has an influence on the total force, and that the lower stiffness panels have a high peak force, Figure 1. 13. They attributed that the variation of the acting force due to the change in local velocity and local deadrise angle along the fluid-structure interface.

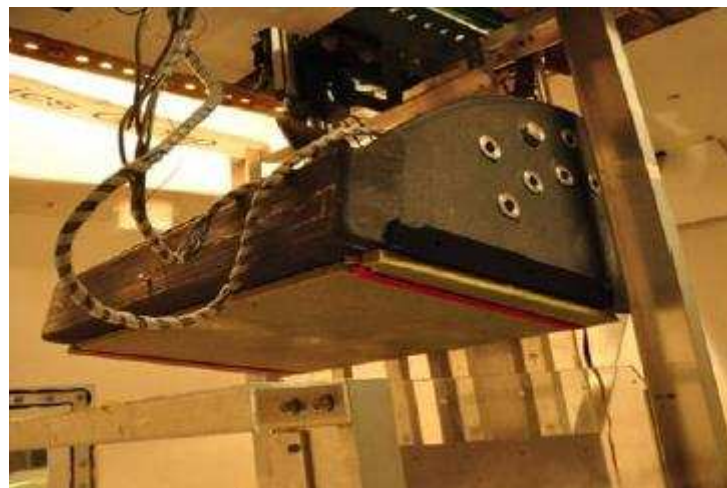


Figure 1. 12. Servo-hydraulic slam testing system (SSTS) [31]

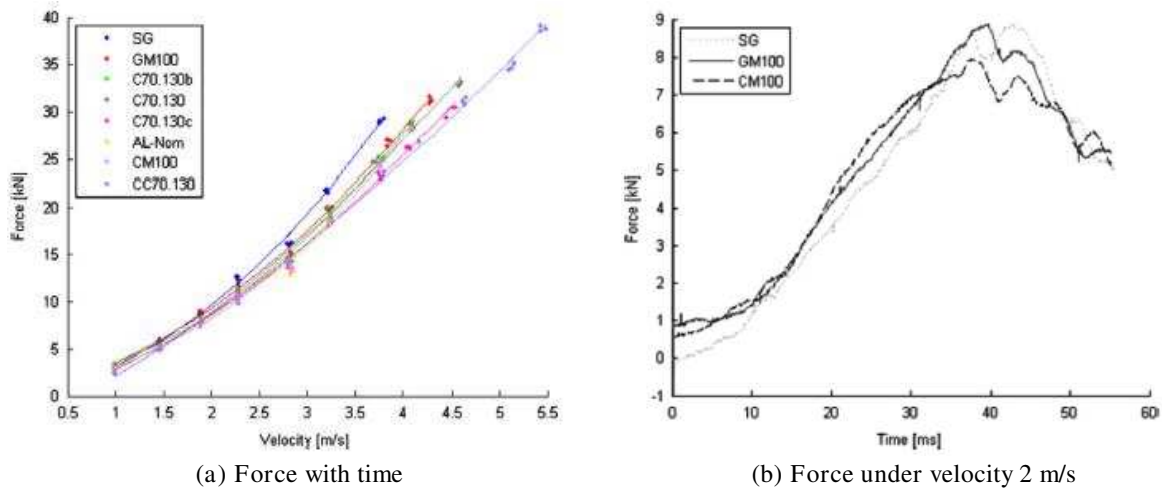


Figure 1. 13. Force with different flexible panels at $\beta=10^\circ$ [30]

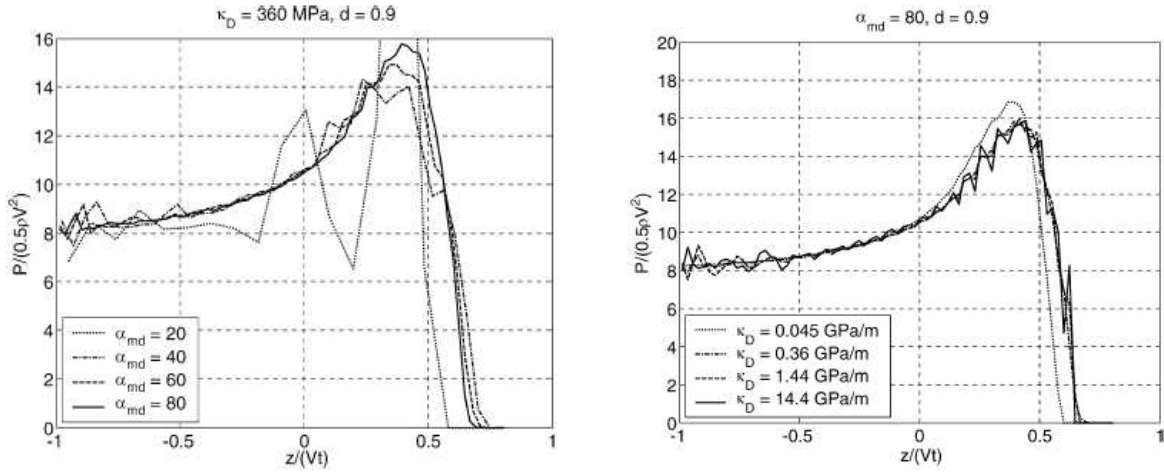
1.5 Numerical modelling of fluid-structure interaction on slamming impact

The Fluid-Structure Interaction problem (FSI) means that the structure interacts with the internal and the surrounding boundaries of the fluid domain, which occurs mainly with deformable structures. Furthermore, the deformation of the structure could modify the fluid flow, thus moderating the hydrodynamic pressure acting on these structures. FSI is an important part of estimating and analysing a variety of engineering applications and is considered a great challenge for many researchers due its nonlinear nature. In the next section, we will examine the different approaches to modelling the FSI problem.

1.5.1 The multiple material Lagrangian-Eulerian ALE model

ALE is a mixture of Lagrangian and Eulerian discretization, which is capable of controlling mesh geometry independently from material geometry [32, 33]. Stenius et al. [34, 35] investigated the water entry problem of hull bottom panels using ALE. A parametric study was performed, which is analysed the effect of the mesh density and contact method, Figure 1. 14. The numerical results showed a good correlation with analytical and experimental approaches. Kaushik and Batra [36] studied the water slamming of deformable sandwich panels using the commercial FE software LSDYNA with the ALE formulation. All geometric nonlinearities were considered when studying deformations of the panel. They take into account the inertia effects in the fluid and solid, assumed the fluid to be compressible. They examined the delamination between the core and the face sheets. The pressure distribution on the wetted panel surface was found to be oscillatory. Wang and Soares [37] investigated the water impact problem for three-dimensional buoys (hemisphere and cones) using the ALE solver based on Eulerian formulation in LS-DYNA software. They concluded

that the mesh density of the fluid is a very important factor to determine the hydrodynamic pressures. The constant impact velocity has a larger influence than those found in the drop test, when comparing total impact force and hydrodynamic pressure.



(a) Normalized pressure distribution for different fluid mesh densities (b) Normalized pressure distribution for increased contact stiffness at constant mesh density

Figure 1. 14. Parametric numerical results for ALE in wedge slamming [34]

ALE model formulations are consists of both a Lagrangian and Eulerian model, the materials arbitrary coordinates are defined corresponding to the reference or global coordinate system. The relationship between these coordinates and the reference coordinate relative to the time were constructed for ALE model as described in Equation (1. 37) [32].

$$\frac{df(X_i, t)}{dt} = \frac{df(x_i, t)}{dt} + w_i \frac{df(x_i, t)}{dx_i} \tag{1. 37}$$

Where X_i , x_i and $w_i = (v - u)$ are the Lagrangian coordinate, Eulerian coordinate and relative velocity respectively. If we defined relative velocity as a difference between the material velocity (v) and the mesh velocity (u), the formulations of the model depended on the conservation equations as followed:

1. Conservation of mass

The conservation of mass means that the material density is constant relative with time and can be described as:

$$\frac{d\rho}{dt} = \rho \frac{dv_i}{dx_i} - w_i \frac{d\rho}{dx_i} \tag{1. 38}$$

Where ρ is the density of the fluid.

2. Conservation of momentum

In the conservation of energy, the governing equation must specify the appropriated initial boundary conditions to represent the ALE description corresponding to Navier-stokes equations:

$$\rho \frac{dv_i}{dt} = \sigma_{ij,j} + \rho b_i - \rho w_i \frac{dv_i}{dx_j} \quad (1.39)$$

σ_{ij} represents the stress tensor and can be described as:

$$\sigma_{ij} = -p\delta_{ij} + \mu(v_{i,j} + v_{j,i}) \quad (1.40)$$

Where μ , is the dynamic viscosity and δ_{ij} is the Kronecker delta function and p is the pressure.

Having defined the initial boundary conditions for the fluid and the body domain as shown in Figure 1. 15, the equations can be solved.

$$\begin{aligned} v_i &= U_i^0 \text{ on } \Gamma 1 & \sigma_{ij}n_j &= 0 \text{ on } \Gamma 2 \\ \Gamma 1 \cap \Gamma 2 &= 0 & \Gamma 1 \cup \Gamma 2 &= 0 \\ V_i(x_i, 0) &= 0 & \text{on } t &= 0 \end{aligned}$$

Where

$\Gamma 1$ is the boundary of the body,

$\Gamma 2$ is the boundary of the fluid,

n_j is the outer unit normal vector on the boundary of $\Gamma 2$,

δ_{ij} is Kronecker's delta function.

3. Energy equation

$$\rho \frac{dE}{dt} = \sigma_{ij}v_{i,j} + \rho b_i v_i - \rho w_j \frac{dE}{dx_j} \quad (1.41)$$

The Eulerian equations used in fluid mechanics can be determined by assuming the velocity of the reference configuration is zero, while the relative velocity between the material

and the reference configuration is the material velocity [38]. w_j is the relative velocity and referred to as the advection term, and is determined from the past material mesh which is transported to the new material mesh. These additional equations make the ALE more difficult to solve than the Lagrangian equations.

To implement the ALE equations to couple the structure-fluid interaction, the time step is divided into two phases. The Lagrangian phase is executed first and then the velocity and the internal energy due to the applied forces are calculated. The equilibrium equations are [38]:

$$\rho \frac{dv_i}{dt} = \sigma_{ij,j} + \rho b_i \quad (1.42)$$

$$\rho \frac{dE}{dt} = \sigma_{ij} v_{i,j} + \rho b_i v_i \quad (1.43)$$

In the Lagrangian phase, mass is automatically conserved, since no material flows across the element boundaries. Secondly, the advection phase is performed, which transports the mass, the internal energy and momentum to the cell boundary.

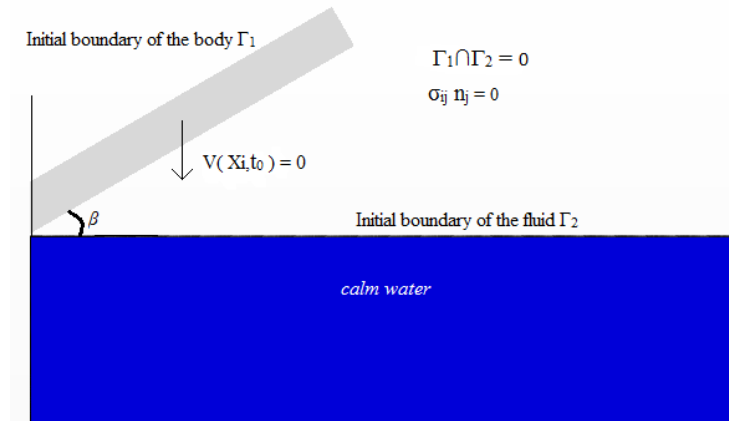


Figure 1. 15. Initial boundary conditions for the fluid and body domain

1.5.2 The Smoothed Particle Hydrodynamics (SPH) model

The smoothed particle hydrodynamics is an effective tool to manipulate the fluid-structure interaction as it replaces the fluid with particles that utilise a Lagrangian approach without mesh. This method was firstly developed by Gingold and Monaghan [39]. The basic formulation of this method is the interpolation procedure of the velocity, mass, force and density for each particle. Therefore, this method requires expensive computational time to

solve the problem which is considered to be the main drawback of this approach. For the water-entry problem, Oger [40] extended the SPH approach by using a new technique based on the particle sampling method. To validate the numerical results, these results were compared with the analytical and experimental approaches, as shown in Figure 1. 16. However, the results obtained were very dependent on the number of practices. Veen and Gourlay [41] investigated the slamming impact on the hull section numerically using the SPH for calculating the slamming load of the vertical velocity in hull cross-sections and added the strip theory to determine three dimensional the nonlinear ship motions. They mentioned that the SPH method is still not recommended to be implemented for events that have a long duration, because it requires significant computation time.

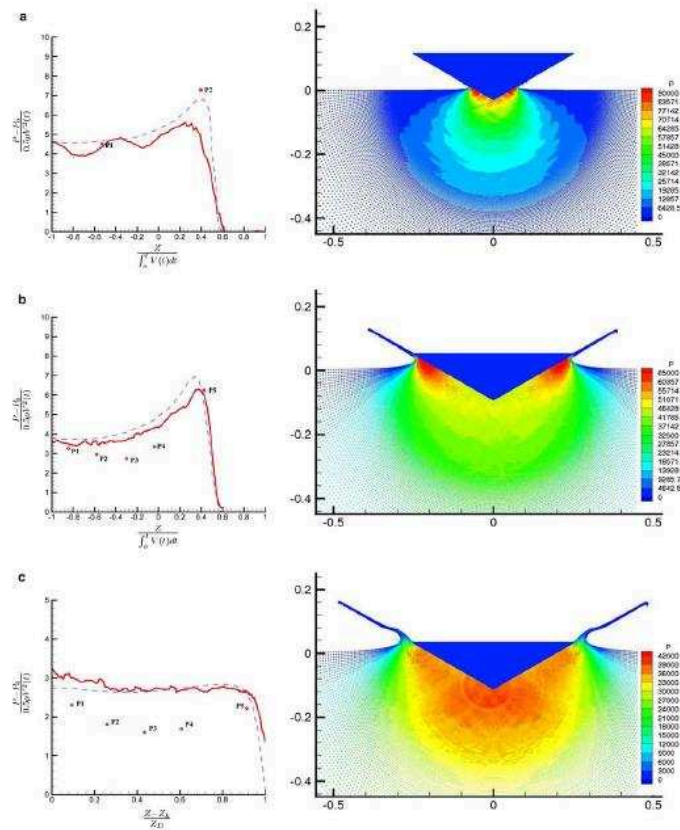


Figure 1. 16. Pressure distribution of SPH results ($\beta=30^\circ$) compared with the analytical and experimental approach carried out by Zhao [40]

Panciroli et al. [42] discussed hydroelastic effects in terms of panel flexibility, impact velocity and deadrise angle using SPH with the built-in the commercial code LS-Dyna. Numerical results were in good agreement with experimental data. They also noted that the different mode shapes dominate the structure deformation with an increase the hydroelastic effects. However, the divergence of the numerical from experimental results was attributed to

the trapped air that occurs during the impact event, therefore they suggested integrating this effect in the numerical model, Figure 1. 17.

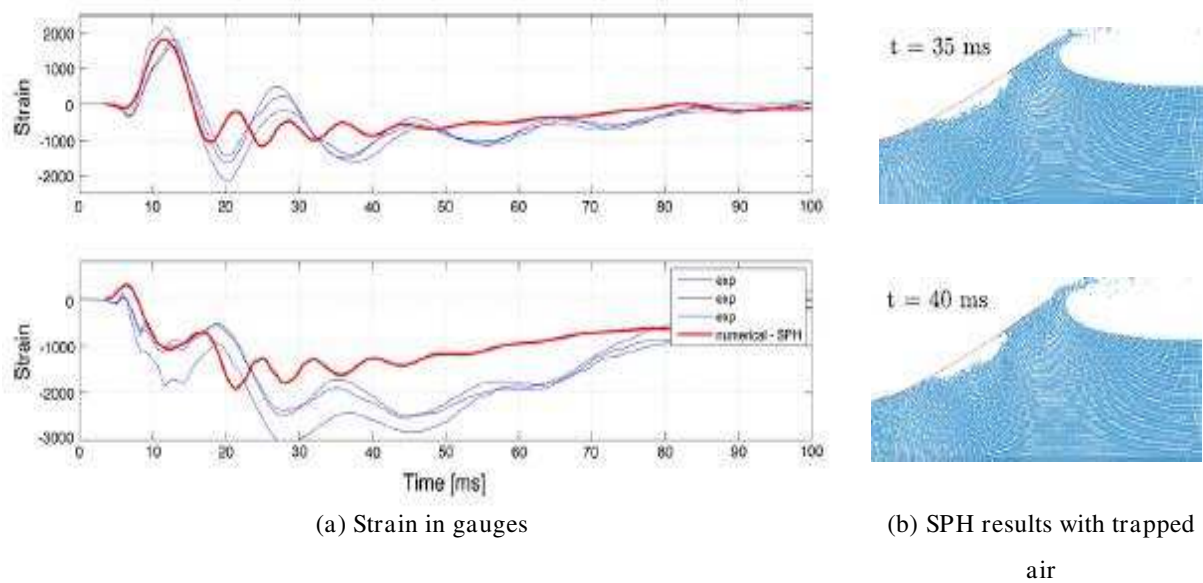


Figure 1. 17. Aluminium wedge impact results ($\beta=15^\circ$), 2 mm, $V = 5$ m/s [42]

1.5.3 Computational Fluid Dynamics (CFD)

The computational fluid dynamics (CFD) method is a mathematical and computational model used to describe fluid flow problems. Maki et al. [3] studied the hydroelastic response of the flexible wedge body as it entered a calm water surface. A combination scheme was performed between the computational fluid mechanics approach built-in Open Foam software and the finite element method in single way coupling. The pressure applied to the rigid body which was calculated in CFD was transferred and adapted to a dry model grid in FEM as a function of time, Figure 1. 18. Authors identified several limitations of this approach, for example, the model has poor time accuracy during impact compared with fully coupled methods.

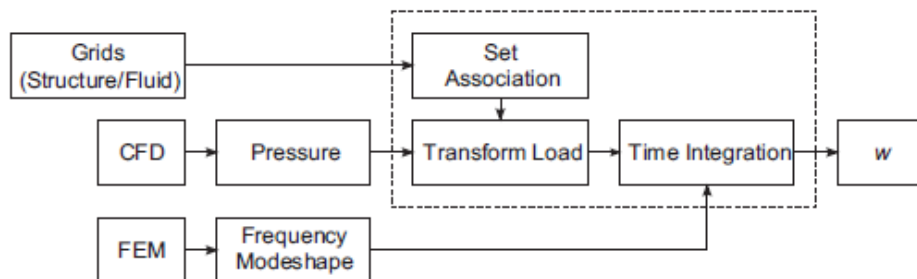
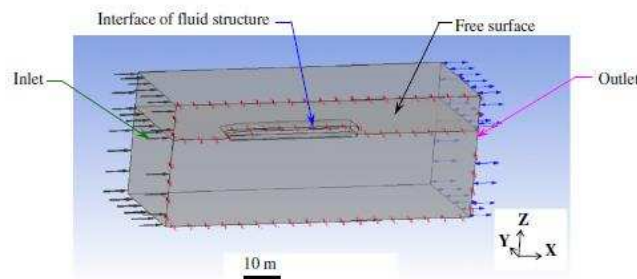
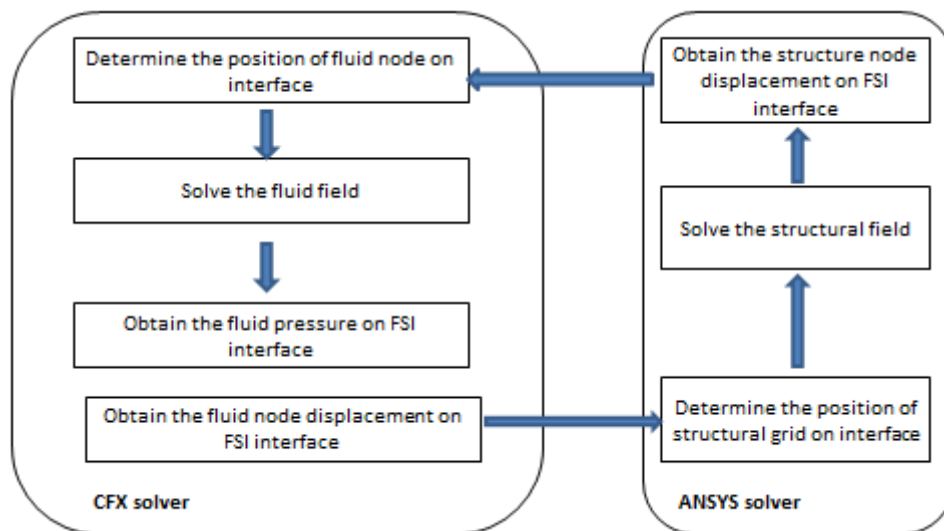


Figure 1. 18. Simulation procedure

Siyauan and Mahfuz [43] used finite element analysis to study the fluid structure interaction (FSI) for sandwich structure. This was accomplished by coupling the finite element analysis (FEA) model with the computational fluid dynamic (CFD) model, Figure 1. 19 a,b. The global model constructed using a composite and foam of the sandwich structure, then the force and displacement form of this model was transported to the sub-model with a refined mesh. The interlaminar and shear stress distribution were determined at the core and faces.



(a) Fluid domain in CFX



(b) Flow chart of two way fluid structure interaction

Figure 1. 19. CFD model [43]

Lu and He [44] solved the fluid structure coupling for two-dimensional slamming V-shapes using the boundary element method (BEM) and the finite element method, Figure 1. 20. They introduced extra jet-elements and some conditions on the jet thickness for better estimation of the jet flow. The hydroelastic influence was studied according to different plate thicknesses and deadrise angle. Another method that deals with different finite element methods was presented by Yang [45] who computed the slamming forces on 2D and 3D bodies entering calm water with constant velocity by employing a CIP method. The nonlinear

water entry problems governed by the Navier-Stokes equations were solved by a CIP-based finite difference method on a fixed Cartesian grid.

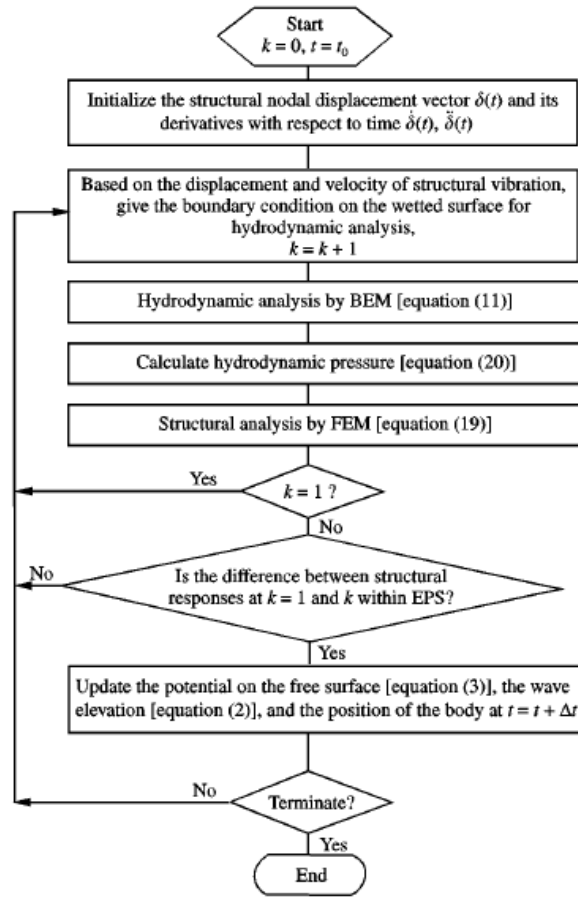


Figure 1. 20. Flowchart of the iteration method [44]

1.6 Hydroelasticity effect on the slamming phenomenon

The main difference in the hydrodynamic loads between the rigid and deformable bodies is the presence of the hydroelastic influence for deformable structures. Elastic structures with low deadrise angles are more subjected to higher dynamic loads when comparing with rigid structures, since a small deflection of the deformable structure could cause a large difference in the elevation of the water surface along water-structure interface and the hydrodynamic loads. This situation is still difficult to analyse and calculate. Therefore, few efforts have been made to find a solution for deformable bodies [5]. Hydroelasticity occurs at a small relative angle between the body surface and the fluid surface, thus these effects must be considered. On the other hand, hydroelasticity is relative to the change in the local deadrise angle and the impact velocity [42]. Therefore, the hydroelastic effect will be a function of the natural

frequency of both the dry structure and the wetting time duration. Vessel designers must have a clear concept of these effects before they can be included in the design specifications. According to Bereznitski [46], in order to specify whether the slamming event has hydroelastic effects, the first natural frequency of the structure must be calculated in the dry phase. The ratio between the wetting time and the dry time of the first natural vibration was determined to quantify the hydroelastic influence. As shown in Figure 1. 21, if the value is less than two this indicated that fluid-structure interaction was important for the structure response.

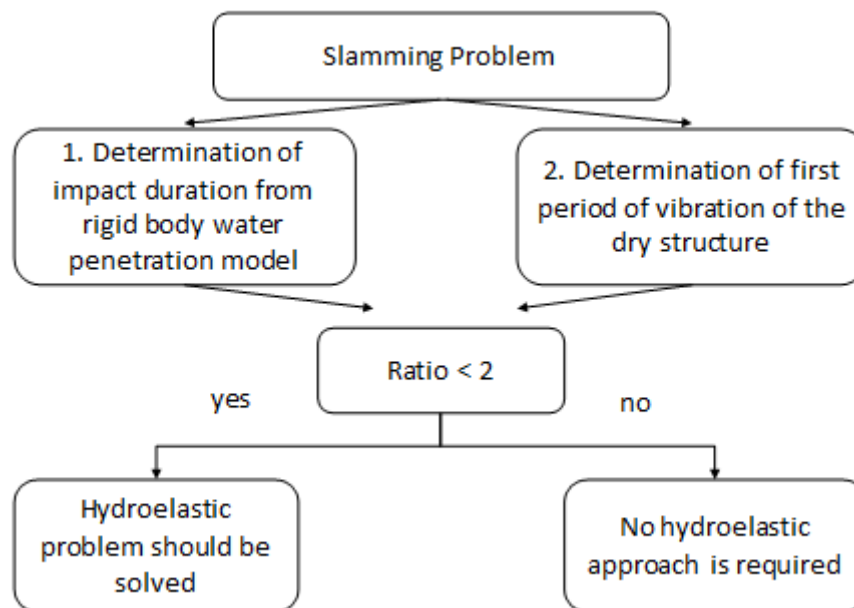


Figure 1. 21. Analysis of the hydroelastic problem [46]

Loads can be important factor even local pressure increased. These effects lead to vibrations in the structure and caused cavitation and ventilation. Faltinsen suggests a non-dimensional parameter that the hydroelasticity effects become important for a wedge shaped cross section when:

$$\frac{\tan\beta}{V\sqrt{\rho L^3/EI}} \leq 0.25 \tag{1. 44}$$

Where EI is the bending stiffness of the structure, L is the length of the structure, ρ is the density of the structure and β is the deadrise angle.

The hydroelastic effects include both dynamic and kinematic effect. Dynamic effects happen due to the interface between the hydrodynamic forces, inertial forces and structure elastic forces, while kinematic effects are related to interactions between the hydrodynamic forces and the change in the local deadrise angles when the structure is deformed [26].

The boundary conditions of the panel have an effect on the hydroelastic effects. Stenius et al. introduced this effect to estimate the relation between the loading period and the natural period as follows [35].

$$R = 4 \left(\frac{\mu_{NP}}{\pi} \right)^2 \frac{\tan\beta}{V} \sqrt{\frac{D}{\pi\rho_w b^3}} \quad (1.45)$$

Where μ_{NP} is the boundary condition factor (for clamped boundaries = 4.73 and for simple support boundaries = π), D , ρ_w and b is bending stiffness, water density and the panel length from keel to the chine edges, respectively. They suggest that the hydroelastic has an influence on slamming event for $2 < R < 5$.

1.7 Effect of the air cushioning on the slamming

In particular, the pressure rises sharply, when the deadrise is lower than 5° so that the slamming phenomenon becomes very important and complex [15]. Occasionally some of the air is trapped between the structure and the free water surface which cause a compression when it cannot escape, that leads to a reduction in pressure. This is called air cushioning that can cause a reduction in the hydrodynamic force acting on the structure. This occurs when the angle between the water and body is too low [47], and when the structure is deformable [48, 49]. Air pressure may, in effect, cause more deformation in both the structure and the free water surface. That is why it is still a challenge to integrate this phenomenon into analytical approaches and therefore, this was limited in experimental studies. Chuang who performed a series of experimental tests to define the effects of the trapped air, indicated that a small amount of air cushioning occurred for deadrise angles higher than 3° . The experiment setup used an electronic detection method to detect the air trapped between the water and the impacted structure [16].

1.8 Conclusions

In the first chapter, we have reviewed several approaches: analytical; experimental and numerical to the water entry problem for both rigid and deformable structures. This review helps comprehend the principles of the slamming phenomenon and identify the strengths and limitations of methods for the assessment of slamming loads. A wide range of works have dealt with the simple shapes of rigid bodies in two-dimensional configuration to simplify the problem. Therefore, they have concentrated on predicting the hydrodynamic loads for fluids rather than for structural responses. Moreover, most experimental tests have been performed using the free drop test, which is not compatible with the concept of analytical methods which determine the slamming loads by supposing a constant vertical velocity during the impact event. Our comparison of the numerical methods has taken into account the feasibility, accuracy and computational-time consumed in handling fluid-structure interaction. In addition, some difficulties present in traditional FSI methods, such as the translation of loads from the fluid to the structural domain and the matching/updating of the mesh in both domains have been examined. This encourages the use of the multi-material simulation model. Consequently, numerical methods based on the Arbitrary Lagrangian-Eulerian (ALE) and Coupled Eulerian Lagrangian (CEL methods) built in Abaqus explicit, have been adopted in this work as this method can simultaneously handle the structure and fluid in a single computation. Therefore, the focus of subsequent chapters is on parametric investigations of numerical methods based on these approaches together with damage modelling in the case of composite materials. Finally, to provide more accurate of the numerical methods, experimental tests were carried out at constant velocity for deformable laminate and sandwich panels.

References

- [1] O. M. Faltinsen, "Slamming, Whipping, and Springing," in *Hydrodynamics of High-Speed Marine Vehicles*, New York, USA, Cambridge University Press, 2005, pp. 302-311.
- [2] R. E. D. Bishop, W. G. Price, "Ship response," in *Hydroelasticity of ships*, London, New York, Melbourne, Cambridge university press, 1979, pp. 1-10.
- [3] K.J. Maki, D. Lee, A.W. Troesch, N.Vlahopoulos, "Hydroelastic impact of a wedge-shaped body," *Ocean Engineering*, vol. 38, pp. 621- 629, (2011).
- [4] O. M. Faltinsen, M. Landrini, M. Greco, "Slamming in marine applications," *Journal of Engineering Mathematics*, vol. 48, pp. 187-217, 2004.
- [5] R. Panciroli, "Hydroelastic impact of deformable wedges," in *Dynamic Failure of Composite and Sandwich Structure*, New York, London, Springer Science, Business Media Dordrecht, 2013, pp. 1-45.
- [6] T. von Kármán , "The impact of seaplane floats during landing," *NACA TN.*, 1929.
- [7] H. Wagner, "Über stoss und gleitvorgänge an der oberfläch von flüssigkeiten," *Zeitschrift fuer Angewandte Mathematik und Mechanik*, vol. 12, pp. 193- 215, 1932.
- [8] ZN. Dobrovolskaya, "On some problems of similarity flow of fluids with a free surface," *Journal of Fluid Mech*, vol. 36, pp. 805-829, 1969.
- [9] R. Zhao, O.M. Faltinsen, "Water entry of two-dimensional bodies," *Fluid Mech*, vol. 246, pp. 593-612, 1993.
- [10] R. Zhao, O.M. Faltinsen , J. Aarsnes, "Water entry of arbitrary two-dimensional sections with and without flow separation," in *Proceedings of the 21st symposium on naval hydrodynamics*, Trondheim, Norway, National Academy Press, Washington, DC, USA, 1996.

- [11] E. Yettou, A. Desrochers, Y. Champoux, "A new analytical model for pressure estimation of symmetrical water impact of a rigid wedge at variable velocities," *Journal of Fluids and Structures*, vol. 23, pp. 501-522, 2007.
- [12] X. Mei, Y. Liu, D. K. Yue, "On the water impact of general two-dimensional sections," *Applied ocean research*, vol. 21, pp. 1-15, 1999.
- [13] Y. M. Scolan, A. A. Korobikn, "Three-dimensional theory of water impact.Part 1. Inverse Wagner problem," *J. Fluid Mech*, vol. 440, pp. 293-326, 2011.
- [14] R. Cointe, "Two-Dimensional Water-Solid Impact," *Journal of Offshore Mechanics and Arctic Engineering*, vol. 111, pp. 109-114, 1989.
- [15] GK. Kapsenberg, "Slamming of ships: where are we now? *Philos Trans Ser A:*," *Philos Trans Ser A: Math Phys Eng Sci*, vol. 369, pp. 2892-919, 2011.
- [16] S. L. Chuang, "Experiments on slamming of wedge-shaped bodies.," *Journal of Ship Research*, pp. 190-198, 1969.
- [17] G.X. Wu, H. Sun, Y.S. He, "Numerical simulation and experimental study of water entry of a wedge in free fall motion," *Journal of Fluids and Structures*, vol. 19, pp. 277-289, 2004.
- [18] B. Peseux, L. Gornet, B. Donguy, "Hydrodynamic impact: Numerical and experiment investigations," *Journal of Fluids and Structures*, vol. 21, pp. 277- 303, 2005.
- [19] G. Backer, M. Vantorre, C. Beels, J. De pré, S. Victor, J. De Rouck, C. Blommaert, W. Van Paepegem, "Experimental investigation of water impact on axisymmetric bodies," *Applied ocean research*, vol. 31, pp. 143-156, 2009.
- [20] T. Tveitnes, A.C. Fairlie-Clarke, K. Varyani, "An experimental investigation into the constant velocity water entry of wedge-shaped sections," *Ocean Engineering*, vol. 35, pp. 1463-1478, 2008.
- [21] A. El Malki Alaoui, A. Nême, A. Tassin, N. Jacques, "Experimental study of coefficients during vertical water entry of axisymmetric rigid shapes at constant speeds," *Applied*

Ocean Research, vol. 37, pp. 183-197, 2012.

- [22] A. El Malki Alaoui, A. Nême, Y.M. Scolan, "Experimental investigation of hydrodynamic loads and pressure distribution during a pyramid water entry," *Journal of Fluids and Structures*, vol. 54, pp. 925-935, 2015.
- [23] D. VanNuffel, K.S. Vepa, I. DeBaere, P. Lavab, M. Kersemans, J. Degrieck, J. DeRouck, W. VanPaepegem, "A comparison between the experimental and theoretical impact pressures acting on a horizontal quasi-rigid cylinder during vertical water entry," *Ocean Engineering*, vol. 77, pp. 42-54, 2014.
- [24] M. Reinhard, A. Korobikin, M. Cooker, "Water entry of a flat elastic plate at high horizontal speed," *J. fluid mech*, vol. 724, pp. 123-153, 2013.
- [25] O. M. Faltinsen, J. Kvålsvold, J. Aarsnes, "Wave impact on a horizontal elastic plate," *Journal of Marine Science and Technology*, vol. 2, no. 2, pp. 87-100, 1997.
- [26] I. Stenius, A. Rose, J. Kuttenukeuler, "Hydroelastic interaction in panel-water impacts of high-speed craft," *Ocean Engineering*, vol. 38, pp. 371-381, 2011.
- [27] R. Panciroli, S. Abrate, G. Minak, "Dynamic Response of Flexible Wedges Entering the Water," *Composite Structures*, vol. 99, pp. 163-171, 2013.
- [28] F.J. Huera-Huarte, D. Jeon, M. Gharib, "Experimental investigation of water slamming loads on panels," *Ocean Engineering*, vol. 38, pp. 1347-1355, 2011.
- [29] T. Allen, "Mechanics of Flexible Composite Hull Panels Subjected to Water Impacts," thesis, 2013.
- [30] T. Allen, M. Battley, "Quantification of hydroelasticity in water impacts of flexible composite hull panels," *Ocean Engineering*, vol. 100, pp. 117-125, 2015.
- [31] M. Battley, T. Allen, "Servo-hydraulic System for Controlled Velocity Water Impact of Marine Sandwich Panels," *Experimental Mechanics*, vol. 52, pp. 95-106, 2012.
- [32] N. Aquelet, M. Souli, "A new ALE formulation for sloshing analysis," *Structural Engineering and Mechanics*, vol. 16, no. 4, pp. 000-000, 2003.

- [33] N. Aquelet, M. Souli, L. Olovsson, "Euler-Lagrange coupling with damping effects: Application to slamming problems," *Computer methods in applied mechanics and engineering*, vol. 195, pp. 110-132, 2006.
- [34] I. Stenius, A. Rosén, J. Kutteneuler, "Explicit FE-modelling of fluid structure interaction in hull-water impacts," *International Shipbuilding Progress*, vol. 53, pp. 103-121, 2006.
- [35] I. Stenius, A. Rosén, J. Kutteneuler, "Explicit FE-modelling of hydroelasticity in panel-water impacts," *International Shipbuilding Progress*, vol. 54, pp. 111-127, 2007.
- [36] Kaushik Das, R. C. Romesh , "Local water slamming impact on sandwich composite hulls," *Journal of Fluids and Structures*, vol. 27, pp. 523- 551, 2011.
- [37] S. Wang, C.G.Souares, "Numerical study on the water impact of 3D bodies by an explicit finite element method," *Ocean Engineering*, vol. 78, pp. 73-88, 2014.
- [38] M. Souli, A. Ouahsine, L. Lewin, "ALE formulation for fluid-structure interaction problems," *Computer Methods in Applied Mechanics and Engineering* , vol. 190, pp. 659-675, 2000.
- [39] R.A. Gingold, J. J. Monaghan, "Smoothed particle hydrodynamics : theory and application to non-spherica lstars," *Mon.Not.R.Astron.Soc.*, vol. 181, pp. 375-389, 1977.
- [40] G. Oger, M. Doring, B. Alessandrini, P. Ferrant, "Two-dimensional SPH simulations of wedge water entries," *Journal of Computational Physics* , vol. 213, pp. 803-822, 2006.
- [41] D. Veen,T. Gourlay, "A combined strip theory and Smoothed Particle Hydrodynamics approach for estimating slamming loads on a ship in head seas," *Ocean Engineering*, vol. 43, pp. 64-71, 2012.
- [42] R. Pancirolia, S. Abrate, G. Minak, A. Zucchelli, "Hydroelasticity in water-entry problems: Comparison between experimental and SPH results," *Composite Structures*, vol. 49, pp. 532-539, 2012.
- [43] S. Ma, H. Mahfuz, "Finite element simulation of composite ship structures with fluid

structure interaction," *Ocean Engineering*, vol. 52, pp. 52-59, 2012.

- [44] C. H. LU, Y. S. HE, "Coupled analysis of nonlinear interaction between fluid and structure during impact," *Journal of Fluids and Structures* , vol. 14, pp. 127-146, 2000.
- [45] Q. Yang, W. Qiu, "Numerical simulation of water impact for 2D and 3D bodies," *Ocean Engineering*, vol. 43, pp. 82- 89, 2012.
- [46] A. Bereznitski , "Slamming: the role of hydroelasticity," *International Shipbuilding Progress*, vol. 48, no. 4, pp. 333-351, 2001.
- [47] K. Varyani, R. Gatiganti, M.Gerigk , "Motions and slamming impact on catamaran," *Ocean engineering*, vol. 27, pp. 729-747, 2000.
- [48] R. Cointe, "Two-Dimensional Water-Solid Impact," *Journal of Offshore Mechanics and Arctic Engineering*, vol. 111, pp. 109-114, 1989.
- [49] O. M. Faltinsen , "Hydroelastic slamming," *Journal of Marine Science and Technology*, vol. 5, pp. 49-65, 2011.

CHAPTER 2

Slamming Numerical Simulation

Contents

2.1 Introduction	44
2.2 The two dimensional numerical slamming model.....	44
2.2.1 Effect of the hourglass control.....	47
2.2.2 Effect of the penalty stiffness factor (PFAC)	49
2.2.2 Effect of the element mesh size	51
2.2.3 Effect of the deadrise angles on hydrodynamic pressure.....	52
2.2.4 Effect of the impact velocity.....	55
2.2.5 Effect of body shape on the slamming.....	59
2.3 Numerical simulation based on the CEL model.....	60
2.3.1 Mesh convergence	62
2.3.2 Effect of the fluid domain.....	64
2.4 Beam theory for a deformable structure	66
2.5 Slamming and sandwich design	70
2.6 Effect of the stacking sequence	74
2.7 Three dimensional numerical slamming model.....	75
2.8 Conclusions	79
References	81

2.1 Introduction

Due to the complication of the response of structures that experience dynamic loads such as impacts, especially during their interaction with fluid, numerical methods are therefore considered an effective approach to predict the structural response with more accurate results. There are various numerical approaches which can simulate the dynamic slamming impact, which are different in their simplification and assumptions in representing fluid/structure interaction. As mentioned in the Chapter One, three main methods can be used for the case under consideration: the Smoothed Particle Hydrodynamics (SPH) model, the Arbitrary Lagrangian-Eulerian (ALE) model and Computational Fluid Dynamic (CFD). This chapter concerns the modelling of the slamming impact phenomenon based on the ALE and Coupled Lagrangian-Eulerian (CEL) methods. Several parameters studied to characterise their influence on the simulation results for both rigid and deformable structures in two and three dimensional schemes. Finally, the numerical model with optimal parameters was applied to different panel stiffnesses for better comprehension of the flexibility effect on the dynamic structural response as well as the hydroelastic effects of the fluid-structure interaction.

2.2 The two dimensional numerical slamming model

For the slamming event with small period duration, large deformations of the fluid occur, which can be lead to mesh distortions. For this reason, suitable simulation models of the interaction between the fluid and the structure are required to prevent this case. The Arbitrary Lagrangian Eulerian (ALE) solver in ABAQUS software was used to allow the mesh elements to move and return to the reference position during their interpolation to another time step. The material in the ALE region flowed as it moved, therefore the mesh re-mapping was adapted to form a new mesh and thus update the fluid nodal velocity and element states, and thus the element mesh not distorted [1].

ALE is a mixture of Lagrangian and Eulerian descriptions. The region in the fluid which is close to the impact area was modelled with a refined mesh size to govern the large deformation of the fluid in this position and used ALE codes with 4-nodes quadrilateral elements type (CPE4R), while the outer region of this domain used another mesh size with triangular linear elements because the deformation in the outer domain of the impact position was still moderate.

Figure 2. illustrates the boundary conditions and the mesh model of the water entry problem. As modelling interaction between a fluid and a structure is very time-consuming, the slamming model of the symmetric wedge enables the application of the symmetric boundary condition about the symmetric plane (wedge with dimensions: length of each arm 0.25 m and width 0.4 m). To prevent the reflected wave effect from external fluid boundaries, fluid domain length was specified as [2]:

$$L \geq \frac{C_0 T}{2} \quad (2.1)$$

Where L is the distance between the impact position and the external surface of the water domain, T is the time of the slamming event and C_0 is the speed of the sound in the fluid. In Abaqus explicit, the equation of state (EOS) can be defined by the linear U_s-U_p formulation of the Mie-Gruneisen equation which can be exploited for the water entry problem. The pressure is determined as a function of the density and the internal energy:

$$P = f(\rho, E_m) \quad (2.2)$$

$$P = PH \left(1 - \frac{\Gamma_0 \eta}{2} \right) + \Gamma_0 \rho_0 E_m \quad (2.3)$$

Where PH, Γ_0 , $\eta = 1 - \rho_0/\rho$ and ρ_0 are the Hugoniot pressure, material constant, nominal volumetric compressive strain and fluid reference density, respectively.

$$PH = \frac{\rho_0 c_0 \eta}{(1 - s\eta)^2} \quad (2.4)$$

Where s represents the linear relationship between shock velocity U_s and particle velocity U_p ($U_s = C_0 + sU_p$).

where U_s , U_p , C_0 and $s = dU_s/dU_p$, are the shock velocity, particle velocity, the velocity of the sound in the fluid and linear Hugoniot slope coefficient, respectively.

Thus the pressure of the fluid can be calculated as [3]:

$$P = \frac{\rho_0 C_0 \eta}{(1 - s\eta)^2} \left(1 - \frac{\Gamma_0 \eta}{2} \right) + \Gamma_0 \rho_0 E_m \tag{2.5}$$

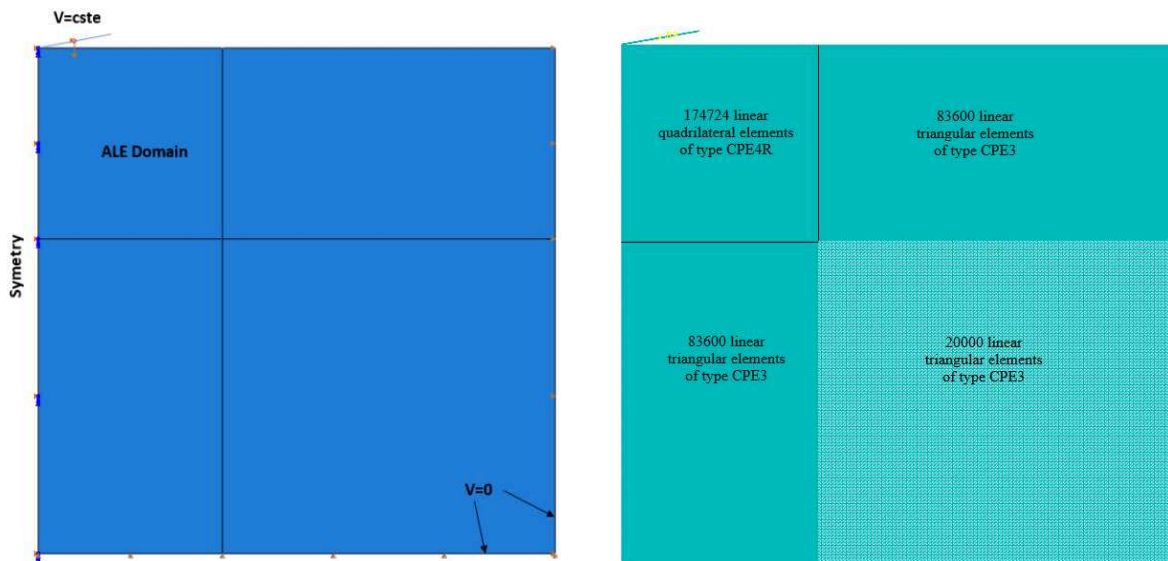


Figure 2. 1. Boundary conditions and mesh regions for the slamming of a two dimensional wedge model

The water parameters were illustrated in Table 2. 1. For the modelling of the solid/fluid contact, the exponential soft contact with frictionless tangential behaviour was used. The mesh convergence was investigated in the region close to the impact position with an element size 0.5mm for the fluid domain.

C_0 (m/sec)	μ (-)	s (-)	Γ_0 (-)	ρ (kg/m^3)
1420	0.001	0	0	1000

Table 2. 1. Parameters of the water in the model

2.2.1 Effect of the hourglass control

The mesh of the Lagrangian domain deforms with the material, while the Eulerian mesh was fixed in the space; and the material flows from one cell to another. Lagrangian is easier to handle (particularly the definition of boundary conditions), but with large mesh deformation, the extreme distorted leads to inaccurate calculations, or even failure. The ALE model combines the advantage of both methods, whereas after a Lagrangian deformation the boundaries of the elements (within an ALE-region) have moved so there is material transport across the boundaries (Eulerian) and the distortion of the elements is controlled (does not become considerable).

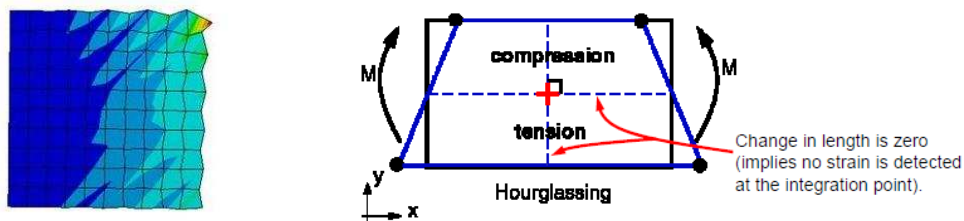


Figure 2. 2. Hourglass behaviour for a single first-order reduced-integration element with no strain

Hourglassing is an extra deformation of a finite element mesh. It was presented as a patchwork of zig-zags or hourglass (Figure 2. 2); some elements deform more than the others. This deformation produces no strain, hence there are no forces to resist. This deformation pattern is called hourglass mode, or zero energy modes.

In this section the hourglass effect was investigated. There are five hourglass controls (combine, enhanced, relax-stiffness, stiffness and viscous) which have added as artificial stiffness for the elements to prevent this kind of deformation, but it must be verified so the total artificial energy which used to control hourglass is small (<1%) relative to the total internal energy [4], as shown in Table 2. 2.

contact	Hourglass control	Artificial energy (ALLAE)	Internal energy (ALLIE)	$\frac{ALLAE}{ALLIE} * 100$ % < 1 %
Kinematic method	Combine	19,288	46,878	41,145
	Enhanced	0,006	14,288	0,042
	Relax-stiffness	0,006	14,356	0,042
	stiffness	0,007	14,277	0,049
	viscous	43,809	67,109	65,280
Penalty method (scale factor = 0.05)	Combine	37,138	56,518	65,710
	Enhanced	0,017	15,571	0,109
	Relax-stiffness	0,017	15,571	0,109
	stiffness	0,004	15,795	0,025
	viscous	44,559	59,940	74,339

Table 2. 2. Comparison of the energy histories of hourglass element controls

By comparison, the value of the energy histories (artificial and internal energy) for two types of the contact methods with different hourglass controls was mentioned on Table 2. 2. The total hydrodynamic forces and the hydrodynamic pressure along the length of the contact surface were also compared for their amplitude values and oscillation as shown in Figure 2. 3 and Figure 2. 4. From those results one can conclude that the penalty contact method is more suitable contact coupling with the best hourglass control (stiffness), while the combine and viscous hourglass controls have less vibration from both hydrodynamic pressure and hydrodynamic force.

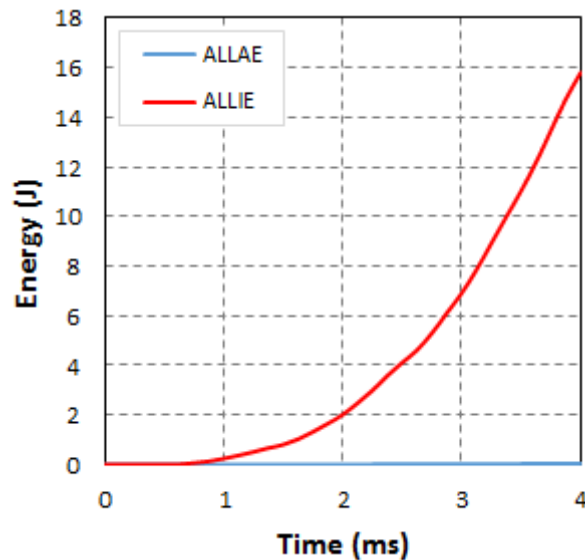


Figure 2. 3. Comparison of the energy histories for combine hourglass

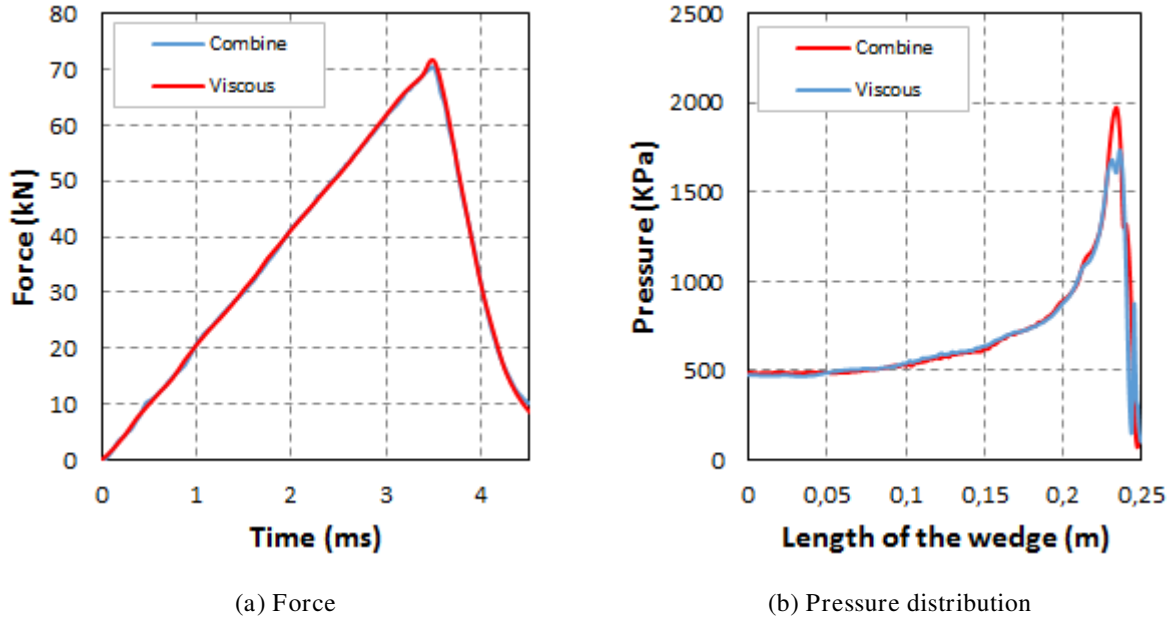


Figure 2. 4. Loading on the wedge surface with penalty contact method and deadrise angle 10° , $V=8\text{m/s}$

2.2.2 Effect of the penalty stiffness factor (PFAC)

The penalty coupling method was employed to define the interaction between the fluid and the structure which is based on the spring and the dashpot were attached to the master and slave node of the fluid and structure. The contact algorithm computes the pressure and the force at the point interface based on the displacement d , $u = u_s - u_f$ relative to the time derivative and velocity derivative of the interface between the fluid and the structure. In the method of both, the fluid and the body are modelling as the slave and master. These forces, due to this contact coupling effects on the nodes on the fluid-structure interface, are prevented the penetration of the fluid in the body structure. For each increment the displacement and relative velocity " $v_s - v_f$ " are computed, where v_s represents the velocity of the structure surface interface node and v_f represents the interpolation of the velocity of finite element fluid nodes.

In particular $t = t^n$, d^n can be updated incrementally as [5]:

$$d^{n+1} = d^n + \left(v_s^{n+\frac{1}{2}} - v_f^{n+\frac{1}{2}} \right) \cdot \Delta t \quad (2.6)$$

Where Δt is the time increment.

The penalty coupling method works as a spring system and the penalty forces are calculated relative to with penetration displacement and the spring stiffness as shown in Figure 2. 5.

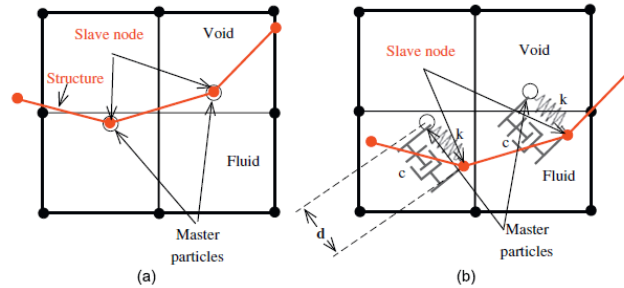


Figure 2. 5. Penalty coupling method for the nodes of fluid-structure interface [5]

The coupling force for the interface fluid-structure can be illustrated as follow:

$$F = Kd \tag{2.7}$$

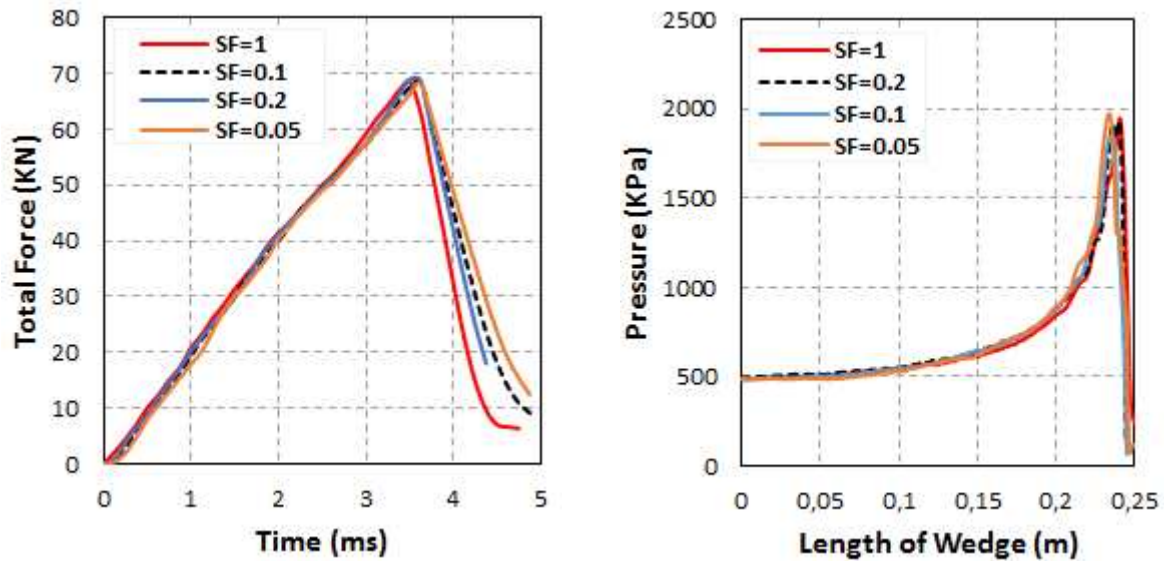
Where K and d represent respectively the spring system stiffness and penetration.

The spring stiffness depends on the scaling factor, bulk modulus of the fluid and the mesh size of fluid were described in Equation(2.8).

$$K = p_f \frac{k A}{V} \tag{2.8}$$

Where p_f ($0 \leq p_f \leq 1$) , A and V are penalty scale factors, the average area of the structure element and the volume of the fluid element, which are in the coupling state.

Applying a range of penalty scale factors (1, 0.2, 0.1 and 0.05), a comparative study of slamming force and pressure distributions was performed. In this model, the default value 0.05 was applied as the optimum value according to the amplitude and profile of the total force and pressure distribution, as shown in Figure 2. 6. This factor has little influence on the numerical results when compared with the mesh density effect. Using a high value of scale factor, coupling stiffness was increased between the nodes of the fluid-structure interface that caused a high oscillation in pressure and the force without penetration. While a low value of scale factor led to decreasing stiffness. Consequently, non-physical penetrations will appear, therefore leakage will occur.



(a) Force

(b) Pressure distribution

Figure 2. 6. Loading on the wedge surface with different stiffness scale factors of penalty contact method, deadrise angle 10° - $V=8\text{m/s}$

2.2.2 Effect of the element mesh size

The mesh density of the wedge has very significant effect on the simulation results and the proper modelling of the fluid-structure interaction. Therefore, different mesh sizes has assigned for the wedge and fluid help to analyse the slamming pressure and slamming force. The analysis results have indicated that the refined mesh had yielded better results but requires more computational time. In this study of the slamming impact on a symmetric wedge, we used a range of mesh sizes (0.15, 2.5, 5, 10, 15 and 25 mm) for the rigid body while for the fluid region near the impact position we used a refined mesh element size $150\mu\text{m}$ of the type linear quadrilateral elements CPE4R. For the pressure along the wedge, we can note that the best convergence of the mesh size for the rigid body is (0.15-10 mm), thus we used the mesh size of 10 mm, as shown in Figure 2. 7. Also, we found that the fluid penetrations into the structure occur when the structure mesh size is much larger than the fluid mesh.

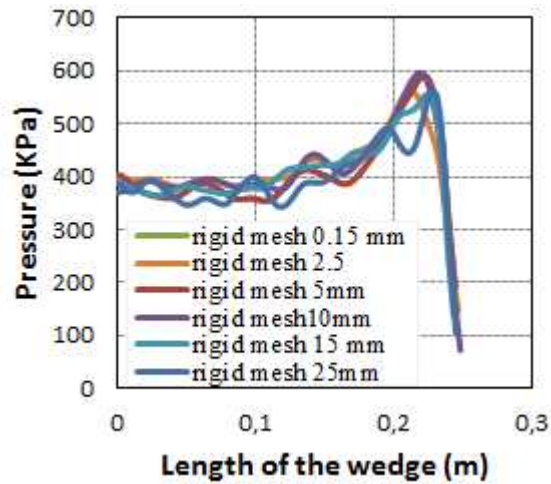


Figure 2. 7. Pressure distribution along the wedge with different mesh sizes, deadrise angle 30° and $V=13\text{m/s}$

2.2.3 Effect of the deadrise angles on hydrodynamic pressure

Slamming phenomena is happens in short time duration. For this situation, a high magnitude pulse peak pressure occurs due to this phenomenon, which is very important to estimate when designing ships for naval applications. This phenomenon can cause damage in the structure due to the interaction between the structure and the fluid. The pressure travels along the panel width; this pressure is largely dependent on the velocity and angle of impact between the structure and the fluid. Hydrodynamic effects are significant when the deadrise angle between the body and the water surface is small [6]. The kinematic boundary of the fluid-structure interface will change when the structure responds to the dynamic pressure. This kinematic coupling between the fluid and the structure is one type of hydroelastic effect [7]. For the rigid body, the pressure decreases with increases in the deadrise angle at a constant velocity because the wedge cuts more easily through the water, Figure 2. 8. In this figure, a good agreement is observed with other analytical methods [8, 9], which make it clear that the coefficient pressure decrease with an increase in the dead angle, and its maximum occurs at a deadrise angle of 10° with constant impact velocity. In Equation (2.9), a non-dimensional pressure corresponding to the deadrise angles which was calculated as:

$$Cp_{max} = \frac{p_{max}}{0.5\rho v^2} \quad (2.9)$$

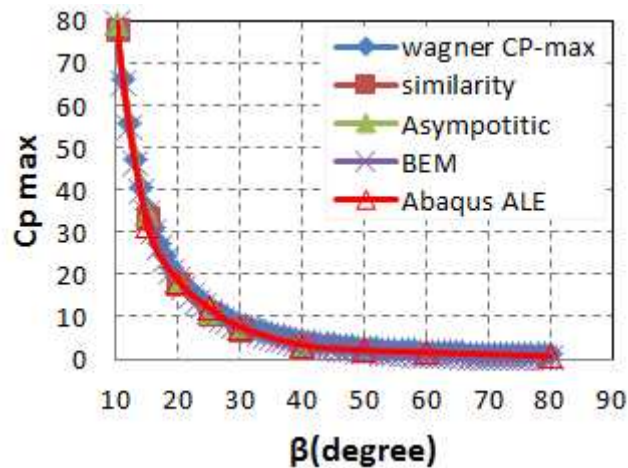


Figure 2. 8. Nondimensional coefficient pressure Cp_{max} according to the deadrise angles

Figure 2. 9 shows the pressure coefficient along the length of the rigid body with constant velocity and initial calm water. The predicted results of the pressure coefficient (Cp) based on the Arbitrary Lagrangian Eulerian (ALE) were determined using the formula (2.9). It can be noted at first impact, the maximum pressure was low, because the pressure was still building up at the time that the output was generated. In the wedge shape, the pressure peak at any penetration depth was almost the same along the wetted surface interface but it decreased significantly after the water separation, as did the slamming force compared with that before flow separation. The maximum pressure obtained was compared with an analytical formula proposed by Zhao and Faltinsen that Cp is increases with a decrease in the deadrise angles and the peak pressure becomes sharply close to the jet flow domain. In contrast, the value of maximum pressure drops quickly for wedges with larger deadrise angles because a sharper object cuts more easily through the water [9]. This was shown in the previous works, Figure 2. 10 [9].

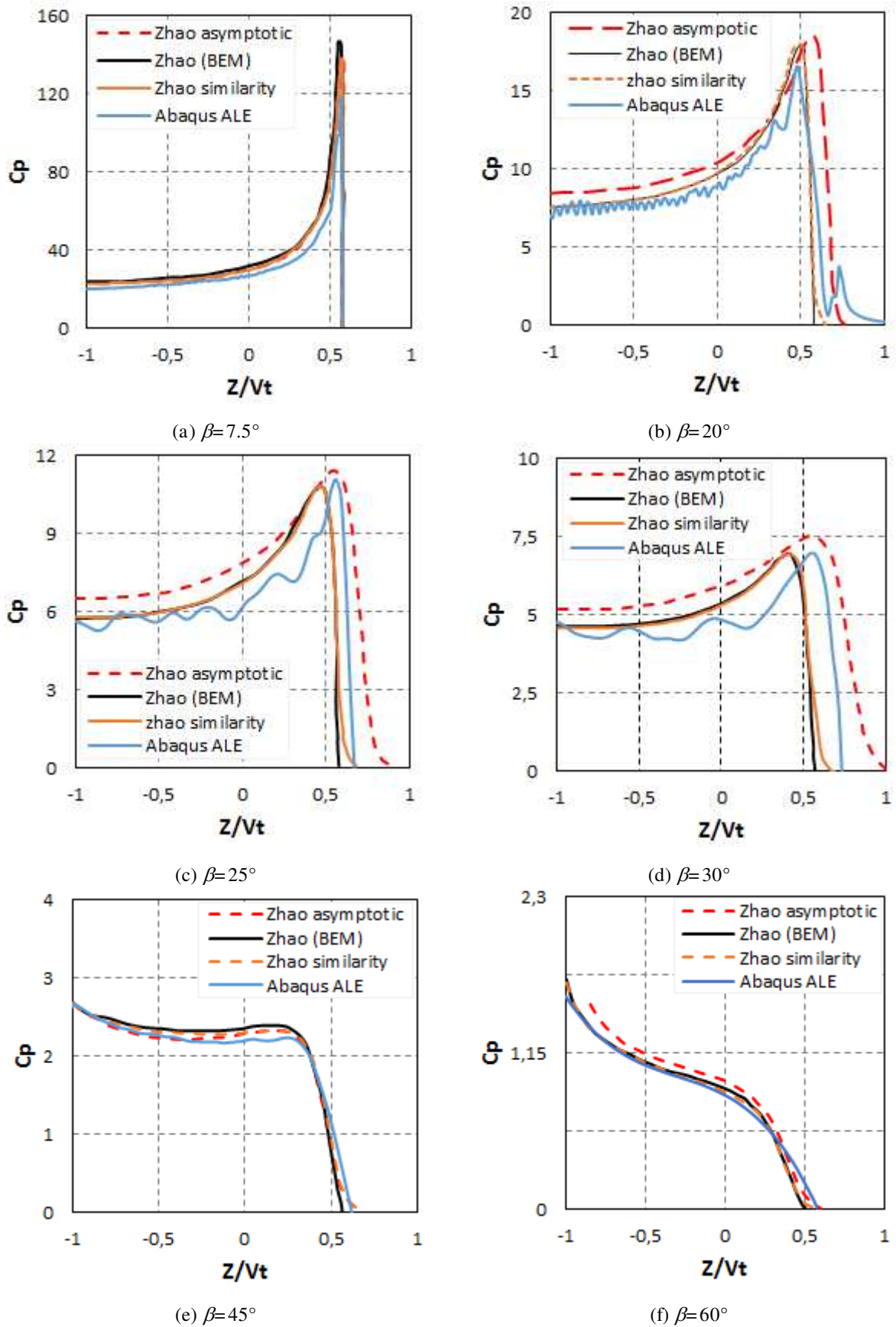


Figure 2. 9. Pressure coefficient distribution for deadrise angle, $V=13\text{m/s}$

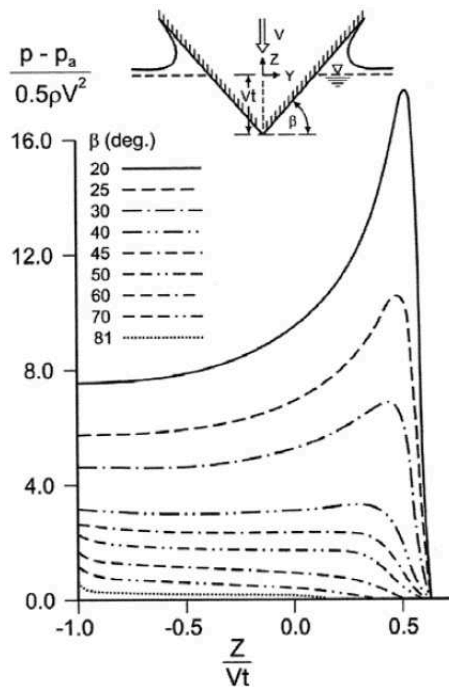


Figure 2. 10. Pressure coefficient distribution for different deadrise angles for wedge entering water [9]

2.2.4 Effect of the impact velocity

Many different impact velocities (1, 2, 3, 4, 5, 6, 7 and 8 m/sec for the vessel velocity less than 15.5 knot) are applied to the wedge to estimate the maximum pressure for the range of values of deadrise angle at 10°, 30° and 45°(small and large deadrise angles), respectively. The comparing numerical result with the analytical methods for an angle of 10° was seen in Figure 2. 11a. It shows that the maximum pressure accruing through the ALE solver increase with an increase in the velocity impact at the same deadrise angle. It can be noted that the model less differs from Wagner’s theory at low velocities. In contrast, the maximum difference in the predicted pressure between analytical methods and the present model occurs when the impact velocity becomes larger. The same thing happens with the angles at 30° and 45° as illustrated in Figure 2. 11 a-b. Below, we have adopted the formulations for the calculation of the maximum pressure.

Analytical formula of maximum pressure proposed by Von Karman [10] and Wegner [8] is calculated by:

$$P_{max} = 0.5\rho V^2 \pi \cot\beta \tag{2.10}$$

Analytical formula of maximum pressure proposed by Zhao and Faltinsen [9]:

$$P_{max} = 0.5\rho V^2 \frac{\pi^2}{\tan^2\beta} \tag{2.11}$$

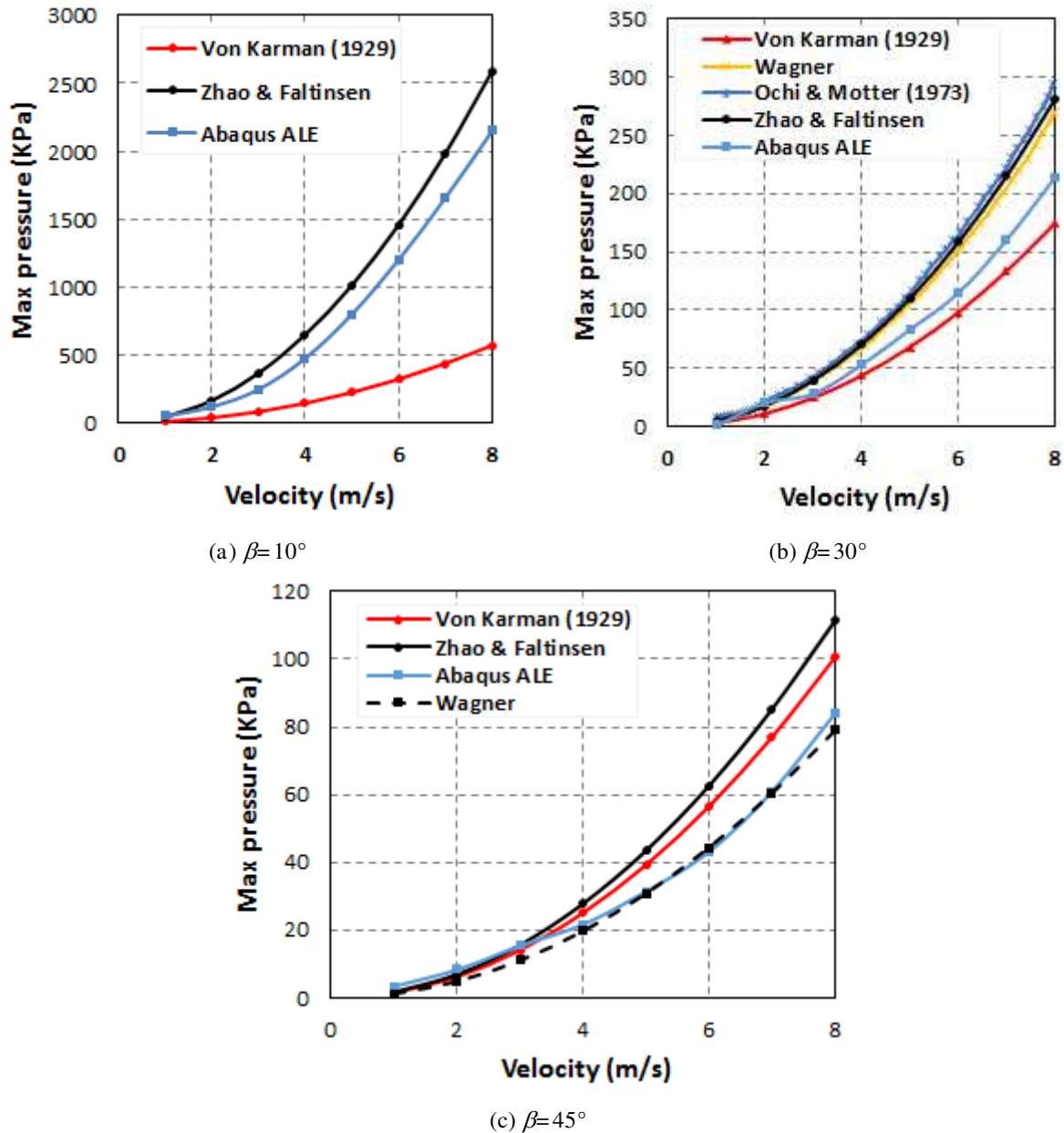


Figure 2. 11. Maximum values of pressures for different impact velocities and deadrise angles

The free water surface elevation and pressure histories for the deadrise angles 10° were illustrated in Figure 2. 12. It can be observed that the maximum pressure is usually close to the jet flow as is the maximum local velocity. Subsequently, the pressure was reduced after the flow separation occurred.

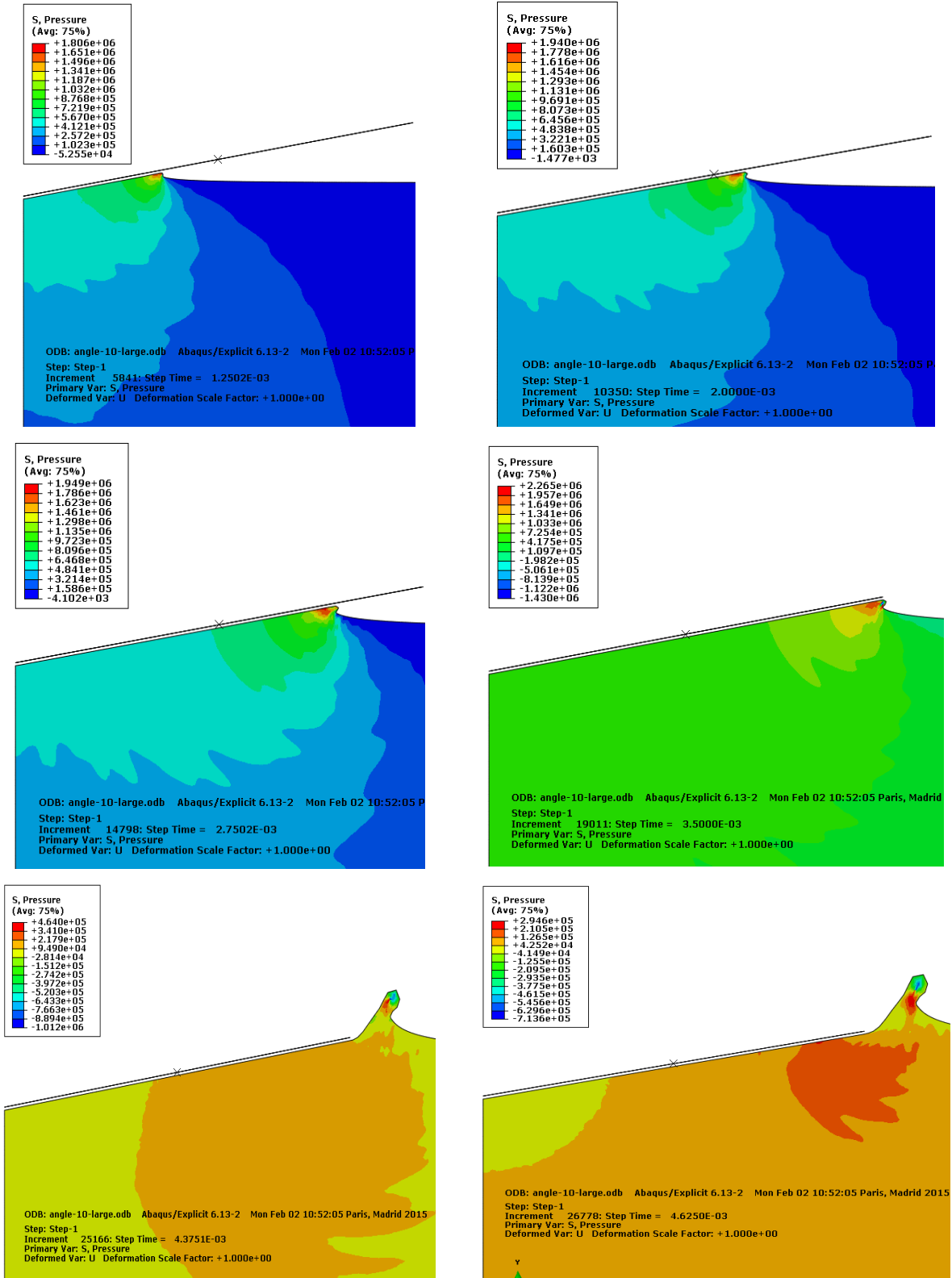


Figure 2. 12. Free water surface and pressure histories for angle at 10°, V=8m/s

A range of deadrise angles was applied to determine the hydrodynamic force. Figure 2. 13 illustrates that the hydrodynamic force increase when the angle between the surface of the free water and the body decreases.

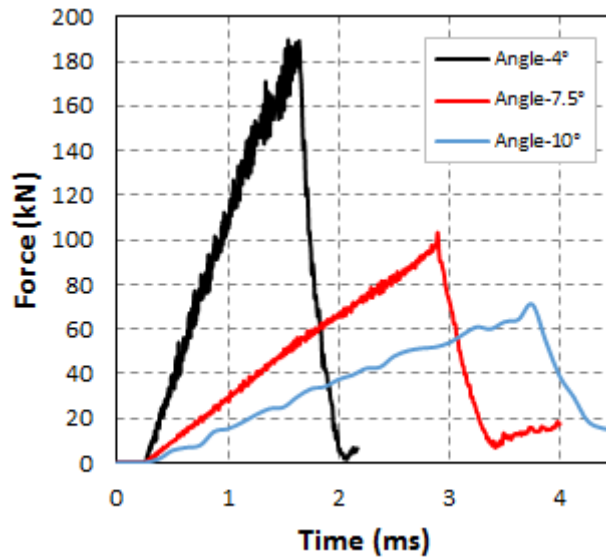


Figure 2. 13. Total vertical force for the wedge for the range of deadrise angles, V=8m/s

Figure 2. 14 presents the non-dimensional hydrodynamic force (hydrodynamic force coefficient C_f) for unit wedge length. It would appear that, analytical results and experimental data indicate that the force coefficient decreases with an increase in deadrise angles.

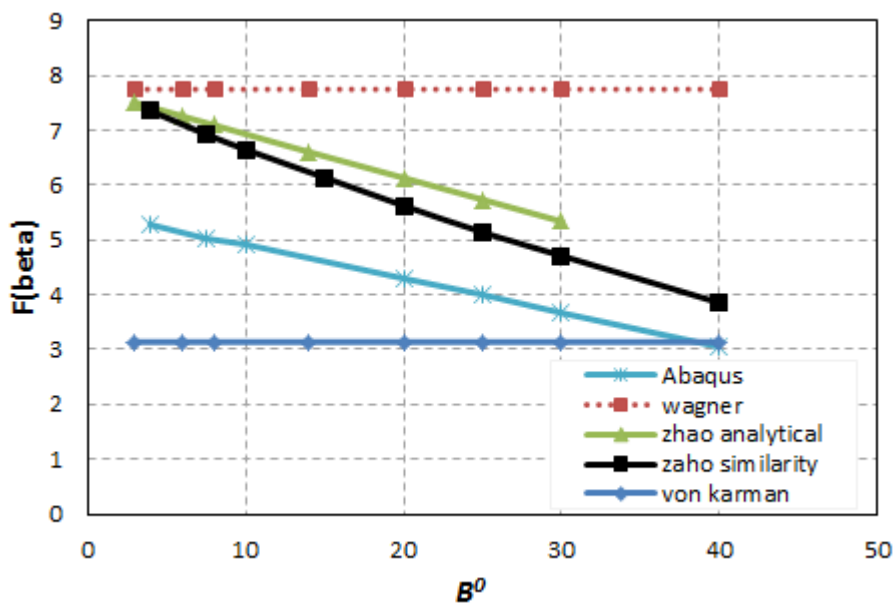


Figure 2. 14. Coefficient force ($C_f = F (\tan \beta)^2 / (L \rho V^3 t)$) versus the deadrise angle

2.2.5 Effect of body shape on the slamming

The shape of the structure's section has an effect on the peak pressure along this section, which means that the deadrise angle between the fluid and structure is very important in the slamming phenomenon. The peak pressure in wedge section is approximately the same value along the wetted surface due to the deadrise angle between the free water surface and rigid body which stays unchanged with constant velocity. Figure 2. 15 and Figure 2. 16 show the pressure histories for three points of hydrodynamic pressure on the wedge. As undesirable noise of the pressure curve was observed, refining mesh at the impact region can overcome this situation.

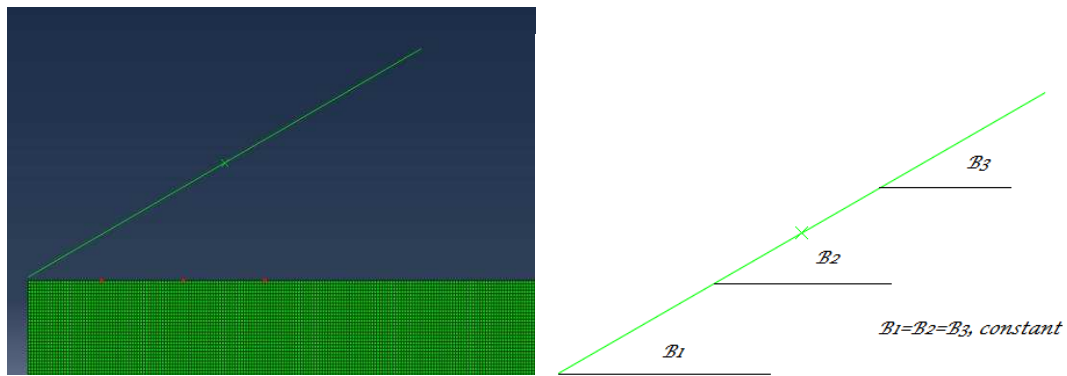


Figure 2. 15. Points position on the free surface of the water

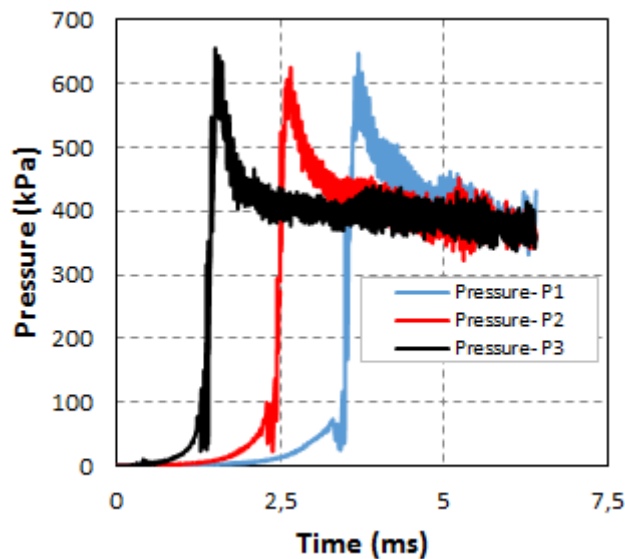


Figure 2. 16. Pressure histories for different points on the wedge, $\beta = 30^\circ$

For the other structure's section, the deadrise angle changed with the penetration rate of the structure, Figure 2. 17 and Figure 2. 18. The effect of the shape section indicates that the flow of the pressure peaks is asymmetrical for the circular section due to the change in the deadrise angle relative to the penetration rate.

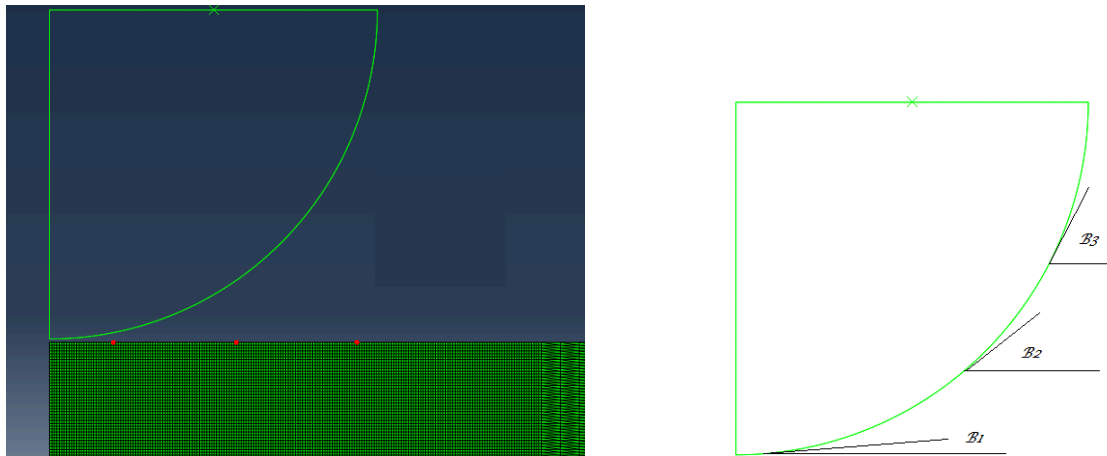


Figure 2. 17. Points position on the free surface of the water for circular section

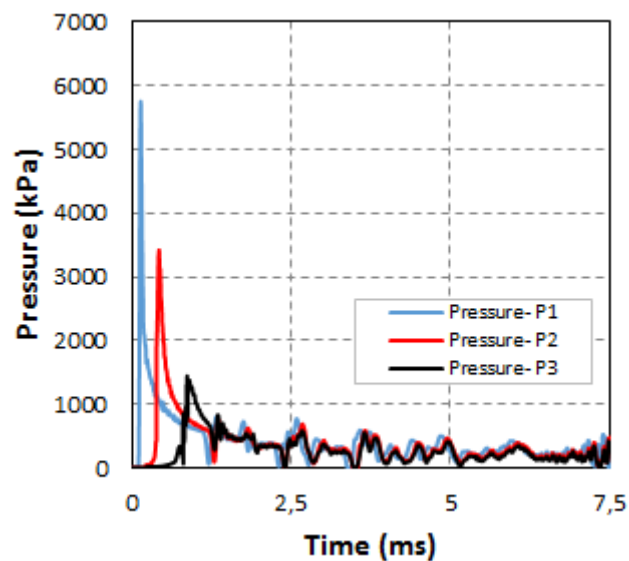


Figure 2. 18. Pressure histories for different points on the body with circular section

2.3 Numerical simulation based on the CEL model

In the CEL model, the coupling between the Lagrangian and Eulerian were employed in explicit Abaqus and can use more than one material. For the water entry impact, there is the

water domain and the structure body. The VOF (Volume of Fluid) method is attractive for solving a broad range of non-linear problems in fluid and solid mechanics, because it allows arbitrary large deformations and enables free surfaces to evolve [11], Figure 2. 19. The Lagrangian phase of the VOF method is simply achieved and incorporated in an explicit ALE finite element method [1]. Before advection, special treatment for the partially voided element has required. As the element has been partially filled, the volume fraction satisfies $0 \leq V_f \leq 1$, thus the total stress σ is calculated by multiplying by the volume fraction weight [1]:

$$\sigma_f = \sigma \cdot V_f \quad (2.12)$$

For voided elements, the stress is zero. In the computational process, the elements loop goes only through elements which are not voided. For free surface problems, the elements that are partially filled ($V_f < 1$) define the free surface.

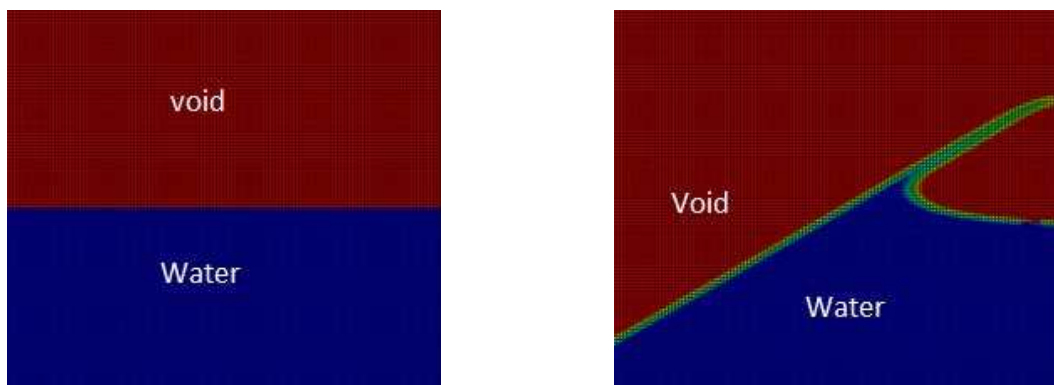


Figure 2. 19. Volume of Fluid method (VOF)

The Eulerian being modelled as multi-material (water and air) based on the equation of state (EOS) means that the fluid has considered to be in thermodynamic equilibrium at all time. The EOS can be defined by linear $U_s - U_p$ formulation of the Mie-Gruneisen equation of state which can be exploited in water entry problems, and can defines the pressure as a function of the density and internal energy as illustrated previously in Section 2.2.

The fluid has treated as Newtonian fluid flow, which means that the viscosity depends on the change in temperature, and thus for our model as the temperature is constant the viscosity is also constant. Coupling response was achieved by occupying initial boundary conditions in both Eulerian and Lagrangian. The coupling was calculated by applying pressure boundary conditions on the Lagrangian mesh from the Eulerian mesh, while the Lagrangian mesh

boundaries supplied velocity boundary conditions on the Eulerian mesh. Based on the volume of the fluid (VOF), the Eulerian cell was assumed to have constant pressure, since when it interacts with the Lagrangian the cell area will change. The area centroid was calculated by the Eulerian area that does not intersect with the Lagrangian and the reconstruction of pressure conditions. According to Benson [12], the element volume was calculated by subtracting the Lagrangian volume from the volume of the Eulerian element. Once these quantities have been established, the stress and pressure were updated. The velocities of the uncovered parts of the element have updated in the normal manner [13, 14]. Generally, boundary conditions are applied to prevent the Eulerian elements from overlapping with the underlying Lagrangian body.

The boundary conditions were applied to the model as seen in Figure 2. 20, and because of the symmetry of the slamming problem, half the model was considered with only one element that constrained all nodes in the x-axis to describe the Eulerian fluid domain. The exterior boundaries were defined as non-reflecting boundaries to avoid reflection waves, which were produced at the fluid boundaries as a result of the pressure influence along the interface between the body and the water surface. The FE mesh was formed with an EC3D8R 8-node linear Eulerian brick with one point integration and combined hourglass control.

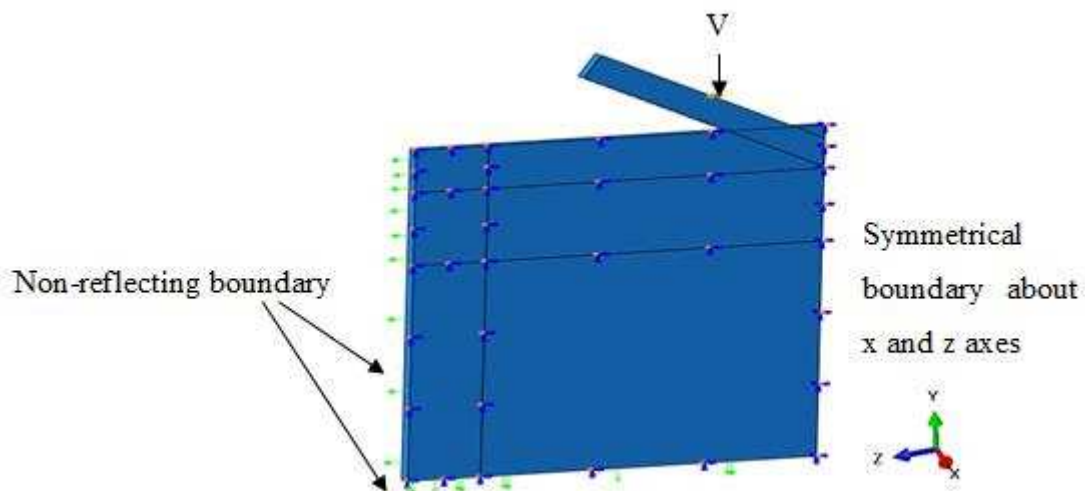


Figure 2. 20. Boundary conditions of CEL water entry model

2.3.1 Mesh convergence

The main effective parameter in the finite element method is the element mesh density. Therefore, mesh convergence was applied to the slamming model for the fluid domain which

was close to the impact region, using different mesh size (0.5, 1, 1.5, 2.5, 5 mm), as mentioned on Figure 2. 21 and Table 2. 3. It can be observed according to the amplitude and the oscillations of pressure as shown in Figure 2. 22a-b, that the best element mesh size was 0.5 mm with less noise and good agreement with analytical methods as well as the non-dimensional coefficient pressure. In the first phase of the impact, some of the high frequency oscillations occurred due to some numerical penetration of the fluid in the body, which can be overcome by refining the mesh in the initial impact position.

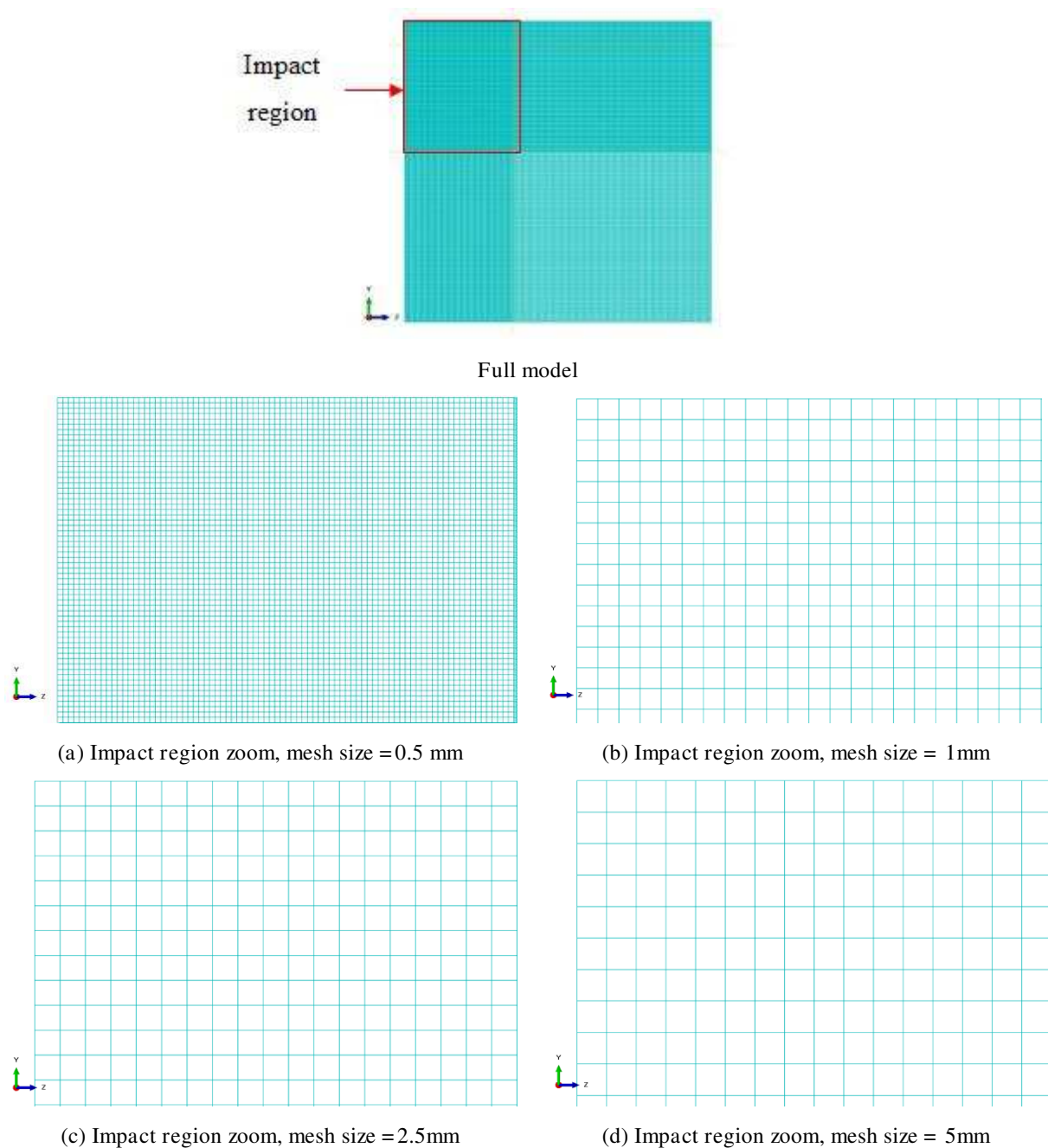


Figure 2. 21. Mesh convergence for the fluid domain

Mesh size (mm)	N° of element	N° of nodes	CPU time
0.5	4950340	9912640	09:18:20
1.0	671993	1345652	09:05:50
1.5	347504	695717	02:03:40
2.5	188834	377759	01:02:16
5.0	203653	102009	00:25:45

Table 2. 3. Mesh convergence and CPU time

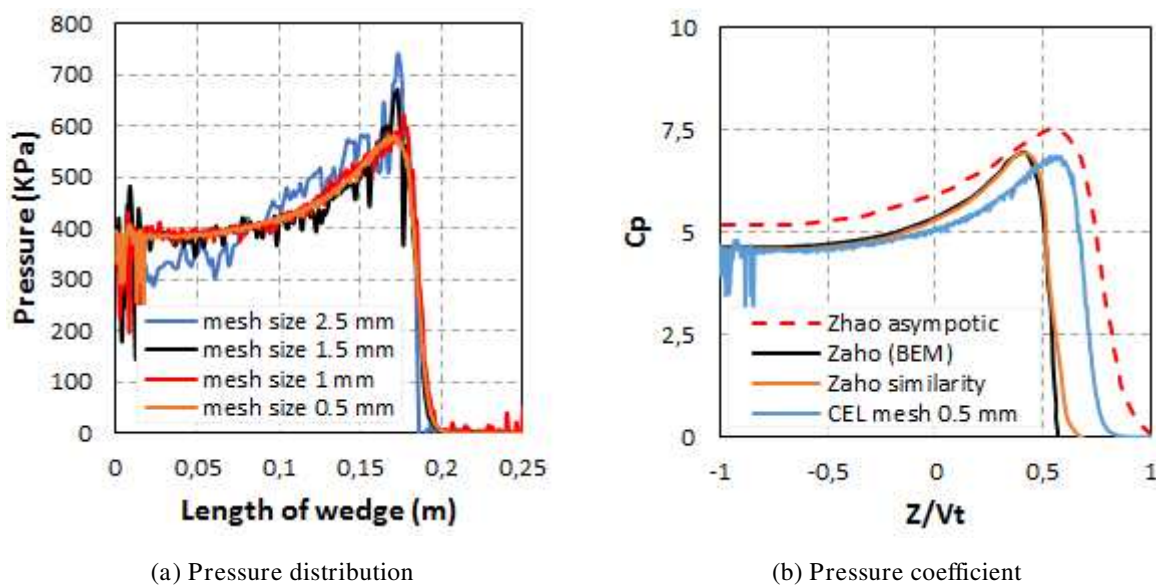


Figure 2. 22. Mesh convergence for fluid domain, $\beta=30^\circ$ and $V=13\text{m/s}$

2.3.2 Effect of the fluid domain

Despite adding the non-reflective boundary to the model, the convergence test was applied to three sizes of the fluid domains to explain the effect of the reflected wave from the exterior boundaries of the fluid relative to the slamming impact duration. In Section 2.2, the speed of the sound in the water was $C_0 = 1420 \text{ m/s}$, and the reflecting wave travelled over a time that had to be less than the fluid domain length. For this reason, the model was constructed with different lengths to instigate the effect of the fluid compressibility, Figure 2. 23. Figure 2. 24 exhibited the hydrodynamic force acting on the wedge with different domain. For a small domain, the force had great amplitude with non-linear profile due to compressibility and the reflected wave of the fluid. With an increase in the fluid domain, the force value decreased

with linear profile and the maximum predicted force value occurred at 0.0065s and then decreased slightly after the flow separation. A larger fluid domain was chosen as the optimal configuration to avoid this effect, which gave the best agreement with the analytical methods and experiment results. Figure 2. 25 clarified the comparison between ALE and CEL with a good correlation. On the other hand, the Abaqus CEL model was more suitable for predicting slamming loads in three dimensions which is important when presenting materials with different properties in all directions.

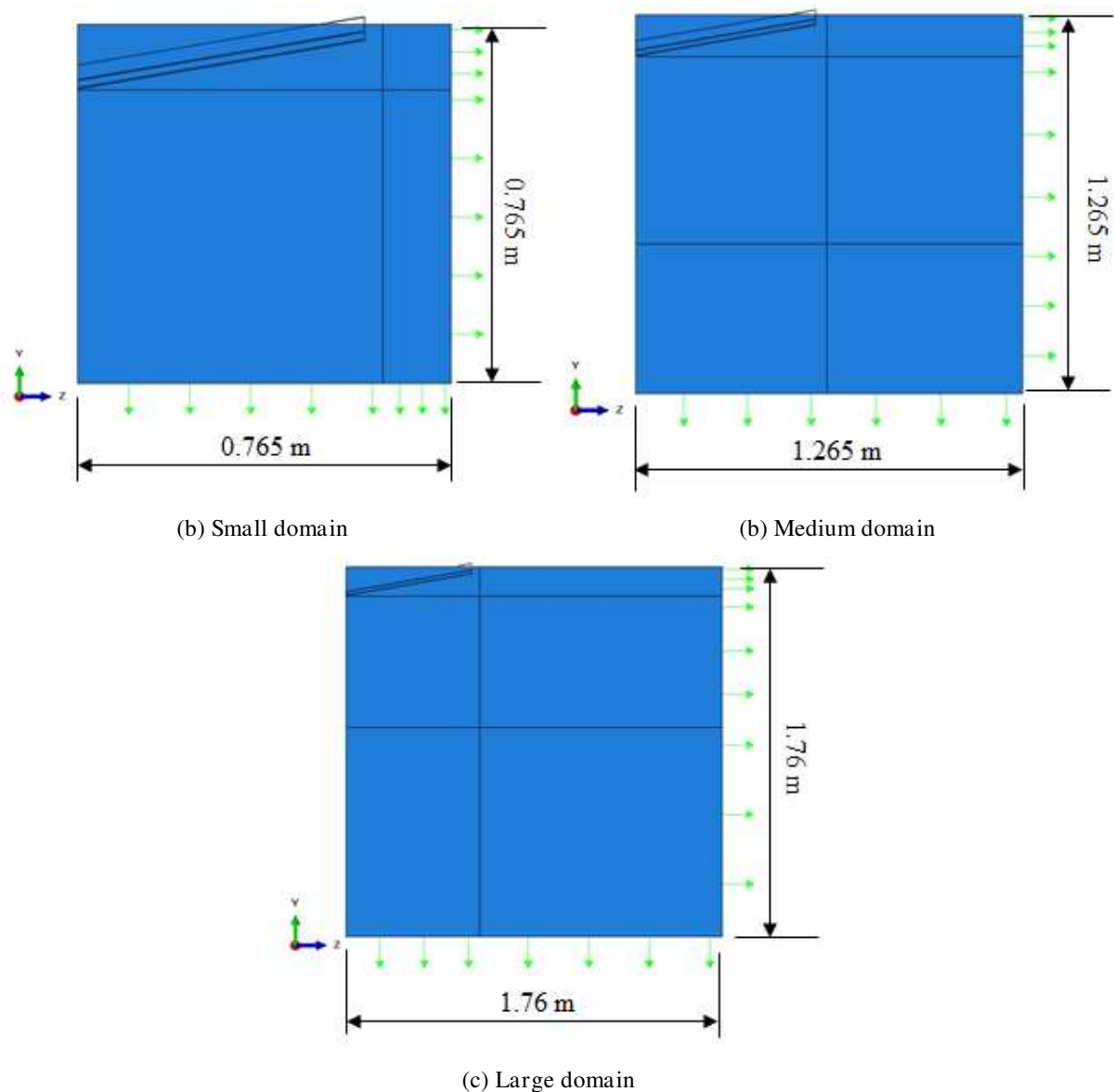


Figure 2. 23. Different domain length of fluid

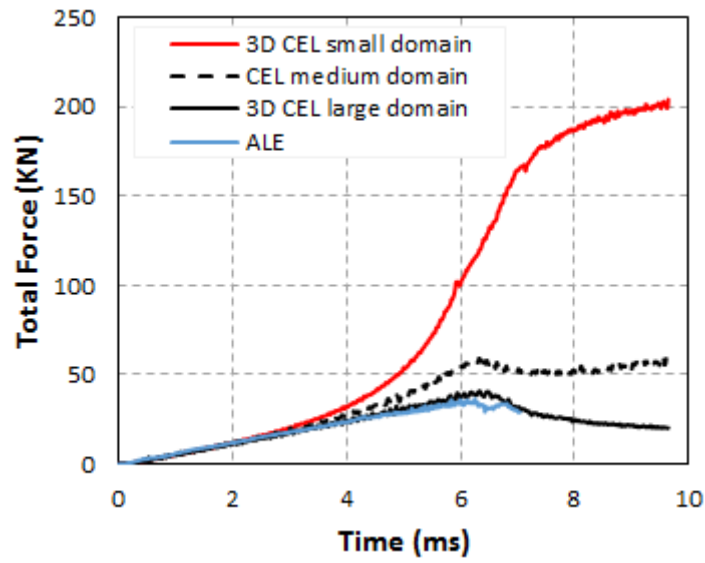


Figure 2. 24. The effect of the fluid domain length

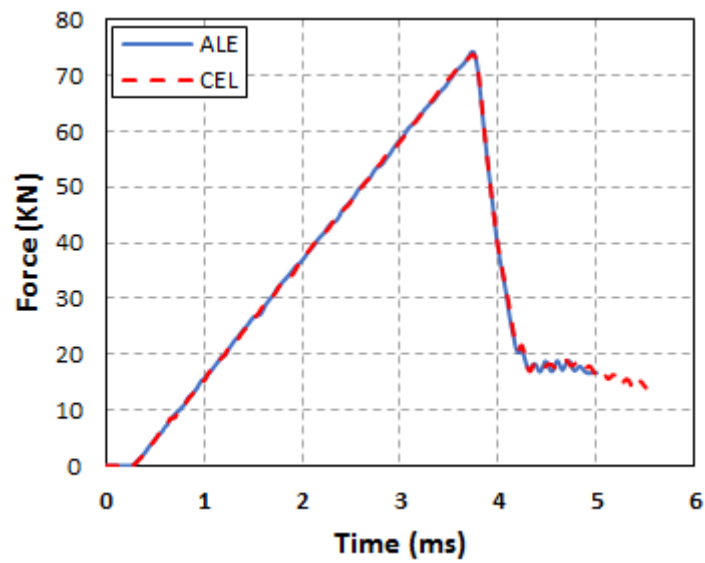


Figure 2. 25. Hydrodynamic force comparison between ALE and CEL models, $\beta=10^\circ$ and $V=8\text{m/s}$

2.4 Beam theory for a deformable structure

The structure in this analysis is assumed to be a beam of constant thickness and width thus the hydroelastic equilibrium equation for the bottom of the wedge can be written as:

$$M_B \frac{d^2w}{dt^2} + EI \frac{d^4w}{dx^4} = p(x, w, t) \tag{2.13}$$

Where w is the beam deflection, t is the time variable, EI is the structural stiffness, x is the longitudinal coordinate with $x=0$ in the middle of the beam, and p is the hydrodynamic pressure as a function of the beam deflection.

The difference between the deformable structure and the rigid body wedge are that the boundary condition on the wedge bottom must account for determining the deflection of the beam as shown in Figure 2. 26. The boundary conditions play an important role in the structural response, therefore conditions along the edges of the plate must be specified [7, 15]. This was expressed as:

- (a) Fully clamped at both ends (CC).
- (b) Cantilevered beam boundary condition (CS*).
- (c) Clamped and simply supported at one end (CS).
- (d) Simple supported boundary condition means that the plates are supported at the two ends, and fixed at the other ends (SS).

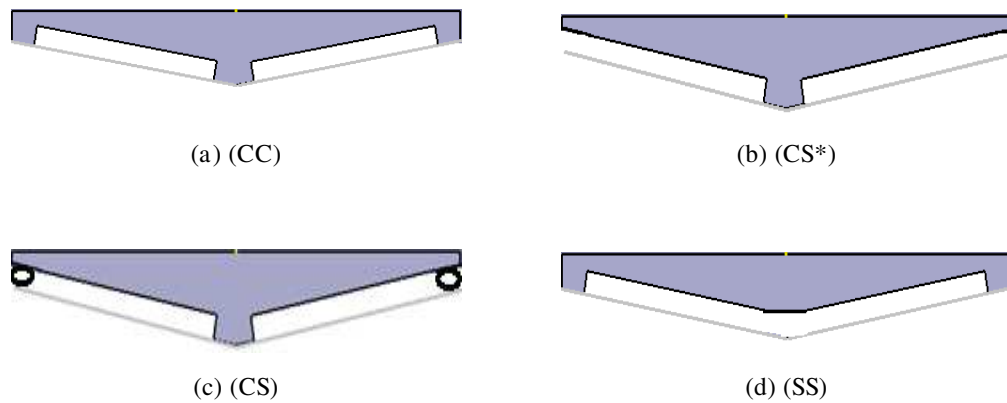


Figure 2. 26. Boundary conditions of supported plates

Material	Density (kg/m ³)	E ₁ (GPa)	E ₂ (GPa)	v ₁₂	v ₂₃	G ₁₂ (GPa)	G ₂₃ (GPa)
E-glass-epoxy	2000	45.6	16.2	0.278	0.4	5.83	5.78
Core-PVC skin E-glass epoxy	130	2.8	-	0.3	-	-	-

Table 2. 4. Material properties of the PVC panels

Figure 2. 27 shows the maximum deflection of the PVC sandwich under different boundary conditions, the material properties have mentioned in Table 2. 4 . It can be seen that the boundary conditions (CS, CS*) have a higher deflection than other cases. According to the structure requirement [16], the max deflection of the sandwich panel must be less than the 2% of the span panel. For all the boundary condition cases which were studied, the max deflection is illustrated in the Table 2. 5.

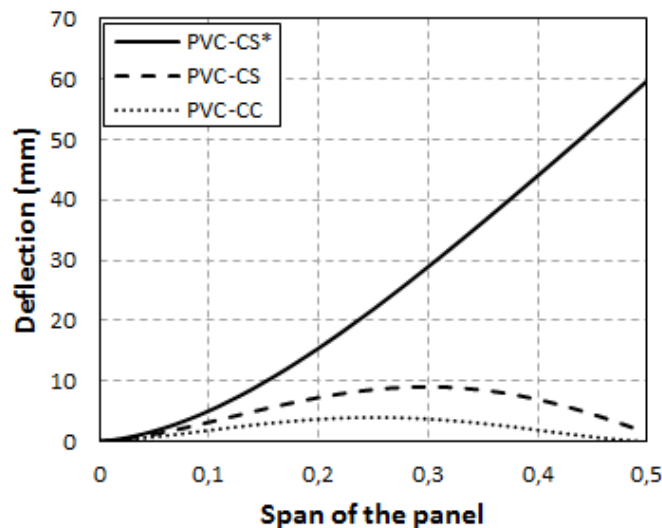
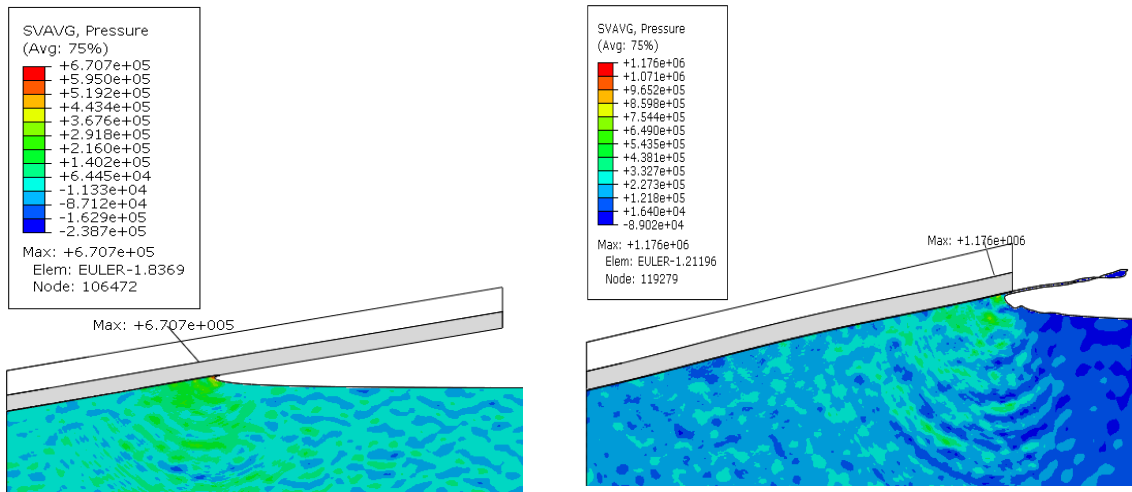


Figure 2. 27. Deflection of the PVC sandwich with different boundary conditions

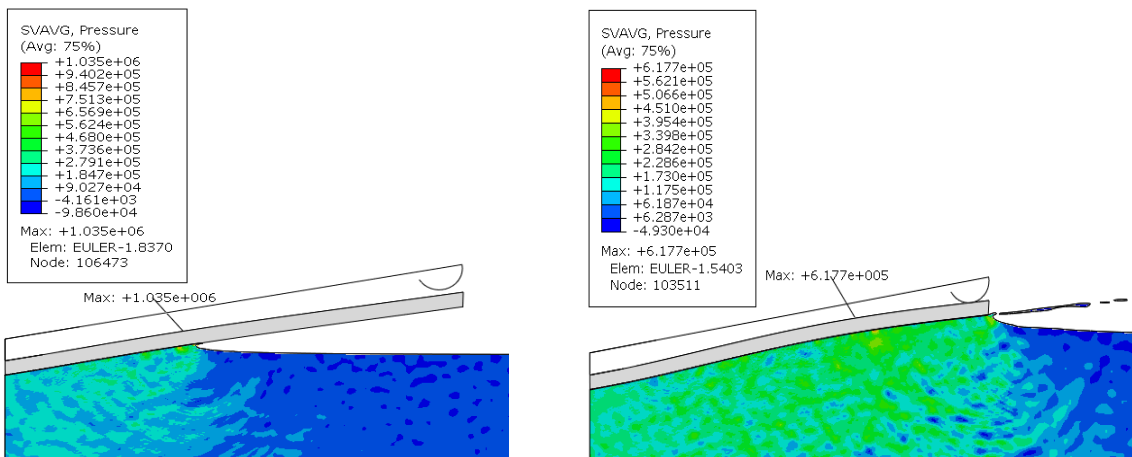
Boundary condition	Max deflection (mm)	Structure requirement (DNV: $w < 2\%$)
CC	3,94	0,79
SC	9,02	1,80
CS*	59,57	11,91

Table 2. 5. Maximum deflection for different boundary conditions

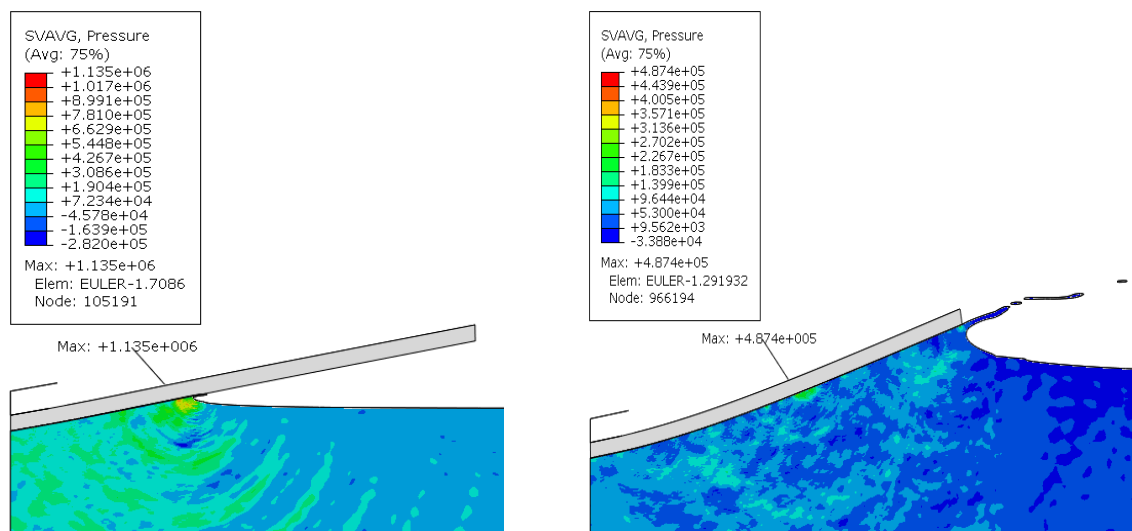
Figure 2. 28 shows the water flow and pressure along the interface with the wedge. This figure indicates a clear difference in the pressure amplitude in the mid depth penetration of the wedges, and the boundary conations with cantilevered beam (CS*) had a higher value. This can be attributed to the structure flexibility which generates an opposite force in the same direction of the wedge velocity that acts on the water surface. Since the deflection of the wedge was increased, the pressure on the water decreasing consequently the hydrodynamic force has been reduced. These effects rise to more careful study of the hydroelastic phenomenon.



(a) Boundary condition CC



(b) Boundary condition CS



(c) Boundary condition CS*

Figure 2. 28. Pressure histories for different boundary conditions of the deformable body, $\beta=10^\circ$ and $V=4\text{m/s}$

2.5 Slamming and sandwich design

Sandwich panels are a very efficient material that provides a high bending stiffness at low weight. Strong face skins support bending loads, while the core is resistant to shear loads, due to the fact of that there are differences in the material properties of the core and skin, with a high elastic modulus of the skin and a low elastic modulus for the core. The appropriate design of sandwich panels depends mainly on their mechanical properties such as strength and stiffness. The bending stiffness was increased by making the beams or panels thicker by using a sandwich construction. This can be achieved by increasing the core thickness with little increase in weight, as mentioned on Table 2. 6.

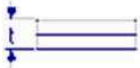
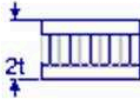
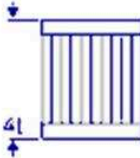
	Solid Material	Core Thickness t	Core Thickness 3t
			
Stiffness	1.0	7.0	37.0
Flexural Strength	1.0	3.5	9.2
Weight	1.0	1.03	1.06

Table 2. 6. Sandwich stiffness and strength relative to geometric variables [17]

We used ordinary theory of bending that depends on the assumption that the cross section of the beam which represents the plane perpendicular to the longitudinal axis is remains unchanged through bending. The equivalent flexural rigidity of the sandwich panel $(EI)_{eq}$ consists of the both rigidity of the skin and the core [18].

The rigidity of the core for any homogeneous cross section can be calculated as:

$$EI_{core} = \frac{E_c b t_c^3}{12} \tag{2.14}$$

While the rigidity of the faces about the central axis of the cross section can be calculated as:

$$EI_{faces} = E_f I_f \quad (2.15)$$

$$I_{faces} = 2 \left[I_f + area \left(\frac{d}{2} \right)^2 \right] = 2 \left[\frac{b t_c^3}{12} + \frac{b t_f d^2}{4} \right] \quad (2.16)$$

Where E_f , E_c , t_f , t_c , d and b are the elasticity of faces modulus, elasticity of the core modulus, thickness of the faces, thickness of the core, total thickness ($d = t_c + t_f$) and width of the specimen respectively.

The Young's modulus varies through the cross section of the sandwich structure and thus ordinary beam theory cannot be used to determine the deflection of the structure. Therefore, Timoshenko beam theory predicts the equivalent flexural rigidity $(EI)_{eq}$ of the sandwich beam which has given by:

$$(EI)_{eq} = \int E z^2 dz \quad (2.17)$$

$$(EI)_{eq} = E_f \frac{b t_f^3}{6} + E_f \frac{b t_f d^2}{2} + E_c \frac{t_c^3}{12} \quad (2.18)$$

In practice, for the sandwich panel, the elastic moduli of the core are very small when compared to the skin elastic moduli, thus the third term of Equation (2.18) can be neglected, and the ratio between first term and the second term $\frac{1}{3} \left(\frac{t_f}{d} \right)^2 \approx 0.0001$ to 0.01 . Thus the $(EI)_{eq}$ can be determined as:

$$(EI)_{eq} \approx E_f \frac{b t_f d^2}{2} \quad (2.19)$$

For three points bending of the sandwich panel, as this loading condition usually happens in the slamming impact, the maximum deflection in the sandwich was divided into two parts: bending stress of the skin and the shear stress of the core.

Total deflection = displacement (bending stress) + displacement (shear stress)

For the bending stiffness of the skin, the deflection can be represented as:

$$\delta = \frac{F L^3}{48 (EI)_{eq}} \quad (2.20)$$

As we demonstrated, when the $(EI)_{eq}$ increases, the deflection of the panel decreases, this is the reason for using a low-density core with a higher thickness to increase the distance between the faces which lead to a rise in the flexural strength and the bending stiffness, as shown in Table 2. 6.

There is another kind of deformation which cause the deflection of a panel, the shear stress of the core were associated to the shear strain. The shear stress of the core at any uniform section is:

$$\tau = \frac{Q}{bd} \quad , \text{ and the shear strain } \gamma = \frac{Q}{G_c bd} \quad (2.21)$$

Where Q and G_c are the shear stress and shear modulus of the core respectively.

$$\frac{\delta}{L/2} = \gamma = \frac{Q}{G_c bd} \quad (2.22)$$

Max deflection due to shear strain is applied by Equation (2.23)

$$\delta = \frac{FL}{4 G_c bd} \quad (2.23)$$

The max deflection of the panel due to the shear stress and the bending can be determined as:

$$\delta = \frac{FL^3}{48 (EI)_{eq}} + \frac{FL}{4 G_c bd} \quad (2.24)$$

For different loading conditions we can express the deflection as:

$$\delta = \frac{FL^3}{B_1 (EI)_{eq}} + \frac{FL}{B_2 G_c bd} \quad (2.25)$$

Where B_1 and B_2 depend on boundary conditions and loading, as shown in Table 2. 7.

Loading Mode	B_1	B_2
Cantilever beam with end load	3	1
Cantilever beam with uniformly distributed load	8	2
Two ends clamped with centre load	192	4
Two ends clamped with uniformly distributed load	384	8

Table 2. 7. Boundary conditions and loading [18]

Three kinds of material were tested numerically with different core materials and the same material faces- E-glass epoxy laminate with transverse isotropy properties. The material properties have mentioned in Table 2. 8. Figure 2. 29 shows the maximum deflection for different panel stiffness.

Material	Density (kg/m^3)	E_1 (GPa)	E_2 (GPa)	ν_{12}	ν_{23}	G_{12} (GPa)	G_{23} (GPa)
E-glass-epoxy	2000	45.6	16.2	0.278	0.4	5.83	5.78
Core-PVC skin E-glass epoxy	130	2.8	-	0.3	-	-	-
Core-Balsa skin E-glass epoxy	151	3.518	0.05	0.5	0.02	0.157	0.157

Table 2. 8. Material properties of the panels

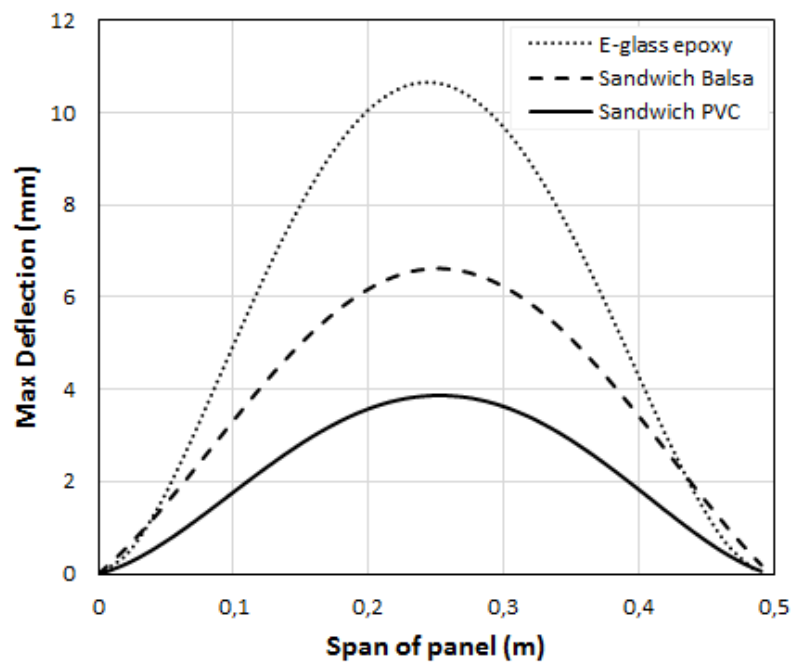


Figure 2. 29. Max deflection for three different panel materials, $V=4\text{m/s}$

2.6 Effect of the stacking sequence

The effect of the stacking sequence on the mechanical performance of the skin of sandwich panel was investigated. Optimisation of the ply stacking sequence in elastic phase (without damage) has tested for the skin corresponding to the max deflection. Whereas the overall laminate thickness in the skin and core remained constant with the same material properties, constant velocity 8m/s and deadrise angle 10°. Due to the difference in their thicknesses and elastic moduli, the shear forces are born by the core and the bending moments by the skin. Thus, the effects of the stacking sequence on the skin in relation to the stiffness requirements are shown in Table 2. 9.

Symbol	Stacking sequence
SS1	(0/90/45/-45) ₂ /PVC/(-45/45/90/0) ₂
SS2	((0) ₈ /PVC/(0) ₈)
SS3	(90/0/90/0) _s /PVC/ (90/0/90/0) _s
SS4	(90/45/0/-45) _s /PVC/ (90/45/0/-45) _s
SS5	((45/-45/45/-45) _s /PVC/ (45/-45/45/-45) _s)
SS6	((90) ₈ /PVC/(90) ₈)

Table 2. 9. Skin stacking sequence and ply orientation

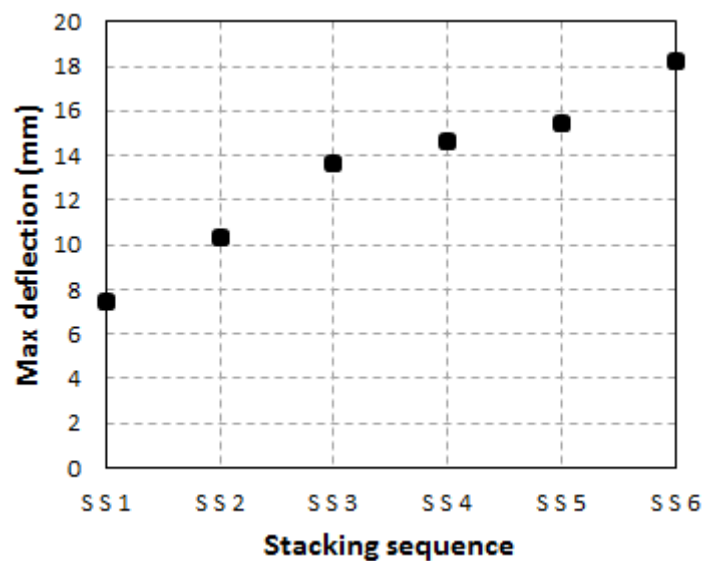


Figure 2. 30. Max deflection corresponding to stacking sequence and ply orientation with Boundary condition (CC)

This can be explained by the fact that the fibres oriented at 0° are more appropriate to flexural loads than the other orientations, as pointed out in Figure 2. 30. It should be noted that the damage in the laminate and the damage between layers due to delamination were not taken into account in this section.

2.7 Three dimensional numerical slamming model

Before validating the numerical model developed, using our experimental tests and numerical results carried out on composite panels (Chapter Five and Six), we shall concentrate on validating our results against those of literature. The numerical model was compared and validated with experimental data found in [19, 20, 21]. The 3D full slamming model was constructed for wedge section based on the CEL method that was handled in Section 2.3. The boundary conditions with non-reflecting wave were applied to the exterior boundaries of Eulerian fluid domain to prevent reflected pressure waves from the wall to the impact location, as shown in Figure 2. 31a. Water domain is divided in many regions as a result of high consuming computational time of the model. The Eulerian domain is meshed with EC3D8R linear element Eulerian brick. A mesh density convergence study was conducted for both the fluid domain and the composite panel as illustrated in section 2.3.1. The mesh is refined close to the impact location between impactor and water surface and becomes coarser toward outer edges to given more accuracy for numerical results, as illustrated in Figure 2. 31b. the composite panel model were created with solid element type of C3D8R.

The experimental test was performed using the servo-hydraulic slam testing system (SSTS) to keep impact velocity approximately constant during impact duration. Biaxial E-glass reinforced epoxy composite panels were considered in this investigation. The panel were simply supported along their edges, as shown in Figure 2. 32, and all panels tested had a (β) 10° deadrise angle. For more details about the SSTS machine, instrumentation and panel properties, refers to the work [19].

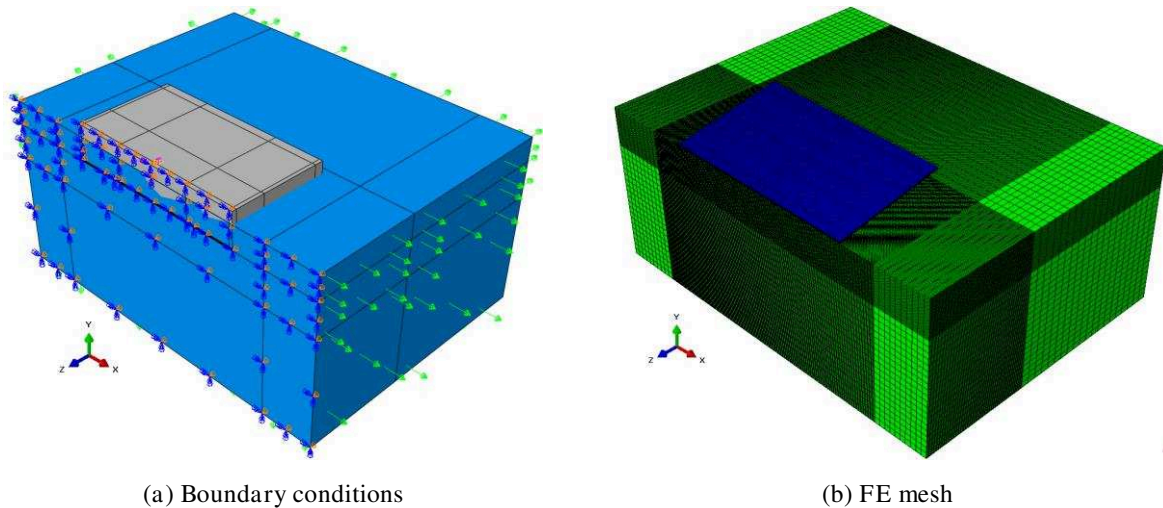


Figure 2. 31. Numerical slamming model

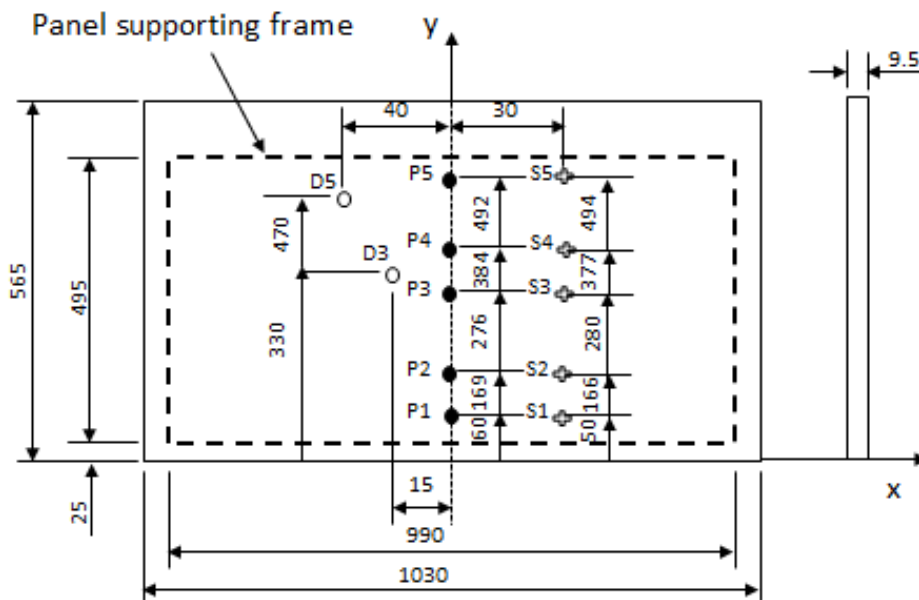


Figure 2. 32. Panel instrumentation and setup

Figure 2. 33, Figure 2. 34 have showed the comparison between the deformation in the centre and close to the chine of panel for the numerical results and the experimental data for two different impact velocities: $V=2\text{m/s}$ and $V=4\text{m/s}$. It can be seen that the numerical results predicted the panel deformation well compared to experimental tests. A small discrepancy was observed in the gauge deformation, this difference can be attributed to boundary conditions in the experimental setup. On the other side, the impact velocity of experimental test was not really constant throughout the penetration time as that defined in numerical model. Figure 2. 35 presents the comparison in the hydrodynamic force between the

experimental and numerical results for different impact velocities. A good agreement was also noted. A snapshot of the model after the impact test was presented in Figure 2. 36.

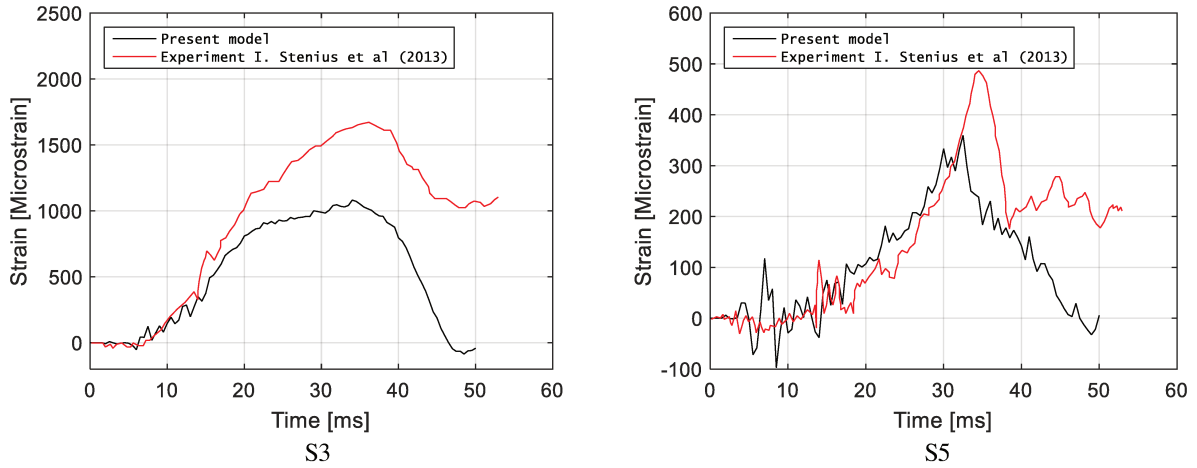


Figure 2. 33. Comparison of the panel deformation between the numerical results and experimental data, $V=2$ m/s.

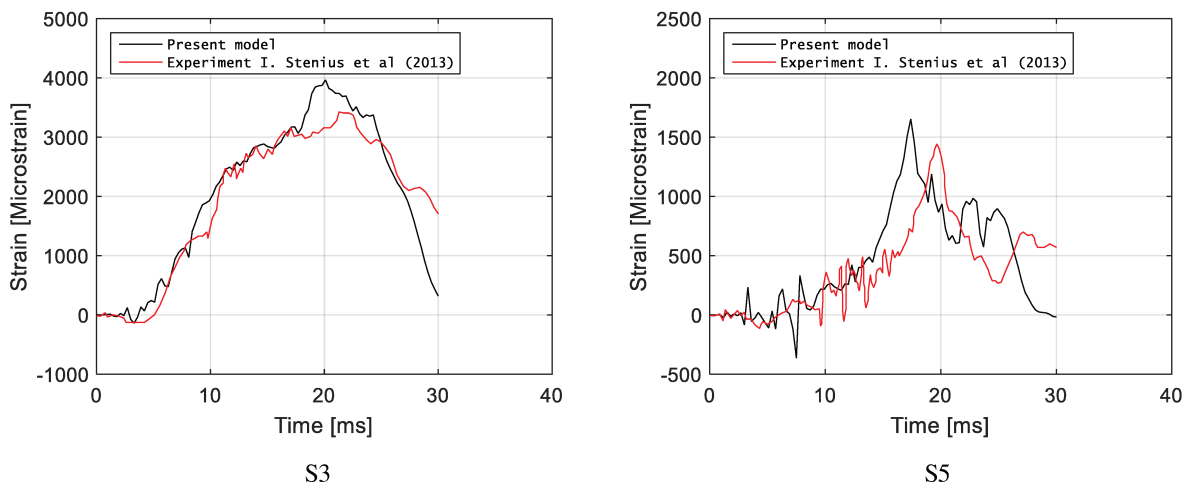


Figure 2. 34. Comparison of the panel deformation between the numerical results and experimental data, $V=4$ m/s.

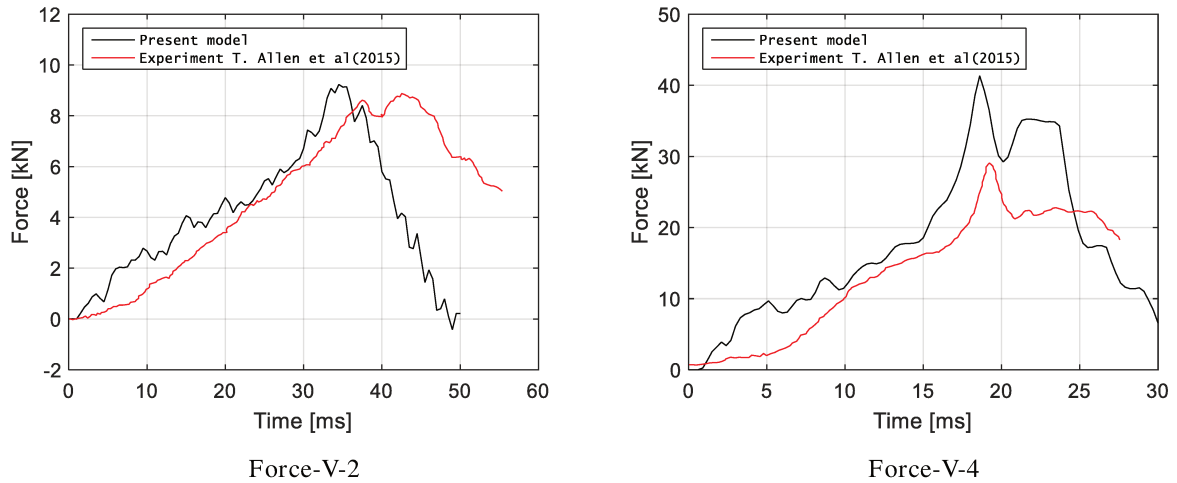


Figure 2. 35. Comparison of the hydrodynamic force between the numerical results and experimental data

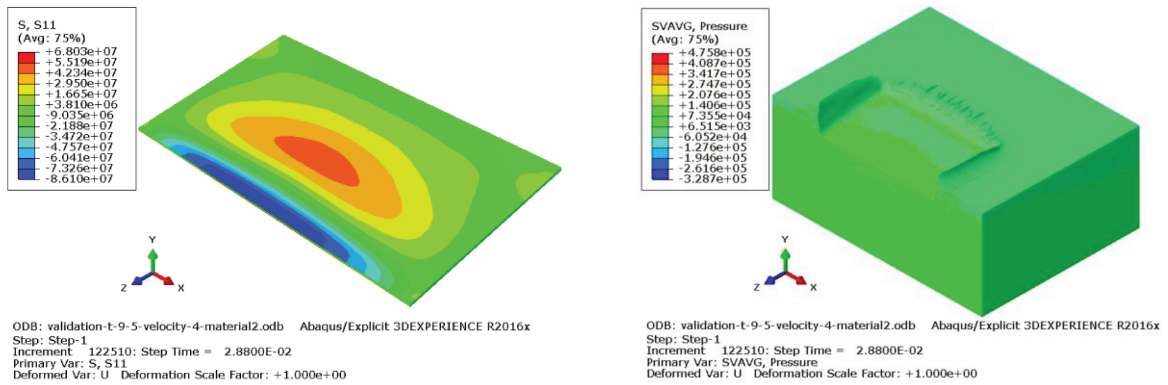


Figure 2. 36. Distribution of stresses and water jet after impact

The pressure obtained from the numerical model of impacted panels at 2 and 4m/s presents from P1 to P5 is illustrated in Figure 2. 37. The initial pressure peak at the keel and the centre of the panel (at P1 to P4) are lower than the pressure at P5 (close to the chine), which linking to the increasing of the panel deformation in these location especially at the centre of the panel, Figure 2. 38 . In contrast, higher pressure close to the chine has happened due to a reduction in the local deadrise angle and changed of the local impact velocity.

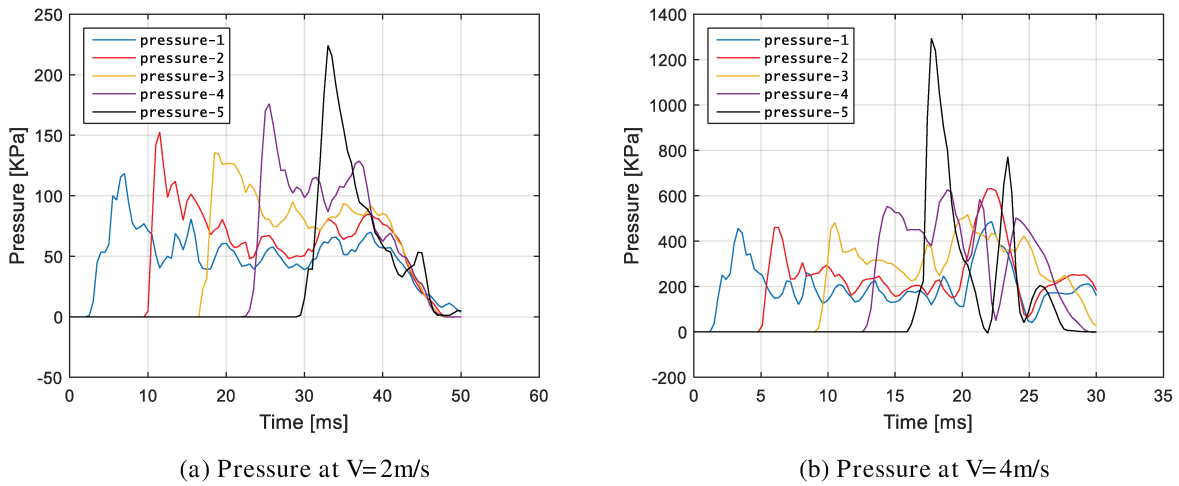


Figure 2. 37. Numerical results of pressure peak time histories

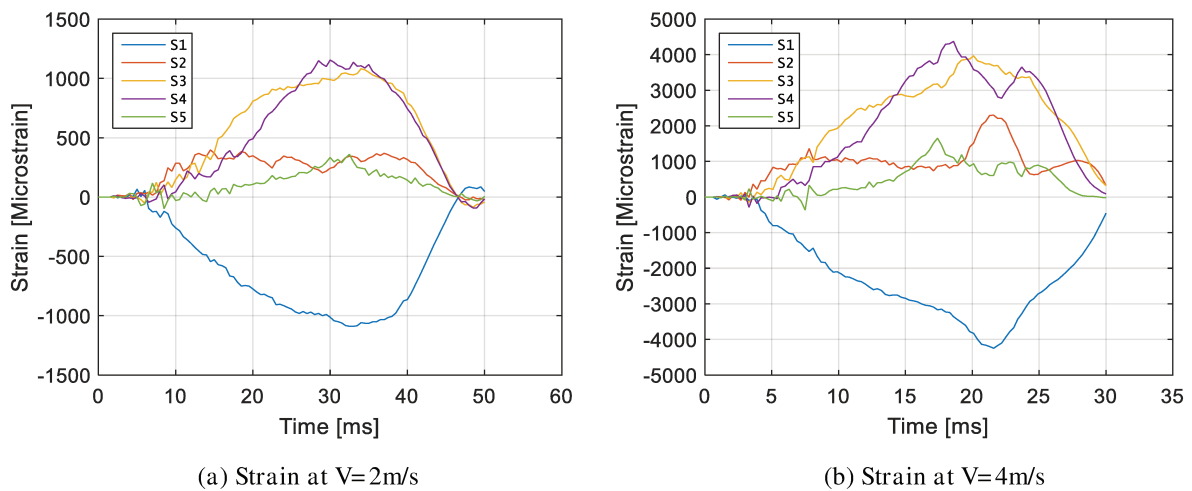


Figure 2. 38. Numerical results of deformation time histories

2.8 Conclusions

In this chapter, the numerical simulation models of the water entry problem for both rigid and deformable composite structures were implemented. Firstly, we have investigated the sensitivity of the Arbitrary Lagrangian Eulerian (ALE) solver in two dimensional schemes for the rigid body. This solver is dependent on the coupling contact, therefore, penalty contact methods were used. By defining the appropriate parameters for this method such as the stiffness scaling factor and mesh density, the stability was satisfied and the penetration was prevented between the rigid body and the water. When comparing this simulation with analytical methods, a good agreement can be observed of measured impact pressures (deadrise angles larger than 30°). Note that pressure peaks on the wedge decreased with an increase in the deadrise angle. For deadrise angles which less than 10°, some differences

occurred when compared with analytical methods, and sharp peak pressure occurred close to the jet flow region. The effects of the vertical impact velocity were also studied to demonstrate the change in the pressure distribution along the fluid/structure interface. However, the main disadvantage of the ALE is an excessive element distortion which can limit the use of this approach for large deformations in the fluid-structure interaction. Unlike the ALE, Coupled Eulerian Lagrangian (CEL) is considered to be physically more accurate and mesh distortion is eliminated. For this reason, it was exploited to represent the water domain as it provides more feasible modelling and allows high deformation in the fluid. The drawback of the CEL solver is the increase in computational time which depends on the number of elements in the fluid domain. The numerical model implemented the water entry problem of the composite wedges that were examined and executed in the previous experimental work, and the simulation results were in good agreement with experimental data.

Due to the lightweight and high strength properties of composites comparing to metallic structures, we investigated on dynamic response of laminate composites and sandwich panels in naval applications. Understanding the failure mechanisms and damage modes in composite materials and sandwich structures, and integrating them in the numerical model can enhance the reliability of these structures in the presented application. In the next chapter we will look at the identification and strive for better knowledge on failure mechanisms and damage models of composite structures.

References

- [1] N. Aquelet, M. Souli, "A new ALE formulation for sloshing analysis," *Structural Engineering and Mechanics*, vol. 16, no. 4, pp. 000-000, 2003.
- [2] A. Tassin, N. Jacques, A. El malki, A. Neme, B. Leblé, "Assessment and comparison of several analytical models of water impact," *Int. Jnl. of Multiphysics* , vol. 4, pp. 125-140, 2010.
- [3] I. Smojver , D. Ivancevic, "Bird strike damage analysis in aircraft structures using Abaqus/Explicit and coupled Eulerian Lagrangian approach," *Composites Science and Technology* , vol. 71, pp. 489-498, 2011.
- [4] ABAQUS/Explicit: Advanced Topics, Lecture 2 Elements, 2005. [Online]. Available: <http://imechanica.org/files/l2-elements.pdf>.
- [5] N. Aquelet, M. Souli, L. Olovsson, "Euler-Lagrange coupling with damping effects: Application to slamming problems," *Computer methods in applied mechanics and engineering*, vol. 195, pp. 110-132, 2006.
- [6] R. Panciroli, "Hydrodynamic impact of deformable wedges," in *Dynamic Failure of Composite and Sandwich Structure*, New York, London, Springer Science, Business Media Dordrecht, 2013, pp. 1-45.
- [7] I. Stenius, A. Rose, J. Kutteneuler, "Hydroelastic interaction in panel-water impacts of high-speed craft," *Ocean Engineering*, vol. 38, pp. 371- 381, 2011.
- [8] H. Wagner, "Uber stoss und gleitvorgange an der oberflach von flussigkeiten," *Zeitschrift fuer Angewandte Mathematik und Mechanik*, vol. 12, pp. 193- 215, 1932.
- [9] R. Zhao, O.M. Faltinsen, "Water entry of two-dimensional bodies," *Fluid Mech*, vol. 246, pp. 593-612, 1993.
- [10] T. von Karman, "The impact of seaplane floats during landing," *NACA TN.*, 1929.
- [11] C. W. Hirt, B. D. Nichols, "Volume of fluid (VOF) method for the dynamics of free boundaries," *Journal of Computational Physics* , vol. 39, pp. 201-225, 1981.

- [12] D. J. Benson, "Computational methods in Lagrangian and Eulerian hydrocodes," Computer Methods in Applied Mechanics and Engineering, vol. 99, pp. 235-394, 1992.
- [13] D. J. Benson, "Contact in a multi-material Eulerian finite element formulation," Computer Methods in Applied Mechanics and Engineering, vol. 193, pp. 4277-4298, 2004.
- [14] A. Aboshio, J. Ye, "Numerical study of the dynamic response of Inflatable Offshore Fender Barrier Structures using the Coupled Eulerian–Lagrangian discretization technique," Ocean Engineering, vol. 112, pp. 265-276, 2016.
- [15] I. Stenius, A. Rosén, J. Kutteneuler, "Explicit FE-modelling of hydroelasticity in panel-water impacts," International Shipbuilding Progress, vol. 54, pp. 111-127, 2007.
- [16] DVN, "Hull Structure Design, Fibre Composite and Sandwich Constructions," in Rule for Classification of High speed, Light Craft and Naval Surface Craft, Part 3, Chapter 4 ,2011.
- [17] "Structural design - FAO," [Online]. Available: www.fao.org/docrep/015/i2433e/i2433e04.pdf.
- [18] V. S. Deshpande, The design of sandwich panels with foam cores, Cambridge university, 2002.
- [19] I. Stenius , A. Rsén ,M.Battley, T.Allen, "Experimantal Hydroelastic Characterization of Slamming Loaded Marine Panels," Ocean Engineering, vol. 74, pp. 1-15, 2013.
- [20] M. A. Battley, T. Allen, P. Pehrson, I. Stenius, A. Rosen, "Effects of panel stiffness on slamming response of composite hull panels," in ICCM17, Edinburgh, UK, 2009.
- [21] T. Allen, M. A. Battley, "Quantification of hydroelasticity in water impacts of flexible composite hull panels," Ocean Engineering, vol. 100, pp. 117-125, 2015.

CHAPTER 3

Damage and Failure Mechanism in Composite Materials

Contents

3.1 Introduction	84
3.2 Composite materials	85
3.2.1 Composite laminates	86
3.2.2 Sandwich structure	87
3.3 Composite material levels	89
3.4 Defects in composite materials	90
3.5 Composite materials Failure Modes	91
3.5.1 Intralaminar failure based Continuum Damage Mechanics (CDM)	92
3.5.1.2 Failure initiation models	93
3.5.1.3 Damage evolution	96
3.5.2 Interlaminar failure (Delamination)	98
3.5.2.1 Constitutive model of the cohesive elements	102
3.5.2.2 Delamination propagation	103
3.6 Effect of the stacking sequence	104
3.7 Effect of velocity impact	106
3.8 Conclusions	107

3.1 Introduction

Composite materials have been used in recent years in many fields such as aerospace, automobile and naval applications due to their properties such as high strength, stiffness, lightweight and their performance capability in critical practical application environments. Moreover, due to the nature of composite material structure which consists of more than one material and principally fibres and matrix, therefore, different kinds of the damage and failure mechanisms can be occurs. For these reasons, they are considered active challenge areas in advanced material structures. The complexity of composite structures exhibits a variety of failure modes and damage compared with metallic materials, Figure 3. 1.



Figure 3. 1. Damage in a naval application [1]

Naval application design is usually constrained by lightweight and strong structures. This has led to exploration of composite materials, which have various specific mechanical properties and low specific weight. The advantages of the composite materials can be described as:

1. High strength and high stiffness to density ratio,
2. Corrosion resistance,
4. Good wear resistance,
5. Low weight,
6. Fatigue life,
7. Temperature-dependent behaviour,
8. Thermal conductivity,
9. Acoustical insulation.

For all of the above mentioned advantages, composite materials are more flexible and on the negative side, consequently suffer from high deflection in a large frame, anisotropy, complexity of structure, nature and variety in the manufacturing processes leading to the presence of different failure mechanisms. From the point of view of ship designers in structure optimisation, the damage in composite materials requires special attention in both the design and the operation phase. This is done by incorporating damage tolerance as a safety factor in the design loads. For composite structures in naval applications, the damage procedure is divided into local (panel) and global (ship) scale to estimate the reduction in strength, as illustrated in Figure 3. 2 [2].

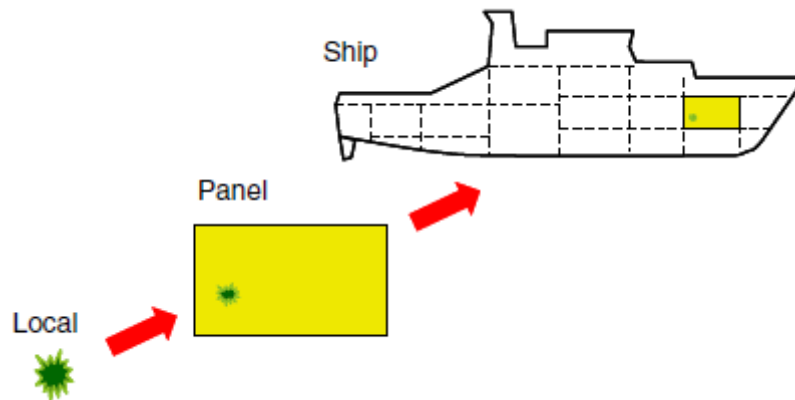
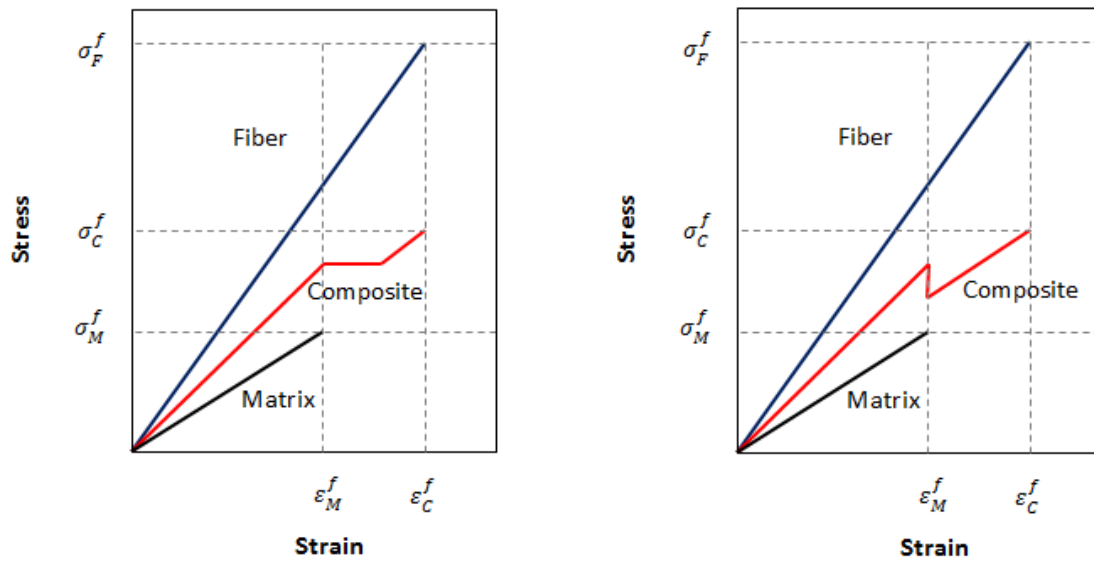


Figure 3. 2. Damage in the ship (local, panel, global scale) [2]

3.2 Composite materials

The physical behaviour of composite materials is different from other engineering materials which are homogeneous and isotropic. Composite materials are dealt with on a micromechanical and macromechanical scale to describe their non-homogeneity. Mechanical properties for both matrices and fibres are combined to define the composite material properties as illustrated in Figure 3. 3.



(a) Under constant loading

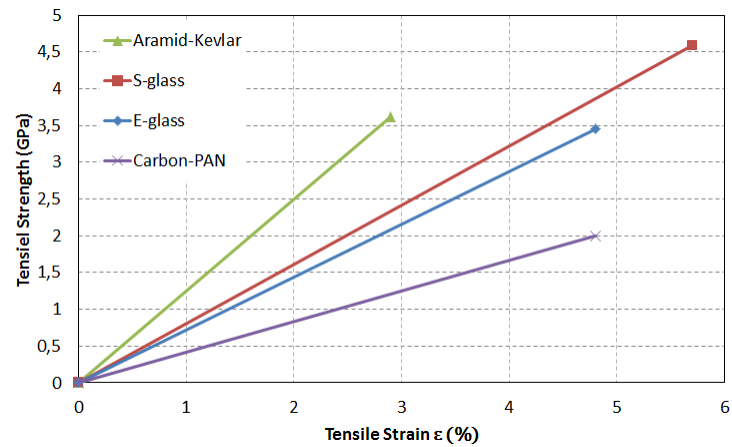
(b) Under constant deflection

Figure 3. 3. Stress-strain curves for brittle composite material

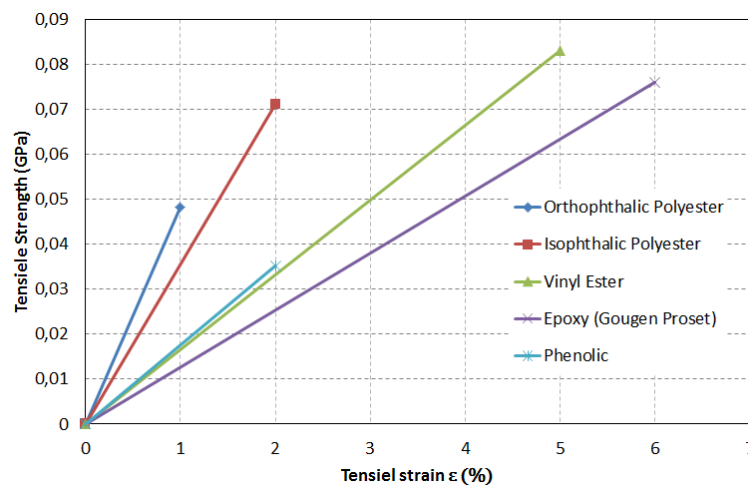
3.2.1 Composite laminates

The material type of both fibres and matrices defines the performance of the composite material. Ship designers usually compare the material characteristics of the hybrid composition of the composite laminate (fibre, matrix) and the sandwich structure (skin, core) to predict the performance and safety factors of the structure in the design optimisation phase, Figure 3. 4.

However, the variety of composite materials gives the designers more opportunities to optimisation the design from the point of view of manufacturing, cost and performance. In general, the complexity of the applied loads and the presence of different failure modes in the composite materials in naval applications have prompted researchers to specify and predict the failure criteria in composite materials, thus supporting the designer in making decisions about damage tolerance [3].



(a) Fibre



(b) Matrix

Figure 3. 4. Material mechanical properties [3]

3.2.2 Sandwich structure

Sandwich composite structure is widely used in lightweight applications and is becoming valued in many fields. The basic concept of these structures is to use two high stiffness sheets that are separated by a relatively thicker material that has a low density and more flexible core Table 3. 1. The property of the sandwich depends on the loading conditions, geometric configurations (faces and core) and the material type (faces, core and adhesive) [4]. Due to the different properties of the core and skin materials, with a high elastic modulus of the skin and low elastic modulus in the core, the resistance to flexural load is born by the skin while through the thickness shear forces are born by the core. For this reason, the most important mechanical properties are strength and stiffness when designing the appropriate sandwich panel. The sandwich structures with a composite skin, PVC and balsa cores are widely used in naval applications [5].

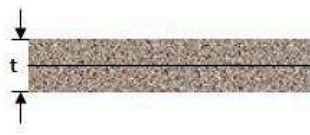
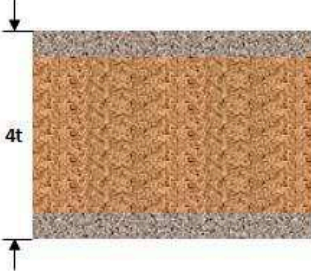
	Solid Composite	Sandwich Core Thickness $2t$	Sandwich Core Thickness $3t$
			
Stiffness	1.0	7.0	37.0
Flexural Strength	1.0	3.5	9.0
Weight	1.0	1.03	1.06

Table 3. 1 Mechanical and physical properties of sandwich structures with different core thicknesses

Failure modes in sandwich structures can be classified as: core local indentation, core shear, debonding between the face sheet and core, core cracking, face sheet buckling, face failure and face wrinkling, Figure 3. 5.

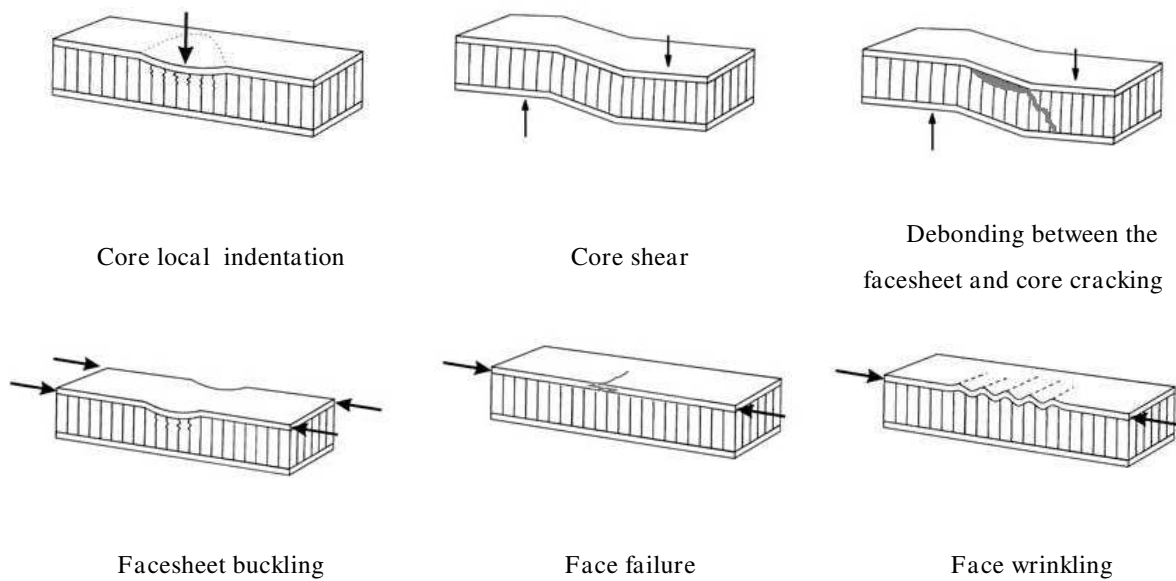


Figure 3. 5. Failure modes of sandwich structures

3.3 Composite material levels

For a better understanding of the failure mechanisms of composite materials, a hierarchical level structure was used to describe multiscale models, to enhance the analysis of composite materials as illustrated as illustrated in Figure 3. 6. A micro-structural level is used which enables the separate treatment of the fibres and matrices and can provide information on the behaviour of fibre-fibre and fibre-matrix interaction. It also allows the description of the complex mechanics of stress and strain in the composites due to the different properties of the fibres, matrices and their elastic moduli.

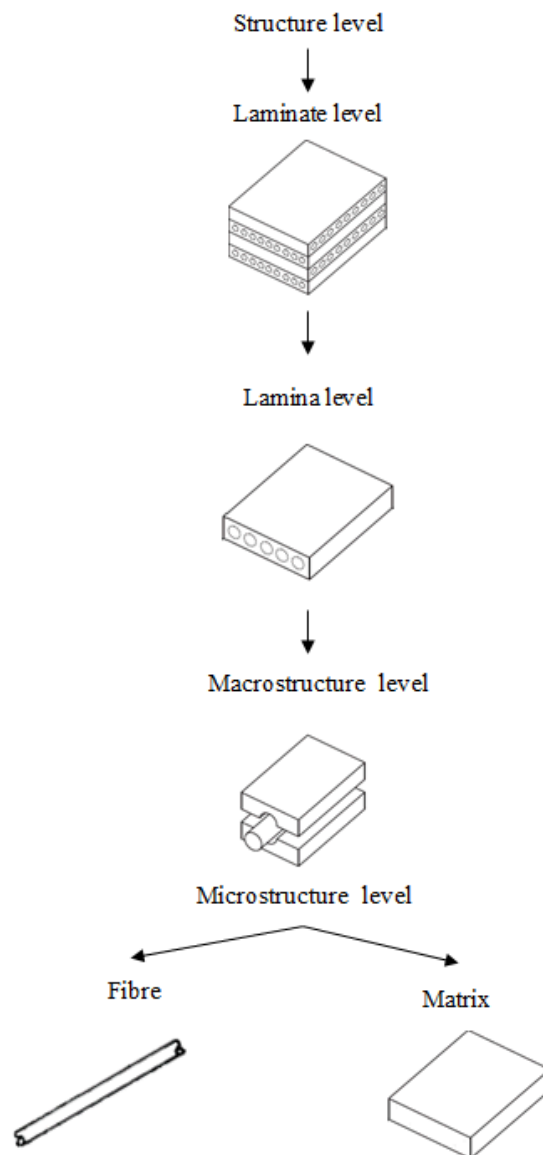


Figure 3. 6. Hierarchical composite material levels

The micro-structure failure mechanisms include fibre breakage, fibre buckling, fibre pullout, fibre/matrix debonding, matrix cracking and void nucleation [6]. Microscopic damage occurs throughout composite materials which contain potential initiators of failure due to different expansion coefficients and the manufacturing method. In fact, the introduction of porosity is normally due to voids in the matrix produced by incorrect pressure or vacuum bleeding of resin. These microscopic defects can lead to macroscopic damage.

This mechanism on a macromechanical scale can be incorporated at the lamina level. However, this is considered to be a basic limitation of composite materials, and can be interpreted as the behaviour of the laminate scale, which leads to the macromechanical analysis treating the composite as a homogeneous material.

3.4 Defects in composite materials

During the manufacturing process of composite materials, many defects appear. These defects consist of one or more cases as follows: incomplete saturation of the fibre, imperfect cure of the resin and incorrect adhesion of the fibre-matrix. Moreover, many voids, bubbles and micro-cracks are produced. These defects work as potential failure initiators and consequently reduce the performance of the structure in service environment [7]. Other defects may be introduced due to the machining process producing holes or corner edges or service damage from dropped or incorrectly handling of materials. These defects are internal damage and in most cases invisible on the external surface of the component and termed as Barely-Visible Impact Damage (BVID), consequently degrading the strength of the composite structure [8]. On the other hand, service defects are dependent upon the loading conditions, material used and practical environment. The major failure in composite structures during their lifetime service can be described as follows, Figure 3. 7:

- Interlaminar damage (delamination).
- Intralaminar damage:
 - Matrix cracking,
 - Fibre failure,
 - Debonding fibre-matrix interface.

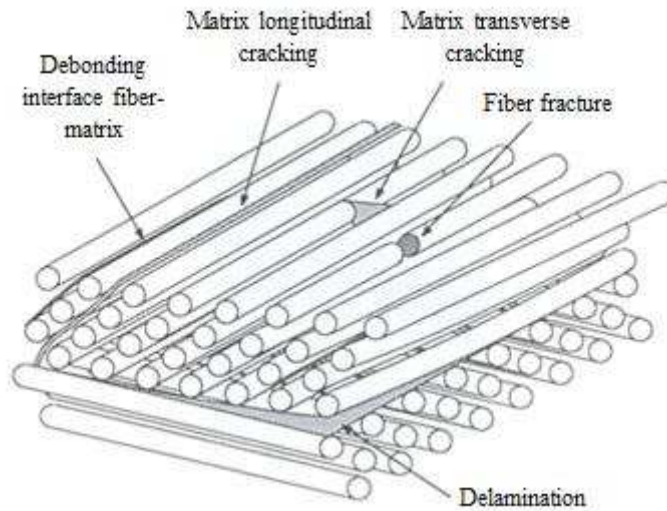


Figure 3. 7. Failure in composite materials [9]

As mentioned before, defects can influence the material stiffness, strength and service reliability. Therefore efforts are encouraged to detect these defects before the onset of the failure criteria that dominate the damage tolerance. This ensures that this damage cannot degrade the structure strength less than the design ultimate load.

3.5 Composite materials Failure Modes

Various researchers have categorised the failure criteria according to the stresses and the energy formulations with non-interactive and interactive combinations, Figure 3. 8. From this point of view, composite material failure modes depend on the fibre and matrix criterion under tension and compression loading. In general, research has been constrained to two modes for fibres due to their anisotropic nature on the other hand, some research studies have identified more than one mode for matrix failure criteria due to their complex morphology.

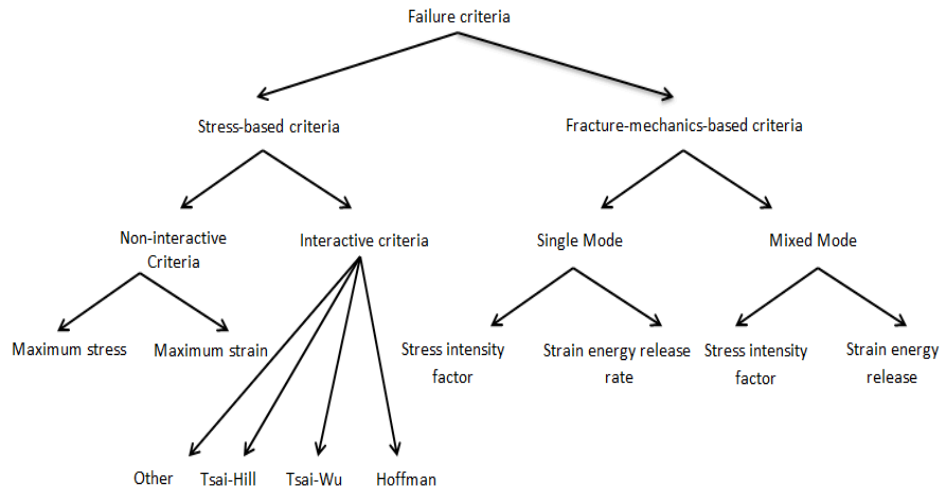


Figure 3. 8. Failure criteria classification [10]

3.5.1 Intralaminar failure based Continuum Damage Mechanics (CDM)

Damage of Composite material is an accumulation of microscopic defects in both fibres and matrices and other types of failure such as the initiation and development of micro-cracks with different scale sizes, on the interior and exterior of the structure, which are considered to be the main factors in the fracture mechanism. These cracks can propagate in many locations without an increase in the applied loads. The propagation of cracks in the structure depends on the atomic bonds, consequently the fracture of these bonds and the evolution of the cracks through the structure produce dissipated energy, Figure 3. 9.

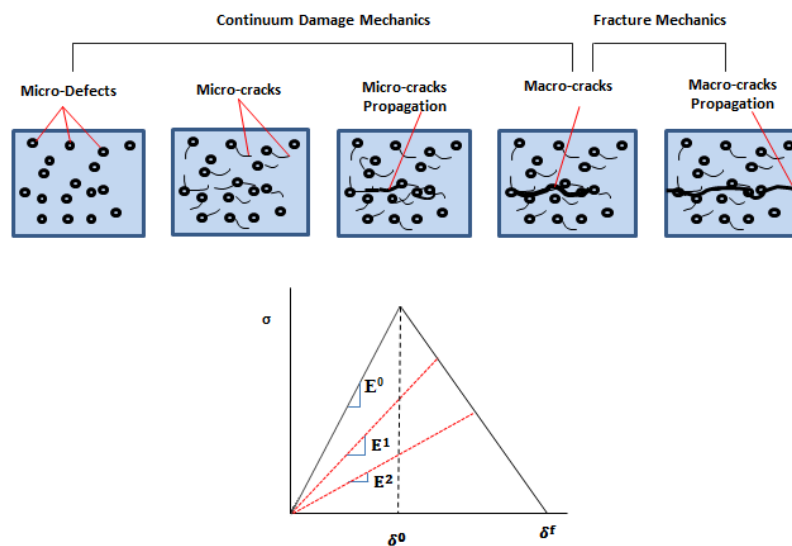


Figure 3. 9. Damage mechanism and evolution

3.5.1.2 Failure initiation models

The laminate damage initiation takes place when the true stress applied to the laminate reaches the ultimate strength of the ply laminate. The debonding interface between the fibre and matrix occurs due to the difference in the fibre transverse compressive modulus and the matrix modulus which represent the main influence on initiation of the damage. For this reason, the stresses are concentrated locally. Various failure criteria models have been adopted to predict damage onset based on a combination of longitudinal, transversal and shear stresses. The most satisfactory criterion is based on Hashin's theory [11].

Tsai-Wu (1971) introduced a method that was based on the maximum stress for transversely isotropic symmetry, since one mode dominates the material failure with seven parameters interacting with each other. This is considered to be the simplest method for the damage onset [12].

Hashin (1980) introduced a method of evaluating failure criteria for a unidirectional fibre composite with second degree polynomial expansion. For more simplicity, failure modes were divided into four modes based on the failure planes perpendicular and aligned with the fibre direction with six parameters, hence the failure of the fibres in the main direction of the fibre-axis, and on the other hand the main failure of the matrix in the transverse direction [13]. This criterion was widely applicable in most commercial finite element software. However, many researchers said that this model did not accurately predict initial failure, especially matrix and fibre compression modes [14].

Christensen (1998) applied criteria to failure under hydrostatic pressure, thereby reducing the parameters from 7 to 5, and reducing the failure mode to three (two modes of fibre and one mode of the matrix) applied conditions where the transverse tensile stress is equal to or less than the transverse compressive stress [15].

Puck (1998, 2002) developed a model representing by Hashin criteria and based on Mohr's method applied to a brittle fibre reinforced composite. However, this approach took into account the non-linear behaviour due to micro-cracks, matrix cracking and a change in fibre direction, incorporating the interfibre fracture (IFF) to detect many of the failure modes, and define the planes acting on the IFF. He believed that the inclination of the fracture plane parallel to the fibre was the main parameter, which would influence the onset of delamination, Figure 3. 10 [16, 17].

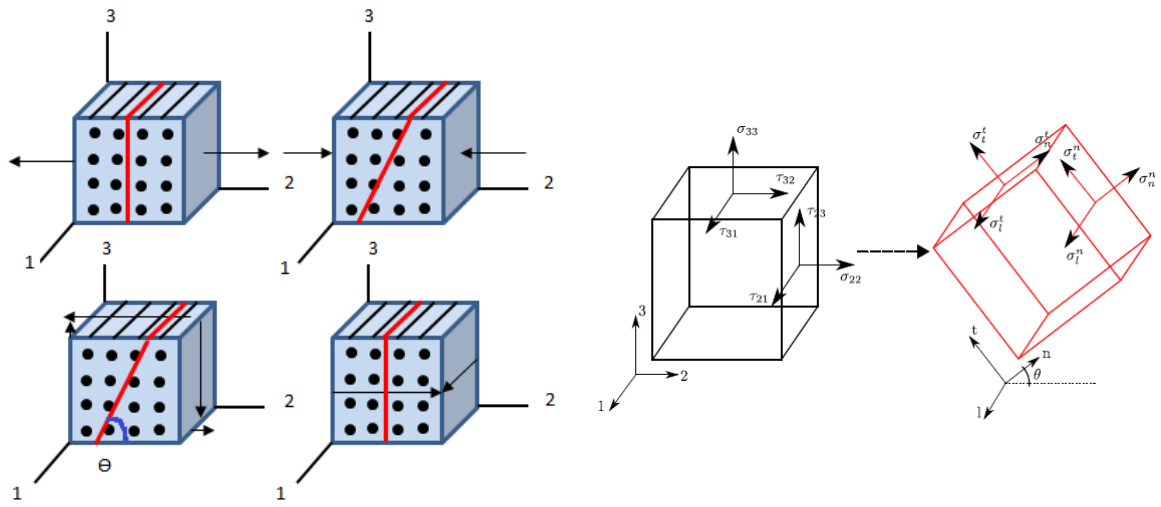


Figure 3. 10. Puck Matrix failure modes: failure with crack inclination parallel to principle fibre axis

Theory	Failure mode	Failure criteria
Tsai-Wu [12]	-	$F_1\sigma_{11} + F_2(\sigma_{22} + \sigma_{33}) + F_{11}\sigma_{11}^2 + F_{22}(\sigma_{22}^2 + \sigma_{33}^2) + 2F_{12}\sigma_{11}(\sigma_{22} + \sigma_{33}) + 2F_{23}\sigma_{22}\sigma_{33} + 2(F_{22} - F_{23}) + F_{66}(\sigma_{31}^2 + \sigma_{31}^2) = 1$
Hashin [11]	Fibre Tensile Failure ($\sigma_{11} \geq 0$)	$f_{ft} = \left(\frac{\sigma_{11}}{X_t}\right)^2 + \left(\frac{\sigma_{12}}{S_{12}}\right)^2 + \left(\frac{\sigma_{13}}{S_{13}}\right)^2 \geq 1$
	Fibre Compression Failure ($\sigma_{11} < 0$)	$f_{fc} = \left(\frac{\sigma_{11}}{X_c}\right)^2 \geq 1$
	Matrix Tensile Failure ($\sigma_{22} \geq 0$)	$f_{mc} = \left(\frac{\sigma_{22}}{Y_t}\right)^2 + \left(\frac{\sigma_{12}}{S_{12}}\right)^2 + \left(\frac{\sigma_{23}}{S_{23}}\right)^2 \geq 1$
	Matrix Compression Failure ($\sigma_{22} < 0$)	$f_{mc} = \left(\frac{\sigma_{22}}{Y_c}\right)^2 + \left(\frac{\sigma_{12}}{S_{12}}\right)^2 + \left(\frac{\sigma_{23}}{S_{23}}\right)^2 \geq 1$
Matzenmiller et al. [18] ($S_{12} = S_{23} = S_c$)	Fibre Tensile Failure ($\sigma_{11} \geq 0$)	$e_m^2 = \left(\frac{\sigma_{11}}{X_t}\right)^2 - 1 \geq 0$
	Fibre Compression Failure ($\sigma_{11} < 0$)	$e_c^2 = \left(\frac{\sigma_{11}}{X_c}\right)^2 - 1 \geq 0$
	Matrix Tensile Failure ($\sigma_{22} \geq 0$)	$e_m^2 = \left(\frac{\sigma_{22}}{y_t}\right)^2 + \left(\frac{\sigma_{12}}{S_c}\right)^2 - 1 \geq 0$
	Matrix Compression Failure ($\sigma_{22} < 0$)	$e_d^2 = \left(\frac{\sigma_{22}}{y_c}\right)^2 + \left(\frac{\sigma_{12}}{S_c}\right)^2 - 1 \geq 0$
Williams et al. [19] ($S_{12} = S_{23} = S$)	Fibre Tensile Failure ($\sigma_{11} \geq 0$)	$\omega_t = \left(\frac{\sigma_{11}}{X_t}\right)^2 - 1 \geq 0$
	Fibre Compression Failure ($\sigma_{11} < 0$)	$\omega_c = \left(\frac{\sigma_{11}}{X_c}\right)^2 - 1 \geq 0$
	Matrix Tensile Failure ($\sigma_{22} \geq 0$)	$\omega_t = \left(\frac{\sigma_{22}}{y_t}\right)^2 + \left(\frac{\sigma_{12}}{S}\right)^2 - 1 \geq 0$
	Matrix Compression Failure ($\sigma_{22} < 0$)	$\omega_c = \left(\frac{\sigma_{22}}{y_c}\right)^2 + \left(\frac{\sigma_{12}}{S}\right)^2 - 1 \geq 0$
Puck [16, 17]	Fibre Tensile Failure ($\sigma_{11} > 0$)	$\frac{\sigma_{11}}{R_t} = 1$
	Fibre Compression Failure ($\sigma_{11} < 0$)	$\frac{\sigma_{11}}{-R_c} = 1$
	Matrix Tensile Failure ($\sigma_{22} + \sigma_{33} \geq 0$)	$\left(\frac{\sigma_{11}}{2X_t}\right)^2 + \frac{(\sigma_{22} + \sigma_{33})^2}{Y_t Y_c} + \left(\frac{\sigma_{12}}{S_{12}}\right)^2 + (\sigma_{22} + \sigma_{33})\left(\frac{1}{Y_t} + \frac{1}{Y_c}\right)$
	Matrix Compression Failure ($\sigma_{22} + \sigma_{33} < 0$)	$\left(\frac{\sigma_{11}}{2X_t}\right)^2 + \frac{(\sigma_{22} + \sigma_{33})^2}{Y_t Y_c} + \left(\frac{\sigma_{12}}{S_{12}}\right)^2 + (\sigma_{22} + \sigma_{33})\left(\frac{1}{Y_t} + \frac{1}{Y_c}\right)$

Table 3. 2. Failure criteria models

A suitable selection of the failure onset criteria depends especially on the structure nature and the loading condition, however, Hashin failure criteria were applied widely in industry. On the other hand, these criteria may not predict accurately the failure initiation, especially in the fibre and matrix under compressive loadings [14]. In general, failure criteria are modelled to predict the failure for particular materials, and load configurations, thus no specific criteria can be adopted for general cases. The complexity of matrix morphology lies in the anisotropy of these materials. Therefore, many studies have concentrated their work on defining more of failure modes to describe the damage behaviour of the matrix, Table 3. 2.

3.5.1.3 Damage evolution

Despite satisfying the initiation of failure modes in composite materials, material stiffness continues to degrade with an increase in the load, the phenomena called damage evolution. The reduction in material's stiffness is controlled by damage variables corresponding to damage modes. The evolution of the damage progression in composite materials consists in a degrading in fibre and matrices. At the beginning, the composite structure maintains the original stiffness until the degradation of the matrix which happens first, since in reality the fibres have high strength compared to the matrix, consequently reducing the stiffness of the composite structure. The predicted fibre failure occurs second, thus reducing the composite stiffness accordingly. The difference between all the models lies mainly in the damage modes and the numerical degradation scheme employed. There are many failure degradation models that are proposed by researchers, and these models depended on the mechanism of material fracture, which can be divided into three categories as shown in Figure 3. 11 [20]:

- **Instantaneous:** means that the material properties are degraded instantaneously to the zero stress value, which corresponds to brittle materials.
- **Gradual loading:** this means that the material property degradation is gradual until the stress reaches to zero value. On the other hand, this behaviour is more common in composite materials [19].
- **Constant stress:** the material properties degraded while conserving a constant stress value.

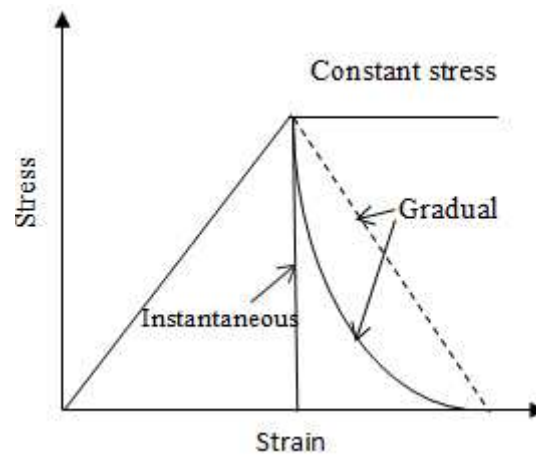


Figure 3. 11. Failure degradation models

Hahn and Tsai (1974) [21] introduced the stiffness degradation model which is considered the first work to describe the post-failure phenomena; they applied their method to the uniaxial behaviour of cross ply laminates, based on longitudinal modulus reduction with the presence of damage after the onset of the failure.

R. Talreja (1985) [22] classified the transverse cracking in cross-ply laminate, corresponding to adjacent plies were considered as constraint plies, and classified the degree of constraint into four types to characterise the deformation response. His classification was based on the descriptions of the oriented damage modes as vector fields and derived their relationship from the stiffness, modulus of elasticity and the damage vector magnitude. The model described the uniaxial and multiaxial loadings, and the strain-stress behaviour. The reduction in the elastic modulus with applied stress showed good agreement with tests and the ply discount method which was suggested by Highsmith and Reifsnider.

Matzenmiller et al (1995) [18] proposed a simple model for elastic-brittle composite materials. The initiation of damage based on the Hashin criteria can be introduced in four modes of the failure criteria depending on the failure plane in the matrix and fibres in tension and compression. Five damage variables control reduction in the elastic stiffness properties corresponding to the failure modes with respect to the effective stress.

Williams (2001) [19] incorporated the Matzenmiller-Lubliner-Taylor (MLT) approach in the LS-DYNA 3D for nonlinear analysis for propagation of damage in composite materials based on the CDM, then validity of the model for the non-penetrating impact by comparison

with previous experimental efforts. He improved the expression of instant behaviour and energy absorption in failure in regard to other recent models by providing the strain softening behaviour. Ireneusz (2007) [14] proposed a model for progressive damage in brittle fibre composite based on the dissipation energy proposed by Matzenmiller [18] and the onset of the failure based on Hashin criteria [13]. He implemented this model in the commercial finite element software-Abaqus, using a characteristic length to reduce the mesh size dependence. Viscous regulation also was studied to alleviate the difficulties in the convergence of the linear softening behaviour of initial failure state as it progressed to the damage state.

Maimi et al. (2007) [23, 24] developed a model based on continuum damage mechanics for quasi-static brittle composite materials for onset and propagation of intralaminar damage. The constitutive model was created based on thermodynamics of the irreversible process, which incorporated the experimental results with the computational rules to avoid incomplete and inaccurate modelling. Four modes of initial failure for both fibre and matrix based fracture planes ($\alpha = 0^\circ, 53^\circ \pm 3$) were used under tension and compression loading. The model results were compared with the experimental results of open-hole carbon fibre specimens under tensile loading.

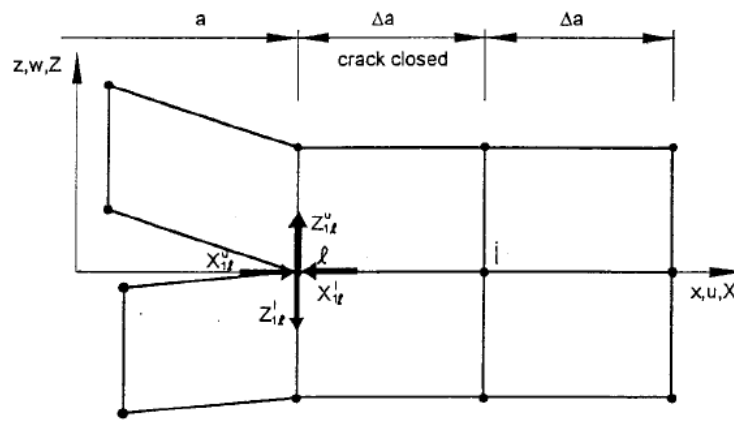
Xin and Wen (2015) [25] modelled a progressive damage model for fibre plastic laminate subjected to impact loading. This model used the initial criteria corresponding to the failure plane in fibre, matrix, and through-thickness delamination. Based on CDM to represent the progression of the damage and stiffness matrix degradation, strain rate effect was considered in this work. A good agreement was noted between the numerical and experimental results for impact loading with high velocity.

3.5.2 Interlaminar failure (Delamination)

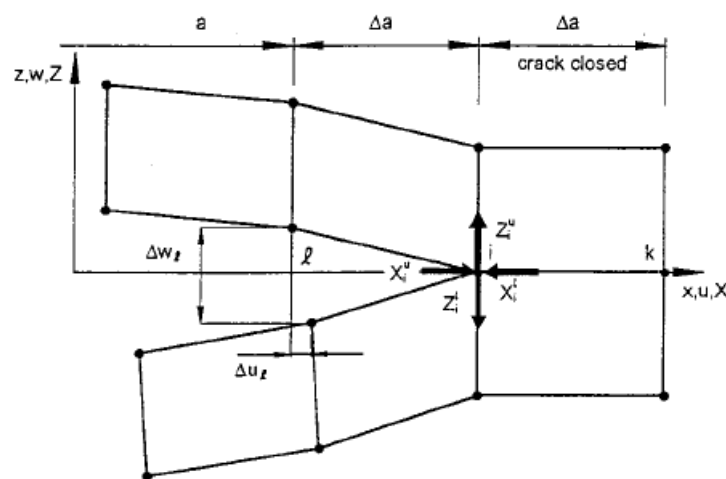
Delamination is considered to be a major type of damage having an influence on the strength of composite structures. It is normally caused by imperfect and weak bonding between the layers, the material morphology in that there is a mismatch between the fracture strength of the interlaminar interface and the reinforced layer. With the presence of the potential defect initiators and the dissimilar layer engineering properties, all these factors induce a concentration of normal stresses and transverse shear. The delamination propagation depends mainly on the matrix fracture toughness, stacking sequence, ply thickness and

loading condition, hence many studies have focused on these factors to improve delamination propagation resistance [8].

Most numerical models of delamination initiation and propagation are based on fracture mechanics and energy release rate. The Virtual crack closure technique (VCCT) was used to evaluate the energy release rate using Irwin's assumption that the energy dissipated to open the crack is equal to the work done to close the crack with the original length. The force and displacement element nodes located on the crack tip, thus evaluate the energy release rate with the change in crack length [26]. Thus, the force and displacements of these nodes are determined in two analytical steps to determine the extent of the crack ($a+\Delta a$), Figure 3. 12.



(a) Closed crack



(b) Crack extended

Figure 3. 12. Modified crack closure method [27]

The energy release rate for both mode I and mode II can be described as [27, 28]:

$$G_I = \frac{1}{2\Delta a} z_i \Delta w_l$$

$$G_{II} = \frac{1}{2\Delta a} X_i \Delta u_l$$
(3. 1)

Where z_i , X_i are the normal and shear forces at a node point and ahead of the crack tip. Δw_l , Δu_l are the differences in the node displacements in normal and shear force respectively.

The cohesive zone method is considered to be a powerful approach compared with other modelling methods, which incorporates the fracture strength approaches. The stress is concentrated on the surface which represents the cohesive zone between the layers of laminates.

The continuum damage model takes into account the irreversible damage consistent with the law of thermodynamics. The cohesive zone model (CZM) is considered to be an extension of Barenblatt–Dugdale (BD) model. This model is based on the concept that stress concentration ahead of the crack tip is constrained by the material yield strength and thus generates a plastic strip at a constant stress ahead of the intended crack path [29]. Hillerborg et al (1976) [30] have integrated fracture mechanics into the finite element method. The model is similar in some respects to the Barenblatt–Dugdale (BD) model, where fracture mechanics give the principal rules for crack evolution, and finite elements make it possible to analyse the complicated cases. The stress in the cohesive zone decreases with an increase in the crack width (w). Needleman (1987) [31] introduced a unified framework for describing the evolution from debonding initiation through to complete separation for the void nucleation based on the cohesive zone model, taking into consideration the finite geometry changes. Xu and Needleman (1994) extended the previous model to simulate numerically the dynamic crack growth in isotropic brittle solids, and for a wider variety of possible cracks paths, potential surfaces of the cohesive zone were inserted into the model [32]. The main advantage of CZM compared to VCCT, is that requires less computation time as there is no need for mesh refinement close to the crack tip, or to determine the initial crack location and direction to predict damage evolution [33, 34].

The cohesive zone model can be divided into groups: continuous cohesive elements and interface cohesive elements. Continuous cohesive elements are integrated between the surfaces which de-cohesion, as a thin layer constructed between the stacking surfaces which leads to a high respect ratio of element mesh in the cohesive zone. To overcome this situation, different types of cohesive element model have been proposed based on the element type (Solid, shell, line) with zero thickness and finite effective thickness [35, 36, 37]. However, a very small thickness of the cohesive element leads to high initial stiffness of the interface [37], Figure 4.13(a). The second method is based on the point (nodal) interface that is identical to a spring element. Each node pair of the surfaces are attached together, their connections are broken when the failure interface criteria is satisfied [38, 39]. Figure 3. 13.(b) represents the schematic diagram of the cohesive zone approach.

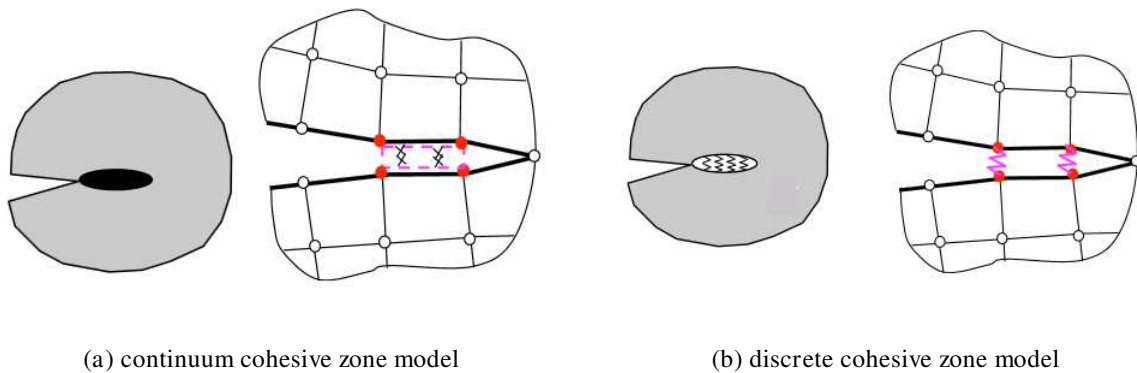


Figure 3. 13. Cohesive element model approach [38]

Alfano (2006) [40] introduced the influence of the shape interface law of cohesive element behaviour. As shown in Figure 3. 14, he studied four types of behaviour law: bilinear, linear-parabolic, exponential and trapezoidal. The same material parameters were applied in the analysis of the above mode laws (initial stiffness K_0 , fracture energy G and the stress traction σ_0) to investigate uniquely the influence of the interface law on the relationship of stress-strain law, based on the hypothesis that the surrounding regions close to the crack are affected by the crack propagation. There are two substantive conclusions in his work. The first, the shape of the interface law has a negligible influence on the finite element results, and the second, the shape of the interface law has an influence on the degree of approximation of the computation time. Finally the bilinear law is considered to be optimal solution in regard to the both the approximation and time computation. Bilinear law predicted the delamination with better agreement with the experiment results than the exponential law. However, defining a delamination behaviour law is based on the experimental results.

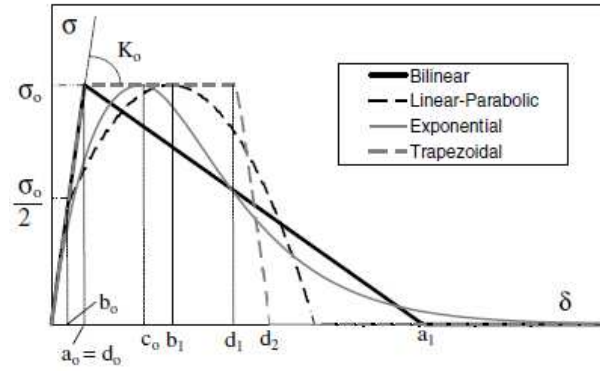


Figure 3. 14. Interface behaviour laws for cohesive elements [40]

3.5.2.1 Constitutive model of the cohesive elements

The delamination model can be divided into two phases: delamination onset and delamination prorogation. The onset of the delamination initially depends on strength based criteria, a quadratic polynomial combination of both normal stress and shear stresses that are applied the surface nodes interface between the layers, based on the traction-separation softening behaviour as [41]:

$$\left(\frac{t_n}{t_n^0}\right)^2 + \left(\frac{t_s}{t_s^0}\right)^2 + \left(\frac{t_t}{t_t^0}\right)^2 = 1 \tag{3.2}$$

Where t_n is the nominal traction stress under normal stress and t_s is the shear stresses determined and corresponding to the elastic stiffness (k) in mode I, mode II and mixed mode I/II multiple with corresponding effective onset displacements (δ) as shown in Figure 3. 15.

$$\delta_I^0 = \frac{t_n^0}{K_I} \quad , \quad \delta_{II}^0 = \frac{t_s^0}{K_{II}} \quad , \quad \delta_I^0 = \frac{t_t^0}{K_{III}} \tag{3.3}$$

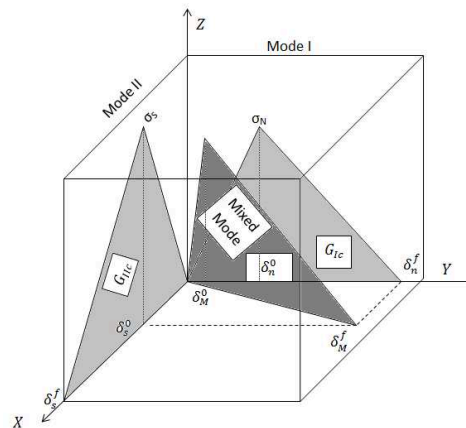


Figure 3. 15. Mixed Mode softening law behaviour [41]

3.5.2.2 Delamination propagation

The delamination propagation is usually based on fracture mechanics are based criteria which on energy release rates for the modes G_I , G_{II} and G_{III} and fracture toughness. The area under the force –displacement curve is equal to energy corresponding to each mode and representing the material property as [41]:

$$\int_0^{\delta_n^f} t_n d\delta_n = G_{IC}$$

$$\int_0^{\delta_s^f} t_s d\delta_s = G_{IIC} \quad (3.4)$$

$$\int_0^{\delta_t^f} t_t d\delta_t = G_{IIIC}$$

Where δ_n^f , δ_s^f and δ_t^f are the failure displacements corresponding to each mode; the crack opening is complete and the stress has been reduced to zero:

$$\delta_n^f = 2 G_{IC}/t_n^0 \quad , \quad \delta_s^f = 2 G_{IIC}/t_s^0 \quad , \quad \delta_t^f = 2 G_{IIIC}/t_t^0 \quad (3.5)$$

The most widely used mode under mixed mode loading is the power law criteria which interacts with the energy release rates in mode I and II as shown in Equation (3.6) [42] :

$$\left(\frac{G_I}{G_{IC}}\right)^\alpha + \left(\frac{G_{II}}{G_{IIC}}\right)^\alpha = 1 \quad (3.6)$$

Where $\alpha=1$ for linear, $\alpha=2$ for quadratic

To take into account the variation in the fracture toughness for the mixed mode, a more appropriate model was proposed by Benzeggagh and Kenane (B-K criterion) that ignores the contribution of the pure modes and combines them into a single mode as shown in Figure 3.16 [43].

$$G_c = G_{Ic} + (G_{IIc} - G_{Ic}) \left(\frac{G_{II}}{G_T}\right)^m \quad (3.7)$$

To compute the energy release rate experimentally for each mode, test Double Cantilever Beam (DCB) for pure mode I, End Notched flexure (ENF) for pure mode II and Mixed mode Bending (MMB) are normally used.

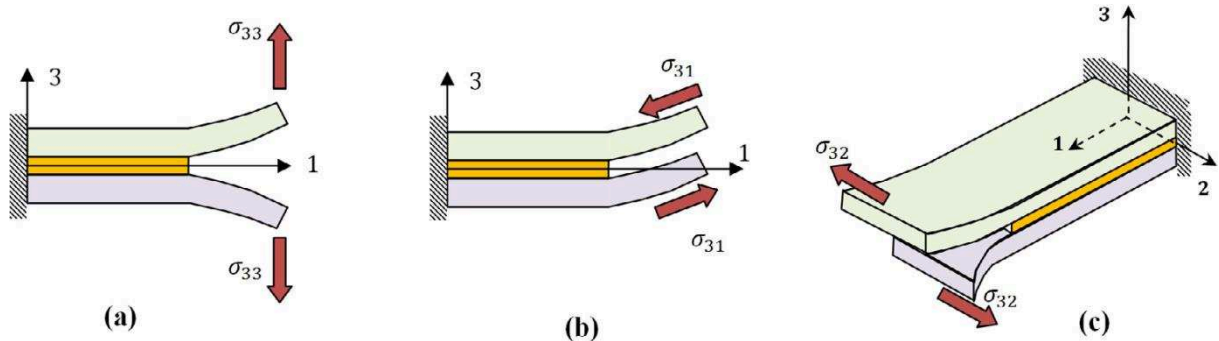


Figure 3. 16. Three modes to determine the energy release rate (a) Mode I (b) Mode II (c) Mode III [44]

3.6 Effect of the stacking sequence

The structure response is sensitive to interlaminar damage with different laminate stacking sequences. The crack faces a different lamina with different fibre orientation (dissimilar in Young's modulus and Poisson's ratio), thus the crack propagates in the interface rather than to the neighbouring layer. However, these scenarios depend mainly on the loading condition, the stress concentration and the deformations in local position.

Hitchen and Kemp (1995) studied the effect of the stacking sequence on the damage impact resistance for carbon fibre/epoxy composite. Inserting the 45° fibres between the adjacent layers and increasing the dissimilar interfaces, the delamination area and absorbed energy increased after the maximum force occurred, noted that fibre fracture has an influence on the delamination shape [45]. Will et al. (2002) experimentally studied the effect of the laminate stacking sequence from point view of energy dissipation under impact loading for carbon/epoxy tubular structure. They used a different laminate with different stacking sequences with the same thickness of the plies [46]. Camanho and Matthews (1999) proved that laminates with more layers stacked together (neighbouring layers) with the same orientations have lower delamination onset loads [47].

N. Hongkarnjanakul et al. (2013) [48] numerically performed the low velocity impact test on the T700GC/M21 laminated plates based on switching ply location using finite element

modelling. Seven stacking sequence configurations were studied showing the influence of the stacking sequence on the delamination areas, Figure 3. 18.

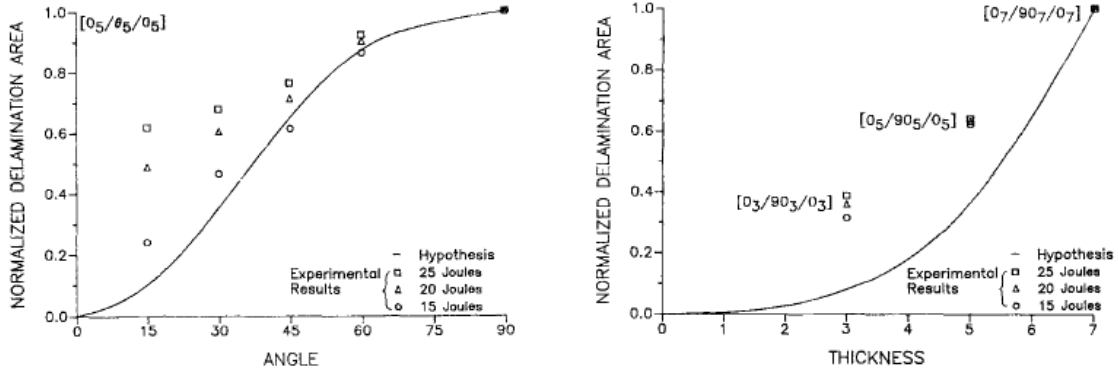


Figure 3. 17. Effect of the fibre orientation angle and the stacking thickness of the laminate [49]

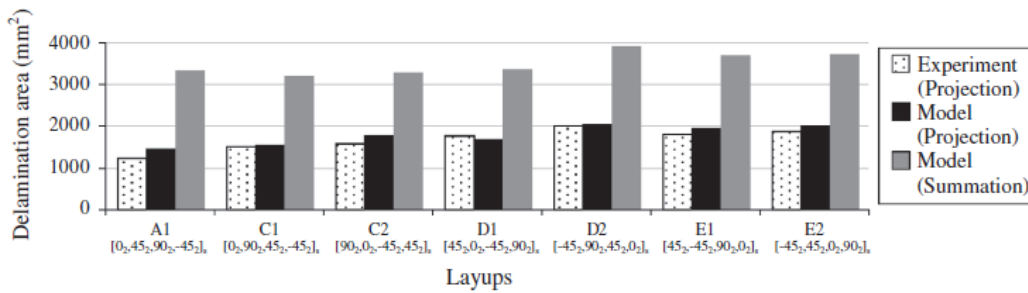


Figure 3. 18. Effect of the stacking sequence on delamination [48]

The thickness of the lamina is another parameter which has the effect of accelerating the delamination in the thicker ply due to an increase in interlaminar stress, Figure 3. 19 [8].

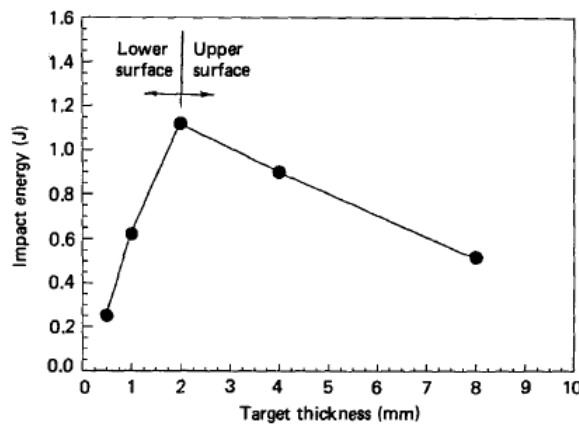


Figure 3. 19. Influence of the thickness of lamina on low velocity impacts, $[\pm 45^\circ]_n$ CFRP composites [50]

3.7 Effect of velocity impact

In the first step in naval structure design, engineers define the loading acting on the structure. Normally, it is not easily to predict the loads that will act on the naval structure without knowing the environmental marine information and such as wave loads and loading situations, thus it is difficult to define the allowable material properties and the configuration dimensions [3]. Structure response under impact loading depends on the velocity and the mass of the projectile. High velocity impact is dominated by stress wave propagation through the material, thus the effects of the boundary conditions are ignored due to the short time it takes the of stress wave to reach edges of the structure. On the other hand, the boundary conditions have an important effect on the structure response under low velocity impact, since the stress wave has a long enough time to propagate through the structure, therefore more energy is absorbed in the elastic phase [51]. The plate behaviour can be classified into three categories that correspond to the velocity impact and impactor mass. Figure 3. 20 (a) shows that the stress wave is propagated through the thickness of the plate and does not have enough time to reach the structure boundary edges due to local deformation which occurs with ballistic impacts, as a result, the plate boundary conditions can be ignored. On one hand, with high impact velocity, Figure 3. 20 (b), the structure response is dominated by the shear and flexure wave. On the other hand Figure 3. 20 (c), under low velocity impact, the structure response occurs due to the shear and flexure waves having a more time to reflect from the impact location and the structure boundary. For this reason the boundary conditions and the plate size have a major effect on the structure response [52, 53].

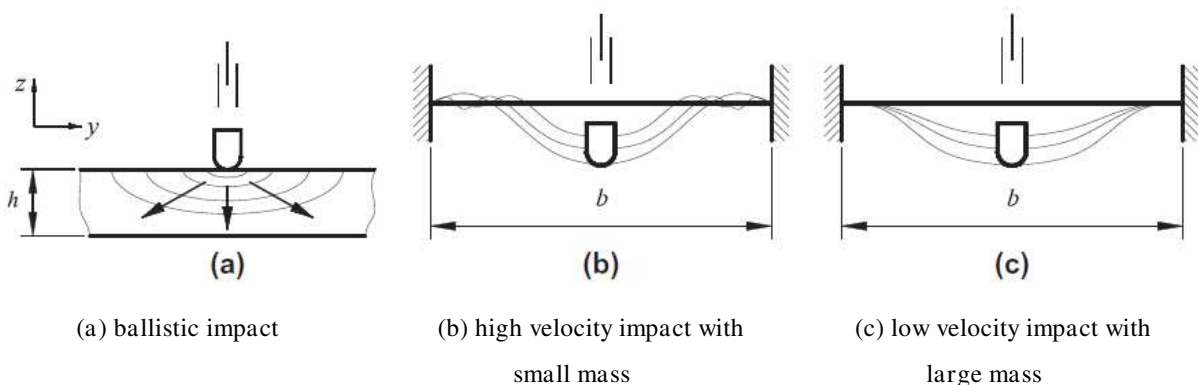


Figure 3. 20. Structure response [53]

3.8 Conclusions

From a practical point of view in shipbuilding, all types of damage must be considered to predict the structural performance in the presence of damage which consequently assists the ship designers to estimate the design requirements. Currently, composite materials are widely used in the ship structures and can sustain different modes of failure which can reduce structural strength. Damage tolerance and damage resistance are the key to the development of composite structures, since predicting the resistance to the initiation and spread of the damage and conserving the strength concerns continuum damage mechanics and fracture mechanics. Therefore, various damage modelling techniques were reviewed and some of their advantages and disadvantages were mentioned.

In short, for the different failure modes of intralaminar damage as summarized in this chapter, some points have been concluded:

1. Continuum damage mechanics is considered to be a powerful tool to predict failure onset in composite materials for the fibre and especially the matrix. On the other hand, fracture mechanics represents the link to predict microscopic damage.
2. The most suitable interlaminar failure criteria are the Hashin quadratic criteria for fibre tension, and matrix tension. In contrast, this criterion cannot predict accurate results for both fibre compression and matrix compression. While the most appropriate criteria for the matrix are Puck criteria due to their taking into account the fracture plane angle based on the fact that due to the nature of the matrix, crack propagation tends to occur in random directions. Although, this is not the general case for composite materials which depend on other factors for a more authentic selection of the failure criteria, for example: load condition, material types and stacking configuration.
3. According to the load conditions, the cause for great concern in low velocity impact is the matrix failure, as matrix cracks have a long time to propagate through the material in different directions and extend over a large area. On the other hand, high velocity impact occurs over a duration and with local deformation close to the impact location, so that fibre failure modes are more important in this case.

Equally important, interlaminar failure (delamination) is considered to be the main failure relating to strength reduction especially with the absence of the reinforcement

through thickness. In summary, some important points help to explain delamination behaviour:

1. For unidirectional laminates, the matrix fracture toughness represents the dominant effective physical factor in interlaminar failure. Of course, there are other factors that influence the onset and acceleration of delamination propagation such as stacking sequences, loading conditions and laminate thickness.
2. Delamination modelling is based on fracture mechanics and energy release rates, the cohesive element model is more appropriate for many reasons compared to other approach. Numerically, it is not necessary to define initially a pre-crack to predict the delamination onset and propagation, furthermore, it requires less computational time.
3. The optimal behaviour law for cohesive models is a bilinear law due to less of computational time, in addition the exponential law is considered to be the most suitable from the point of view of the solution convergence.
4. In our opinion, the cohesive interface element model is more applicable in numerical simulations, with a zero thickness of the cohesive layer, thus a high initial stiffness requires to delamination onset. In addition, a finite thickness of the cohesive layer leads to a reduction in the mesh aspect ratio compared with the neighbouring composite lamina.
5. Numerically, in the implicit procedure (quasi-static and static loading) with a high time step, the solution convergence for nonlinear cohesive behaviour is difficult to obtain, therefore artificial viscosity is added to the model. In contrast, the explicit scheme (dynamic loading) with low step time can converge better the solution for cohesive elements.
6. For composite structures which are more robust, it would be more appropriate to avoid a large difference in fibre orientation of neighbouring laminas to reduce dissimilar mechanical properties in the interface. On the other hand, reinforcement through thickness is also a good solution.
7. To account for the variation in fracture toughness as a function of the mixed mode, especially in the uniaxial loading, the most appropriate model is Benzeggagh and Kenane (B-K criterion) which combines pure modes into a single mode.

Finally, for sandwich structure under slamming impact, the debonding between the core and the faces is considered to be most common failure mode, occurring due to flexural loading and shear stresses. To identify the intralaminar damage mode in composite structures,

a three dimensional constitutive progressive degradation model was developed and write using VUMAT subroutine coded in FORTRAN program, in addition to modelling of interlaminar damage mode that implemented in the Abaqus explicit code. These would be covered in the next chapter.

References

- [1] Christian Berggreen, "Damage tolerance of debonding sandwich structures," Phd thesis , Technical University of Denmark, Department of Mechanical Engineering, 2004.
- [2] D. Zenkert , A. Shipsha , P. Bull, B. Hayman , "Damage tolerance assessment of composite sandwich panels with localised damage," Composites Science and Technology, vol. 65, pp. 2597-2611, 2005.
- [3] E. Green, "Design guide for marine applications of composites," Ship Structure committee, Washington, 1997.
- [4] I. M. Danial, E. E. Gdoutos, "Failure modes of composite sandwich beams," in Major Accomplishments in Composite Materials and Sandwich structures, Heidelberg London New York, springer, 2009, pp. 197-227.
- [5] K. Shivakumar, H. Chen, "Structural performance of eco-core sandwich panels," in Major Accomplishments in Composite Materials and Sandwich Structures, Dordrecht Heidelberg London New York, Springer Science, 2009, pp. 381-406.
- [6] R. C. Batra, N. M. Hassan , "Modeling of Progressive Damage in High Strain-Rate Deformations of Fiber-Reinforced Composites," in Major Accomplishments in Composite Materials and Sandwich Structures, Springer Dordrech Heidelberg London New York, 2009, pp. 89-111.
- [7] W. Johanson, S.K.Ghosh , "Review some Physical Defects Arising in Composite Material Fabrication," Journal of the Materials Science, vol. 16, pp. 285-301, 1981.
- [8] A.C. Garg , "Delamination-A Damage Mode in Composite structures," Engineering Frachue Meckanics, vol. 29, no. 5, pp. 557-584, 1988.
- [9] B. Jean-Marie, Matériaux Composites: Comportement mécanique et analyse des structures, TEC & DOC, 2005.
- [10] M.R. Wisnom, M.Jones, "A comparision of failure criteria to predict delamination od

unidirectional glass/epoxy specimens waisted through the thickness,” Composites, vol. 23, pp. 158-166.

- [11] Z. Hashin, “Fatigue Failure Criteria for Unidirectional Fiber Composites,” Journal of Applied Mechanics, vol. 48, pp. 846-852, 1981.
- [12] S. W. Tsa, E. M. Wu , “A general theory of strength for anisotropic materials,” Journal of Composite Materials, vol. 5, pp. 58-80, 1971.
- [13] Z. Hashin , “failure criteria for unidirectional fiber composites,” Journal of Applied Mechanics, vol. 31, pp. 223-232, 1980.
- [14] Ireneusz Lapczyk, Juan A. Hurtado, “Progressive damage modeling in fiber-reinforced materials,” Composites Part A: Applied science and manufacturing, vol. part A 38, pp. 2333-2341, 2007.
- [15] R. M. Christensen, “The numbers of elastic properties and failure parameters for fiber composites,” Journal of Engineering Materials and Technology, vol. 120, pp. 110-113, 1998.
- [16] A. Puck, H. Schurmann, “Failure analysis of FRP laminates by means of physically based phenomenological models,” Composites Science and Technology, vol. 58, pp. 1045-1067, 1998.
- [17] A. Puck, H. Schurmann , “Failure analysis of FRP laminates by means of physically based phenomenological models,” Composites Science and Technology, vol. 62, pp. 1633-1662, 2002.
- [18] A. Matzenmiller, R. Lubline, J. R L Taylor, “A Constitutive Model for Anisotropic Damage in Fiber-Composites,” Mechanics of Materials, vol. 20, p. 125–152, 1995.
- [19] K. V. Williams, R. Vaziri, “Application od a damage mechanics model for predicting the impact response of composite materials,” Computers & Structures, vol. 79, pp. 997-1011, 2001.
- [20] G.Perillo, N. P. Vedvik, A. Echtermeyer, “Numerical application of three-dimensional failure criteria for laminated composite materials,” SIMULIA Customer Conference,

2011.

- [21] T. H. Hahn, S. w.Tsai , “On the Behavior of Composite Laminates After Inatial Failure,”
Journal of Composite Materials, vol. 8, pp. 288-305, 1974.
- [22] R. Talreja, “Transverse Cracking and Stiffness Reduuction in Composite Laminates,”
Journal of Composite Materials, vol. 19, pp. 355-375, 1985.
- [23] P. Maimi, P.P. Camanho, J.A.Mayugo, C.G. Davila, “Acontinum damage model for
composite laminates: Part I- Consitutive model,” Mechanics of Materials, vol. 39, pp.
897-908, 2007.
- [24] P. Maimi, P.P.Camanho, J. A. Mayugo, C.G. Davila , “A Continuum damage model for
composite laminates: Part II- Computational implementation and validation,” Mechanics
of Materials, vol. 39, pp. 909-919, 2007.
- [25] S.H. Xin, H. M. Wen , “A Progressive Damage Model for Fiber Reinforced Plastic
Composites Subjected to Impact Loading,” Impact Engineering, vol. 75, pp. 40-52, 2015.
- [26] E. F. Rybicki, M. F.Kanninen , “A finit element calculation of stress intensity factors by
a modified crack closure integral,” Engineering Fracture Mechanics, vol. 9, pp. 931-938,
1977.
- [27] R. Krueger, “Virtual crack closure technique: History, approach, and application,” Appl
Mech Rev, vol. 57, no. 2, pp. 109-143, 2004.
- [28] R. Sethuraman, S. K.Maiti , “Finite element based computation of strain energy release
rate by modified crack closure integral,” Engineering Fracture Mechanics, vol. 30, no. 2,
pp. 227-231, 1988.
- [29] De Xie, Anthony, M. Waas , “Discrete cohesive zone model for mixed-mode fracture
using finite element analysis,” Engineering Fracture Mechanics, vol. 73, pp. 1783-1796,
2006.
- [30] A. Hillerborg, M. Modeerand, P-E. Petersson, “Analysis of crack formation and crack
growth in concrete by means of fracture mechanics and finite elements,” CEMENT and

CONCRETE RESEARCH, vol. 6, pp. 773-782, 1976.

- [31] A. Needleman , “A continuum model for void nucleation by inclusion debonding,”
Journal of applied mechanics, vol. 54, pp. 525-531, 1987.
- [32] X. P. Xu, A. Needleman , “Numerical simulations of fast crack growth in brittle solids,”
J.Mech.Phys.Solids, vol. 42, no. 9, pp. 1397-1434, 1994.
- [33] L. Hamitouche, M. Tarfaoui, A. Vautrin , “An Interface Debonding Law Subject to
Viscous Regularization for Avoiding Instability: Application to the Delamination
Problems,” Engineering Fracture Mechanics, vol. 75, pp. 3084 - 3100, 2008.
- [34] S.Jacques, I. De Baere, Van Paepegem , “Analysis of the numerical and geometrical
parameters influencing the simulation of Mode I and Mode II delamination growth in
unidirectional and textile composites,” springer, pp. 1-32, 12 December 2014.
- [35] De Moura, M. F., Gongalves J. P. , Marques A. T., de Castro P. T., “Modeling
Compression Failure After Low Velocity Impact on Laminated Composites Using
Interface Elements,” Journal of Composite Materials, vol. 31, no. 15, pp. 1462-1479,
1997.
- [36] E. D. Reedy, F. J. Mello, T. R. Guess , “Modeling the inatiation and growth of
delaminations in composite structures,” Journal of composite materials, vol. 31, no. 8,
pp. 812-831, 1997.
- [37] Y. Mi, M. A. Crisfield, G. A. Davies , “Progressive delamination using interface
elements,” Journal of Composite Materials, vol. 32, no. 14, pp. 1246-1272, 1997.
- [38] De Xie, A. M. Waas , “Discrete cohesive zone model for mixed-mode fracture using
finite element analysis,” Engineering Fracture Mechanics, vol. 73, pp. 1783-1796, 2006.
- [39] K. W. Shahwan, A. M. Waas , “Non-self-similar decohesion along a finit interface of
Unilaterally Constrained Delaminations,” Proceedings of the Royal Society of London,
vol. 453, pp. 515-550, 1997.
- [40] G. Alfano, “On the influence of the shape of the interface law on the application of

- cohesive-zone models,” *Composites Science and Technology*, vol. 66, pp. 723-730, 2006.
- [41] P.P. Camanho, G. C. Davila , “Mixed-Mode Decohesion Finite Elements for the Simulation of Delamination in Composite Materials”,” NASA/TM,, "pp. 1-37, 2002..
- [42] Y. Mi, “Progressive Delamination Using Interface Element,” *Journal of Composite Materials*, vol. 32, pp. 347-358, 1998.
- [43] X. J. Gong, M. L. Benzeggah, “Determination of the Mixed Mode Delamination Toughness Using an Imposed Displacement Cantilever Beam Test Method,” in *ECCM 5, Bordeaux*, 1992.
- [44] A. Amir Shojaei ,A.B. Guoqiang Li , P.J. Tan, Jacob Fish, “Dynamic delamination in laminated fiber reinforced composites: A continuum damage mechanics approach,” *International Journal of Solids and Structures*.
- [45] S. A. Hitchen, R. M. J. Kemp , “The effect of stacking sequence on impact damage in a carbon fibre/epoxy composite,” *COMPOSITES*, vol. 26, no. 3, pp. 207-214, 1995.
- [46] M. A. Will, T. Franz, G. N.Nurick , “The effect of laminate stacking sequence of CFRP Filament wound tubes subjected to projectile impact,” *Composite Structures*, vol. 58, pp. 259-270, 2002.
- [47] P.P. Camanho, F.L. Matthews , “Delamination Onset Prediction in Mechanically Fastened Joints in Composite Laminates,” *Journal of Composite Materials*, vol. 33, pp. 906-926, 1999.
- [48] N. Hongkarnjanakul, C. Bouvet, S. Rivallant , “Validation of low velocity impact modelling on different stacking sequences of CFRP laminates and influence of fibre failure,” *Composite Structures*, vol. 106, pp. 549-559, 2013.
- [49] S. Hong, D. Liu, “On the relationship between impact energy and delamination area,” *Experimental Mechanics*, pp. 115-120, 1989.
- [50] W.J. Cantwell, J. Morton, “The impact resistance of composite materials-a review,” *COMPOSITES*, vol. 22, no. 5, pp. 347-362, 1991.

- [51] M. O. W. Richardson, M. J. Wisheart , “Review of low-velocity impact properties of composite materials,” composite part A, vol. 27 A, pp. 1123-1131, 1996.
- [52] R. Olsson, “Impact response of composite laminates – a guide to closed form solutions,” The Aeronautical Research Institute of Sweden, 1993.
- [53] E.V. González, P. Maimí, P.P. Camanho , C.S. Lopes, N. Blanco , “Effects of ply clustering in laminated composite plates under low-velocity impact loading,” Composites Science and Technology, vol. 71, pp. 805-817, 2011.

CHAPTER 4

Damage Modelling and Simulation Results

Contents

4.1 Introduction	118
4.2 Constitutive progressive degradation of composite material	118
4.2.1 Intralaminar failure criteria	120
4.2.2 Damage evolution	121
4.3 Validation of the intralaminar model	125
4.3.1 Single element model.....	125
4.3.1.1 Effect of damage propagation energy	126
4.3.1.2 Tension and compression in the longitudinal direction	127
4.3.1.3 Tension and compression in the transversal direction	129
4.3.1.4 Mesh convergence.....	131
4.3.2 High velocity impact test	132
4.4 Conclusions	139
Bibliographie	140

4.1 Introduction

Damage tolerance and resistance is of primordial in lightweight structures, especially in aerospace and naval applications. Thus, in practice, the engineering design requires information about the material resistance properties in the elastic behaviour phase to estimate the performance of the structure. The lack of ability to predict the damage tolerance leads to allowing high factors of safety design requirements. In contrast, highly expensive costs, and true that composite materials are extremely supersensitive to defects. Therefore, optimisation of these factors must be achieved to reduce production costs and predict the maintenance schedule. In the evaluation of the response of composite structures and to maintain their performance subsequent to damage, the implicit residual strength should not exceed the damage tolerance requirements. The failure mechanism of the composite materials is not yet fully integrated in the numerical models. Therefore, it is necessary to develop accurate models that can predict the failure modes, in order to fully exploit the potential of these structures. Numerically, many researchers have attempted to model an appropriate constitutive law to include damage in their models. Consequently, this provides significant assistance through incorporating their influence in the structural design. Their efforts concentrate on handling dynamic impacts with high and low impact velocity/energy based on continuum damage mechanics (CDM) and fracture mechanics (FM) for both intralaminar and interlaminar damage. In this chapter, damage modelling based on the degradation of the material stiffness of the material used, the user material subroutine VUMAT, implemented and executed in Abaqus/explicit finite element code, together with interlaminar damage based on the cohesive zone model (CZM) will be examined.

4.2 Constitutive progressive degradation of composite material

Progressive failure models have been adopted in finite element simulations, to model the onset of damage and its propagation in composite laminate based on the concept of continuum damage mechanics (CDM). Material behaviour can be characterised in two substantial phases namely the elastic and the failure phases. An elastic region is the area where the material can return to its original dimensions without deformation during unloading. This phenomenon appears because the material has an elastic energy which depends on the material nature type. On the other hand, the second phase represents a failure region, which is subsequent to the onset of the damage of the material, by either stress or strain-based failure criteria. Further

loading leads to degradation of mechanical properties of the structure and subsequently a reduction in stiffness.

Figure 4. 1 illustrates the relationship between effective stress and nominal stress. The relationship between effective stress ($\hat{\sigma}$) and nominal stress (σ) can be defined as :

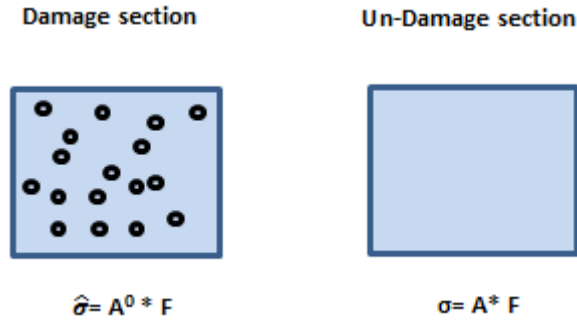


Figure 4. 1. Effective stress and nominal stress

$$\hat{\sigma} = M * \sigma \tag{4.1}$$

Where $\hat{\sigma}$, σ and M are respectively the effective stress, nominal stress and the damage operator which can be as follows [1]:

$$M = \begin{bmatrix} \frac{1}{1 - d_f} & 0 & 0 \\ 0 & \frac{1}{1 - d_m} & 0 \\ 0 & 0 & \frac{1}{1 - d_s} \end{bmatrix} \tag{4.2}$$

Where d_f , d_m and d_s are the damage variables for fibre, matrix and shear failure mode respectively .

$$\sigma_{i,j} = C_{i,j}(d) \cdot \varepsilon_{i,j} \tag{4.3}$$

where C represents the undamaged orthotropic stiffness matrix. This matrix takes the following form:

$$C(d) = \begin{bmatrix} C_{11} & C_{12} & C_{13} & 0 & 0 & 0 \\ C_{12} & C_{22} & C_{23} & 0 & 0 & 0 \\ C_{13} & C_{23} & C_{33} & 0 & 0 & 0 \\ 0 & 0 & 0 & C_{44} & 0 & 0 \\ 0 & 0 & 0 & 0 & C_{55} & 0 \\ 0 & 0 & 0 & 0 & 0 & C_{66} \end{bmatrix} \quad (4.4)$$

Thus the damage stiffness matrix is as follows [2]:

$$\begin{aligned} dC_{11} &= (1 - d_f)E_1(1 - v_{23}^2)\Gamma \\ dC_{22} &= (1 - d_f)(1 - d_m)E_2(1 - v_{13}^2)\Gamma \\ dC_{33} &= (1 - d_f)(1 - d_m)E_3(1 - v_{21}^2)\Gamma \\ dC_{12} &= (1 - d_f)(1 - d_m)E_1(v_{21} - v_{31}v_{23})\Gamma \\ dC_{23} &= (1 - d_f)(1 - d_m)E_2(v_{32} - v_{12}v_{31})\Gamma \\ dC_{31} &= (1 - d_f)(1 - d_m)E_1(v_{31} - v_{21}v_{32})\Gamma \\ dC_{44} &= (1 - d_f)(1 - d_{mt}s_{mt})E_1(1 - d_{mc}s_{mc})G_{12} \\ dC_{55} &= (1 - d_f)(1 - d_{mt}s_{mt})E_1(1 - d_{mc}s_{mc})G_{23} \\ dC_{66} &= (1 - d_f)(1 - d_{mt}s_{mt})E_1(1 - d_{mc}s_{mc})G_{13} \end{aligned} \quad (4.5)$$

Where d_{ft} , d_{fc} corresponds to the fibre failure mode in tension and compression, and d_{mt} , d_{mc} the matrix failure mode in tension and compression. The variables s_{mt} and s_{mc} are damage variables due to the shear stress in matrix tensile and compression failure respectively. The values of the two variables s_{mt} and s_{mc} are estimated empirically equal to 0.8 and 0.5 respectively. The global damage variables for both fibres and matrix and Γ are given by equation (4.6)[2].

$$\begin{aligned} d_f &= 1 - (1 - d_{ft})(1 - d_{fc}) \\ d_m &= 1 - (1 - d_{mt})(1 - d_{mc}) \\ \Gamma &= 1/(1 - v_{12}^2 - v_{23}^2 - v_{13}^2 - 2v_{12}v_{23}v_{13}) \end{aligned} \quad (4.6)$$

4.2.1 Intralaminar failure criteria

The damage initiation occurs when the true applied stress in the laminate composite reaches the ultimate strength of the ply laminate. Explicitly, damage occurs to the interface due to a difference between the transverse compressive fibre modulus and the matrix modulus, which represents the main cause of damage initiation. A user material VUMAT subroutine was coded in FORTRAN language and executed by the finite element explicit

Abaqus software to characterise the intralaminar damage. The failure onset was based on Hashin failure criteria in three dimensional form for fibres and matrices. These criteria have been widely applied to predict the initiation of damage in unidirectional composites [3, 4]. In the current study, these criteria were proposed for both fibres and matrices, and listed in Table 4. 1.

Failure Mode	Failure Criteria
Fibre Tensile Failure ($\sigma_{11} \geq 0$)	$f_{ft} = \left(\frac{\sigma_{11}}{X_t}\right)^2 \geq 1$
Fibre Compression Failure ($\sigma_{11} < 0$)	$f_{fc} = \left(\frac{\sigma_{11}}{X_c}\right)^2 \geq 1$
Matrix Tensile Failure ($\sigma_{22} + \sigma_{33} \geq 0$)	$f_{mt} = \frac{(\sigma_{22} + \sigma_{33})^2}{Y_t^2} + \frac{\sigma_{23}^2 - \sigma_{22}\sigma_{33}}{S_{23}^2} + \left(\frac{\sigma_{12}}{S_{12}}\right)^2 + \left(\frac{\sigma_{13}}{S_{13}}\right)^2 \geq 1$
Matrix Compression Failure ($\sigma_{22} + \sigma_{33} < 0$)	$f_{mc} = \frac{1}{Y_c} \left(\left(\frac{Y_c}{2S_{23}} \right)^2 - 1 \right) (\sigma_{22} + \sigma_{33}) + \frac{(\sigma_{22} + \sigma_{33})^2}{4S_{23}^2} + \frac{\sigma_{23}^2 - \sigma_{22}\sigma_{33}}{S_{23}^2} + \left(\frac{\sigma_{12}}{S_{12}}\right)^2 + \left(\frac{\sigma_{13}}{S_{13}}\right)^2 \geq 1$

Table 4. 1. Hashin Failure criteria [3]

4.2.2 Damage evolution

As previously stated, after the initial failure criteria have been satisfied, further loading leads to regression of material stiffness. Based on the relationship between the effective stress and displacement, damage evolution can be constituted. Therefore, damage variables for each mode in the fibres and matrices are expressed in the form of the displacement:

$$d_i = \frac{\delta_{i,eq}^f (\delta_{i,eq} - \delta_{i,eq}^0)}{\delta_{i,eq}^f (\delta_{i,eq}^f - \delta_{i,eq}^0)} , \quad \delta_{i,eq}^0 \leq \delta_{i,eq} \leq \delta_{i,eq}^f \quad (4.7)$$

Where d_i is the damage variable defined for each damage mode. The variables δ_{eq}^0 , δ_{eq} and $\delta_{i,eq}^f$ represent respectively the initial displacement when the failure criterion is reached, the equivalent displacement and the equivalent failure displacement. These displacements can be computed from the fracture energy corresponding to each damage variable as follow:

$$G_i = \int_{\delta_{i,eq}^0}^{\delta_{i,eq}^f} \sigma d\varepsilon = \frac{1}{2} (\delta_{i,eq}^f - \delta_{i,eq}^0) \sigma_{i,eq}^0$$

$$\delta_{i,eq}^f - \delta_{i,eq}^0 = \frac{2G_i}{\sigma_{i,eq}^0}$$
(4.8)

$$\delta_{i,eq}^0 = \delta_{i,eq} / \sqrt{f_i}$$

$$\sigma_{i,eq}^0 = \sigma_{i,eq} / \sqrt{f_i}$$

$\sigma_{i,eq}$, $\sigma_{i,eq}^0$, f_i and G_i are equivalent stress, equivalent initial stress, initial failure and the fracture energy corresponding to each mode, respectively. These variables are computed for each element's integration point to describe the material's stiffness degradation for every damage mode, as described in Table 4. 2. This scheme is shown in Figure 4. 2. The equivalent displacement and equivalent stress are determined for each iteration until the complete failure ($d_f = 0$) of element occurs. At this point, the element deletes from the model and its stresses become zero [5].

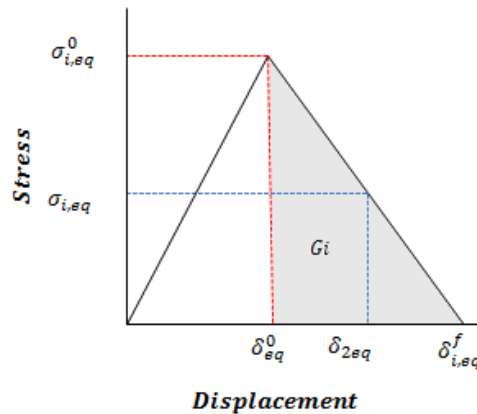


Figure 4. 2. Typical behaviour of material stiffness degradation

Failure mode	$\delta_{i,eq}$	$\sigma_{i,eq}$
Fibre tensile damage mode	$L_c \sqrt{(\varepsilon_{11})^2 + (\varepsilon_{12})^2 + (\varepsilon_{31})^2}$	$L_c (\sigma_{11} \varepsilon_{11} + \sigma_{12} \varepsilon_{12} + \sigma_{31} \varepsilon_{31}) / \delta_{1,eq}$
Fibre compressive damage mode	$L_c \sqrt{(-\varepsilon_{11} - \frac{\langle \varepsilon_{33} \rangle \cdot E_{33}}{E_{11}})^2}$	$L_c (E_{11} (-\varepsilon_{11} - \frac{\langle \varepsilon_{33} \rangle \cdot E_{33}}{E_{11}})) / \delta_{2,eq}$
Matrix tensile damage mode	$L_c \sqrt{(\varepsilon_{22})^2 + (\varepsilon_{12})^2 + (\varepsilon_{23})^2}$	$L_c (\sigma_{22} \varepsilon_{22} + \sigma_{12} \varepsilon_{12} + \sigma_{23} \varepsilon_{23}) / \delta_{3,eq}$
Matrix compressive damage mode	$L_c \sqrt{(-\varepsilon_{22} - \frac{\langle \varepsilon_{33} \rangle \cdot E_{33}}{E_{22}})^2 + (\varepsilon_{12})^2}$	$L_c (E_{22} (-\varepsilon_{22} - \frac{\langle \varepsilon_{33} \rangle \cdot E_{33}}{E_{22}}) + \sigma_{12} \varepsilon_{12}) / \delta_{2,eq}$

Table 4. 2. Equivalent displacement and equivalent stress for each mode [5]

Where $\langle \varepsilon_{ii} \rangle$ is the Macaulay operator and calculated as:

$$\langle \varepsilon_{ii} \rangle = \frac{\varepsilon_{ii} + |\varepsilon_{ii}|}{2} \quad (4.9)$$

L_c is characteristic length, which is defined to overcome the strain localisation when the material exhibits strain-softening behaviour [1], and thus is integrated into the model to render the absorbed energy independent of the mesh sensitivity. In the solid element case, the characteristic length is obtained by the cube root of the area associated with the material point.

The flowchart of the intralaminar damage model, incorporated in the VUMAT subroutine is explained in Figure 4. 3.

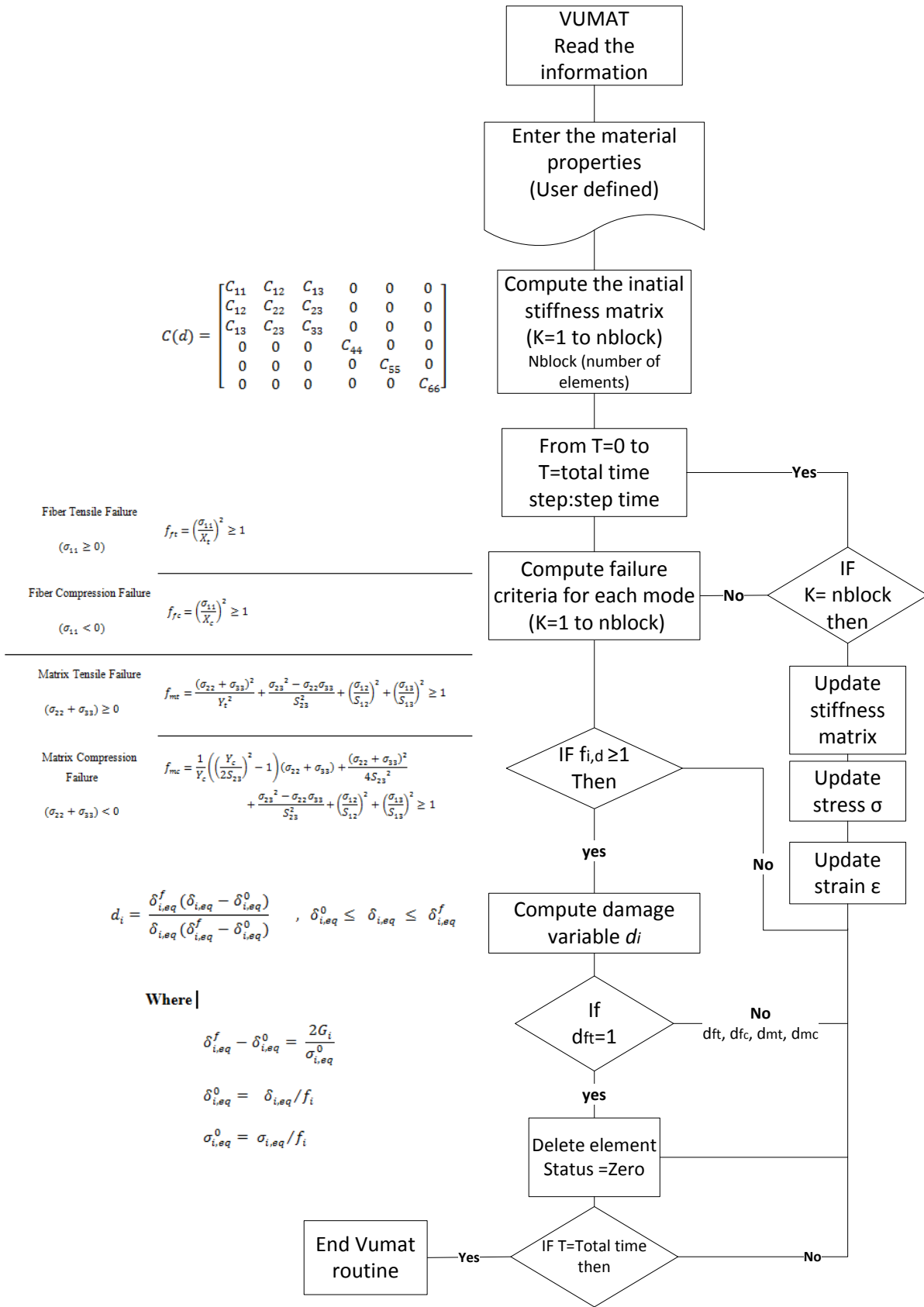


Figure 4. 3. Flowchart VUMAT subroutine intralaminar damage model

4.3 Validation of the intralaminar model

In the following sections, the intralaminar model is verified and performed in a sequence procedure to the test validity of the results. For this reason the model implemented is single element subjected to simple unidirectional loading, and under a high velocity impact test for the composite plate.

4.3.1 Single element model

Firstly, validation of the intralaminar damage model must be implemented. Therefore, a single square element of dimensions (length= 5mm, width= 5mm and finite thickness of 0.25mm) was subjected to unidirectional loading conditions (tension and compression) aligned with the fibres in the longitudinal and transverse directions, to identify the failure mode in both fibres and the matrix. The boundary conditions were specified as clamped on one side of the plate and tension/compression on the other, with a velocity rate of 5m/s, as shown in Figure 4.4. The plate was modelled a of glass-epoxy composite material with the mechanical properties stated in Table 4. 3. In order to clarify the failure of intralaminar damage in a three dimensional form (for accurate results of stress and strain), the subroutine VUMAT was implemented. Different fracture energy values for the fibres and matrix were applied to quantify their effect on the damage evolution.

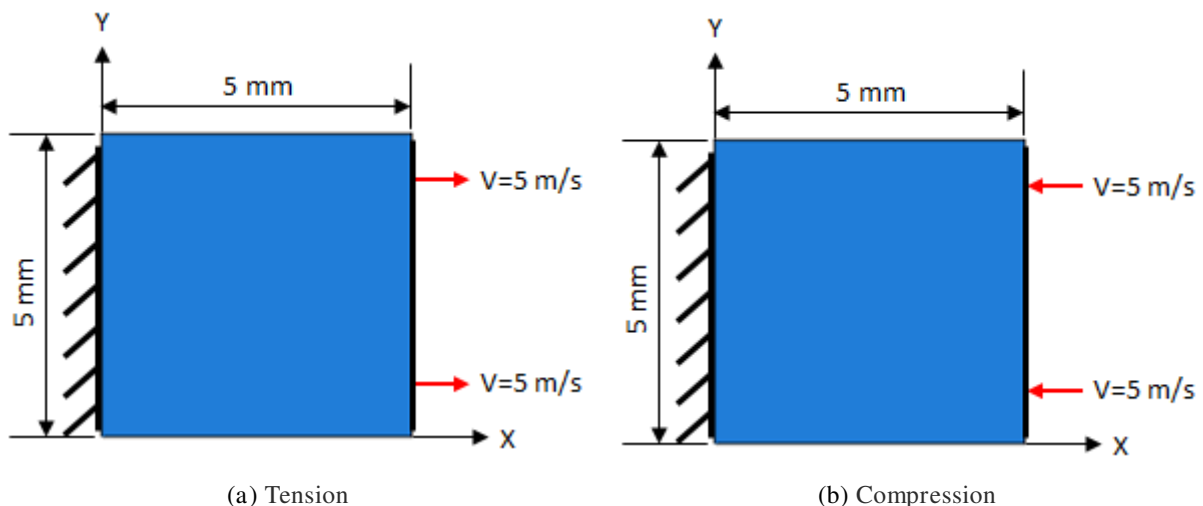


Figure 4.4. Orthotropic composite ply subjected to longitudinal loading (fibres oriented to 0°)

Propriety	Values
Density (kg/m^3)	1960
Young's modulus (MPa)	$E_1 = 45847, E_2 = E_3 = 17506$
Poisson's ratio	$\nu_{12} = \nu_{13} = 0.1, \nu_{23} = 0.331$
Shear modulus (MPa)	$G_{12} = G_{13} = 5000, G_{23} = 5600$
Longitudinal Tensile strength (MPa)	$X_t = 1120$
Longitudinal compressive strength (MPa)	$X_c = 900$
Transversal tensile strength (MPa)	$y_t = Z_t = 39$
Transversal compressive strength (MPa)	$y_c = Z_c = 134$
Shear strength (MPa)	$S_{12} = S_{13} = S_{23} = 77$

Table 4. 3. Mechanical proprieties of orthotropic layer (glass/epoxy)

4.3.1.1 Effect of damage propagation energy

The changes in model sensitivity to the fracture energy were studied by predicting its response to the damage evolution, therefore different fracture energy enters the model corresponding to each mode as stated in Table 4. 4. As proof, the elastic phase remains at the same value and keeps its linear behaviour and within the initiation failure strain. In general, the fibres has large tensile and strain strength, therefore they absorb high energy before exceeding the strain failure level. Clearly different and inversely, the matrix has low energy until failure. Composite materials with high critical energy have extensive damage tolerance and this allows them a long life time and to achieve their function without catastrophic structural failure occurring.

Fracture Energy (J/m²)	High energy	Medium energy	Low energy
Fibre tension mode-1 (G_{Ft})	10	5	1
Fibre compression mode-2 (G_{Fc})	10	5	1
Matrix tension mode-3 (G_{Mt})	5	2.5	0.5
Matrix compression mode-4 (G_{Mc})	5	2.5	0.5

Table 4. 4. Fracture energy for damage evolution

4.3.1.2 Tension and compression in the longitudinal direction

The composite orthotropic plate was subjected to tension and compression loading in the direction of the fibre. As shown in Figure 4.5 and Figure 4. 6, the first initial damage happens in the matrix (dm_t) and then the fibre damage (df_t), as the stresses in the fibre direction are predominantly carried by the fibres. It can be noted that the maximum value of the stress correspond to the mechanical properties of ultimate tensile and compression strength of the fibres.

Figure 4. 7 shows the force-displacement curves under tension and compression of various fracture energies for both the fibres and matrix. Throughout the analyses, it can be observed that the material strength under tension and compression loading aligned with the fibre orientation, and thus it depended on the fibre strength, reflected in the plate having a high initial failure strain and high strength.

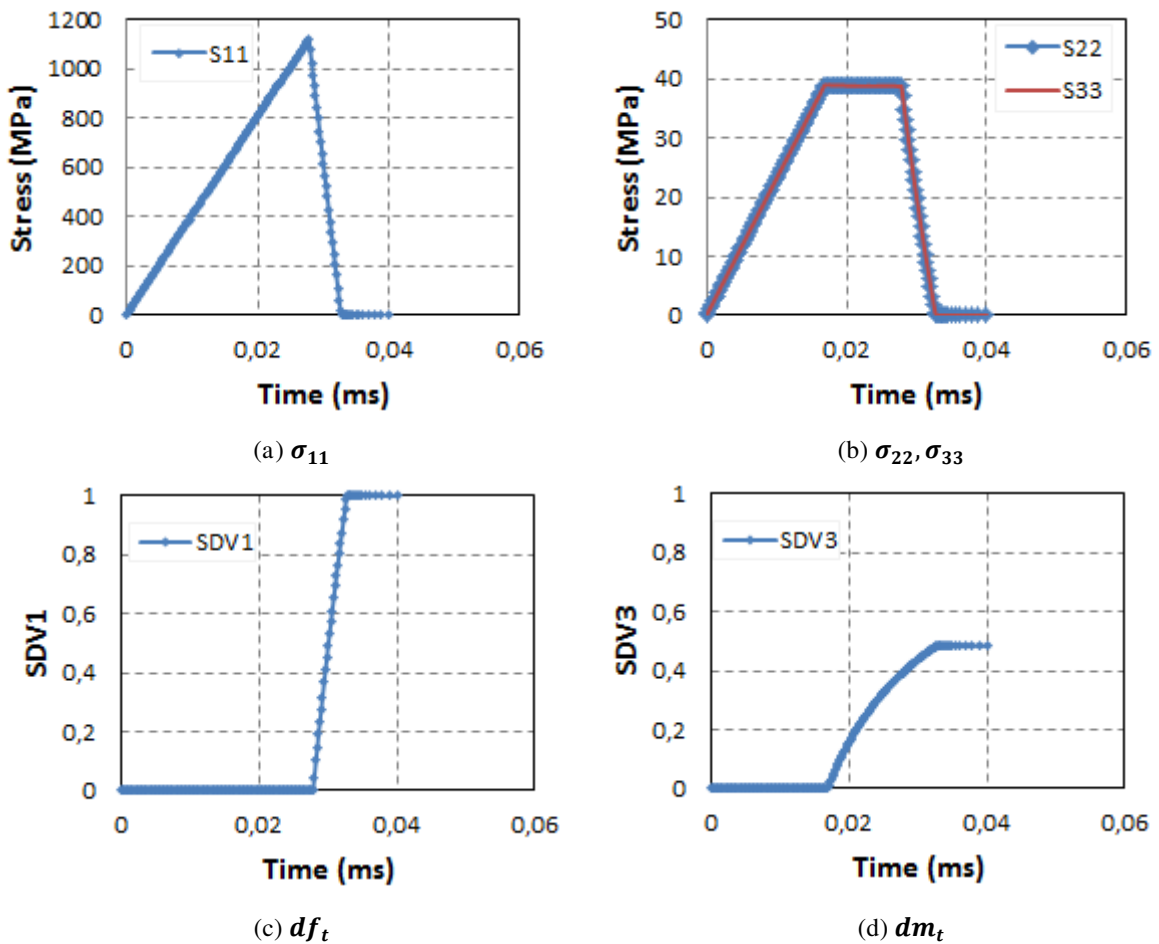


Figure 4.5. Evolution of dynamic response of orthotropic ply under longitudinal tension

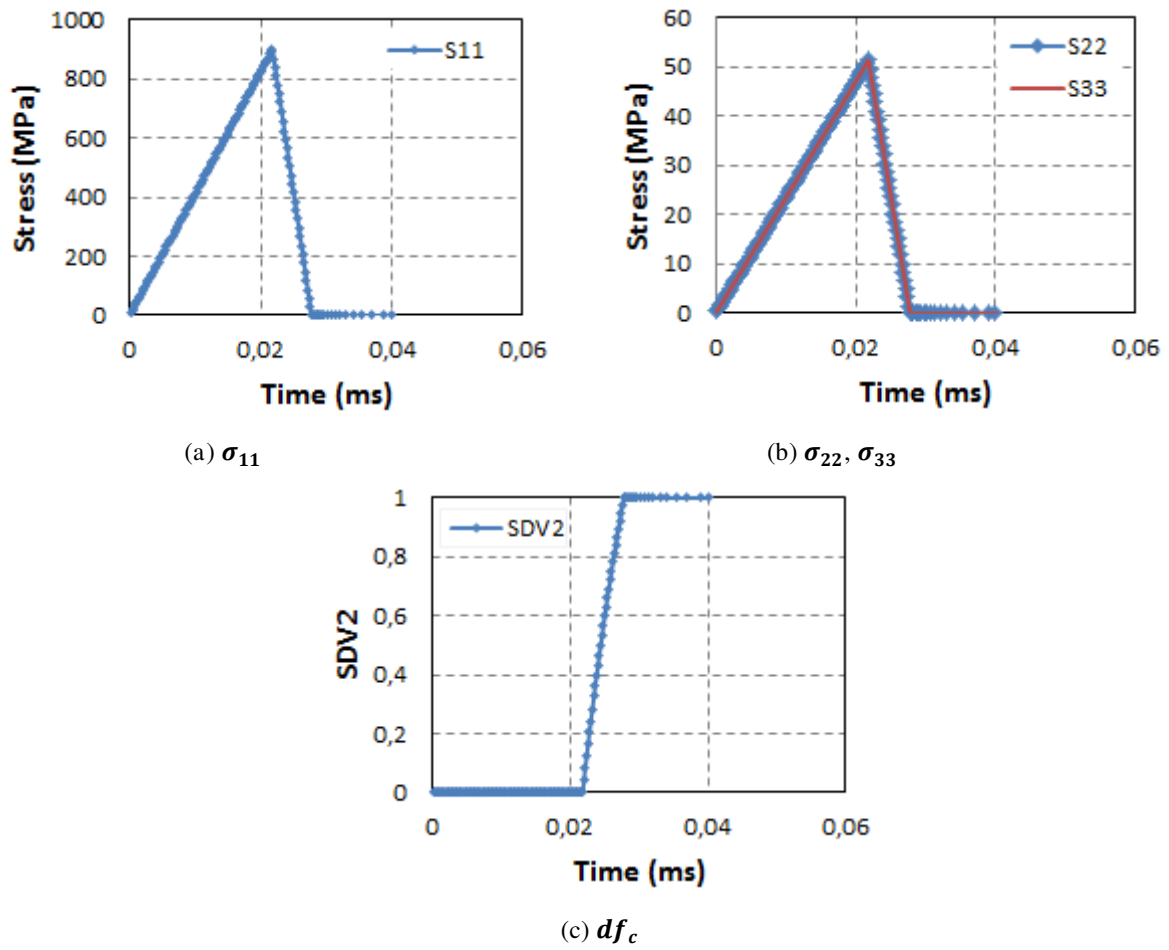


Figure 4. 6. Evolution of dynamic response of orthotropic ply under longitudinal compression

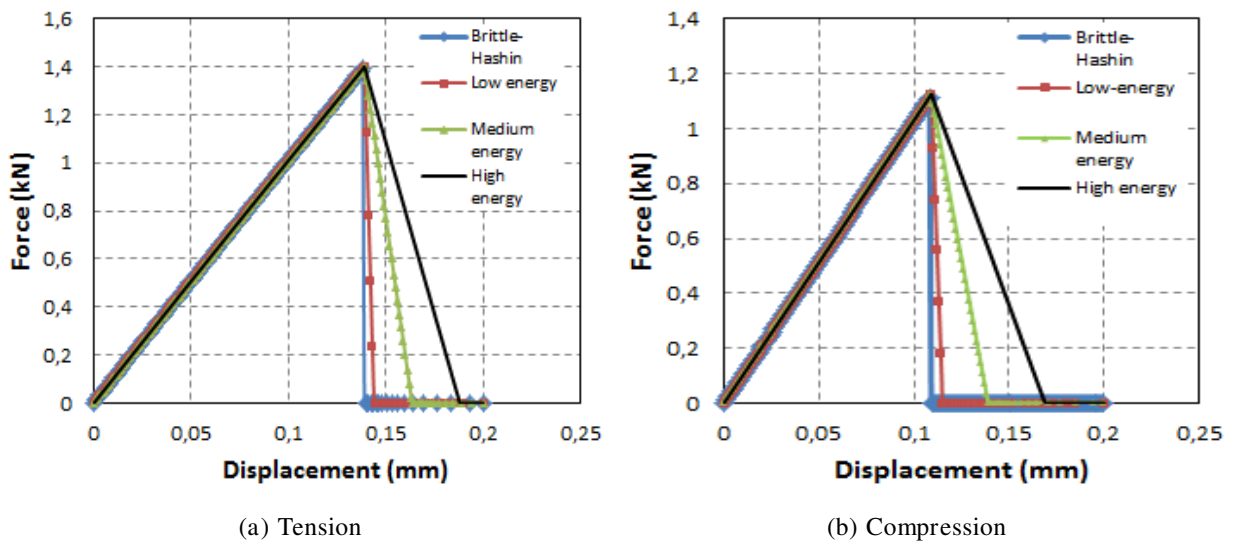


Figure 4. 7. Test of one element, longitudinal direction

4.3.1.3 Tension and compression in the transversal direction

In contrast, Figure 4.8 and Figure 4.9 depict that the matrix failure mode (d_m) dominates the failure response under the transverse tensile and compression loading. It can be observed that the material failure needed a low strength, strain and low energy. This is illustrated in Figure 4.10. It was noted that the fibre damage variable was not present in this case, because the element deletion from the model occurred when it reached the condition of maximum and minimum deformation. In this model assumed that ($\epsilon_{max} = 1$) and ($\epsilon_{min} = -0.8$).

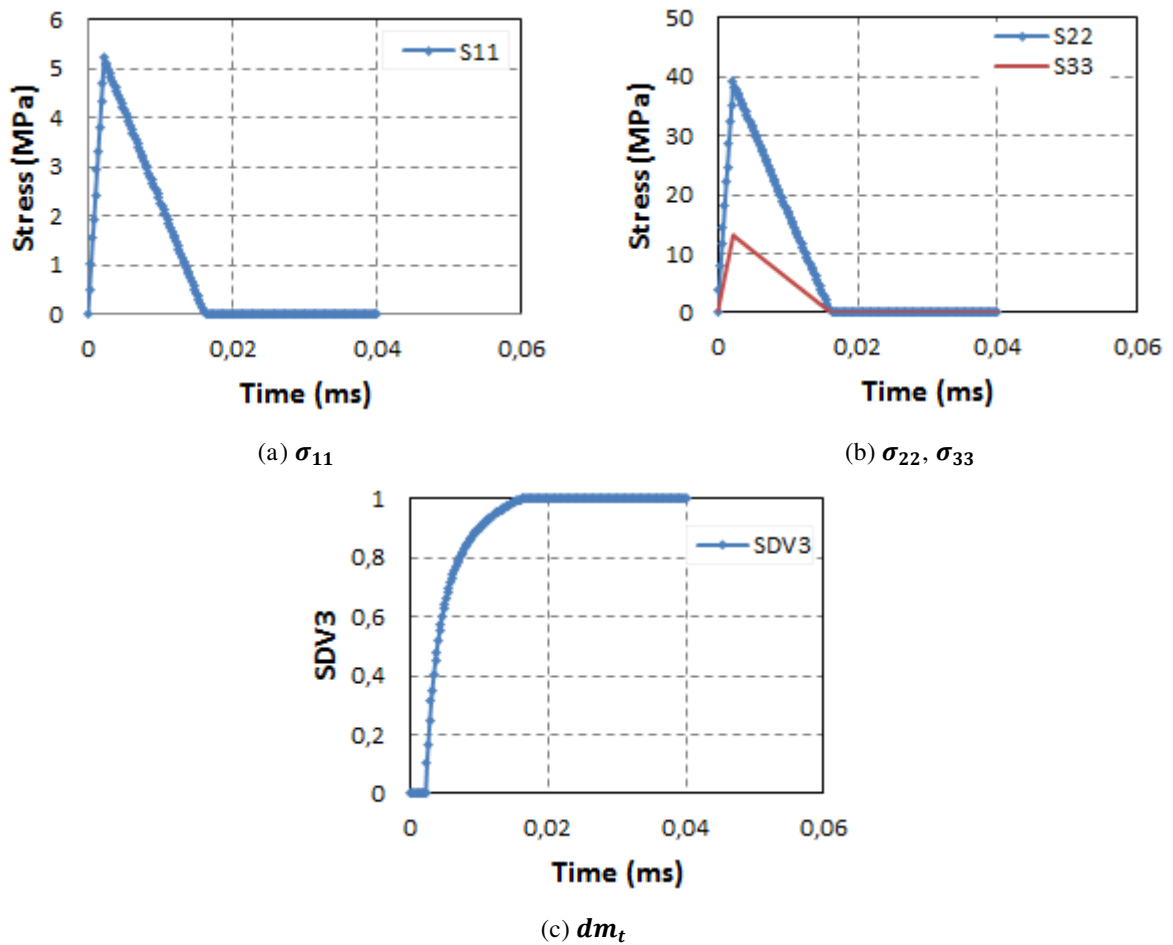


Figure 4.8. Evolution of dynamic response of orthotropic ply under transverse tension

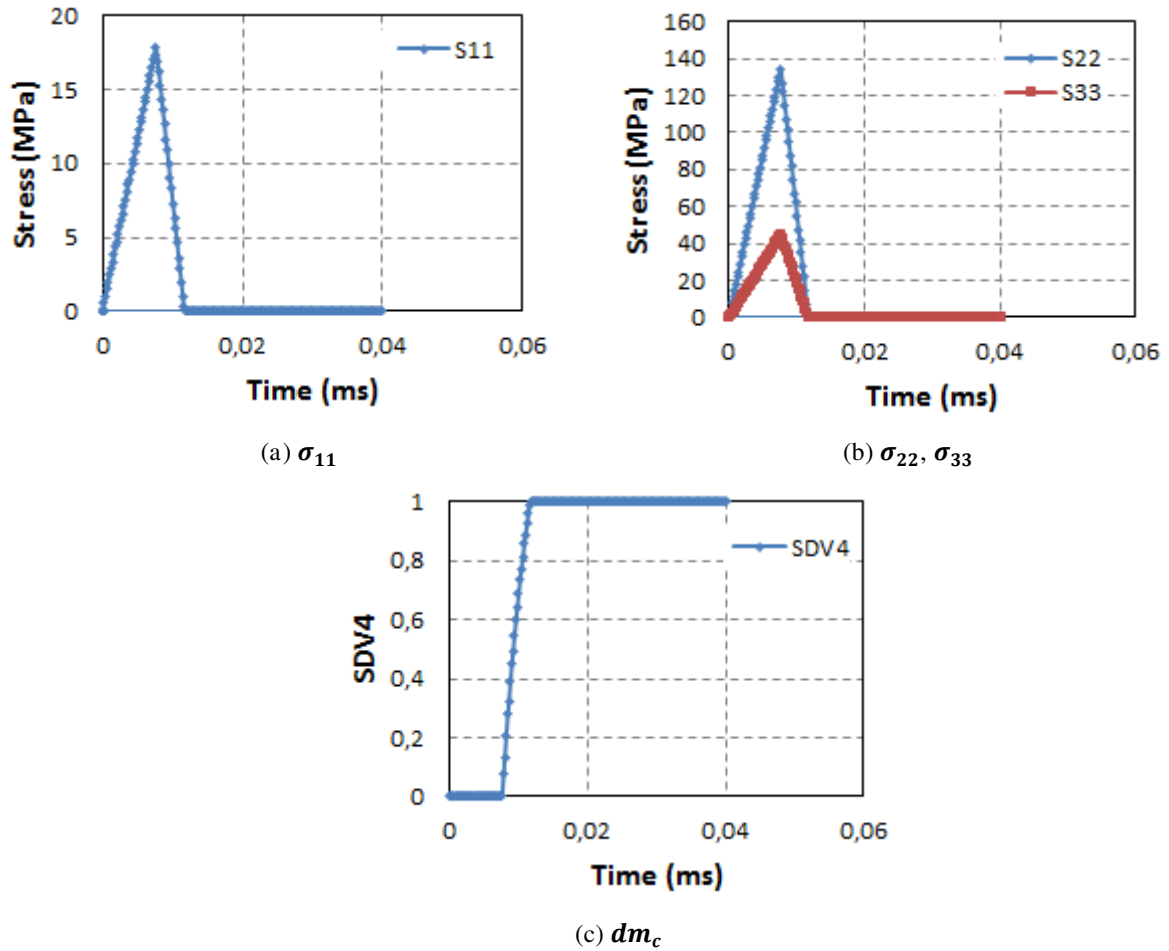


Figure 4. 9. Evolution of dynamic response of orthotropic ply under transverse compression

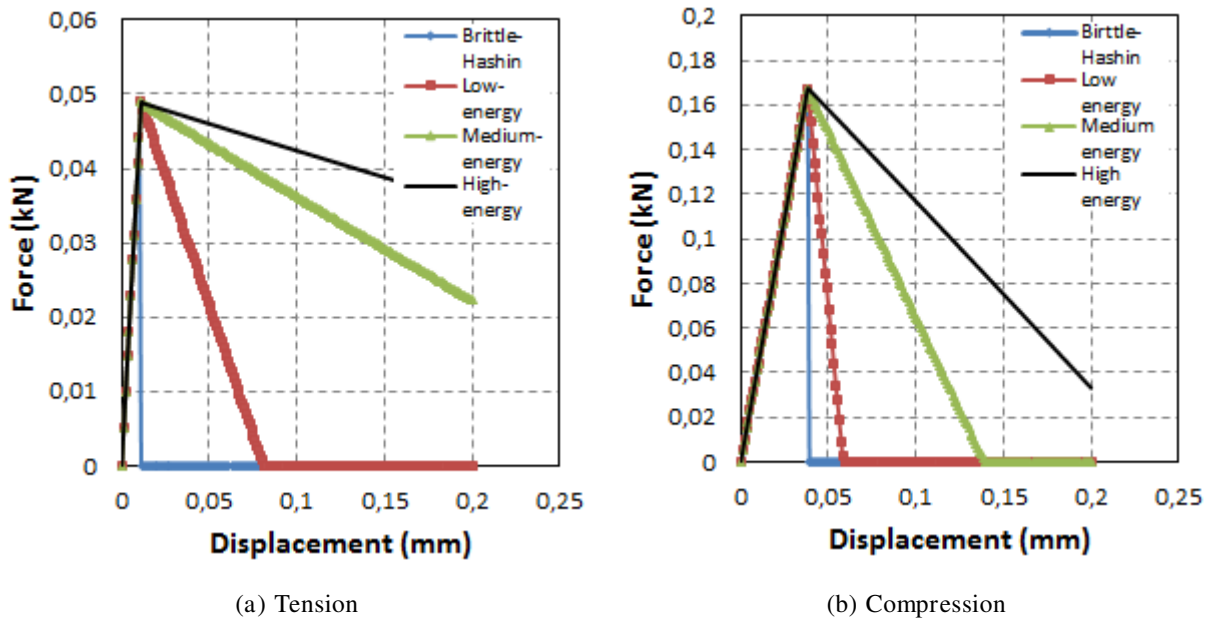


Figure 4. 10. Test of one element, transversal direction

The ultimate stress in the direction of the fibres with different ultimate tensile strength for the fibres was compared to verify the stress-displacement curve. It was noted that the curve kept the same linear elastic phase with the same energy ($d_{ft} = 1, d_{fc} = 1, d_{mt} = 0.5, d_{mc} = 0.5$) in all states of loading of different tensile strength, as shown in Figure 4. 11.

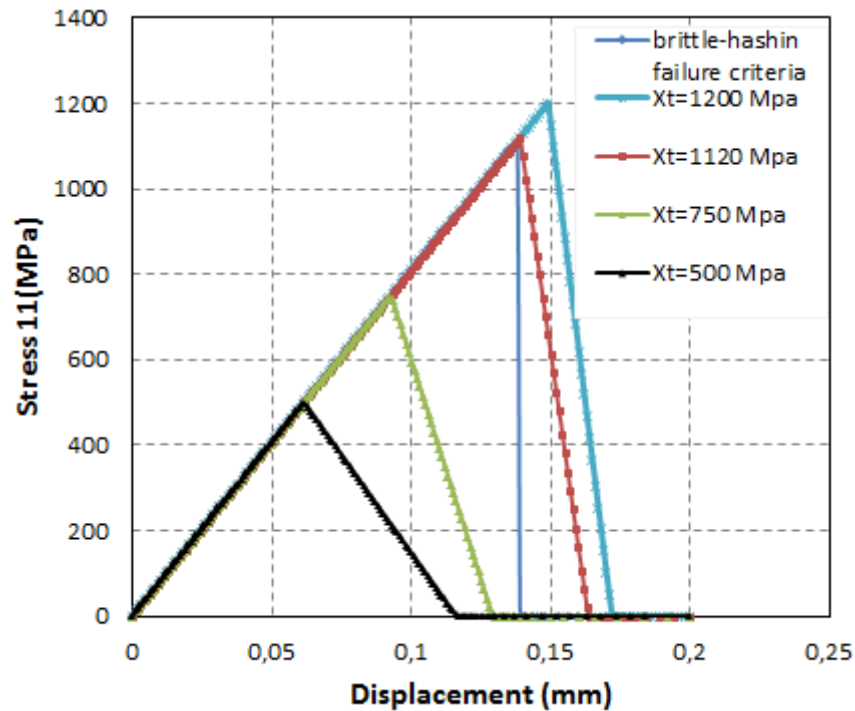


Figure 4. 11. Effect of ultimate tensile strengths for one element under tensile test, longitudinal direction

4.3.1.4 Mesh convergence

Progressive damage modelling often tends to experience severe difficulties such as those concerning the mesh density. The energy dissipated according to the mesh density has a significant influence on the numerical results. For this reason, different mesh densities were applied (1, 4, 8 and 16 elements) to the model under tensile loading aligned with direction of the fibres, Figure 4. 12. The force- displacement curve shows that the mesh densities have small effect on the behaviour of the studied material, Figure 4. 13. Indeed, the characteristic length of elements reduced the mesh density influence on the strain localization and energy dissipation. However, the characteristic length was not able to completely eliminate the dependency on the mesh, but reduced the influence in this case [1].

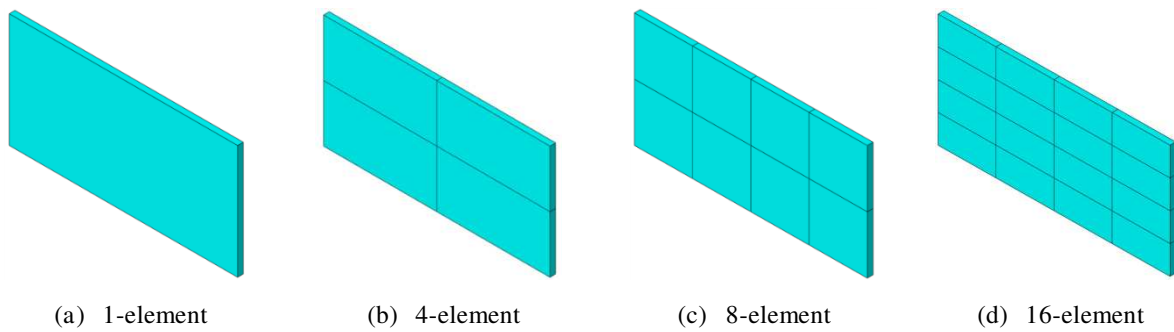


Figure 4.12. Mesh size effect

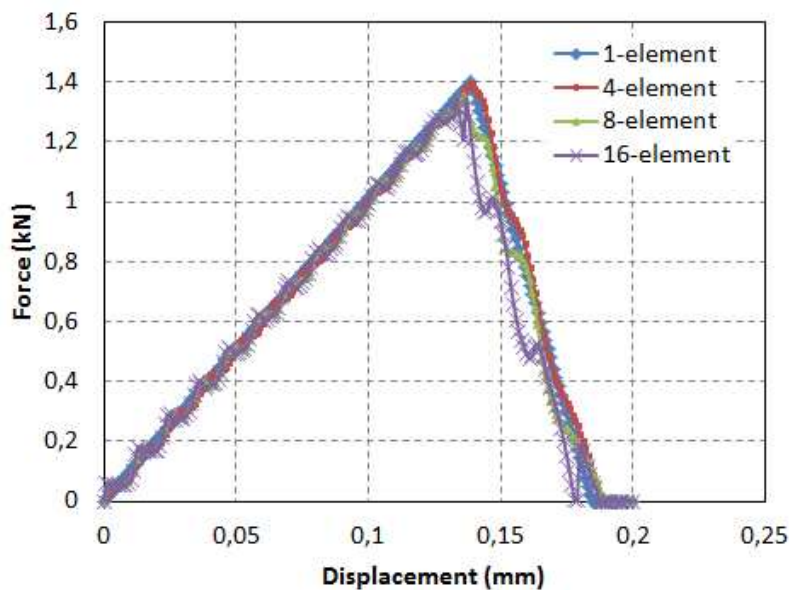


Figure 4.13. Influence of mesh density on the energy dissipation

4.3.2 High velocity impact test

In this section, the intralaminar damage model was tested under a high velocity impact. This is appropriate for high dynamic loading, as the damage is mainly due to the propagation of cracks perpendicular to the fibres, whereas micro-cracks are growth fast under loading conditions in the thickness direction. These cracks produce debonding between the fibres and matrix or the fibre failure.

The composite plate of carbon fibre-epoxy was simulated that has mechanical properties illustrate in Table 4. 5. The square composite plate was modelling with dimensions $100 \times 100 \times 3.6$ mm, and the steel spherical projectile with a diameter = 5mm and mass = 0.51g, Figure 4. 14a [6]. The laminate consisted of 18 separated laminas with stacking sequence $[(0/90/0)_3]_s$ and 3D element type of 8-node linear bricks and reduced integration C3D8R. To avoid high computational time consumption, a symmetric quarter plate was modelled and

analysed. In the local impact region, a refined mesh was used which was progressively coarser toward the external plate edges, with one thick element for each layer. The plate was fully clamped in the outer boundaries as shown in Figure 4. 14b. this incorporated a subroutine VUMAT in Abaqus explicit software employed to describe the intra-lamina damage for both the onset and propagation of the damage based on the Hashin failure criteria for the fibres and Puck criteria for the matrix.

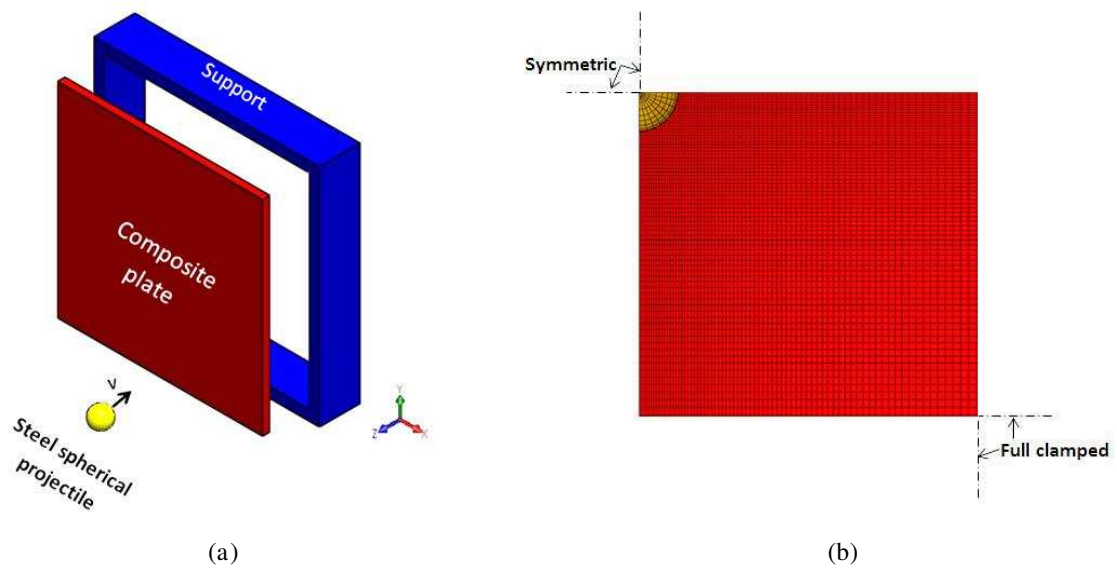


Figure 4. 14. Typical finite element model under high velocity impact

Elastic moduli (GPa)			Poisson's ratios (-)			Shear moduli (GPa)		
E_{11}	E_{22}	E_{33}	ν_{12}	ν_{13}	ν_{23}	G_{12}	G_{13}	G_{23}
235	17	17	0.32	0.32	0.45	4.5	4.5	2.5
Ultimate tensile and compression strengths (MPa)						Ultimate Shear strengths (MPa)		
X_t	X_c	Y_t	Y_c	X_{3t}	X_{3c}	S_{12}	S_{13}	S_{23}
3900	2400	111	290	50	290	120	137	90

Table 4. 5. Carbon fibre-epoxy material properties [7]

A good agreement between the simulation and the experimental results of Kasano [7] demonstrates the model capability to predict the intralaminar damage in high velocity

impacts, as shown in Figure 4. 15. Table 4. 7 indicates the percentage error of the residual velocity between the simulation and experimental results.

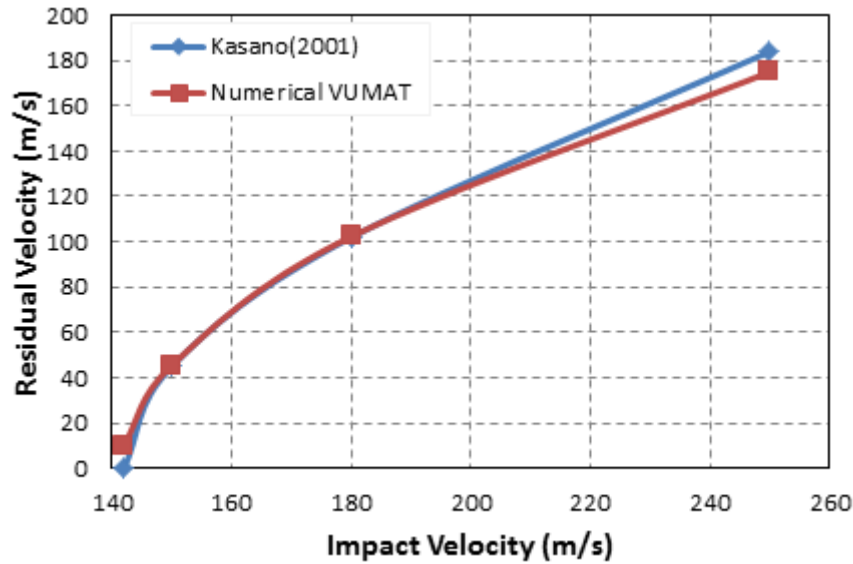


Figure 4. 15. Correlation between the VUMAT and experimental results

Impact velocity (m/s)	Experiment residual velocity	Numerical residual velocity	Error %
142	0	10,17	10,17
150	45	45,52	0,52
180	102	102,35	0,35
250	184	188,15	4,15

Table 4. 6. Compare simulation results with experiment results

Optimisation of structural resistance according to the stacking sequence was performed using a three stacking sequence $[(0/90/0)_3]_s$, $[(45/0/45)_3]_s$ and $[(0/45/90)_3]_s$. Consequently, the optimum stacking sequence was compared according to projectile residual velocity and penetration resistance force, as to which material exhibited more resistance and low residual velocity as illustrated in Figure 4. 16a-b. It can be observed that plates with different stacking sequences gave approximately the same force and the residual velocity response. Note: the interlaminar failure was not taken into account in the numerical model. Therefore, the

following section integrated the interlaminar failure between layers using the cohesive zone model (CZM).

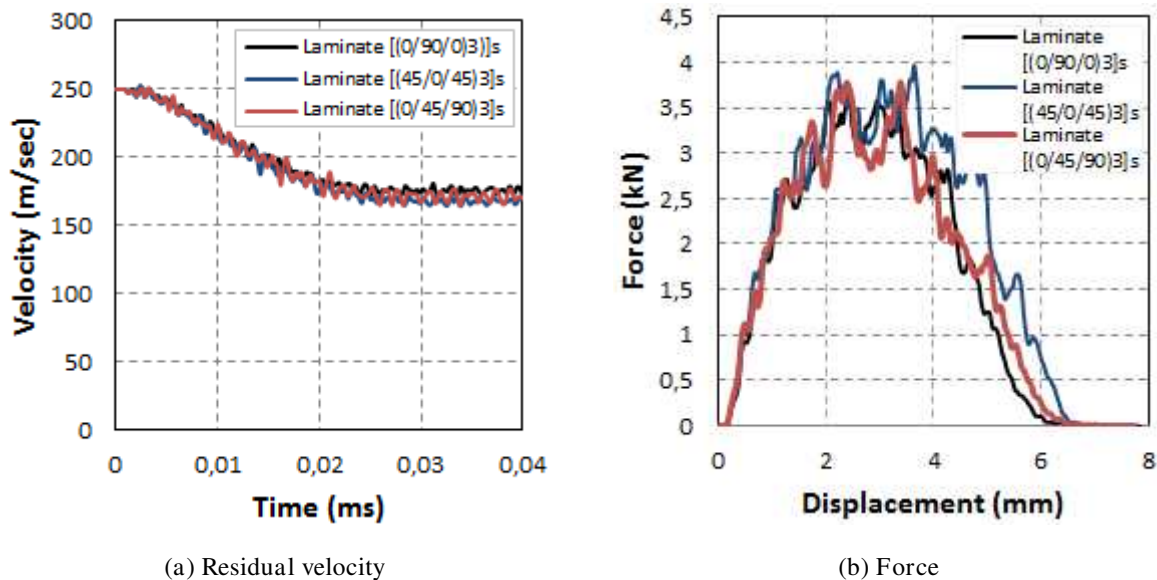


Figure 4. 16. Effect of stacking sequence under impact velocity 250 m/s. 4.3.4.2 Interlaminar (delamination) failure effect with high velocity impact

Due to the fact that the composite material structure was comprised of a multilayer stack, separation of the layers could occur. Delamination is considered to be the most usual damage type that has an influence on the strength of composite structure. Normally, it is caused by imperfect and weak bonding between layers, a mismatch in the strength fractures of the interlaminar interface compared to the strength of the layers, and with the presence of initial defects in the structure. All of these factors considered the main resource of this type of damage. Therefore, concentration of the normal stresses and transverse shear due to these factors leads to debonding the interface between the stacked layers.

The delamination was modelled by implementing the constitutive model which was built in the finite element model based on cohesive surface interaction with a zero cohesive layer thickness. However, the damage onset criterion based on the strength that expresses in a quadratic polynomial combination of both normal stress and shear stresses was applied to the surface nodes interface between the layers. Thus, the delamination occurred when the combination of normal stress and shear stresses satisfied the strength criterion, as illustrated by the traction-separation law [8].

$$\left(\frac{t_n}{t_n^0}\right)^2 + \left(\frac{t_s}{t_s^0}\right)^2 + \left(\frac{t_t}{t_t^0}\right)^2 = 1 \tag{4.10}$$

Where t_n , t_s , t_t , are respectively the nominal traction stresses under normal and shear load determined and corresponding to the elastic stiffness in mode I, mode II and mode III.

Based on the fracture criteria of Benzeggah et al. [9] for the propagation of damage; the total fracture energy is given by Equation (4.11).

$$G_{TC} = G_{Ic} + (G_{IIc} - G_{Ic}) \left(\frac{G_{II} + G_{III}}{G_T}\right)^\eta \tag{4.11}$$

Where G_{TC} , G_{Ic} , G_{IIc} , G_T ($G_{Ic} + G_{II} + G_{III}$) and η are respectively the total critical energy release rate, mode I critical energy release rate, mode II critical energy release rate, total energy release rate and the material parameter. The properties of the cohesive element are illustrated in Table 4. 7.

Initial elastic stiffness (N/mm ²)			Strength (MPa)			Energy (N/mm)		
K_n	K_t	K_s	t_n	t_s	t_t	G_{Ic}	G_{IIc}	G_{IIIc}
1.7E+06	1.7E+06	1.7E+06	65	72	52	0.345	0.63	0.63

Table 4. 7. Cohesive properties [10]

In low or high velocity impact loading, interlaminar reduces the material stiffness and strength due to the local strain deformation close to impact position; therefore the response force of the structure decreased. The matrix damage density was closely related to delamination expansion, the largest delamination taking place in the back plies of the panel due to the saturation of the matrix cracking density damage under the tensile loading which is shown in Figure 4.17.

The structure was sensitivity to interlaminar damage, Figure 4.17 and Figure 4. 18. However, the delamination redistributed the stresses to undamaged lamina which caused an increase the normal and shear stresses in these laminas. The most extensive delamination failure mode occurred between the plies having a largely different stacking orientation which

was directional aligned with the maximum tensile stress, that is obvious in 0° or 90° lamina under impact loading.

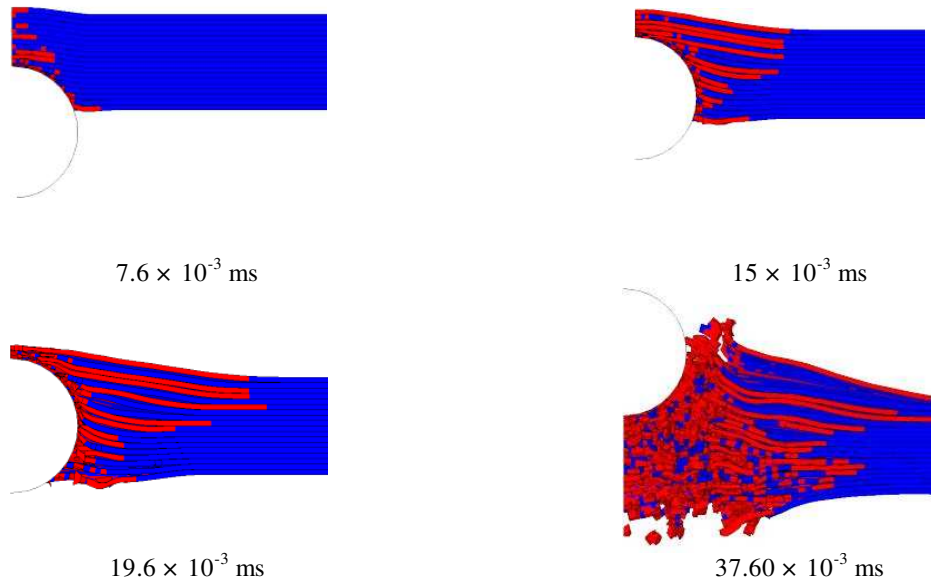


Figure 4.17. Time histories for damaged laminate under impact velocity of 250 m/s

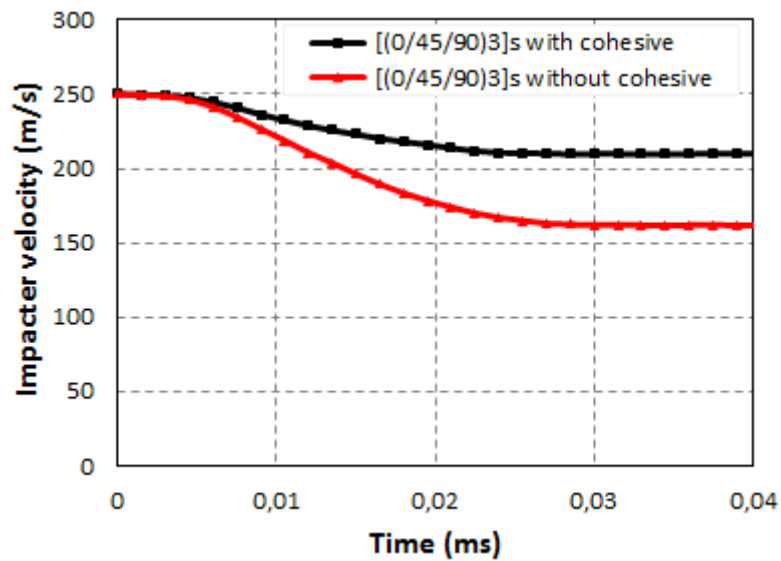


Figure 4. 18. Influence of the delamination on the projectile residual velocity

The interlaminar damage has an influence on the structure resistance. When a higher delamination occurred, this made the structure more flexible and absorbs even more energy for delamination propagation. As a result, delamination accelerated the matrix damage close to the impact location that aligned with its direction, and consequently absorbed a higher amount of energy required for damage propagation, Figure 4. 19 and Figure 4. 20.

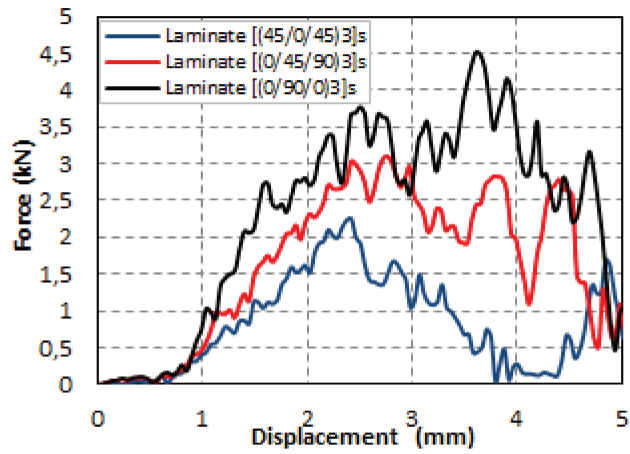


Figure 4. 19. Effect of the stacking sequence on the structure strength

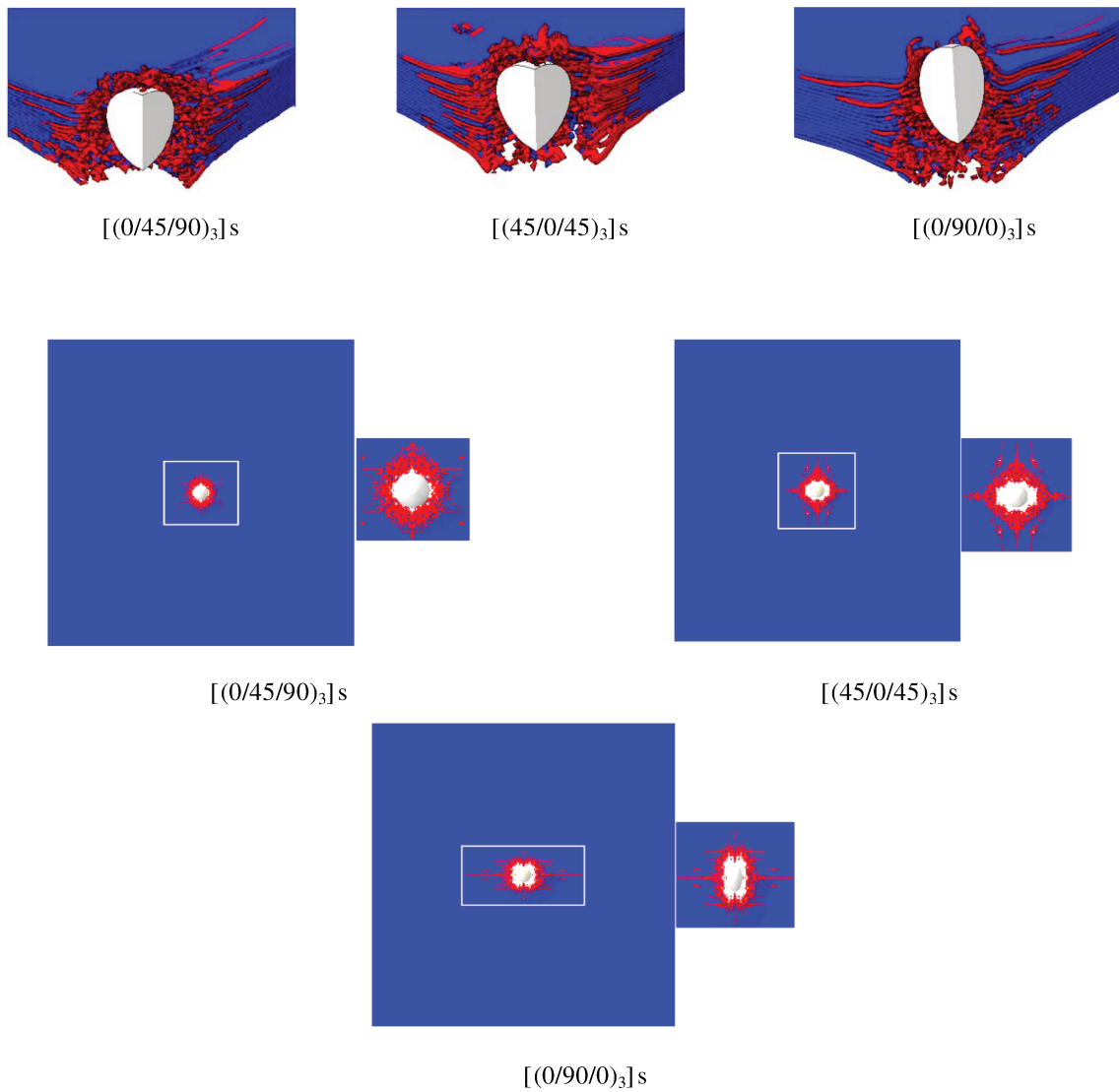


Figure 4. 20. Damage matrix tension and delamination with different stacking sequence

The main objective of the validation an intralaminar and interlaminar (delamination) model is to investigate the damage of a composite structure under water slamming impacts. Sometimes the stress wave impact causes local damage in the composite panel, especially close to the supporter and stiffeners, and with repetitive waves can cause local indentations or rupture of the structure [11]. Therefore, due to the damage mechanism in composite materials under slamming impacts, it is more important to restrict the use of composite materials in naval applications and help the designers predict the critical locations in the structure [12].

4.4 Conclusions

In this chapter, numerical damage models for both intralaminar and interlaminar failure have implemented and discussed. To begin, we constructed a three dimensional constitutive model to describe the progressive degradation of the intralaminar damage for unidirectional composite materials. Thus, the user-material subroutine VUMAT was incorporated in the explicit finite element (Abaqus) software based on continuum damage mechanics for intralaminar damage together with CZM for interlaminar damage. However, a sequence procedure was applied to verify and evaluate the validity of the numerical results. For this reason, the model was tested as a single element with different loading conditions, and different fracture energies. The test was followed with more complicated loads under high velocity impacts, and the effect of the staking sequence of the laminates was studied to identify the interlaminar damage effect on the global response. The Damage model correctly predicted the damage initiation and gave accurate estimations for the damage evolution of other failure mechanisms in the fibres and matrices. Consequently, this gave the validation to apply it to slamming impact simulations. A summary of the main damage modes occurring in the composite laminates is that matrix cracks and delamination propagated and developed quickly, especially in the matrix and through the thickness of the structure. This damage caused rupture in the fibres which led to catastrophic failure, which is the case of repeated slamming waves [13, 14]. Subsequently, this investigation can be help the ship designer to predict damage tolerance and give reasonable safety factors to design requirements for composite materials. For further confirmation of the numerical model results, experimental tests were performed for different structural rigidities of composite materials and sandwich panels, which will be discussed in the following chapters.

References

- [1] Ireneusz Lapczyk, Juan A. Hurtado, "Progressive damage modeling in fiber-reinforced materials," *Composites Part A: Applied science and manufacturing*, vol. part A 38, pp. 2333-2341, 2007.
- [2] Wei Guo, Pu Xue, Jun Yang, "Nonlinear progressive damage model for composite laminates used for low-velocity impact," *Applied Mathematics and Mechanics*, vol. 34, n° 19, pp. 1145-1154, 2013.
- [3] Z. Hashin, "failure criteria for unidirectional fiber composites," *Journal of Applied Mechanics*, vol. 31, pp. 223-232, 1980.
- [4] S. Wang, L. Wu, L. Ma, "Low-velocity impact and residual tensile strength analysis to carbon fiber composite laminates," *Materials and Design*, vol. 31, pp. 118-125, 2010.
- [5] S.H. Xin, H. M. Wen, "A Progressive Damage Model for Fiber Reinforced Plastic Composites Subjected to Impact Loading," *Impact Engineering*, vol. 75, pp. 40-52, 2015.
- [6] Abaqus Technology Brief, "Projectile Impact on a Carbon Fiber Reinforced Plate," Simulia, April, 2007.
- [7] H. Kasano, "Impact Perforation of orthotropic and quasi-isotropic CFRP laminate by a steel ball projectile," *Adv Composite Mate*, vol. 10, n° 14, pp. 309-318, 2001.
- [8] P. P. Camanho, C. G. Davila, "Mixed-Mode Decohesion Finite Elements for the Simulation of Delamination in Composite Materials," *NASA/TM*, pp. 1-37, 2002.
- [9] X. J. Gong, M. L. Benzeggah, "Determination of the Mixed Mode Delamination Toughness Using an Imposed Displacement Cantilever Beam Test Method," *ECCM 5*, Bordeaux, 1992.
- [10] A. Chiminelli, B. Garcia, P. Sanchez, M. Lizaranzu, M.A. Jimenez, "Application of Cohesive Element Simulation Techniques to Model Delamination and Fiber-Bridging in

Composite materials," *Anales de Mecanica de la fractura* 28, vol. 2, 2011.

- [11] K. Varyani, M. Gatiganti, M.Gerigk , "Motions and slamming impact on catamaran," *Ocean Engineering*, vol. 27, pp. 729-747, 2000.
- [12] T. Allen, Tom David, "Mechanics of Flexible Composite Hull Panels Subjected to Water Impacts," thesis, 2013.
- [13] S. Charca, B. Shafiq, "Repeating slamming of sandwich composite panels on water," *Journal of Sandwich Structures and Materials*, vol. 11, pp. 409-424, 2009.
- [14] B. Shafiq, S. Charca, F. Just, "Repeated slamming of foam core sandwich composite panels on water," ICCM17, Edinburgh, UK, 27-31 July 2009.

CHAPTER 5

Slamming Experimental Results

Contents

5.1 Introduction	144
5.2 Experiment setup configuration.....	145
5.2.1 Servo-test Machine	145
5.2.3 Machine Instruments.....	146
5.3 Composite Panels and fixture	147
5.4 Machines parameters calibration	148
5.5 Composite panel test results	150
5.5.1 Flexible panels (thickness =8mm)	151
5.5.2 Semi-flexible panels (thickness =13 mm)	154
5.5.3 Effect of the slamming impact along panel width	157
5.6 Comparison of different impact velocities	158
5.6.1 Hydrodynamic force	158
5.6.2 Deformation response	159
5.7 PVC Sandwich material results	162
5.7.1 Dynamic response.....	163
a) Sandwich panels, thickness=27mm.....	163
b) Sandwich panels, thickness=37mm.....	165
5.7.2 Damage assessment	167
5.8 General discussions	170
5.9 Conclusions	172
References	174

5.1 Introduction

The water entry problem is the impact loads between the structure and the free water surface which is considered one of critical design issues in ship structures. Therefore, it is recommended to determine the global and local loads. Early work in this area attempted to predicate the hydrodynamic forces of rigid rather than deformable structures [1]. The main difference between the rigid body and deformable structures is the presence of the hydroelastic influence along the fluid-structure interface. This explains why the hull flexibility has significant effects on the design of these structures, which can change the behaviour of the fluid-structure interaction. Moreover, a deadrise angle between the water and the structure is considered to be an important factor to presence this phenomenon, especially small deadrise angles [2, 3]. The hydroelastic effects exert of both dynamic and kinematic influences. The dynamic effects occur due to the interaction between the water and the structure, while the kinematic effects are produced due to the inertia effect and the change in the local deadrise angle along fluid-structure interface [4]. The fast development of composite materials in the last decade has encouraged the use of these materials in naval structures, due to their lightweight, high strength and stiffness to density ratios. For this reason, many researchers have studied their behaviour to ascertain the performance and reliability over the life time. Consequently, this assists ship designers to estimate and specify hydroelastic effects and damage mechanism before suggesting a final design load.

In this chapter, the experimental study of the slamming impact was performed for deformable laminate composite and sandwich panels. The composite panels consisted of vinylester resin reinforced with glass fibres, and the sandwich panels were manufactured with polymeric skins and PVC foam cores. The deformations and response forces of the panels were investigated as indicators to describe the hydroelastic effect and the structural analysis during water-structure interaction.

5.2 Experiment setup configuration

5.2.1 Servo-test Machine

A high speed shock machine with a velocity control system was used to calibrate and maintain the velocity approximately constant throughout the water impact as illustrated in Figure 5. 1. As a result, the impact velocity is virtually unchanged due to the change in the added mass. The performance specifications of the machine were distinct from other traditional machines, since could apply more than 100 kN (200kN) and achieve velocities of up to 20 m/s (10 m/s). The fixture system was made of steel 355S with a weight 58.5 kg, which was attached to the hydraulic piston, while the total weight of flexible ($t=8\text{mm}$) composite panels was 3.7 kg and semi-flexible ($t=13\text{mm}$) composite panels was 6.8 kg. Numerical natural frequency analysis of fixture system based on the FEM was determined and reported in Appendix (A). The machine came with a 1.1 m water tank (3m in length, 2m width, and 2m depth), in which to implement the tests.

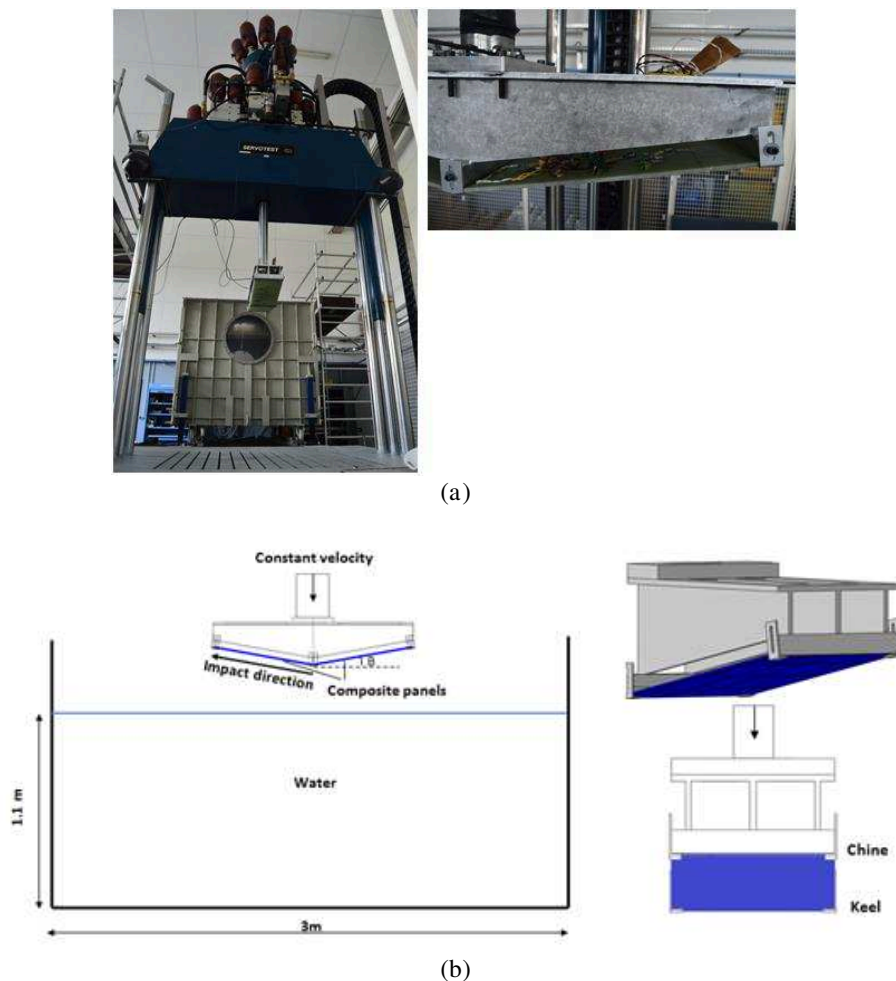


Figure 5. 1. Experimental setup and Schematic representation

5.2.3 Machine Instruments

The impact force was measured by using a force sensor which was mounted on the machine piston as shown in Figure 5. 2a. Due to the location of this sensor, the force did not represent the real hydrodynamic force of impacted panels, as some inertial force of the fixture system and panels led to some variation in the total hydrodynamic force. For this reason, an accelerometer (model EGAS-FS-250/V12/L8M/X) was used to measure the acceleration of velocity, as shown in Figure 5. 2a. This sensor is used to determine the inertial force during the impact, especially, in the period of interest, in the approximate constant velocity. For more details see [5, 6].

Data acquisition illustrated in Figure 5. 2b was used to monitor the machine (Servo-test machine software) and data acquisition (genesis model) to receive and manipulate different measurements of the strain gauges for the deformation, force, displacement sensor and contact sensor for detection during the moment of fluid–structure contact. A high speed camera of the type Photron FASTCAM (SA-X2) was used to capture images of water flow during the slamming event, and also to clarify the phenomenon of the fluid-structure interaction. The camera specifications were 12500 frames per second and the resolution 1.024 x 1.024. A schematic overview of the camera set-up is shown in Figure 5. 2c.

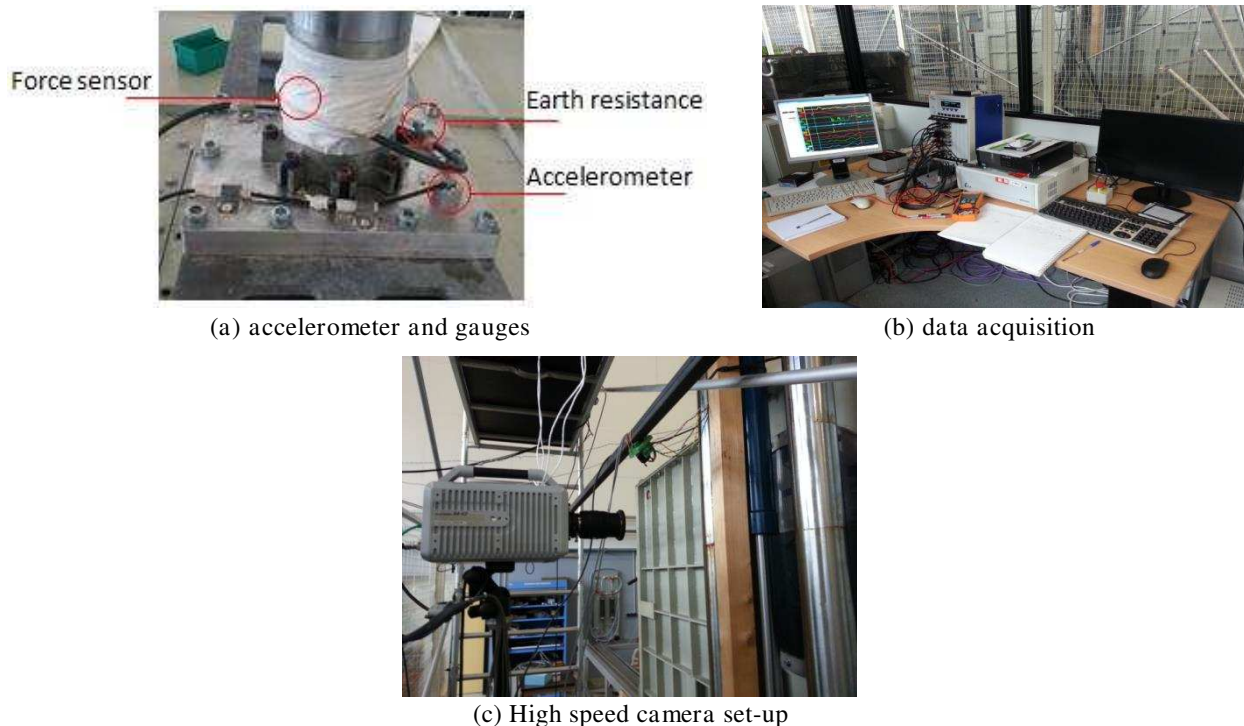
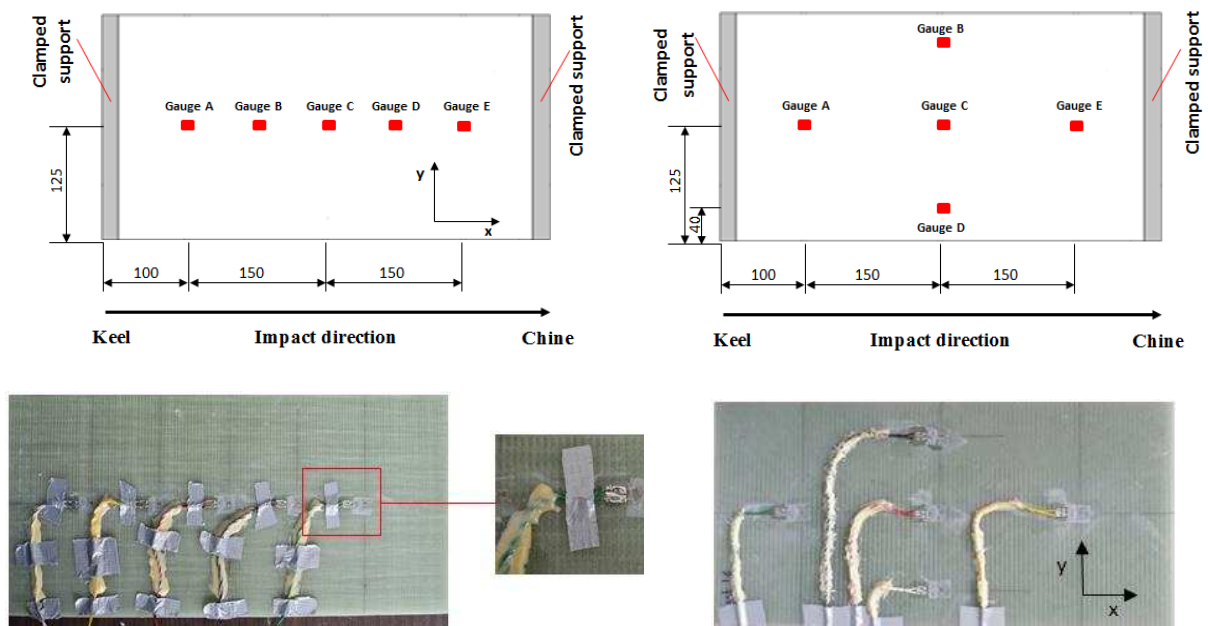


Figure 5. 2. Measurement Instruments

5.3 Composite Panels and fixture

The wedge was composed of the two composite panels (500 × 250 mm) that had a fully clamped boundary condition at the panel edges (keel and chine), this condition is usually made for composite hull [7], as illustrated in Figure 5. 3. However, in order to investigate the hydroelastic influence, glass/vinylester composite panels with different thickness namely semi-flexible (SF) =13mm, flexible (F) =8 mm were tested. The woven E-glass/vinylester laminate composites samples used in this work were provided by EADS composites and manufactured for naval and aeronautic applications. The samples had 22 layers for (SF) and 12 layers for (F) panels with a vinylester resin matrix DION 9102. Each layer was of a plain weave construction (50% weft yarns per 50% warp yarns) made of E-glass fabric, which created orthotropic mechanical properties in three orthogonal directions. Laminate and sandwich panels were produced using the vacuum resin infusion process, the fabrication process is given in Appendix (B).



(a) First configuration :Panel dimensions and strain gauge location

(b) Second configuration Panel dimensions and strain gauge location

Gauge reference	A	B	C	D	E
Direction of the deformation	X	X	X	X	X

Figure 5. 3. Diagram of panels and positioning of strain gauges, dimensions in mm

The hydroelastic effects are greatest in the impacted wedges with a deadrise angle of 5° to 20°, while the 30° angles behave as a rigid [7]. Therefore, in this study, all of the panels examined had a deadrise angle of 10°. The panels were mounted with strain gauges (SG) in five different positions along the span of panel to provide the direct measurements of structural response and cover mode shapes of natural frequency, Figure 5. 4.

The positions of the strain gauges were predicted from the natural mode frequencies of the dry panels using finite element code (Appendix A), as shown in Figure 5. 4. Note that the second configuration of gauge positions was used to identify three-dimensional effects along the panel width. The details of the panel’s mechanical properties are given in Table 5. 1.

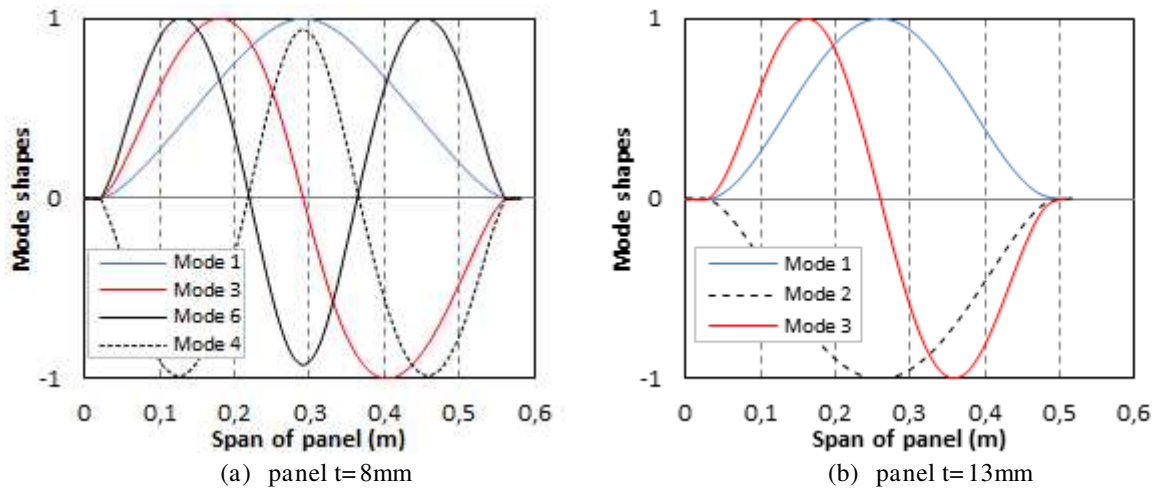


Figure 5. 4. Mode shapes of the dry panels

Elastic moduli (GPa)			Position ratios (-)			Shear moduli (GPa)		
E_{11}	E_{22}	E_{33}	ν_{12}	ν_{13}	ν_{23}	G_{12}	G_{13}	G_{23}
48.16	11.21	11.21	0.274	0.274	0.096	4.42	4.42	9
Ultimate tensile and compression strengths (MPa)						Ultimate Shear strengths (MPa)		
X_t	X_c	Y_t	Y_c	Z_t	Z_c	S_{12}	S_{13}	S_{23}
1021	978	29.5	171.8	15	171.8	70	70	30

Table 5. 1. Properties of two composite panels with different thicknesses (8 mm and 13 mm)

5.4 Machines parameters calibration

To prove the validity of the experimental results, a procedure was followed to calibrate the machine performance to ensure that the robustness of test was satisfactory in terms of stability and approximately constant velocity. All data were manipulated (post-processing) to convert them to respective units from the voltage unit using Matlab software. To show how the data

obtained was interpreted, an example of a flexible composite panel with a velocity of 6 m/s is presented. Figure 5. 5 illustrates the acceleration profile, velocity and electrical signal for the moment of contact. It can be observed, that the acceleration profile (Figure 5. 5a) at the beginning of the test rises until it reaches the desired velocity, then maintains a more stable at approximate zero value (Figure 5. 5b) before and during the impact duration, after which it tends to decelerate. The interesting velocity period (Figure 5. 5c) is recognized from the results of the contact sensor which detects the instant of the fluid-structure contact, Figure 5. 5d.

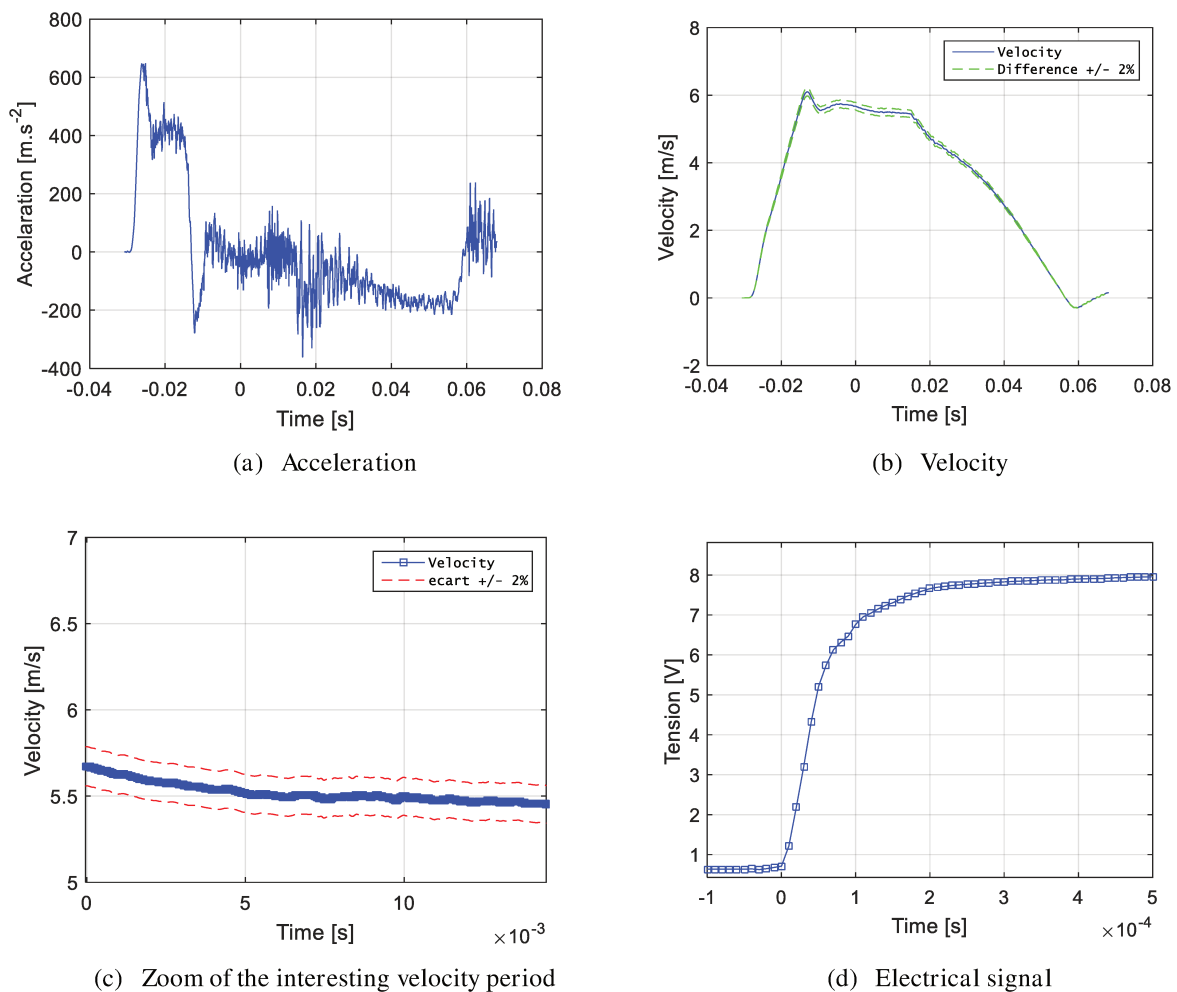


Figure 5. 5. Calibration of the machine with flexible composite panel, $V=6\text{m/s}$

The responses of the composite panels were estimated from both force and deformation, the hydrodynamic force was determined by subtracting the inertial load from the total experimental load to take the inertial load effect of fixture system and composite panels,

Figure 5. 6a-b. The deformation detected by the gauge sensors in different locations on the panel is shown in Figure 5. 6c.

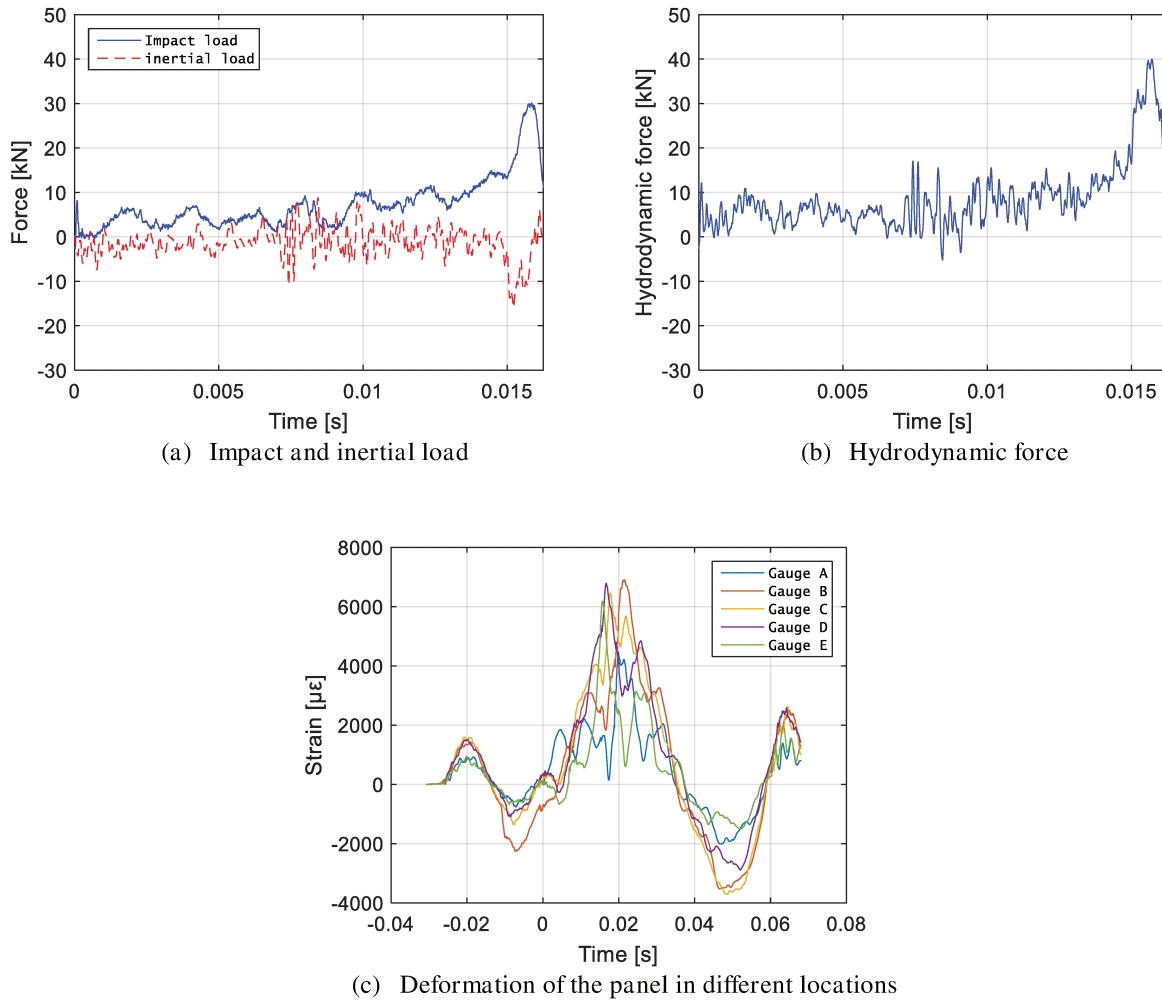


Figure 5. 6. Structure response with flexible composite panel, $V=6\text{m/s}$

5.5 Composite panel test results

In order to investigate the influence of hydroelastic behaviour, a series of tests was performed with two different rigidities of composite panels as mentioned in Section 5.3. The dynamic impact of the deformable structure means that the local velocity and the local deadrise angle along the fluid-structure interaction change due to the structure deformation, therefore the hydrodynamic force and pressure differ from those observed for the rigid body [8].

5.5.1 Flexible panels (thickness =8mm)

For the composite laminate panel, we can note that there is a good repeatability in all measurement tests. In velocity 4 m/s (Figure 5. 7a), stability in the force distribution over time (0.005, 0.0176 sec) can be observed. This can be attributed to the fluid flow separation and loss of contact between the water and panel surface due to hydroelastic effects. After that, the water flow keeps in direct contact with the panel surface, causing a more rapid rise in the force magnitude close to chine. At higher velocities (Figure 5. 7 c-b), this phenomenon manifests itself as an increase in the impact velocity.

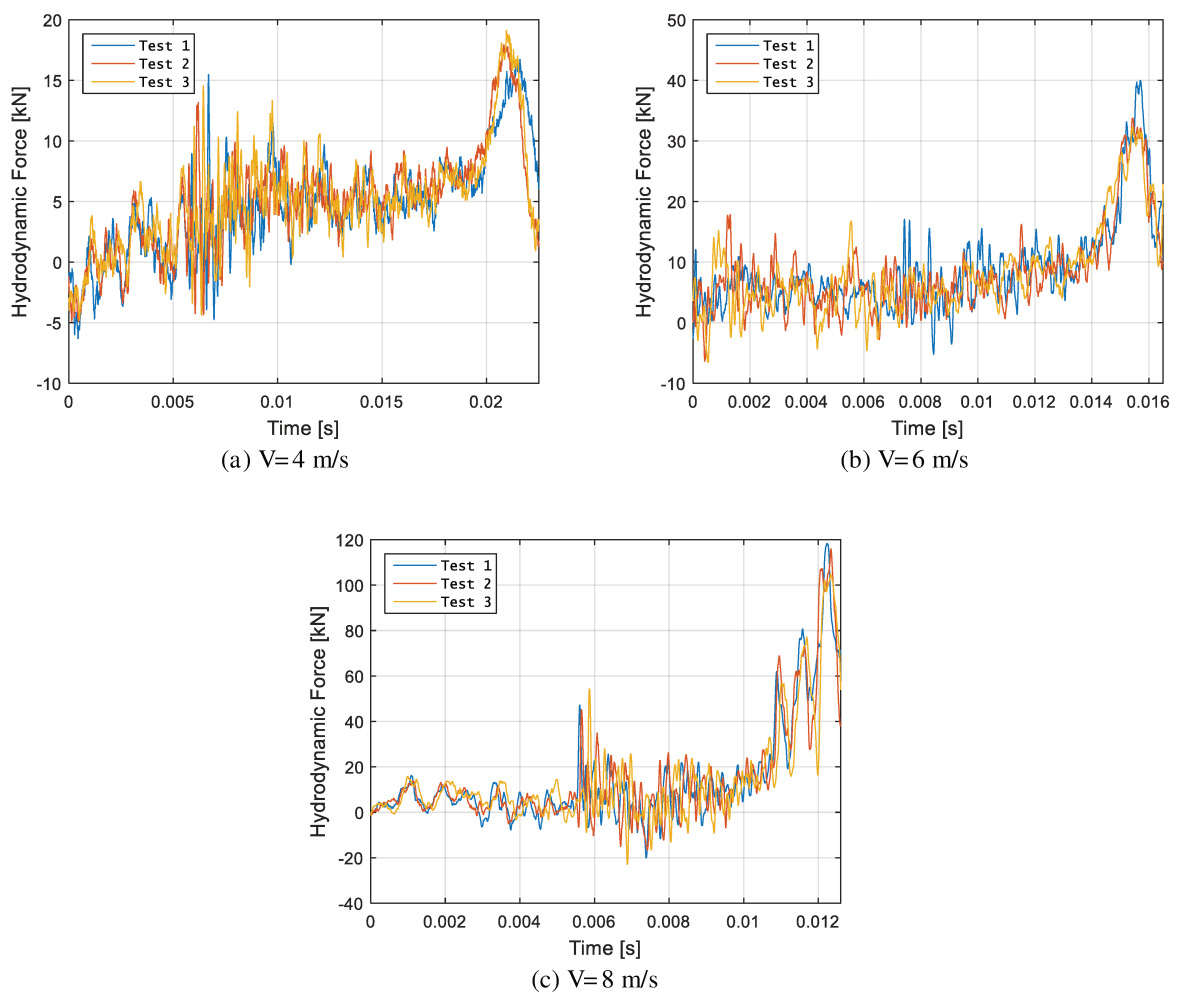


Figure 5. 7. Repeatability of tests for flexible wedge

As far as the recorded deformation is concerned, all panels sustain various vibration modes that obviously have negative and positive strain values. Consequently, a change in local pressure can occurs, Figure 5. 8. In the acceleration period, all the gauge sensors have the same profile as the mode, and then will be keep the same mode and increase towards the

chine edge. The maximum strain occurs between gauges C and D approximately at 320 mm from the keel. While the longitudinal strain at gauge A is much lower than the strain at other gauge sensors because the panel does not have enough loading to be deflected. For different velocities, more variation in the strain has observed that relates to increase the velocity.

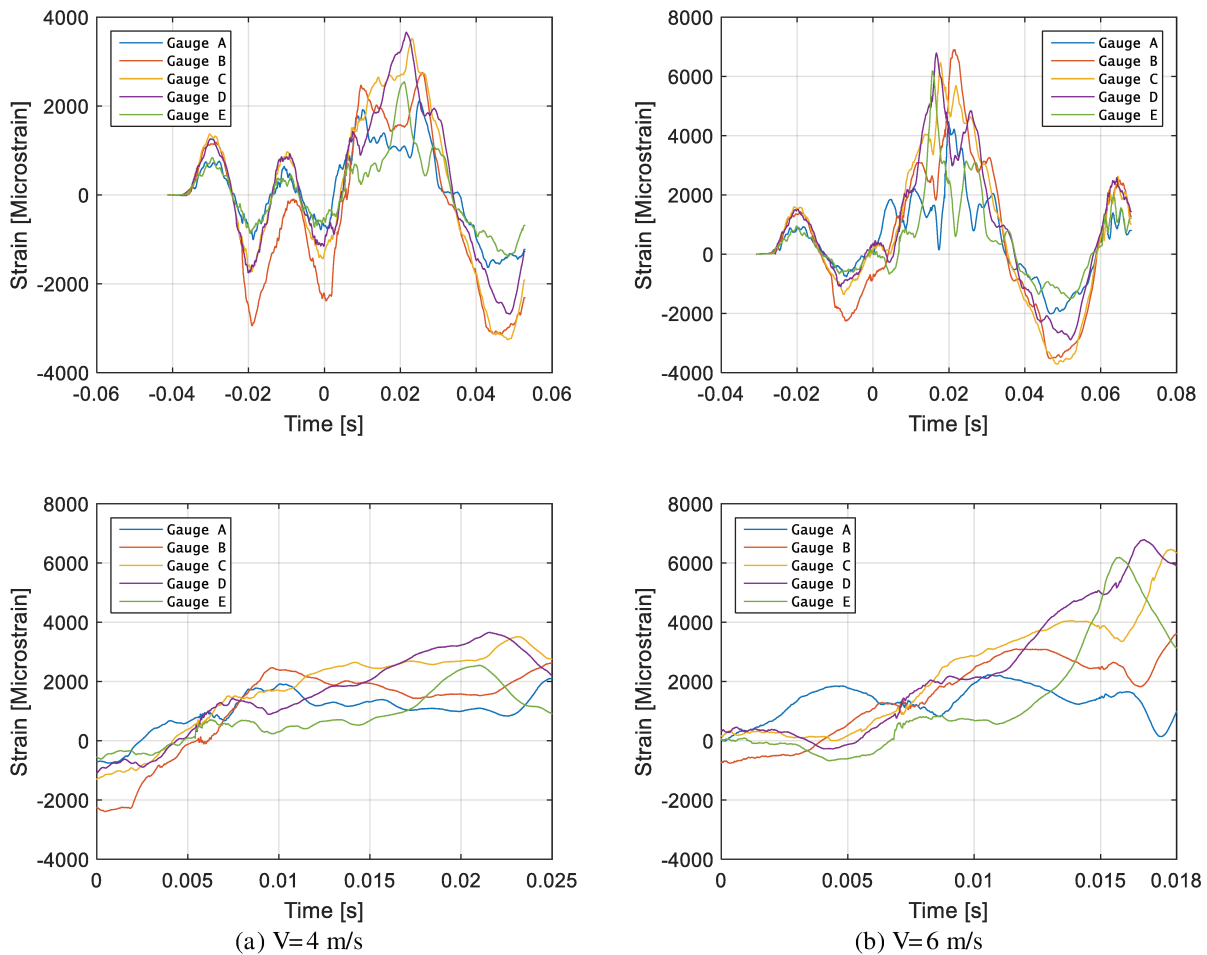


Figure 5. 8. Deformation measured by strain gauges

The strain mode shapes of a wet panel can be generally assessed from the fitting measured dynamic deformations of the strain gauges which are mounted along the panel span, relative with the submerged depth (d_i) (initial water contact $d_i= 0$ m, complete submerged $d_i= 0.0868$ m). At the first moment of contact, the panel deforms in opposite direction of impact velocity due to the inertia effect, and with rise of the penetration rate of the composite wedge, one single mode of deformation was dominated the panel deflection due to increasing of the hydrodynamic loads. According to these shapes, one can observe that an increase in the impact velocity leads to a reduction in the impact duration and appears more than one vibrating mode, Figure 5. 9. In this case, the hydroelastic effect becomes more significant [9, 3].

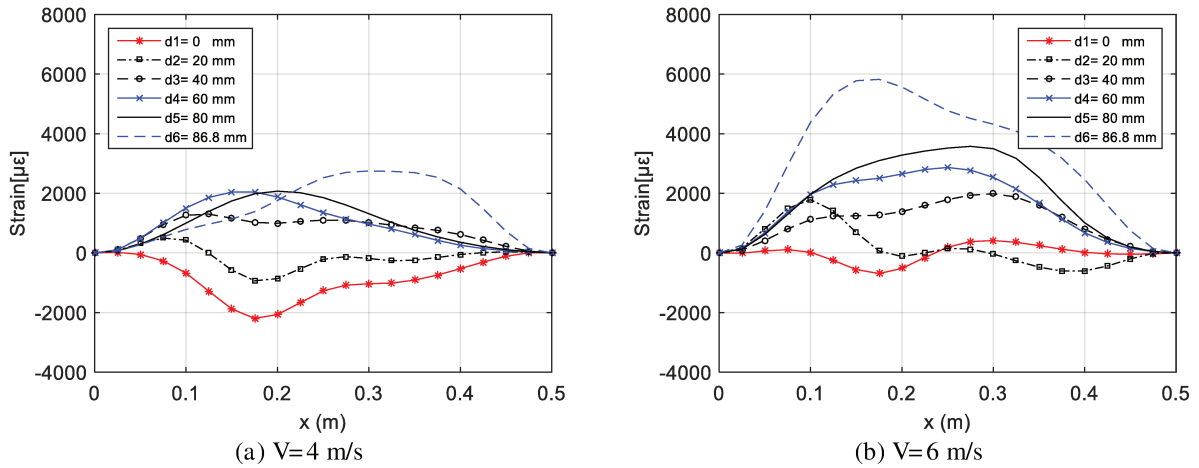


Figure 5. 9. Mode shape histories from strain gauges along wet panel

Figure 5. 10 and Figure 5. 11 show the images captured by high speed camera during the water entry for velocities 4 m/s and 6 m/s. These images correspond to time periods in the hydrodynamic force curve:

- The first image shows the moment of impact on the keel edge.
- The second shows the contact between fluid and structure in the panel centre.
- The third image shows the penetration of the impactor.
- The fourth image shows the formation of a water jet before flow separation.

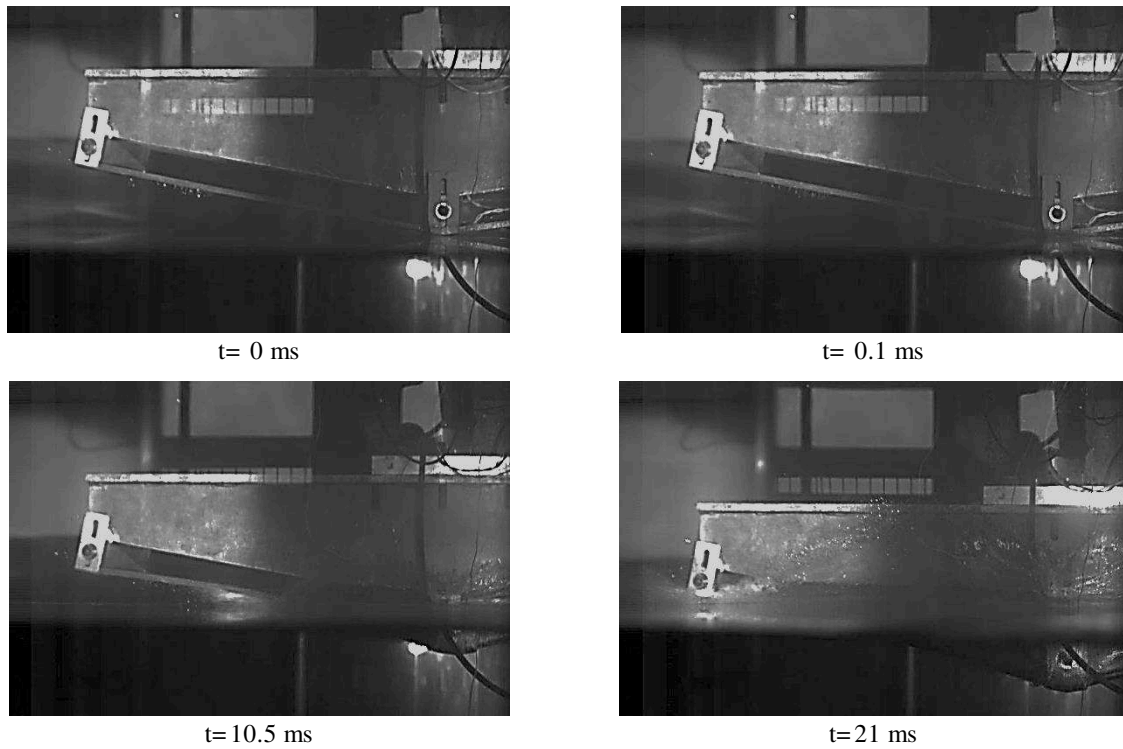


Figure 5. 10. Camera images, $V = 4$ m/s

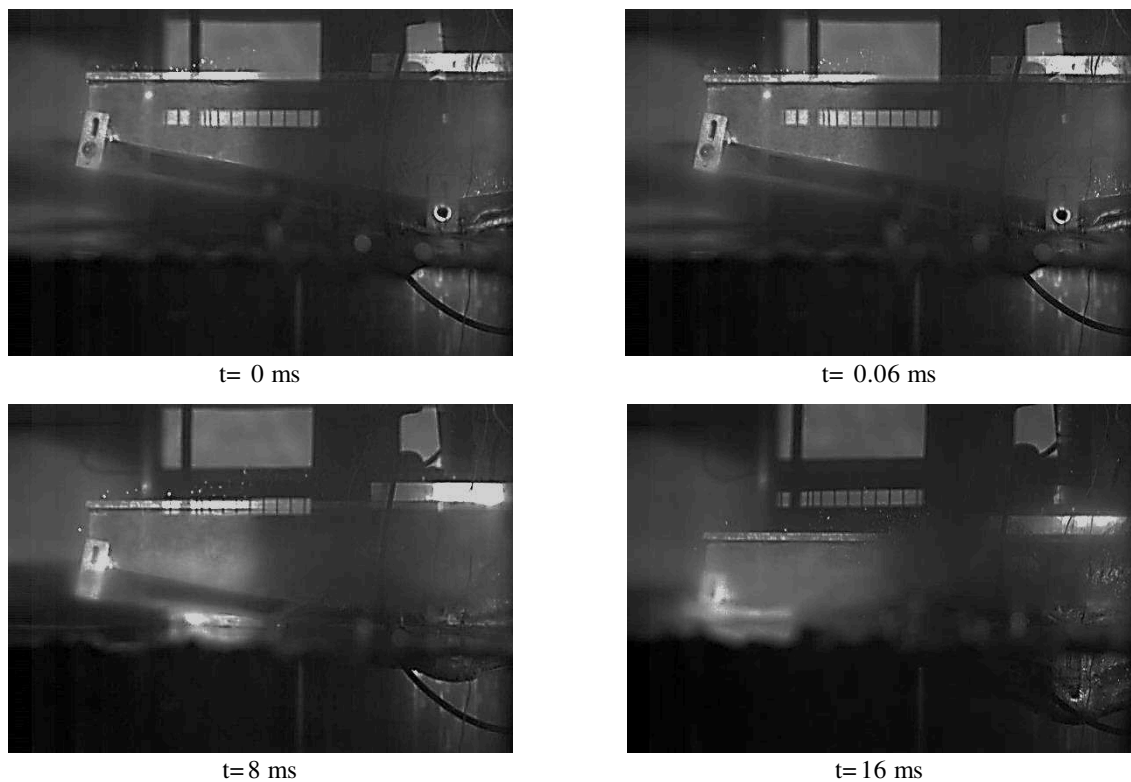


Figure 5. 11. Camera images, $V = 6$ m/s

5.5.2 Semi-flexible panels (thickness =13 mm)

In the panel with more stiffness, a higher impact velocity was implemented to allow more deformation. This led to a reduction in ratio between the duration of impact and the first

period frequency mode of the dry panel [2]. The hydrodynamic force has a linear profile at low impact velocity, $V=6\text{m/s}$, as that happen in rigid wedge, while it behaves an exponential profile along the span of panel at higher velocity (8 -10 m/s) due to the nonlinear behaviour of the water-deformable structure interaction. It is also important to mention that the oscillations on the load curves increased as velocity increased. These oscillations were caused by the kinematic effects related with the panel flexibility, Figure 5. 12. For the Sandwich panels, we can note that there is a good repeatability in all measurement tests.

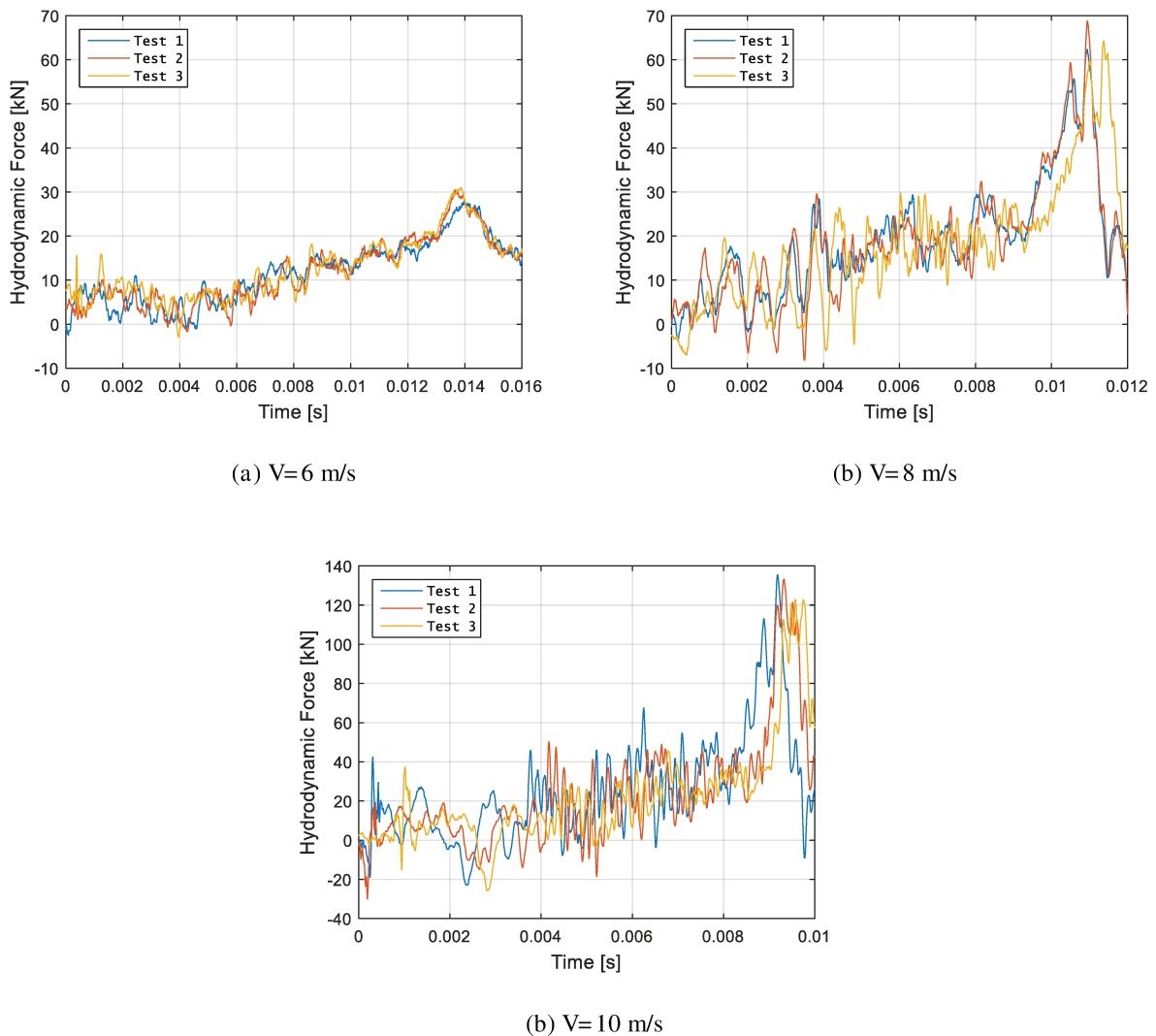


Figure 5. 12. Repeatability of semi-flexible wedge tests

Concerning the deformation, negative values of the strain appeared less in the highest stiffness panels (SFP) due to less inertia effect and more frequent with an increase in impact velocity. Elevation of the wet surface, thus the shape of the deformation in all locations takes

the same form, as shown in Figure 5. 13. Note that the maximum deformation is always at gauges C and D that corresponds to the maximum hydrodynamic force.

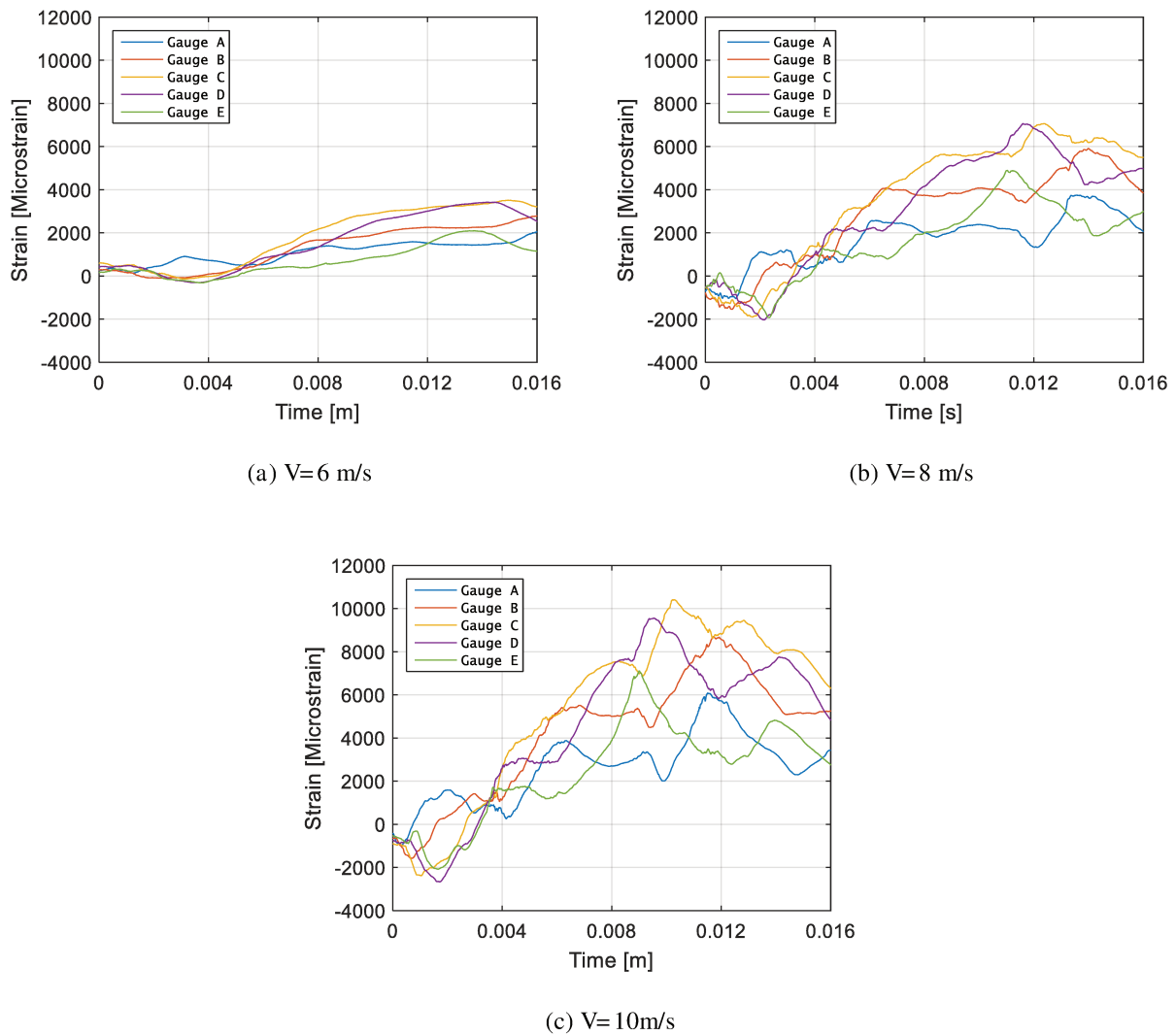


Figure 5. 13. Deformation in strain gauge

Figure 5. 14 shows the effect of the impact velocity on the strain mode shape of panels relative to the submerged depth (d), which is the same situation as for the flexible panel as explained previously. In contrast, the inertial effect of the panel appears less at the initial time of impact and becoming significantly more frequently observed with the highest impact velocity.

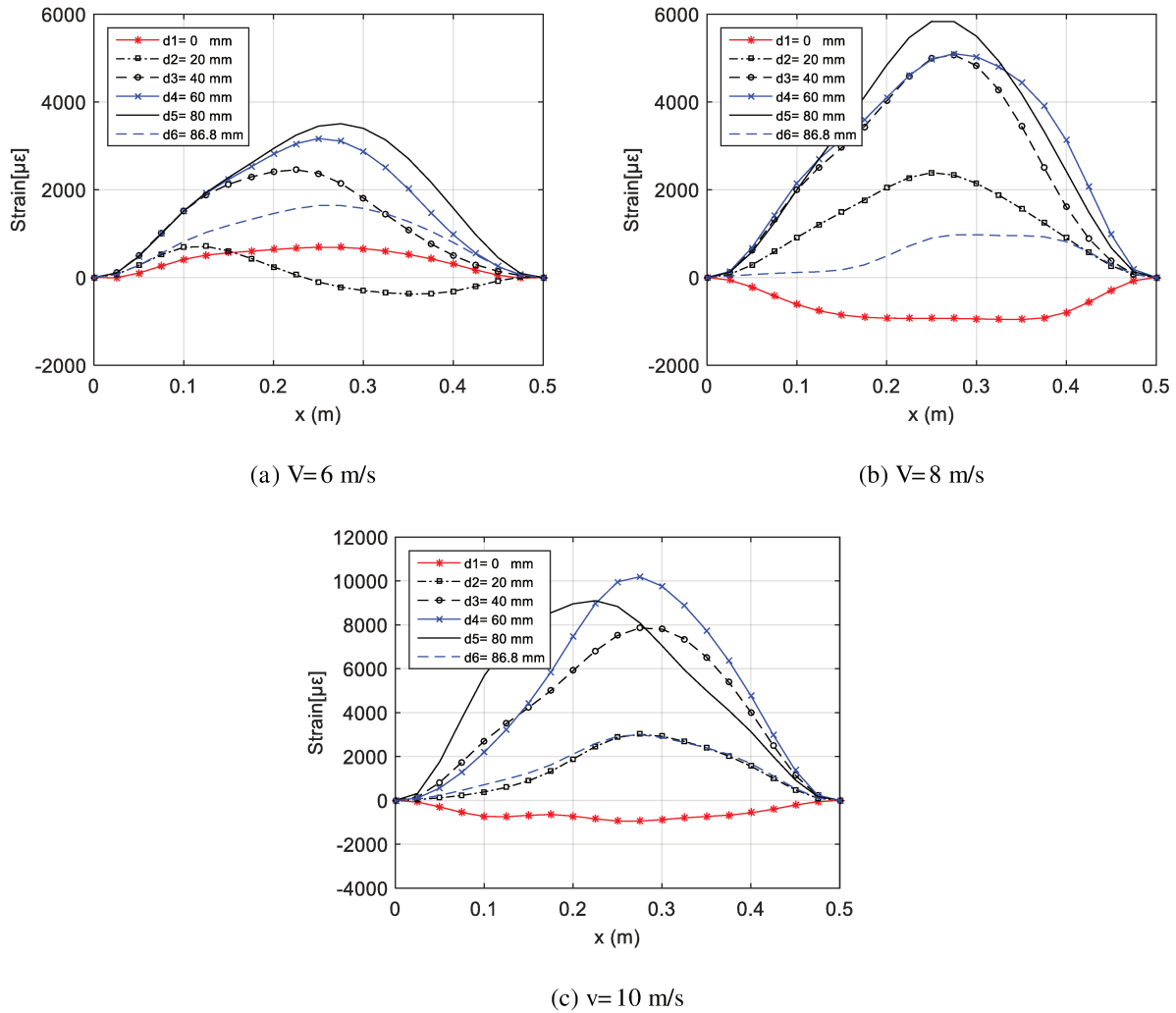


Figure 5. 14. Mode shapes histories from strain gauges along wet panel, $t=13\text{ms}$

5.5.3 Effect of the slamming impact along panel width

To be specific, for the three dimensional effect of the deformation through width of the panel in the gauge locations (GC, GB, GD) in the semi-flexible panel, gauges B, D exhibit a difference in deformation of about 20% and 13.4% respectively from GC as illustrated in Figure 5. 15. This effect can arise with an increase the impact velocity and panel width.

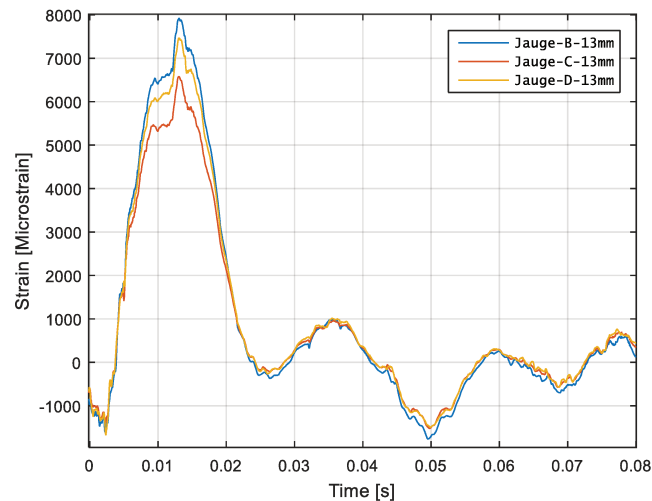


Figure 5. 15. Three dimensional effect, $t=13\text{mm}$ and $V=8\text{m/s}$

5.6 Comparison of different impact velocities

5.6.1 Hydrodynamic force

It can be seen that the flexibility of the panel has a great influence on the profile and amplitude of the maximum hydrodynamic load. Therefore, more flexible panels have higher peak force and a clear imprint on the structural oscillations along the impact direction, Figure 5. 16a. These effects increase by increasing impact velocity as shown in Figure 5. 16b. Panels with more rigidity have less peak force and lower vibration in the force histories. This can be attributed to less appearance of the hydroelastic effects. In all the tested panels, it can be observed that the maximum force is near the chine as the wetting surface of the panel-water interface has been increased. This leads to the generation of high hydrodynamic pressure in this location which may be intensive enough to cause damage (local delamination in the fixture support and micro-matrix cracks near to the chine) in composite material as illustrated in Figure 5. 17.

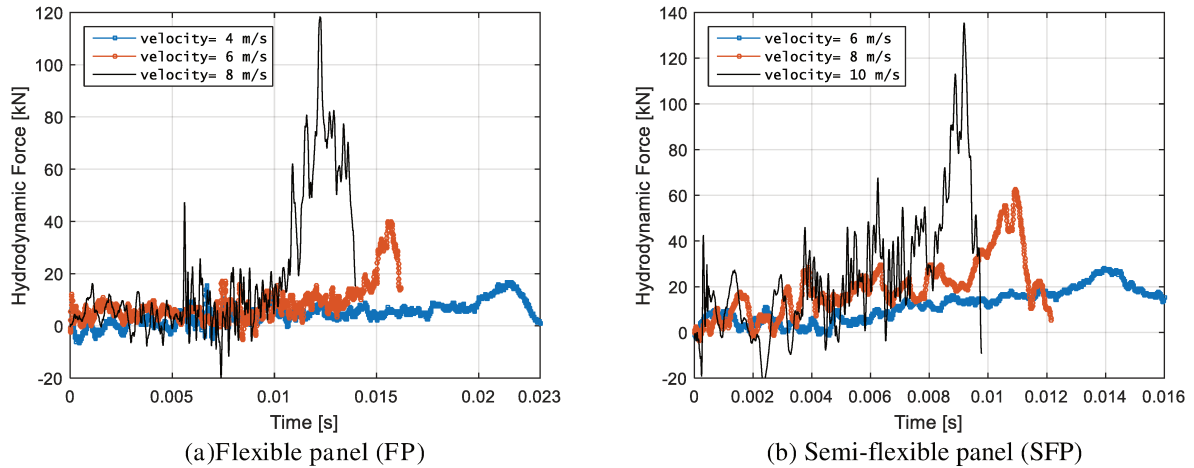


Figure 5. 16. Hydrodynamic load for different rigidity and impact velocities

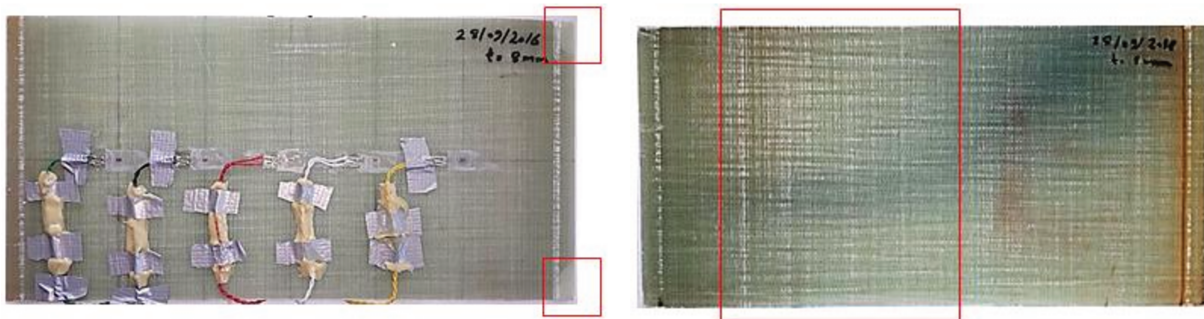


Figure 5. 17. Damage in the flexible composite panel

5.6.2 Deformation response

The maximum strain in different gauges for both flexible (FP) and semi-flexible (SFP) panels is summarized in Figure 5. 18. On the other hand, Det Norske Veritas (DNV) classification societies [10] for the structural requirements of naval vessel have been considered. This DNV classification requires that the allowable strain does not exceed $\epsilon_{\text{allowable}} = 0.3 \epsilon_{\text{ultimate}}$. In this study, the ultimate strain for woven E-glass/vinylester laminate composites $\approx 2\%$, therefore the allowable strain equal to 6000 micro-strain. This corresponds to the velocity 6m/s in the flexible panel and 8 m/s in the semi-flexible panel.

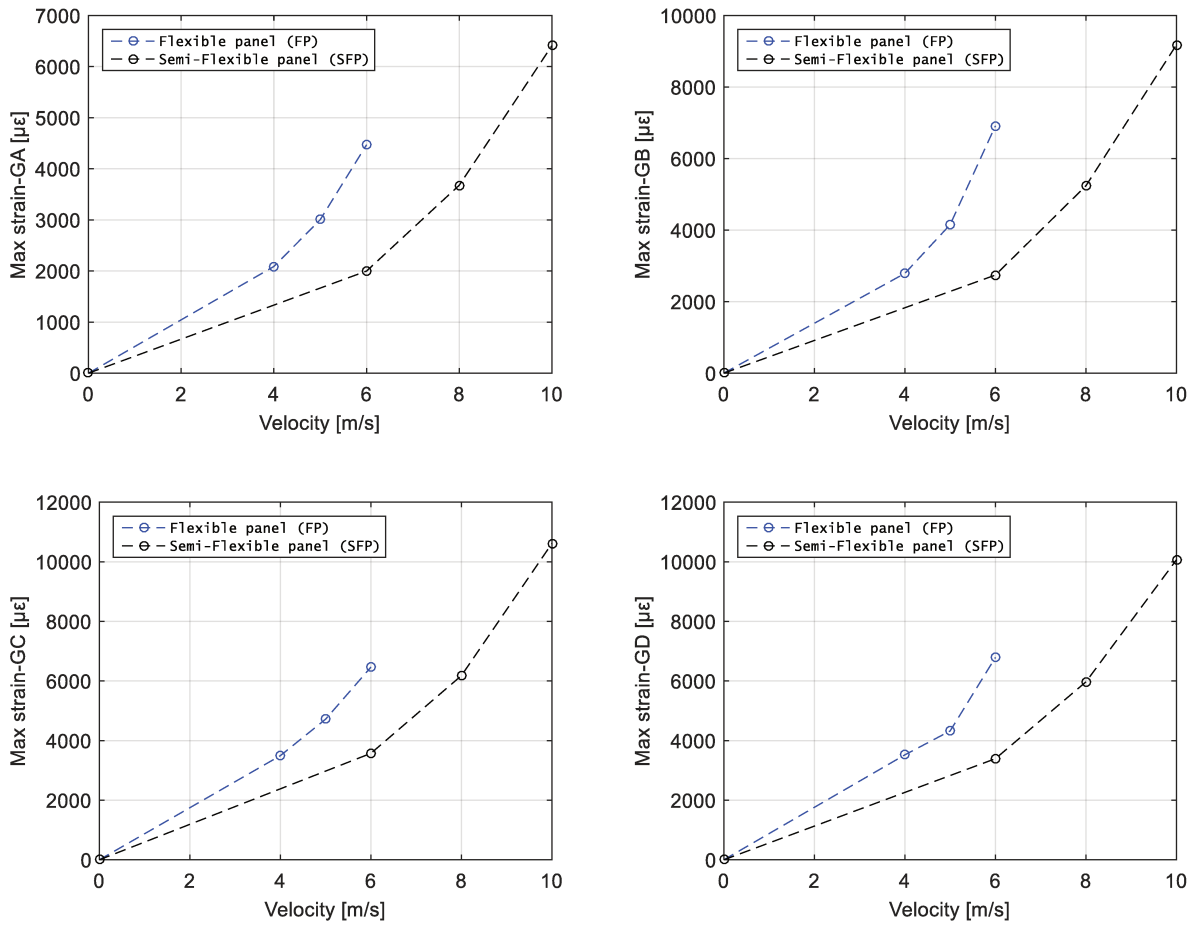


Figure 5. 18. Maximum experimental strain for different gauges in (FP) and (SFP) panels

For more details on the panels deformation, Figure 5. 19 shows the deformation of panels with different stiffness at different gauges under a velocity of 6 m/s. It can be noted that the deformation that occurs at GA, GB and GC has almost the same values, and becomes more significant in the flexible panel at gauges GD and GE, which are close to the chine edge. This sudden increase is attributed to the high pressure in these locations due to the change of the deadrise angle and fluid local velocity.

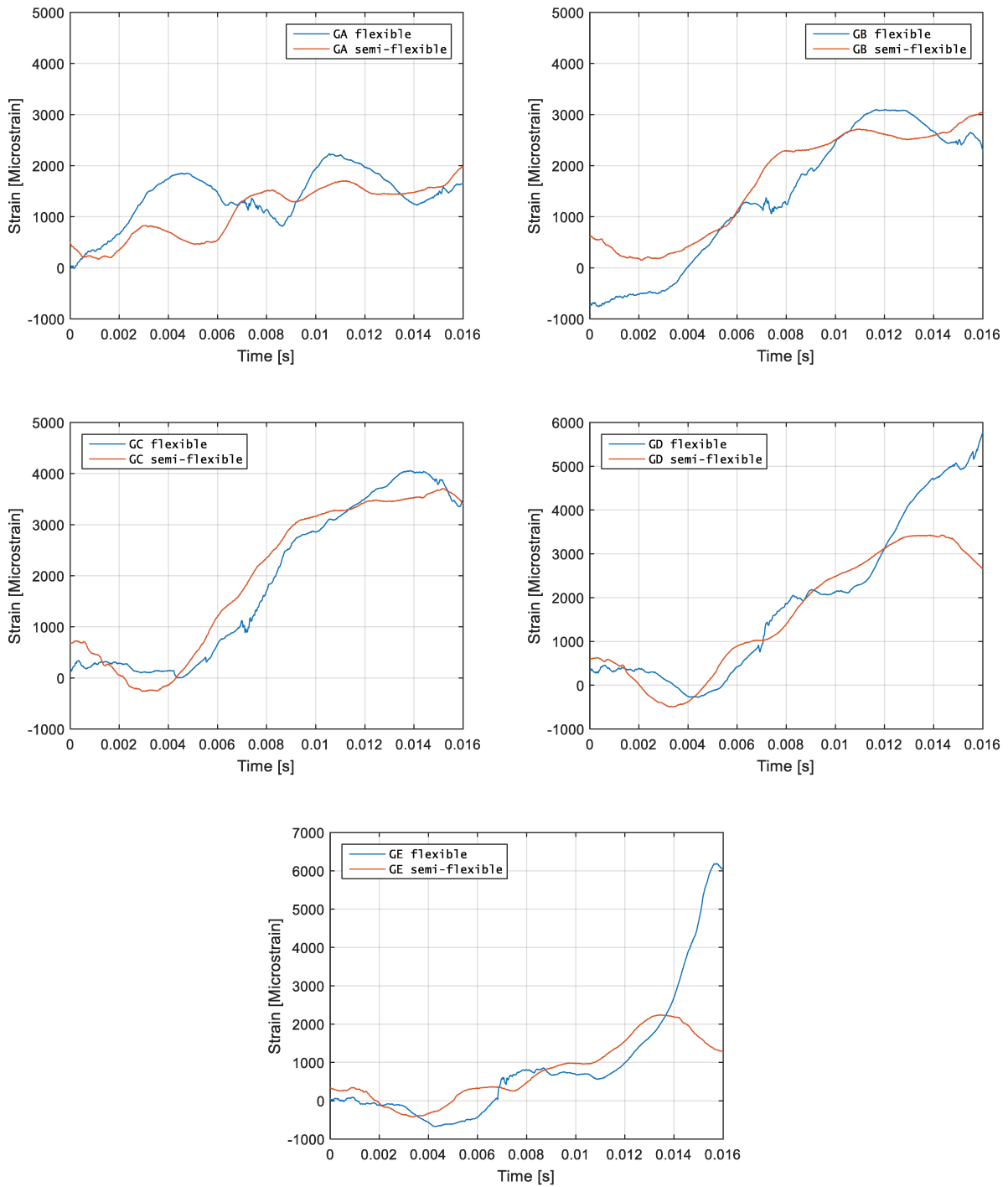


Figure 5. 19. Comparison of the deformation between flexible and semi-flexible panels,

$$V=6\text{m/s}$$

5.7 PVC Sandwich material results

Sandwich material structures have been widely used in marine applications due to their properties such as high weight/strength ratio. In contrast, the failure mechanism of these structures has a significant effect on the stress state, the most common failure modes in these structures are skin/core debonding and core shear. In this section, the dynamic response of composite sandwich panels is analysed. Figure 5. 20 illustrate the sandwich experiment setup. Sandwich structures consist of polymeric skins and PVC foam cores. Static characterisation of these specimens has been presented in previous works [11, 12]. Details of the mechanical properties of the panel are shown in Table 5. 2.

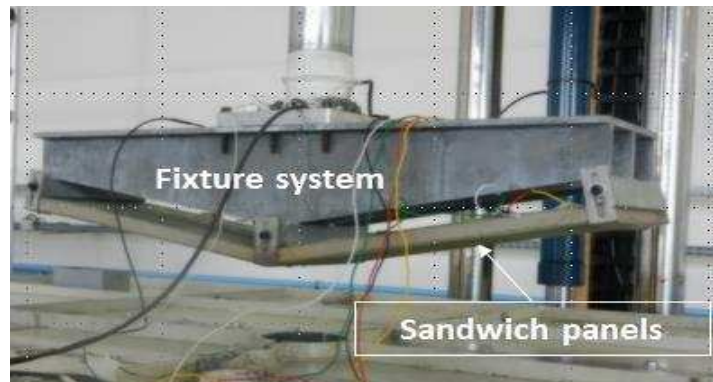


Figure 5. 20. Sandwich experiment set up configuration

	Density (kg/m ³)	t(mm)	Elastic moduli (GPa)			Poisson's ratios (-)			Shear moduli (GPa)		
			E ₁₁	E ₂₂	E ₃₃	ν_{12}	ν_{13}	ν_{23}	G ₁₂	G ₁₃	G ₂₃
Skin	1960	$t_f=7$	48.16	11.21	11.21	0.274	0.274	0.096	4.42	4.42	9
Core	80	t_c 20 and 30	0.077	0.077	0.110	0.3	0.3	0.3	0.029	0.029	0.029

Table 5. 2. Sandwich panel mechanical properties [11, 12]

5.7.1 Dynamic response

a) Sandwich panels, thickness=27mm

For each panel, the repeatability of the measurements was performed more than one test, which seems to be a good repeatability for all tests, Figure 5. 21. As in composite panels, it can be noted that the flexibility of sandwich panels has a significant influence on the dynamic noise and the peak force. The dynamic noise can be attributed to kinematic hydroelastic effects such as the change in the local deadrise angle and the panel deflections along the fluid structure interface. Moreover, the lower hydroelastic effects appear in these panels which behave like the rigid body in the velocity range (4-8 m/s). The damage begins to occur in the core and skin/core interface at 10 m/s.

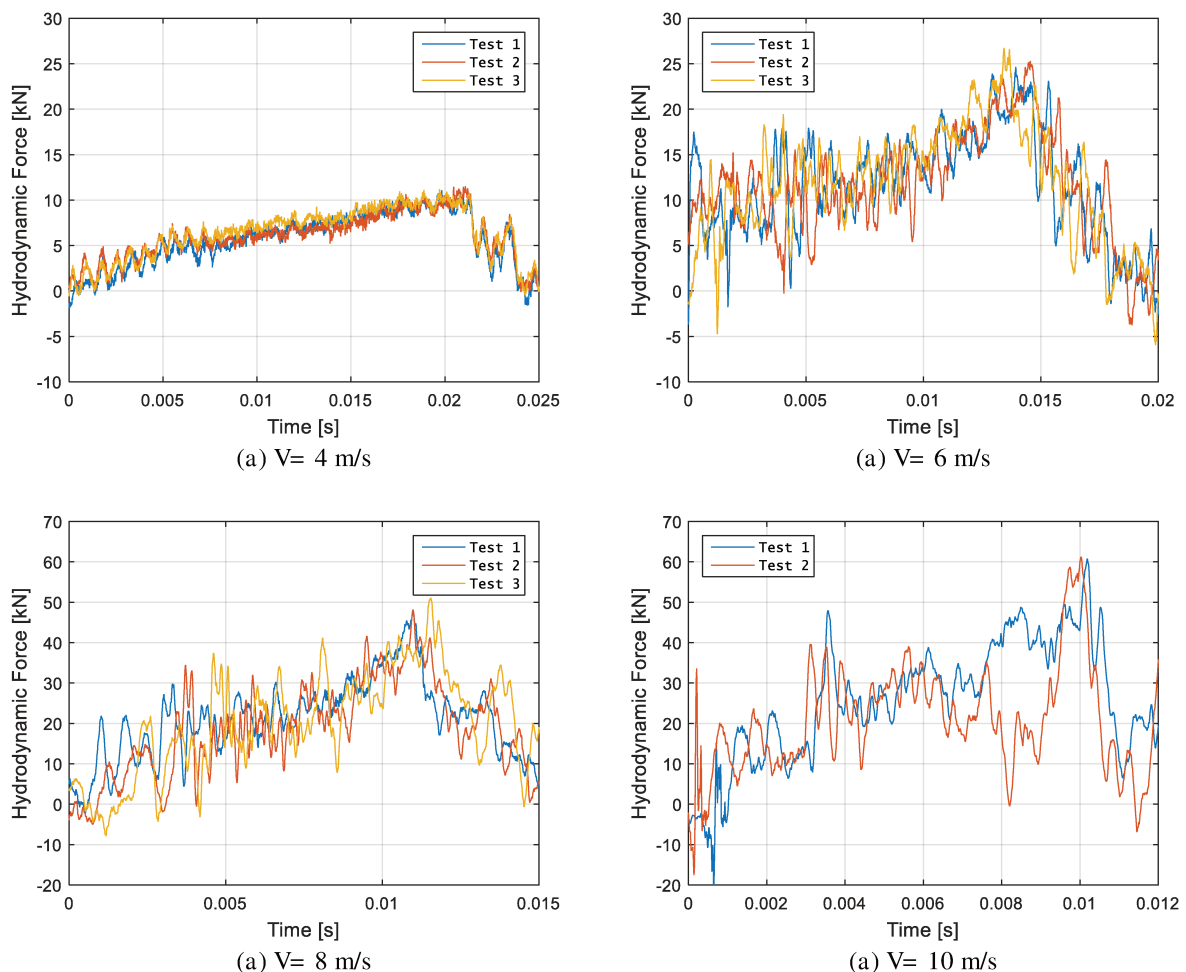


Figure 5. 21. The repeatability of tests on PVC sandwich, $t=27\text{mm}$

The panels withstand greater deformation response as the impact velocity increase, as shown in Figure 5. 22. It should be mentioned that sandwich panels exhibit a similar deformation profile response at impact velocity of less than 10 m/s and exhibit elastic deformation, but the responses of deformation in the strain gauge (GE) at V=10 m/s diverge and increase rapidly. This can indicate that the panel was exceeded the elastic deformation and it exposed to damage. Indeed, we can also note that the gauges B, D and C give almost the same rate of deformation. This shows that we do not have the phenomenon of 3D deformation; all points on the width of the panel follow the same deformation and thereafter see the same strain.

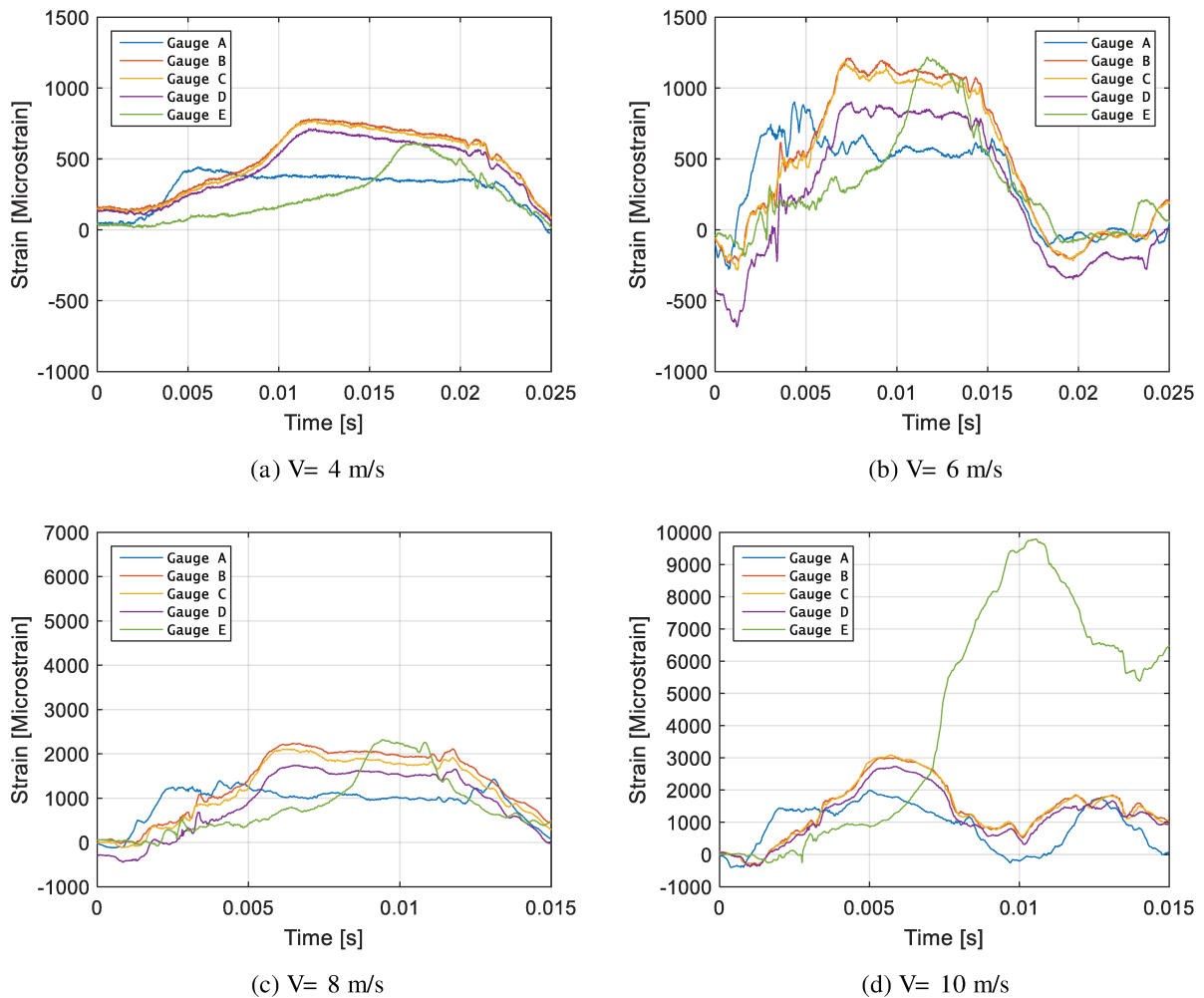


Figure 5. 22. Deformation in the strain gauges, $t=27\text{mm}$

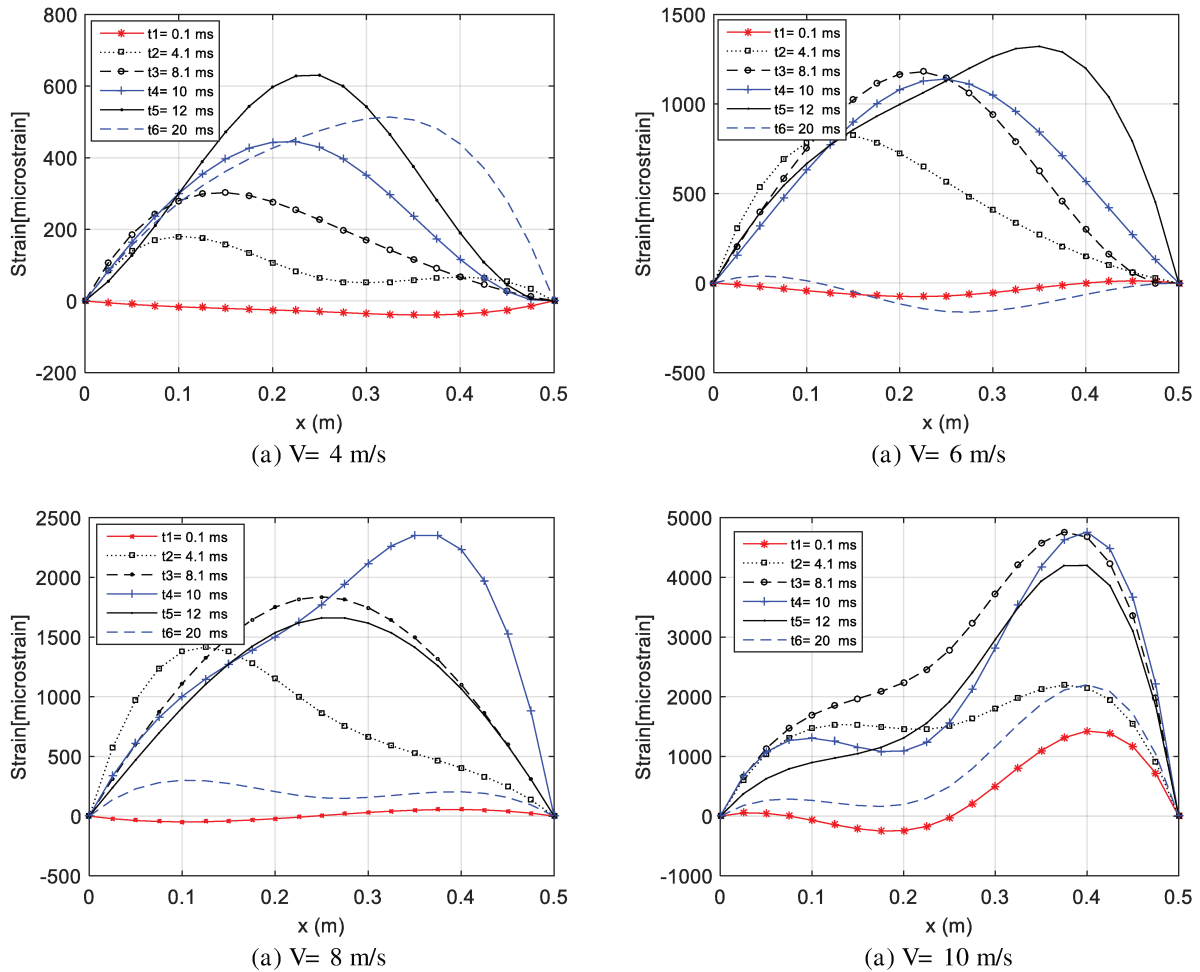


Figure 5. 23. Mode shapes histories from strain gauges along wet sandwich panel, $t=27$ mm

b) Sandwich panels, thickness=37mm

Higher stiffness sandwich panels ($t=37$ mm) sustain lower hydrodynamic impact as impact velocity increases, Figure 5. 24 . However, the same behaviour has observed for less stiff panels as presented previously which have less dynamic noise due to the lower flexibility of the panel during the interaction with fluid. Figure 5. 25 shows the deformation of the sandwich panel for a range of the impact velocities.

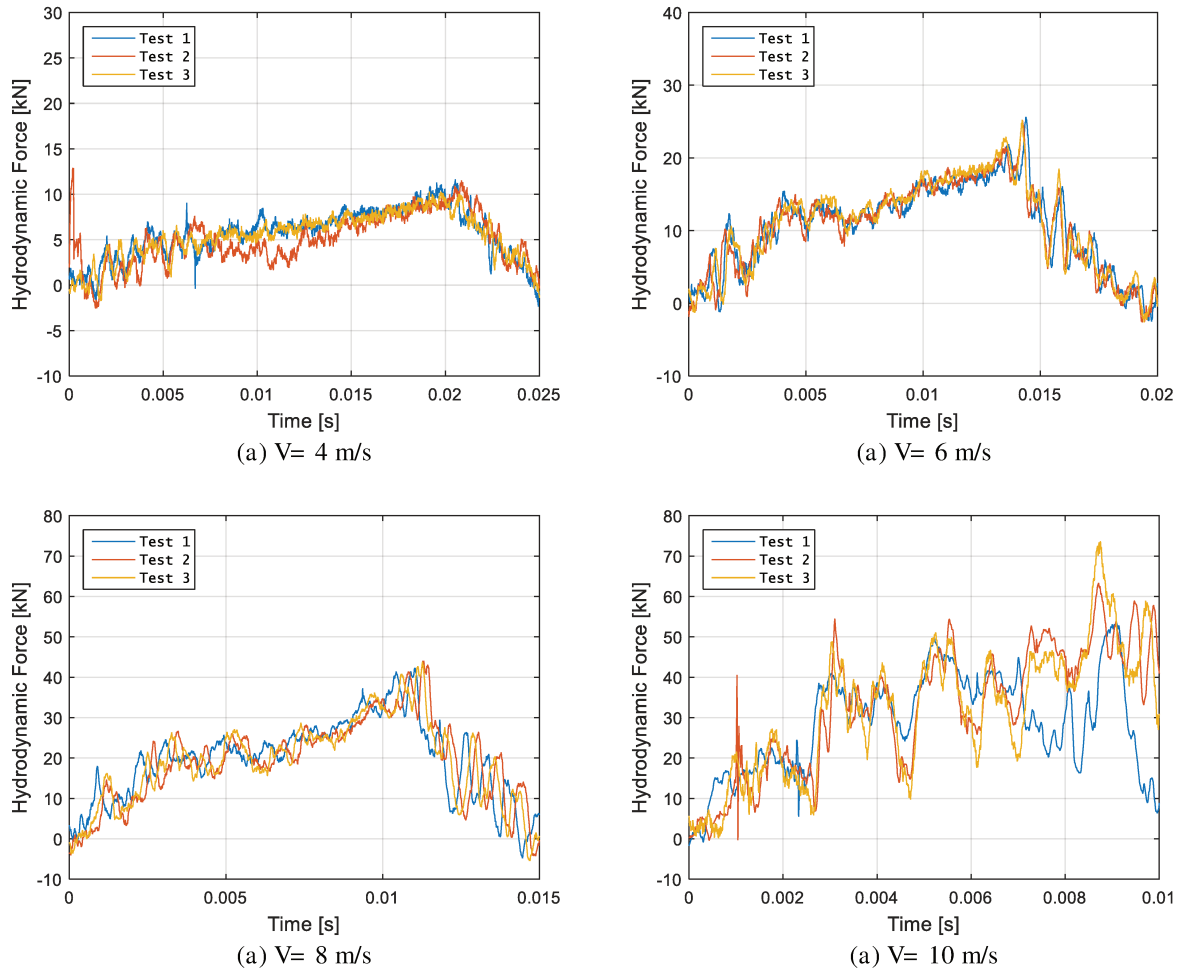


Figure 5. 24. The repeatability of the tests on PVC sandwich, $t=37\text{mm}$

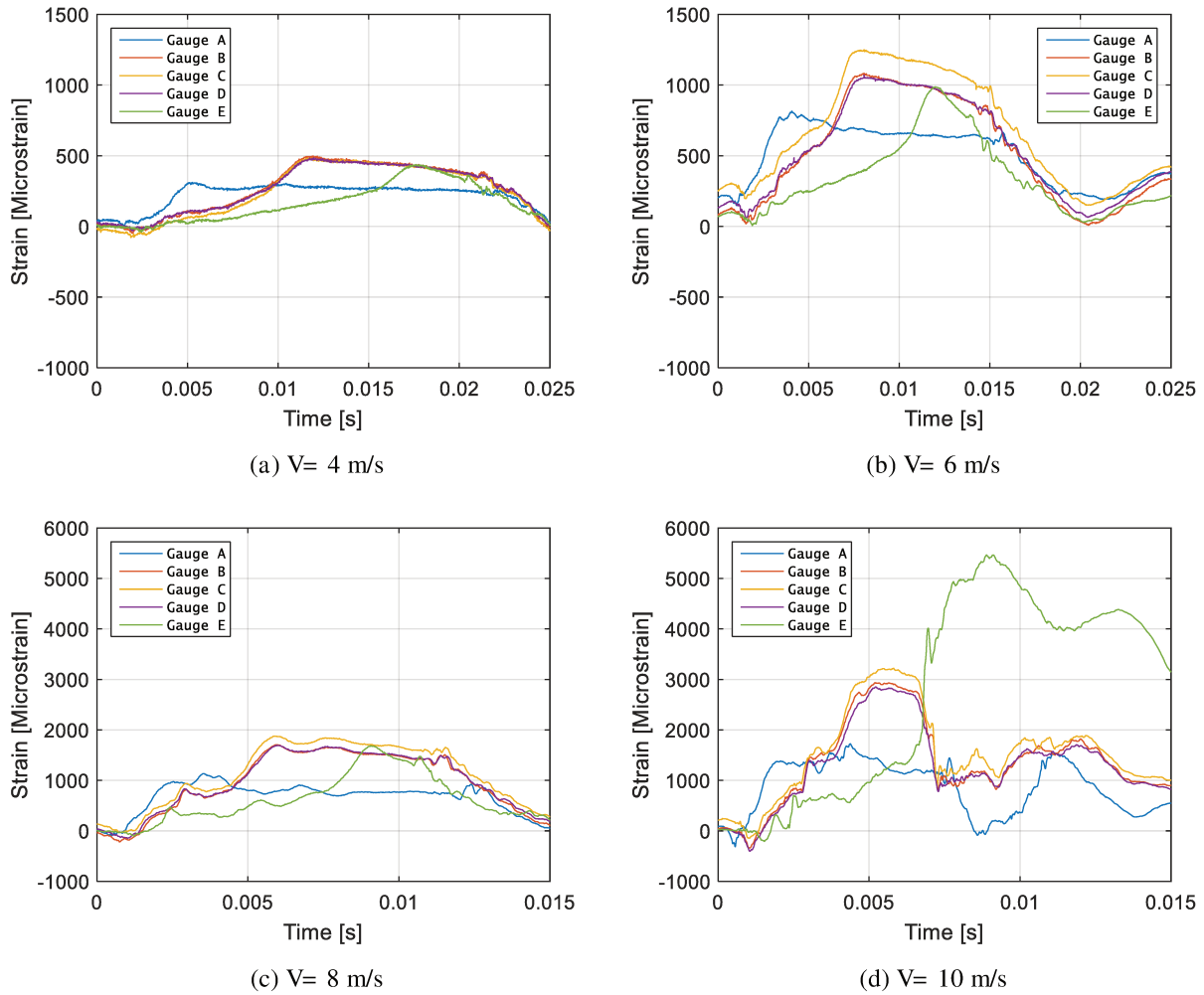


Figure 5. 25. Deformation in strain gauges of PVC sandwich, $t=37\text{mm}$

5.7.2 Damage assessment

Work on the damage modes of the sandwich panels is especially important for marine vessel design, especially on predicting the structure performance under slamming impacts. This enables the ship designers to estimate and optimise the design configurations in the critical regions. Core shear damage mode is considered a common damage for sandwich structures, which depends on the density of the core.

Figure 5. 26 shows snapshots during the slamming impact at the velocity of 10 m/s (from initial contact $t=0$). The damage development history of the sandwich panel and the water jet elevation can be observed. Generally, the damage firstly appears in the ends of the panel in the clamped zone, and progresses in the core that directly affects the stress state and leads to debonding of the skin/core interface [13].

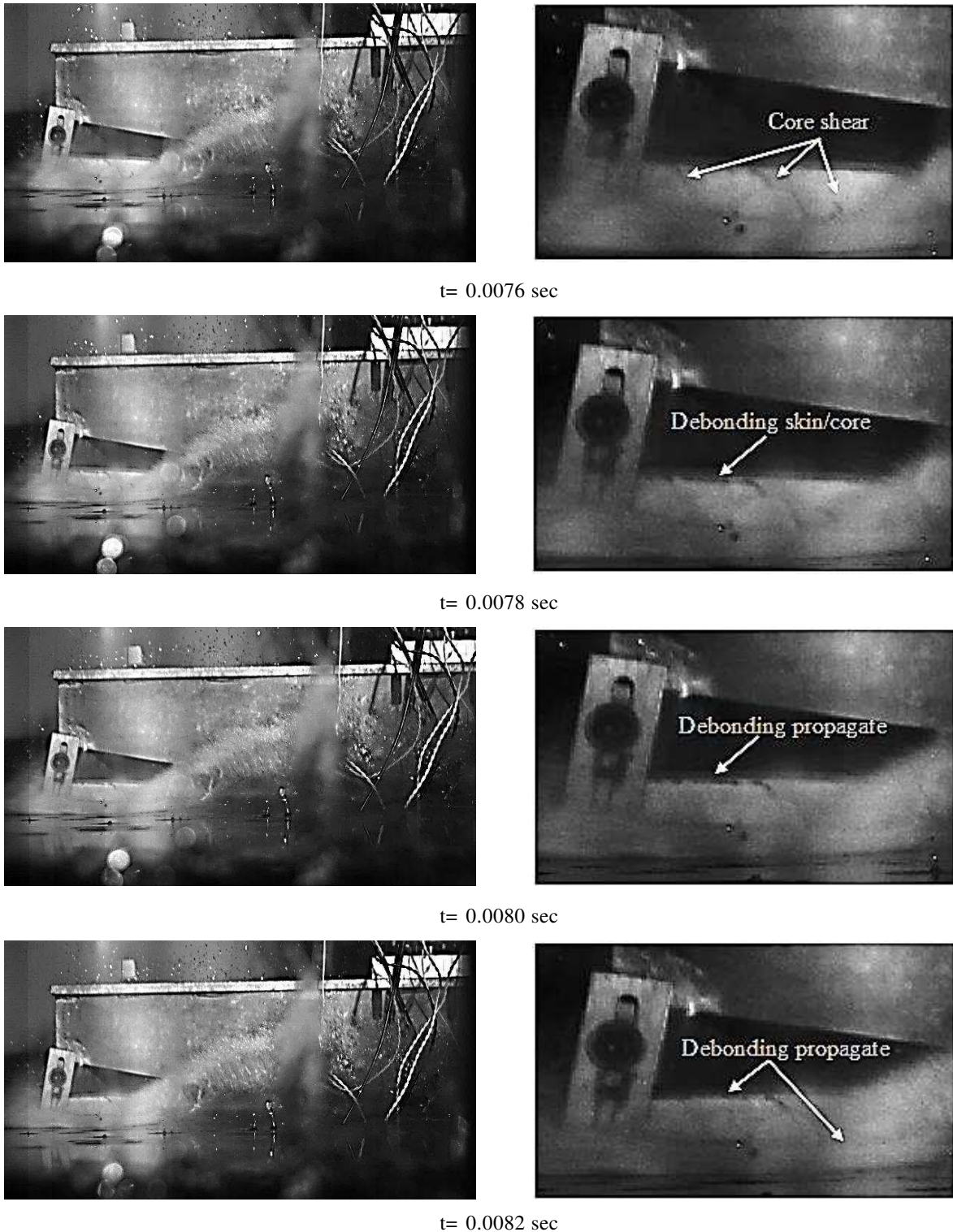


Figure 5. 26. Damage history in sandwich PVC t=27mm

In Figure 5. 27, we can see the different failure modes which have appeared in the sandwich panels with the different configurations represented by the separation of the interface between the core and the skin, micro-cracks and propagation of cracks in the core due to the shearing force. The initiation of cracks in the core seems to occur first. Consequently, this causes the skin/core debonding to initiate and propagate, as in reality

where the failure always occurs in the weakest regions. A large deformation of the structure exposed the core to a high bending tensile shear stress and compressive shear stress above and below the neutral plane. Thus, the crack cannot be easily propagated vertically through the thickness. For this reason, the crack propagates at an oblique angle due to a large difference between the skin and core shear stresses. On the other hand, the shear stress in the core is higher compare to normal stresses. Therefore, failure in the core due to shear stress occurs, as shown in Figure 5. 27 and Figure 5. 28.

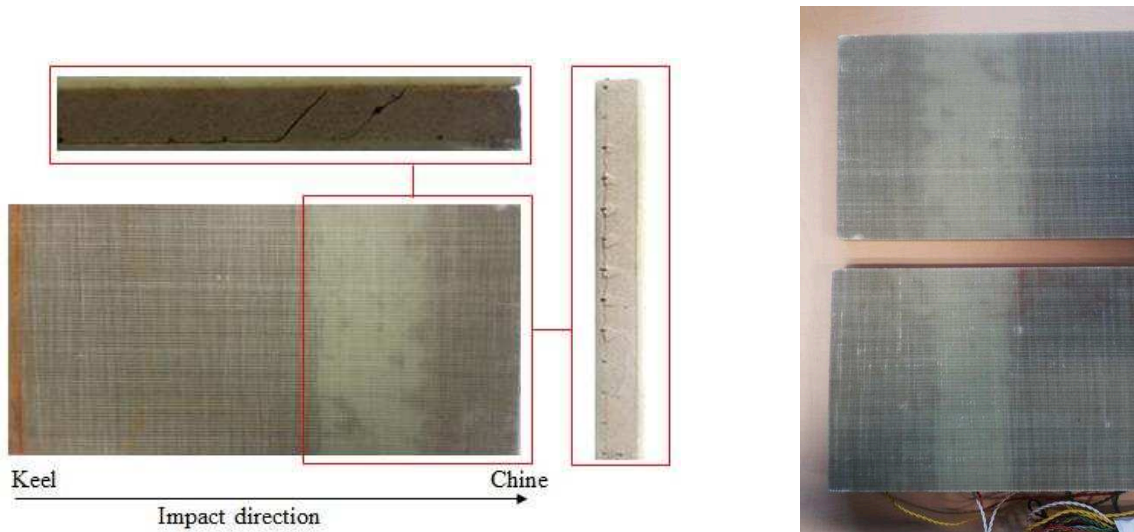


Figure 5. 27. Damage modes in sandwich panel

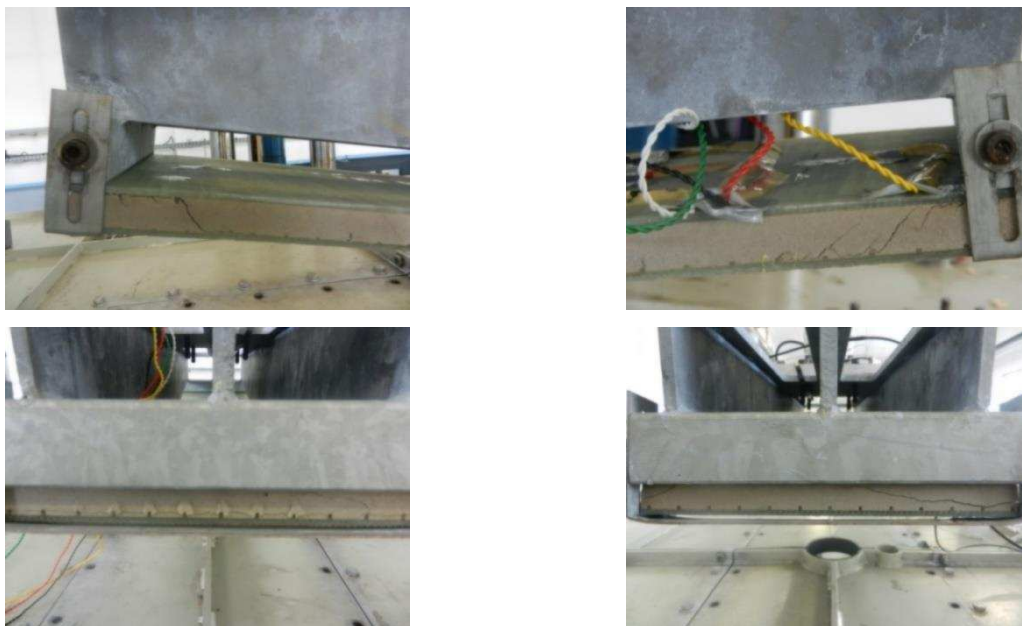


Figure 5. 28. Damage in PVC sandwich t=27 velocity= 10 m/s

5.8 General discussions

This section discusses the experimental tests, which provide clearer guidance in marine structural design by taking into account the change in hydrodynamic loads due to the interaction of different structural rigidities with water surface. In summary, the more flexible structures can take higher hydrodynamic loads which exceed the expected loads in the rigid body, Figure 5. 29 . This could be attributed to the interaction of the elastic structure with the fluid as illustrated in the previous sections. Table 5. 3 illustrates the experimental results of the panels with different stiffnesses and impact velocities.

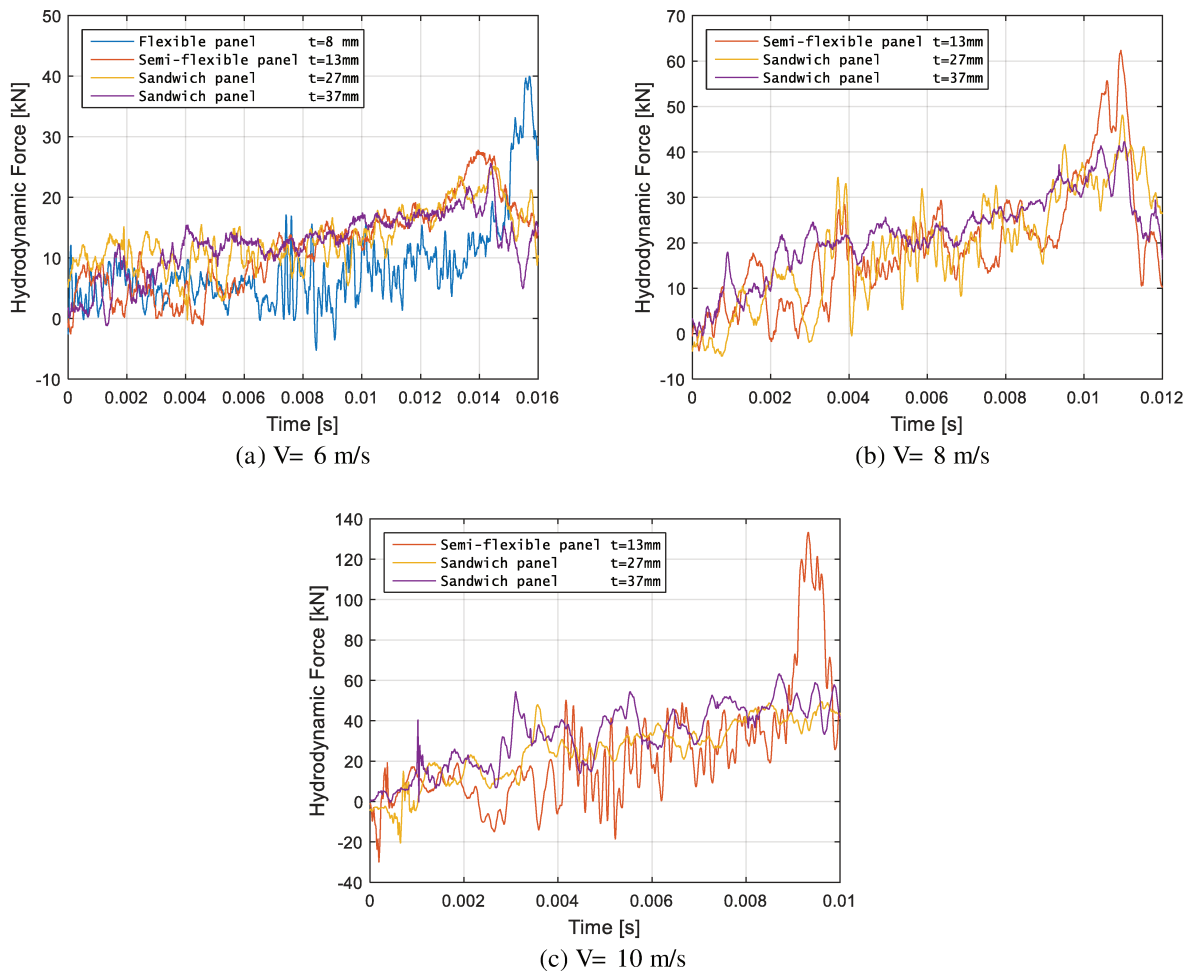


Figure 5. 29. Hydrodynamic loads for different structural stiffnesses

Impact velocity (m/s)	specimens	Composite		Sandwich	
		(FP) t=8mm	(SFP) t=13mm	Panel t=27 mm	panel t=37 mm
		Hydrodynamic force kN			
4	Test 1	16.75	-	11.08	11.65
	Test 2	17.95	-	11.50	11.17
	Test 3	19.15	-	11.20	10.30
	Mean	17.95	-	11.26	11.04
	Std.	1,2	-	0,21633308	0,68432448
6	Test 1	40.03	27.85	24.66	25.63
	Test 2	33.75	30.47	25.28	25.16
	Test 3	32.32	31.02	23.25	25.25
	Mean	35.36	29.78	24.39	25.34
	Std.	4,10	1,69	1,04	0,25
8	Test 1	-	61.77	47.77	42.27
	Test 2	-	68.84	48.14	44.08
	Test 3	-	64.26	51.04	43.77
	Mean	-	64.95	48.98	43.37
	Std.		3,59	1,79	0,97
10	Test 1	-	135.4	-	55.58
	Test 2	-	133.30	61.62	63.34
	Test 3	-	122.90	67.34	73.86
	Mean	-	130.53	64.48	64.26
	Std.	-	6,69	4,04	9,17

Table 5. 3. Hydrodynamic force for different panel stiffnesses and different velocities

To show how the hydroelastic effects depend on the impact velocity, bending stiffness, a nondimensional parameter has been used. Faltinsen introduced the nondimensional parameter as the ratio between the wetting time and the lowest natural frequency of the structure. He has considered that the hydroelastic effect had become significant for a wedge shaped cross section when [3]:

$$\frac{\tan\beta}{V\sqrt{\rho L^3/EI}} \leq 0.25 \tag{5.1}$$

Where EI is the bending stiffness of the structure (Chapter One), L is the length of the structure, ρ is the density of the material and β is the deadrise angle.

According to this parameter (according to obtained results), experimental tests for different rigidities of composite and sandwich panels corresponding to velocities over 4 m/s for flexible and semi-flexible composite panels, while this parameter has influence on sandwich panels over ≈ 6 m/s, as shown in Figure 5. 30.

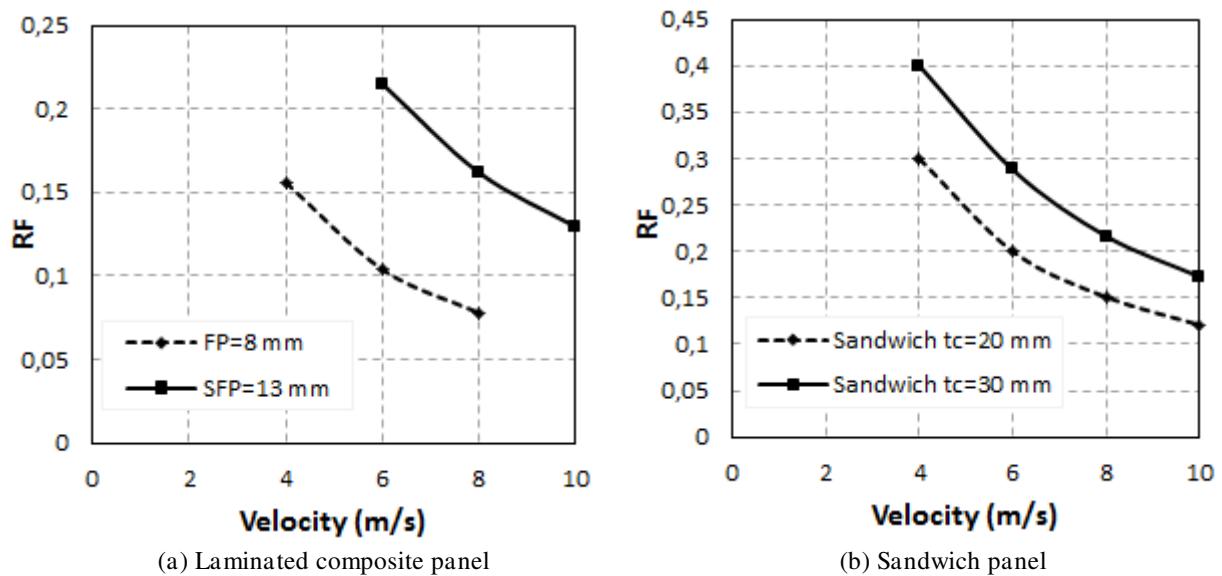


Figure 5. 30. Non-dimensional hydroelasticity relative to impact velocity and different rigidities

5.9 Conclusions

This chapter discussed the experimental results of the slamming impact for composite laminate and sandwich panels. Different velocities and panels rigidities were tested to identify the hydroelastic influence. The structural response including the hydrodynamic force and the panel deformation were analysed to identify the maximum structure resistance, according to increasing impact velocity. According to these tests, some important observations are summarised as follow:

1. The inertia effect was noted in the early stage of the impact event and its influence depends on the loading rate. Therefore, it appears more at a lower impact velocity, which has a longer wetting time than the first natural frequency of the dry structure.
2. Kinematic effects along the water-panel interface exerted a great hydroelastic influence due to structure flexibility and the change in local deadrise angle. Consequently, these effects can reduce or increase the slamming loads.
3. Kinematic effects notably appeared at higher impact velocity, especially in the centre and at the end edges of the panel.
4. The Flexible panel had a higher peak force and significant dynamic noise than the highest stiffness panels. This indicated that water-structure interaction has an influence on the hydrodynamic response.
5. Maximum force and deformation occur near the chine have sufficient capacity to cause damage in the structure and lead to catastrophic failure. Consequently, repetition of the slamming impact leads to a reduction in the material stiffness properties. For this reason, more attention must be paid to this location during the design phase, such as reinforcing the structure (for example, transverse stiffeners, heavy core density and high bending skin).
6. Additionally, this study gives quantitative data which provides clear guidance in design phase and lifetime performance, for marine structure designers.

References

- [1] R. Zhao, O.M. Faltinsen, “Water entry of two-dimensional bodies,” *Fluid Mech*, vol. 246, pp. 593-612, 1993.
- [2] O. M. Faltinsen, “Hydroelastic Salmming,” *journal of Marine Science and Technolgy*, vol. 5, pp. 49-65, 2000.
- [3] O.M. Faltinsen, “Slamming, Whipping, and Springing,” in *Hydrodynamics of High-Speed Marine Vehicles*, New york, USA, Cambrige University Press, 2005, pp. 302-311.
- [4] I. Stenius, “Finite Element Modelling of Hydroelasticity,” 2006.
- [5] A. El Malki Alaoui, A. Nême, A. Tassin, N. Jacques, “Experimental study of coefficients during vertical water entry of axisymmetric rigid shapes at constant speeds,” *Applied Ocean Research*, vol. 37, pp. 183-197, 2012.
- [6] A. El Malki Alaoui, A. Nême, Y.M. Scolan, “Experimental investigation of hydrodynamic loads and pressure distribution during a pyramid water entry,” *Journal of Fluids and Structures*, vol. 54, pp. 925-935, 2015.
- [7] R. Cointe, “Two-Dimensional Water-Solid Impact,” *Journal of Offshore Mechanics and Arctic Engineering*, vol. 111, pp. 109-114, 1989.
- [8] T. Allen, M. A. Battley, “Quantification of hydroelasticity in water impacts of flexible composite hull panels,” *Ocean Engineering*, vol. 100, pp. 117-125, 2015.
- [9] A. Bereznitski, “Slamming: the role of hydroelasticity,” *International Shipbuilding Progress*, vol. 48, no. 4, pp. 333-351, 2001.
- [10] DVN, “Hull Structure Design, Fiber Composite and Sandwich Constructions,” in *Rule for Classification of High speed, Light Craft and Naval Surface Craft, Part 3, Chapter 4*, 2011.
- [11] Owaisur Rahman Shah, M. Tarfaoui, “Effect of adhesive thickness on the Mode I and II strain energy release rates. Comparative study between different approaches for the

calculation of Mode I & II SERR's," Composites Part B: Engineering, vol. 96, pp. 354-363, 1 July 2016.

[12] I. M. Daniel, "Influence of core properties on the failure of composite sandwich beams," Journal of mechanics of materials and structures, vol. 4, no. 7-8, pp. 1271-1286, 2009.

[13] I. Stenius, A. Rsén, M.A. Battley, T. Allen, "Experimantal Hydroelastic Characterization of Slamming Loaded Marine Panels," Ocean Engineering, vol. 74, pp. 1-15, 2013.

CHAPTER 6

Numerical Validation with Experimental Results

Contents

6.1 Three dimensional numerical slamming model of deformable composite panels	178
6.1.1 Hydroelastic effects along the water-structure interaction	181
6.1.2 Hydroelastic effects and structural response	187
6.1.3 Hydroelastic influence	189
6.2 Composite panel	190
6.2.1 Force response	190
6.2.2 Deformation response	193
6.2.3 Damage assessment	195
6.3 Sandwich panel.....	200
6.3.1 Force response	200
6.3.2 Deformation response	201
6.3.3 Damage comparison of sandwich panels.....	203
6.4 Discussion, non-dimensional slamming force.....	206
6.5 Conclusions	209
References	211

In general, slamming experimental tests are expensive and time-consuming to be achieved. Therefore, this is not appropriate for ship construction when designing the hull section needs to solve complex shapes. Additionally, several of constraints have to be considered in the experimental tests such as the unavailability of some measurement instruments and low capabilities of their performance under dynamic loading. Therefore, many researches concentrated their work on analytical approaches and numerical methods. Numerical methods are mainly used for complex, physically or geometrically problems. In chapter two, it was found that the Coupled Eulerian-Lagrangian Model (CEL) was capable of simulating the water entry problem for both rigid and deformable structures. Subsequently, this chapter presents the validation of the numerical results compared with our previous experimental results (Chapter five) to confirm the validity of this model for estimating slamming loads. On the other hand, failure modes (Chapter 4) in composite laminate and sandwich panels were incorporated into this numerical model to predict and understood the damage mechanism of composite structures subjected to slamming impacts.

6.1 Three dimensional numerical slamming model of deformable composite panels

The numerical model was based on the Coupled Eulerian-Lagrangian Model (CEL), due to the symmetry of the slamming problem, the full 3D slamming model, Figure 6. 1a, was reduced to a 3D quarter model, Figure 6. 1b, this minimise the computational time. The length and width of the fluid domain are 3 m and 1 m, respectively, and the depth of the water is 0.86 m, while the depth of the air domain is 0.14 m. The support fixture was clearly observed in the void part. Only the translation movement of cylinder of the hydraulic machine along the Y-direction was considered, Figure 6. 1c. The exterior boundaries of the Eulerian fluid domain are defined as non-reflecting boundaries to avoid reflection pressure waves. Due to a high time consumption spent on calculation, the water domain is divided into many regions. Furthermore, it is meshed using the element type EC3D8R linear element Eulerian brick. A mesh density convergence study was conducted for both fluid domain and elastic wedge panel as we have discussed in Chapter two. The total mesh of the water model was composed of 1078000 cubic elements. It should be noted that the mesh had to be refined uniformly in all directions close to the impact location between the impactor and the fluid surface and its became coarser toward the extremes, Figure 6. 1b. The composite panel was meshed with 8-

node linear reduced integration solid elements (C3D8R), each lamina had a solid element in the through-thickness direction.

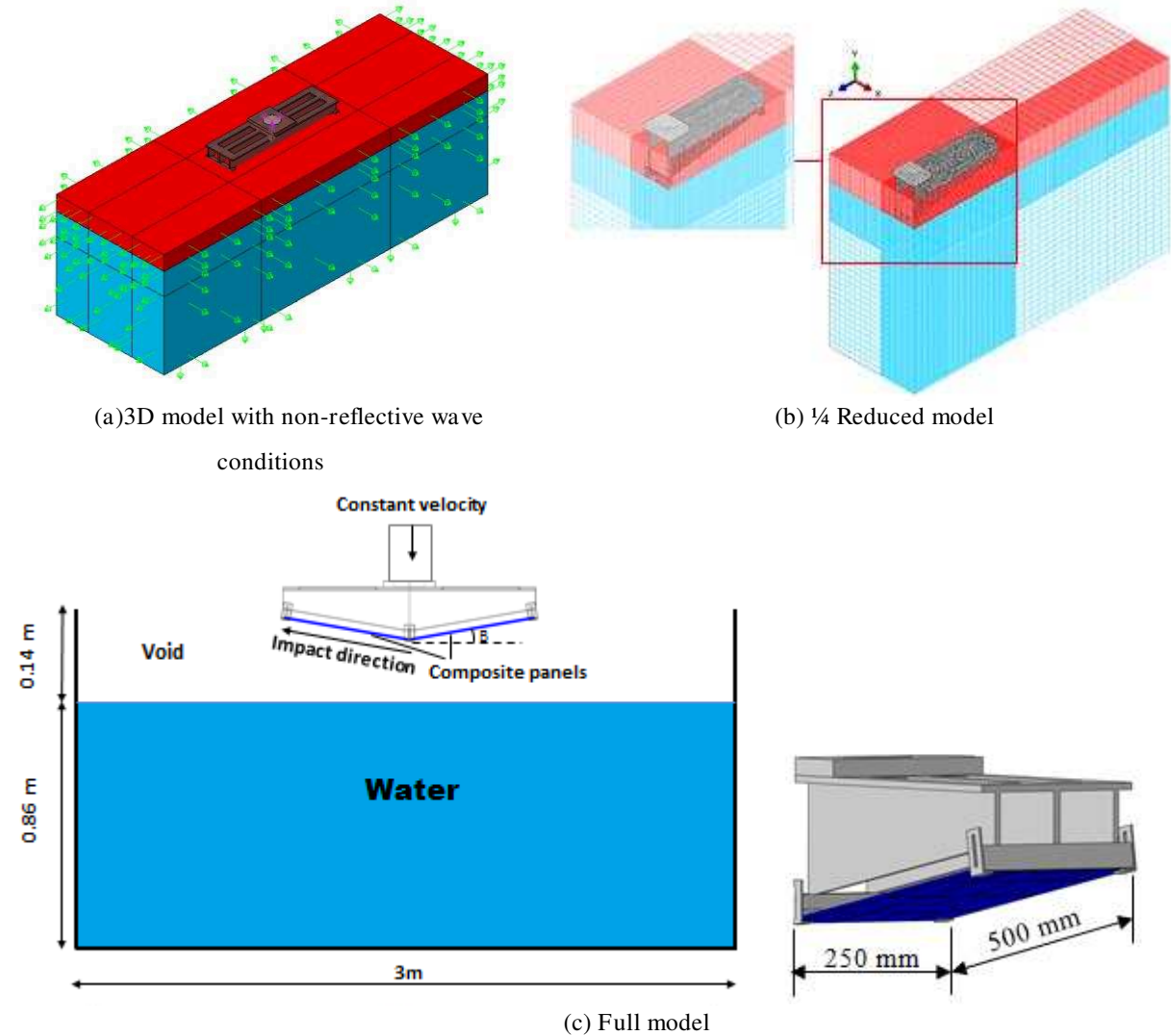


Figure 6. 1. Schematic representation of numerical slamming model

The numerical model was constructed as that performed in experimental test which previously identified in Chapter Five. Composite panels (500 mm × 250 mm) have fully clamped boundaries conditions as illustrated in Figure 6. 2. Glass/vinylester composite panels with different thicknesses were tested: semi-flexible (SF)-(t=13mm), flexible (F)-(t=8 mm) and the stacking sequence of [45/-45]₉ and [0/90]₆ respectively. In addition, sandwich panels with glass-fibre-vinylester laminate ($t_f = 7$ mm) and PVC cores ($t_c = 20$ and 30mm) were studied and analysed. Steel panels (t=13 mm) with high stiffness (Young’s modulus of E= 210 GPa and Poisson’s ratio of $\nu = 0.3$) were considered as a rigid wedge. Faltinsen observed that hydroelasticity effects greatly appears in impacted wedges with deadrise angles of 5° to

20°, while the 30° behaves as if rigid [1]. Therefore, in this study, all of the panels examined had a deadrise angle of 10°. The strain gauges (SG) and the pressure sensors were located in three different positions along the span of the panel to cover mode shapes natural frequency. The details of the panel’s mechanical properties are given in Table 6. 1 and Table 6. 2.

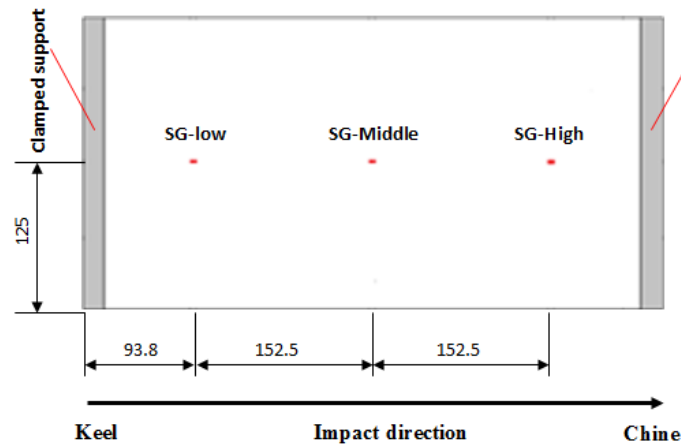


Figure 6. 2. Model configuration: model boundary conditions, panel dimensions and strain gauge location

	Density (kg/m ³)	t (mm)	Elastic moduli (GPa)			Poisson’s ratios (-)			Shear moduli		
			E ₁₁	E ₂₂	E ₃₃	ν ₁₂	ν ₁₃	ν ₂₃	G ₁₂	G ₁₃	G ₂₃
Skin	1960	7	48.16	11.21	11.21	0.274	0.274	0.096	4.42	4.42	9
Core	80	20	0.077	0.077	0.110	0.3					

Table 6. 1. PVC sandwich and composite panel properties considered [2, 3]

Initial elastic stiffness (N/mm ²)			Strength (MPa)			Energy (N/mm)		
K _n	K _t	K _s	t _n	t _s	t _t	G _{IC}	G _{IIc}	G _{IIIc}
2E+06	2E+06	2E+06	2.5	5	5	0.484	0.296	0.296

Table 6. 2. Cohesive properties of the skin/core interface sandwich [4]

As shown in Figure 6. 3, we have determined analytically the max deflection relative to the impact velocity, equation (2.25 in Chapter two) and uniform average pressure calculated using by Wagner’s theory [5].

$$P_{wagner,ave} = \frac{\rho \pi^2 v^2}{4 \sin\beta \cos\beta} \tag{6. 1}$$

Therefore, according to DNV [6] the structural requirements for max deflection were required not exceed 2% of the span length. Consequently, the maximum velocity applied to each panel could be approximately predicted analytically.

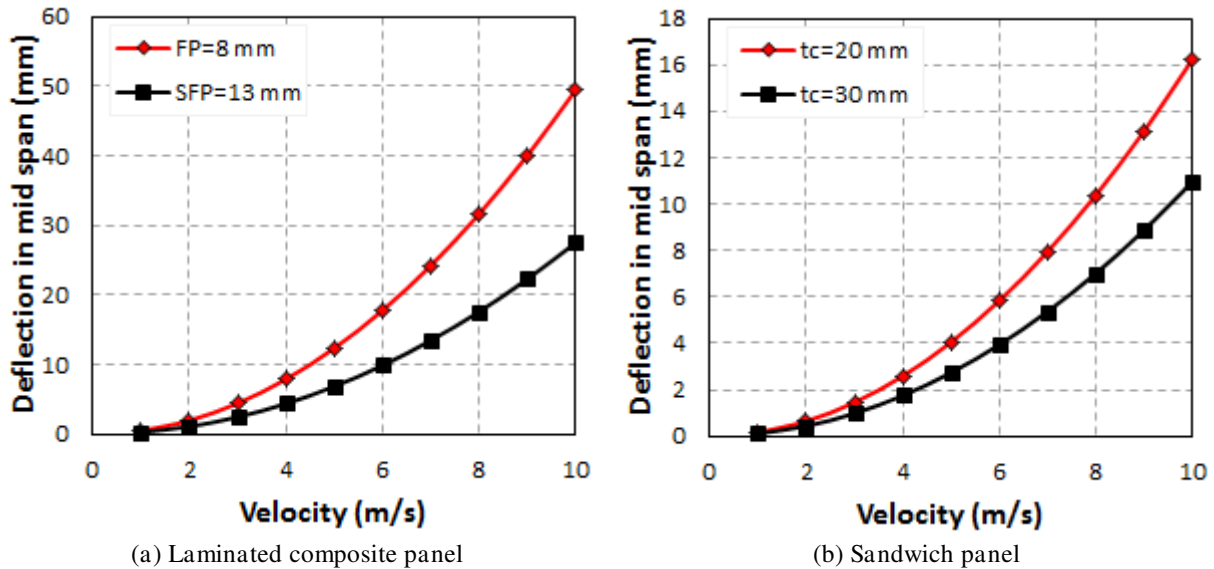


Figure 6. 3. Analytical Quasi-Static maximum deflection (B-CC) vs. impact velocity, $\beta=10^\circ$

6.1.1 Hydroelastic effects along the water-structure interaction

The structures used in the ship building sector have different forms, different materials and different stiffnesses. As regards the stiffness of the structures, one finds those have greatest stiffness are generally assimilated to rigid bodies, while the structures which have more flexibility are categorized into two cases as semi-flexible and flexible structures. The slamming phenomena of rigid bodies have been widely investigated. On the other hand, relatively few efforts have been dedicated to the other two classes. Firstly, we investigated the effects of structural flexibility. Therefore, composite panels were tested: semi-flexible (SF) and flexible (F) cases as mentioned in previous section and previous chapter. The hydro-elastic response was affected by the flexibility of the panels, in that the boundary conditions of the water structure interface changed due to the variation in the local deadrise angle, Figure 6. 4. In the case of flexible panels, Figure 6. 5 shows more flexibility of the panel leading to an increase in the panel deflection and local deadrise angle. This can explain the reason behind high pressure near the chine due to the change in kinematic influence and loading of the fluid particles close to the interface.

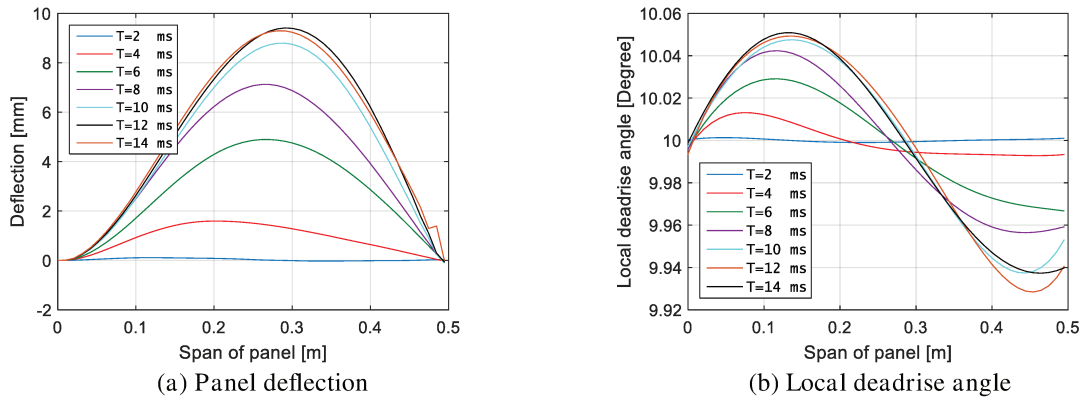


Figure 6. 4. Histories of kinematic effect of semi-flexible panel, $V= 6$ m/s

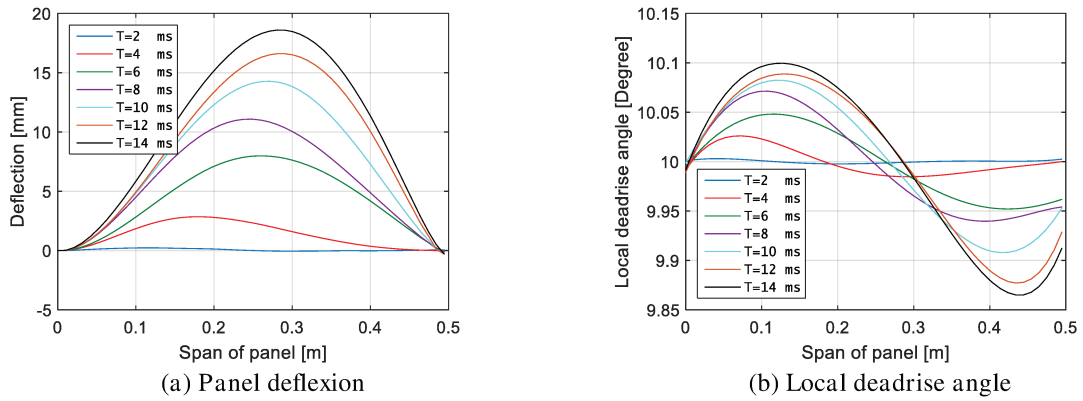


Figure 6. 5. Histories of kinematic effect of flexible panel, $V= 6$ m/s

The hydroelastic effect increases relative to the impact velocity that leads to a variation in water pressure and the local deadrise angle. This gives a clear perception of increasing of the deflection and longitudinal strains in the centre of the panel. The longitudinal strain indicates that the panel sustained different vibrational modes, consequently high local water pressure can be occur. In the initial impact, the inertia effect of panel dominates the structural response that can caused high pressure. For this reason, negative values of the strain have seen in the first wedge impact on the free surface. Increase of wetted area, the deflection dominates the hydroelastic influence leading to positive values of strain at the centre and the edges of the panel, Figure 6. 6 and Figure 6. 7.

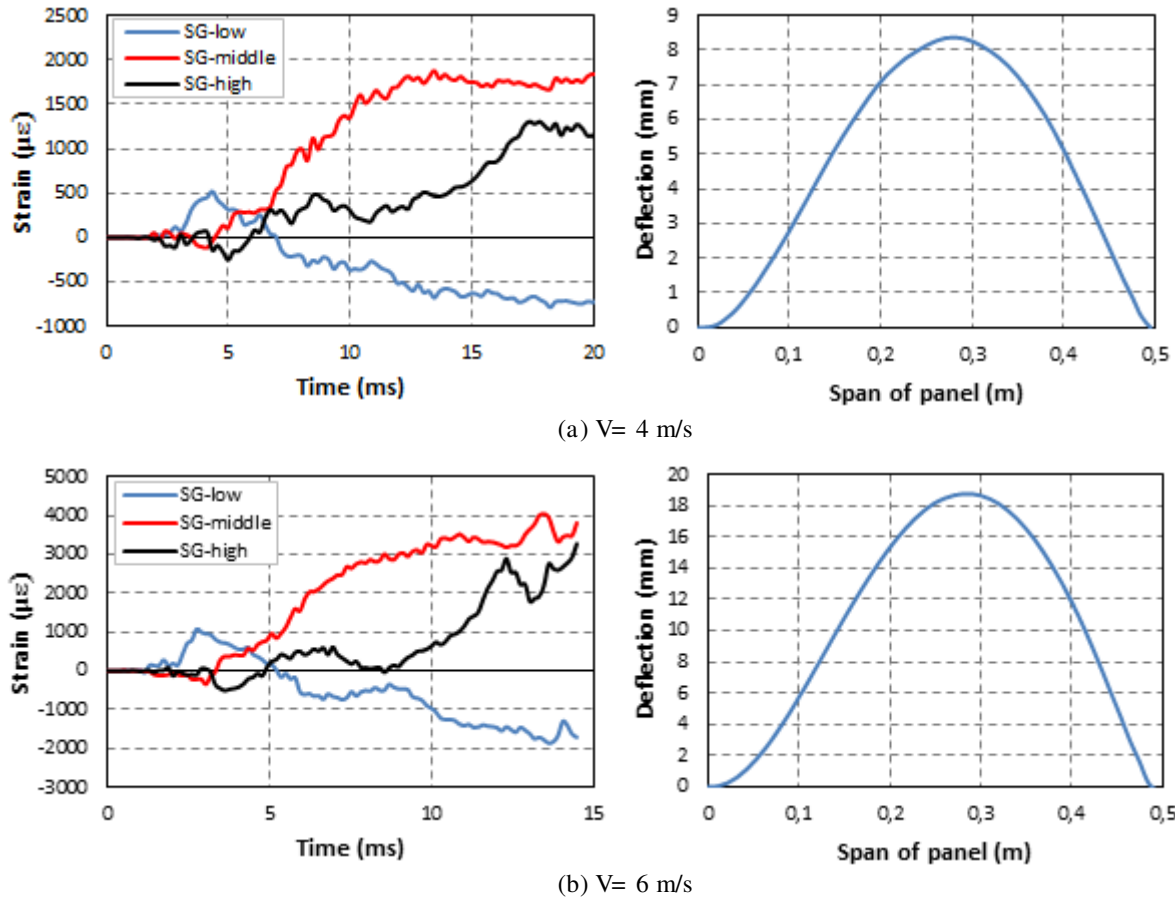
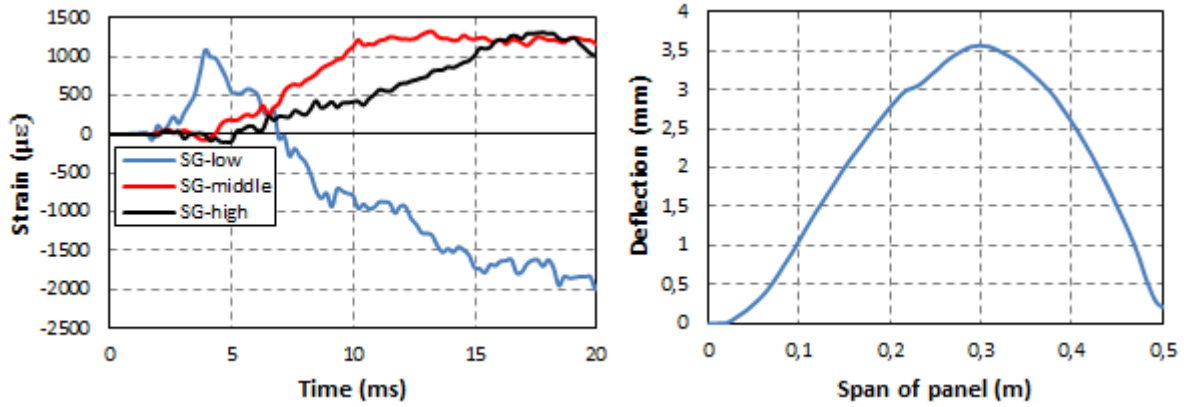
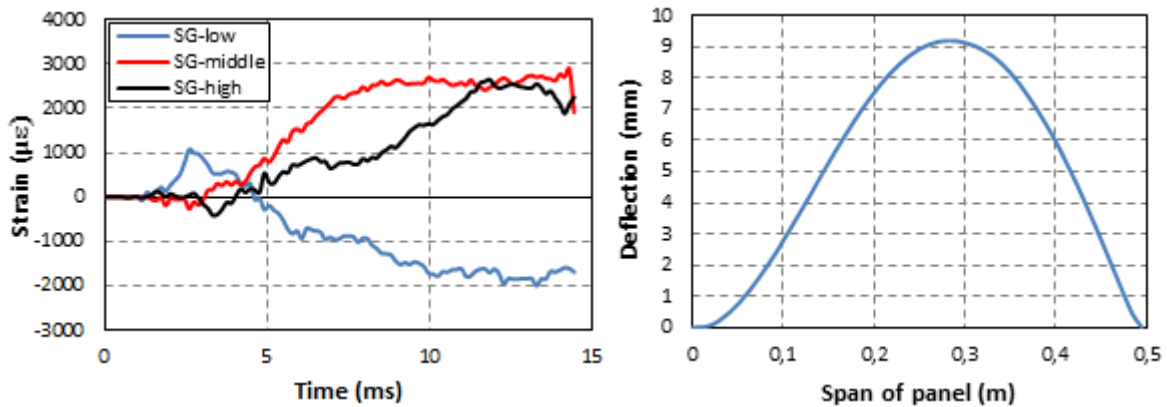


Figure 6. 6. Strain at different positions along span of the panel and max deflection for flexible composite material

In order to understand the effect of vibration mode, we consider the time history of max pressure for semi-flexible and flexible panels. Pressure-time histories along the panel-water interaction of semi-flexible panel at different velocities were compared to those of the rigid body. The results of semi-flexible composite panels were reported in Figure 6. 8 and Figure 6. 9 for 4 m/s and 6 m/s, respectively. From these figures, it appears that the inertia effect obvious in all pressure time histories corresponds to that of the rigid body. Pressure amplitude close to the keel has a lower value than the rigid pressure, and continues to decrease especially in maximum panel deflection. This reduction was attributed to the change of kinematic conditions along the fluid-structure interface, increase of the local deadrise angle and decrease of the local impact velocity. In the position close to the chine, a high peak pressure is observed which occurred due to great variation in the kinematic effects.



(a) $V= 4 \text{ m/s}$



(b) $V= 6 \text{ m/s}$

Figure 6. 7. Strain at different positions along span panel and max deflection for semi-flexible composite material

On the other hand, the hydroelastic inertia effects appear more in a more flexible panel and increase relative to a decrease in rigidity of the panel. Therefore, a more flexible panel with lower bending stiffness suffers great hydrodynamic loads. However, the pressure close to the chine edge has high amplitude and exceeds the pressure in the rigid body, which implies that the high hydroelastic influence has been occurred. Figure 6. 10 illustrates snapshots of the max pressure (at pressure-high) for the flexible composite panel and rigid body close to the chine edge. Note that the water flow for the flexible panel reaches panel edge slower than in the rigid body case due to the flexibility of the panel.

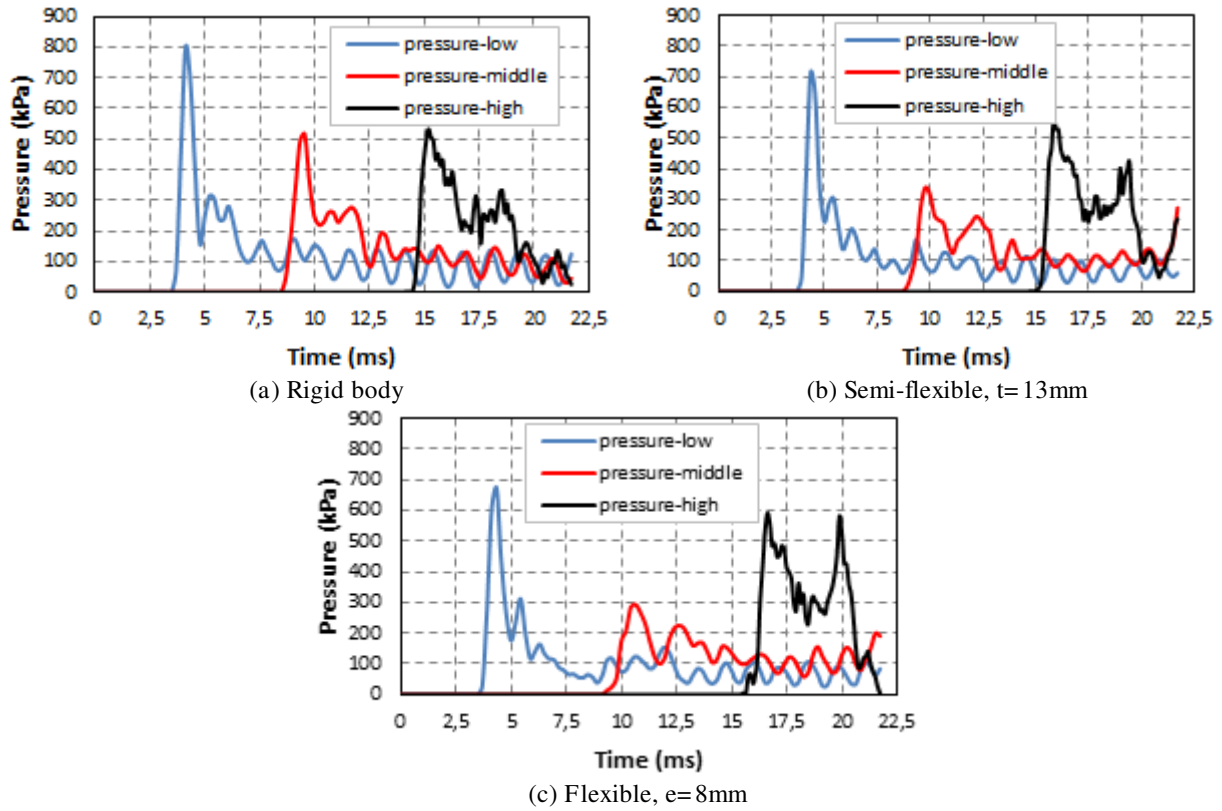


Figure 6. 8. Pressure time histories, $V=4$ m/s

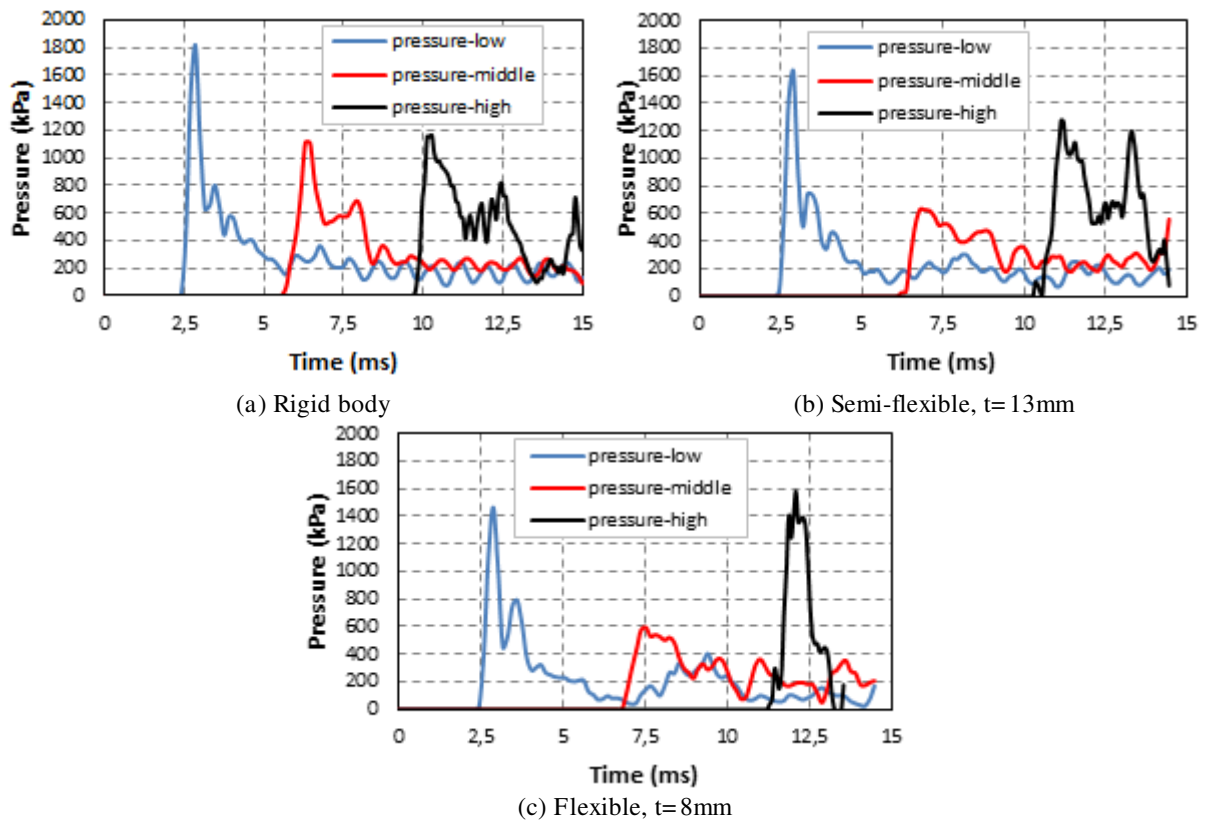
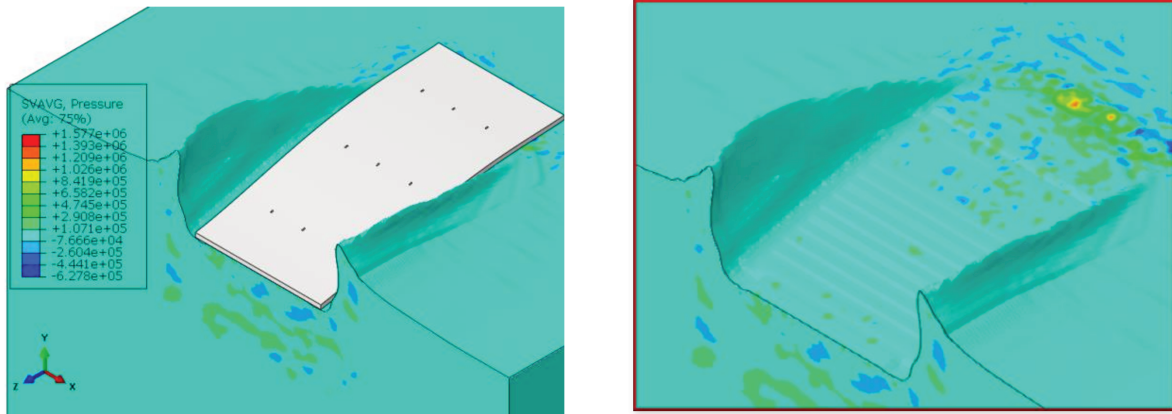
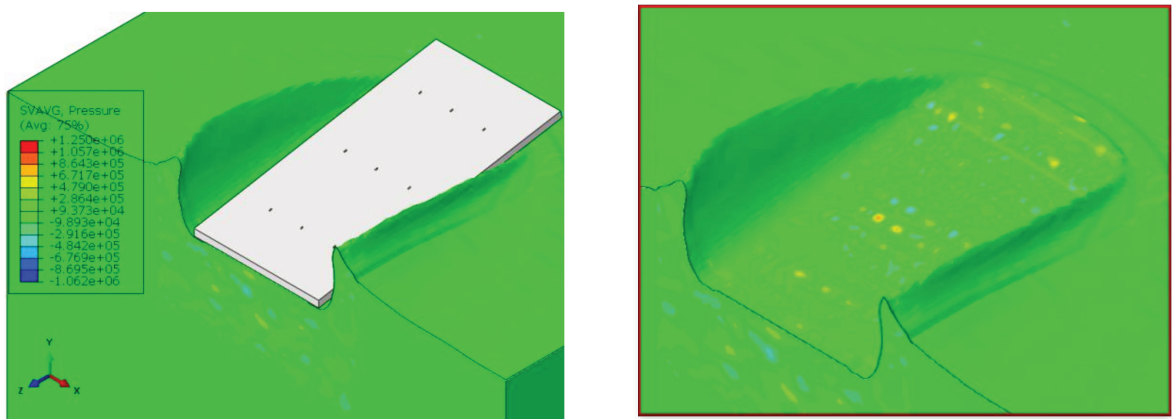


Figure 6. 9. Pressure time histories, $V=6$ m/s



(b) Flexible composite, t= 12 ms



(c) Rigid body, t= 10.2 ms

Figure 6. 10. Pressure distribution during a virtual slamming test, V= 6 m/s

Maximum pressures close to the chine in both flexible and semi-flexible composite panels were compared with the theoretical approaches of [5, 7] and experimental results of [8] to identify the hydroelastic effects relative to the impact velocity. Mathematical expressions of analytical approaches were given by Equations (6.2) and (6.3). A comparison of the different approaches is presented in Figure 6. 11.

- Analytical formula of maximum pressure proposed by Von Karman [7]

$$P_{max} = 0.5\rho V^2 \pi \cot \beta \tag{6.2}$$

- Analytical formula of maximum pressure proposed by Wagner [5]

$$P_{max} = 0.5\rho V^2 \frac{\pi^2}{\tan \beta^2} \tag{6.3}$$

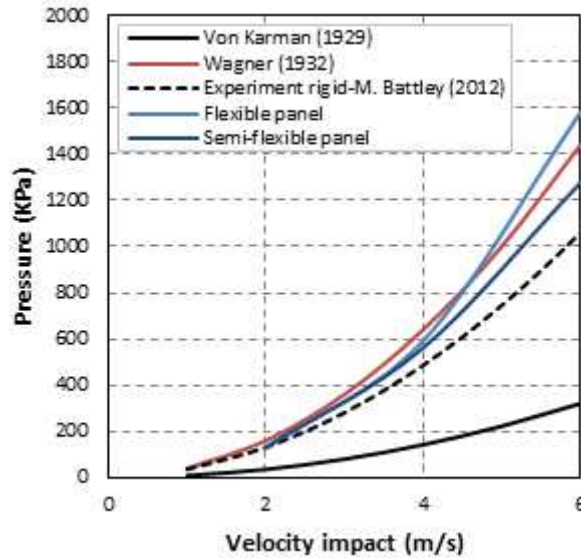


Figure 6. 11. Maximum pressure close to the chine compared to theoretical approaches

6.1.2 Hydroelastic effects and structural response

The structural response was analysed with regard to stresses and force acting on the panel. A high pressure at the end of the panel edge has regarded as a significant source of local damage in composite panels due to normal and transverse shear stress. Hence, it was generally considered to be a critical region in the marine structural design. Stress concentration in local positions can cause different failure modes in composite materials [9]. Figure 6. 12 illustrates stress concentration induced by the slamming impact on our composite panels. Therefore, repetition of the slamming impact leads to a reduction of the material's stiffness properties. Damage is mainly due to the transmission of cracks perpendicular to the fibres, since micro-cracks grow rapidly under thickness loading conditions. These cracks produce debonding between the fibres and matrix or rupture the fibre. It seems that the damage can propagate rapidly in flexible panels confronted with the semi-flexible case. This can be linked to the flexible nature of panels which encourages crack propagation. In order to predict damage initiation precisely in composite panels, Hashin's damage criteria should be applied as failure criteria. This was examined in Chapter four.

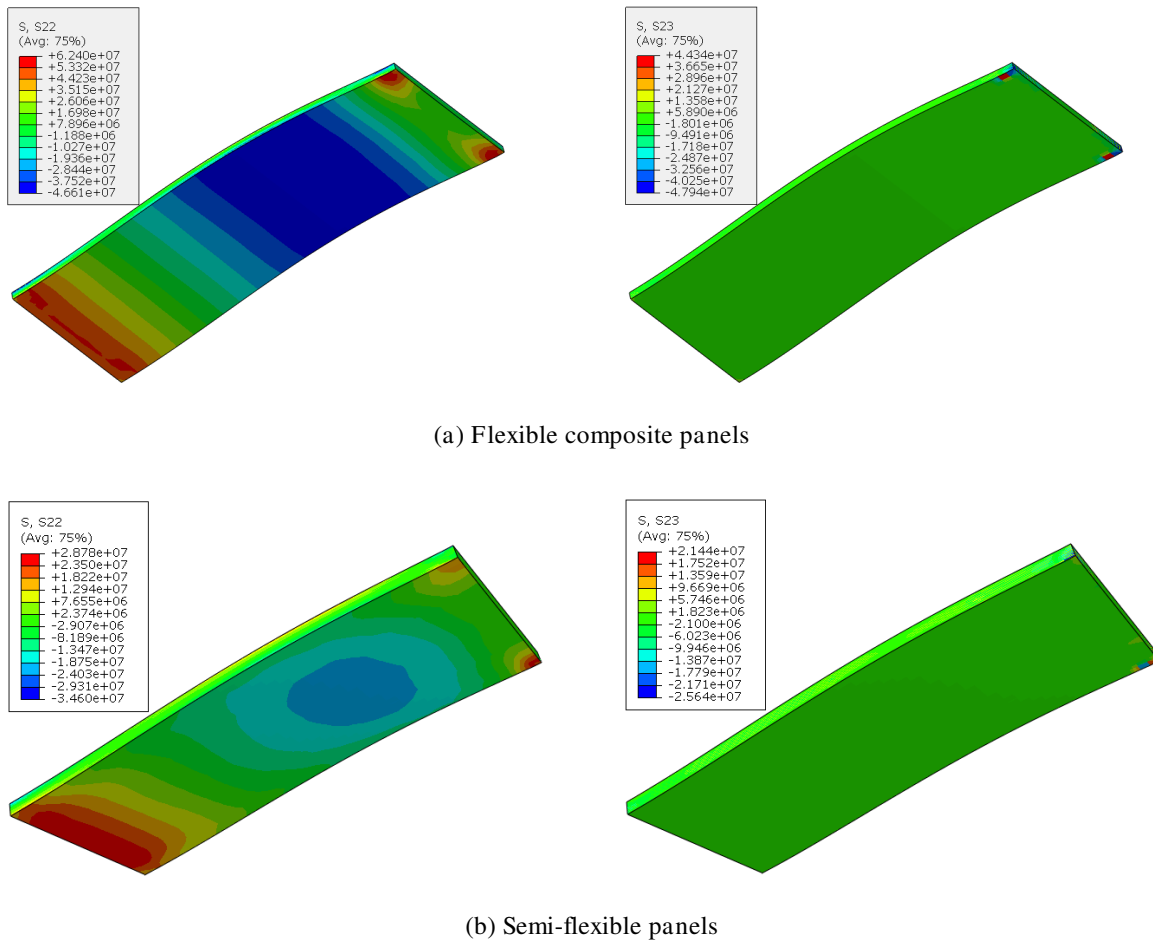


Figure 6. 12. Stress concentration close to the chine edge, t=12 ms

As for the total hydrodynamic forces that obtained during the impact duration, more flexible panels have a great peak value of the force comparing with high stiffness panels, T. Allen and M. Battley [10] have been recently investigated this situation experimentally. It can be seen that in the early impact stage, the time-force histories in different panels have the same profile, they consequently behave like a rigid body. In contrast, more divergence in their forms and amplitudes relative to the development of panel deflection toward the chine can be observed, as shown in Figure 6. 13. In brief, this situation of the force peak can be interpreted as occurrence of greater presence of hydroelastic influence in low stiffness panels.

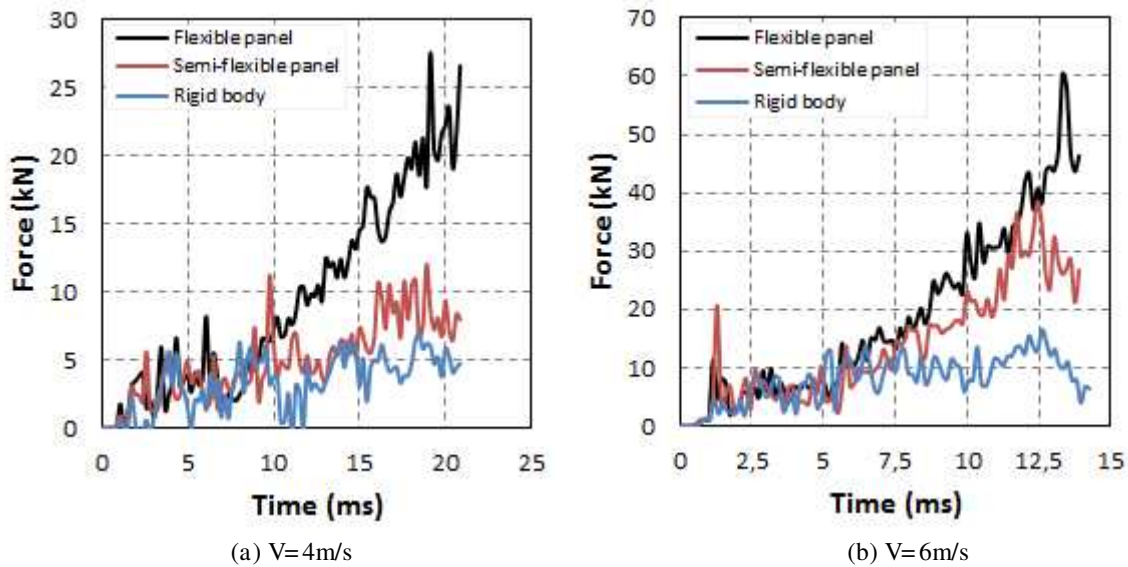


Figure 6. 13. Slamming force of wedge

6.1.3 Hydroelastic influence

In order to show how the hydroelastic influence depends on the impact velocity, the nondimensional parameter was used to frame the impact velocities caused by hydroelastic effects (Eq (1. 44), Chapter one). This nondimensional parameter is dependent upon the change in the velocity and the relative deadrise angle. On the other hand, Det Norske Veritas (DNV) classification societies [6] for structural requirements of naval vessels were considered. This standard requires the allowable deflection of the panel does not exceed 2% of the shortest panel span and for the strain: $\epsilon_{\text{allowable}} = 0.3 \epsilon_{\text{ultimate}}$. Figure 6. 14 shows the variation in the deflection vs impact velocity for flexible and semi-flexible composite panels, respectively. In this figure, we can conclude that the impact velocity is in accordance with hydroelastic criteria and the DNV classification. In the present study, two velocities were applied, namely 4 m/s and 6 m/s.

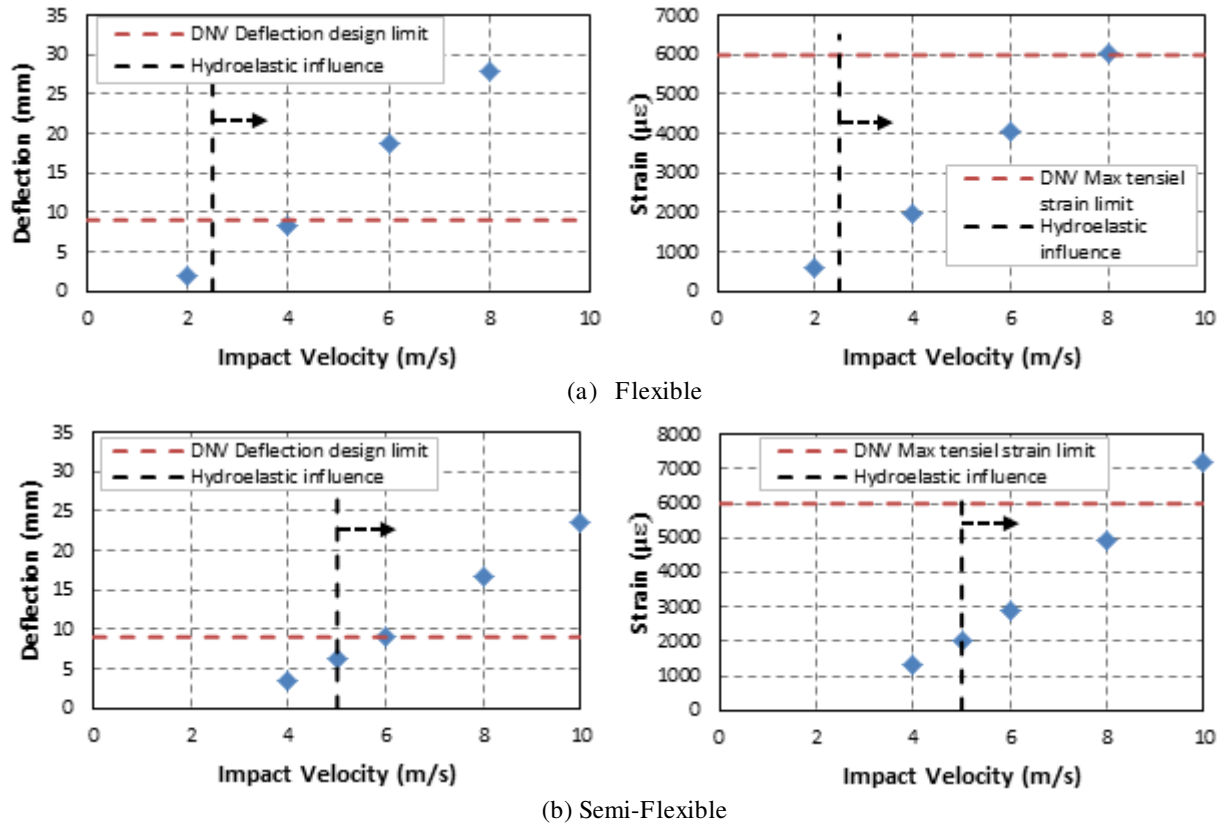


Figure 6. 14. Deflection design limit and strain versus impact velocity for composite material

6.2 Composite panel

6.2.1 Force response

Varying panel rigidity demonstrates the effect of hydroelasticity on the hydrodynamic force. Figure 6. 15 and Figure 6. 16 exemplify experimental data and the corresponding numerical results for composite panels with different stiffnesses. The results have presented for different impact velocities with a 10° deadrise angle. In general analysis, it can be observed that the maximum peak force in more flexible panels has higher values and the dynamic noise increase as the impact velocity increases. The results well agree with those observed in other studies [10]. The numerical results show good agreement in estimating the maximum force and its shape, in spite of slight differences compared to the experiment results. This can be attributed to the instability of the experimental velocity during the impact duration of interest that is considered to be approximately constant velocity, Figure 6. 17. The profile of the velocity shows a small difference in the impact velocity. In contrast, the numerical model assigned initially retains a constant velocity.

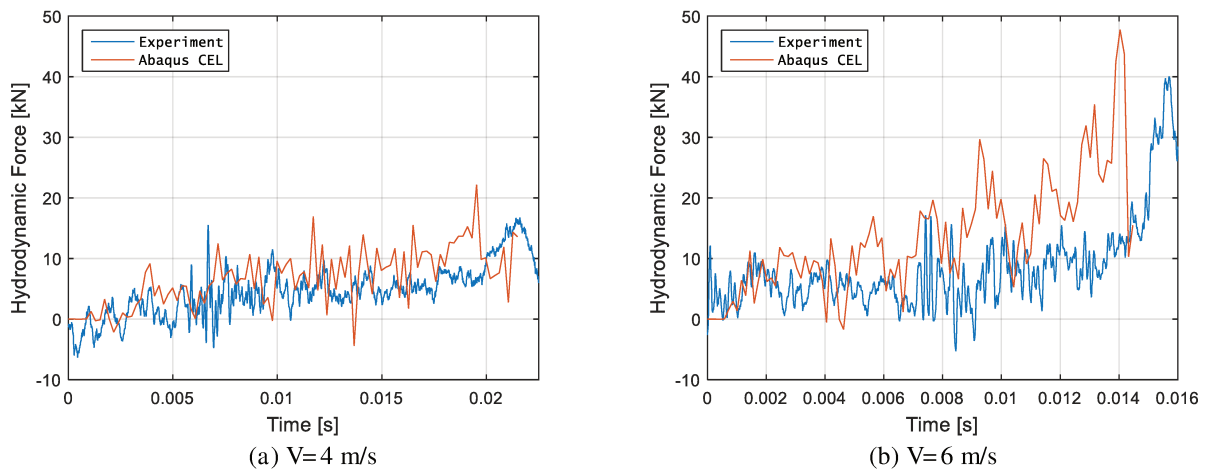


Figure 6. 15. Comparison of hydrodynamic force between numerical and experimental results (FP)

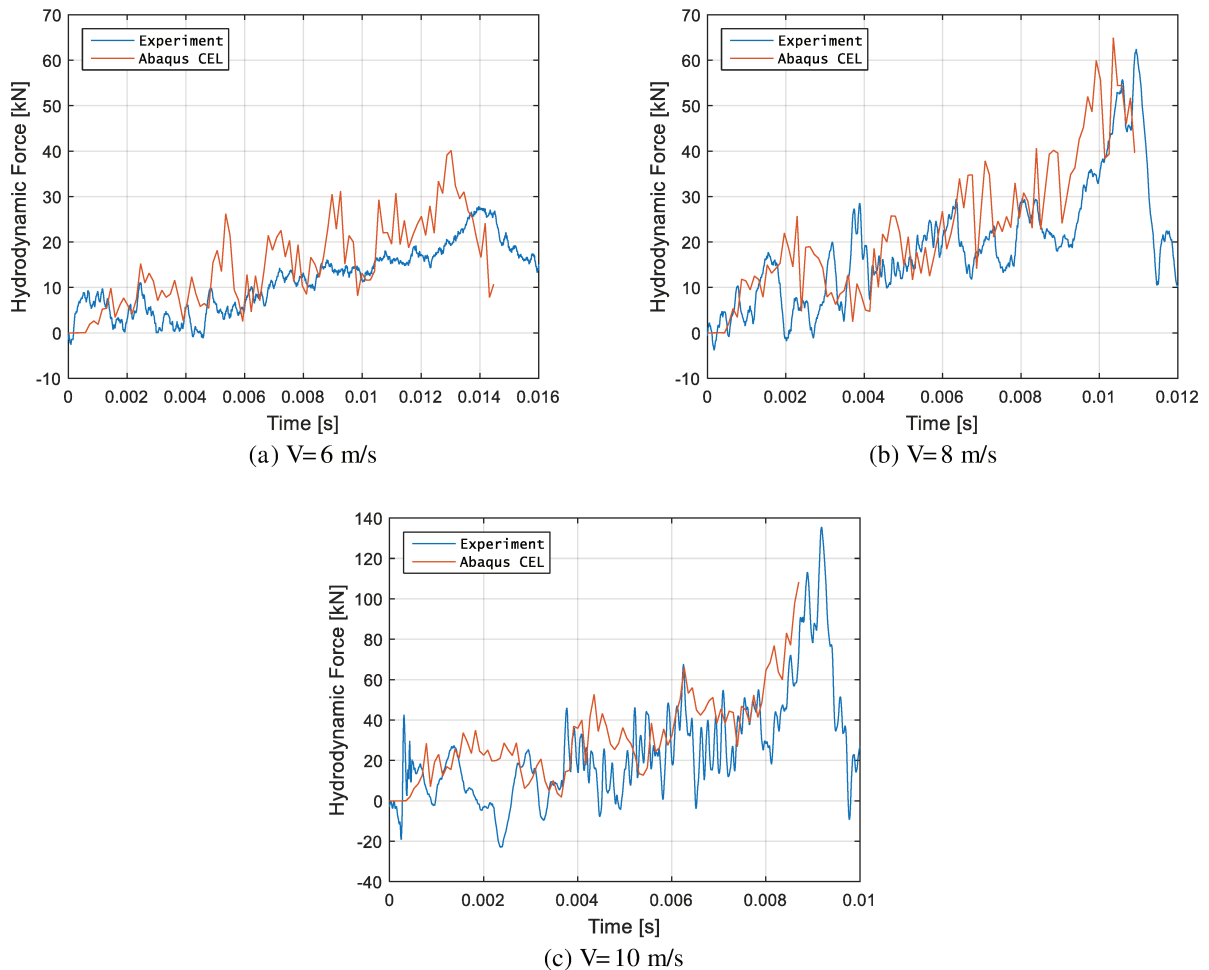


Figure 6. 16. Comparison of hydrodynamic force between numerical and experimental results (SFP)

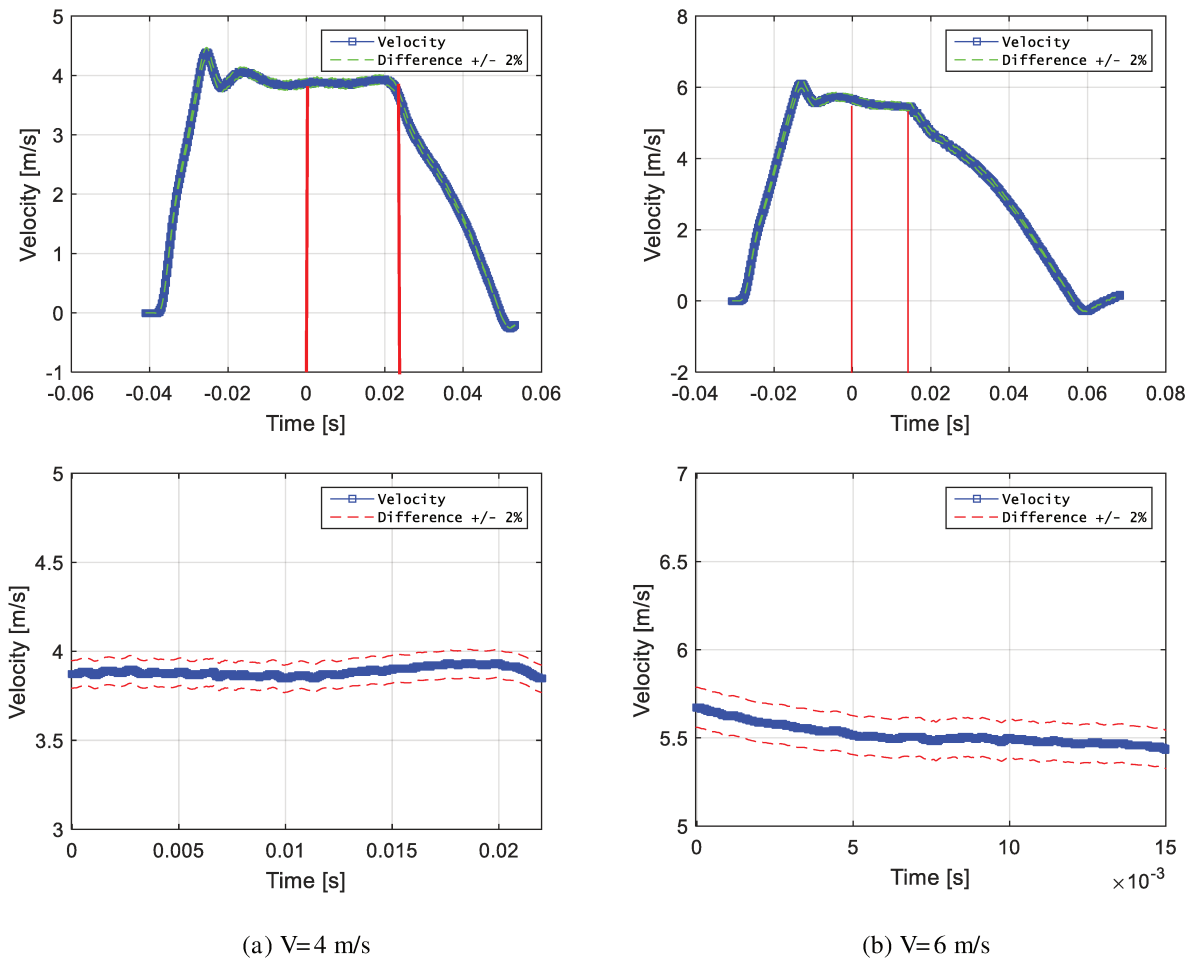


Figure 6. 17. Experimental impact velocities

Figure 6. 18 shows the comparison of time histories for the water jet elevation and the deformation of the flexible wedge ($V=4$ m/s) for both the numerical model and the experimental test. Good agreement can be observed in predicting the water jet flow compared with experimental data for different time histories. In the initial time of the impact, the panel inertia caused the panel to deform (≈ 5 ms). The maximum deformation (≈ 14 ms) occurred approximately in the centre of the panel and then the panel began to bend in the opposite direction leading to an increase in the local impact velocity and decrease in the local deadrise angle. Therefore, the maximum force at (≈ 21 ms) occurs when the wedge was completely submerged in water and before the water separation occurred.

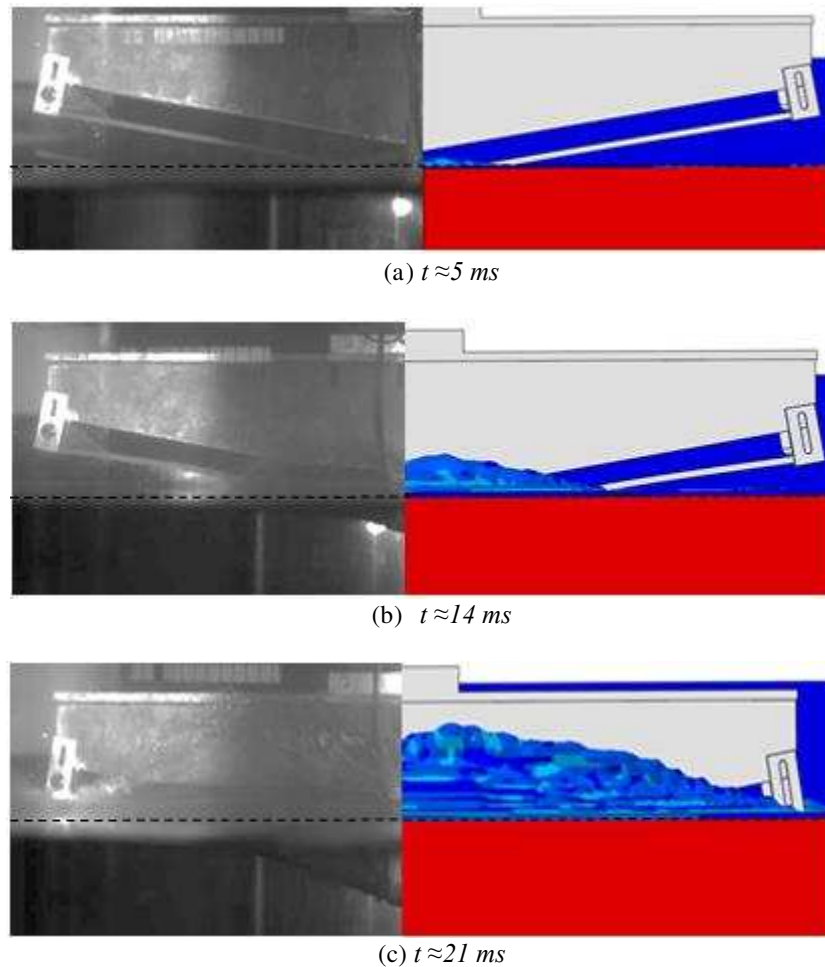


Figure 6. 18. Time histories of water jet elevation in the flexible panel, $V=4\text{m/s}$

6.2.2 Deformation response

The measured longitudinal strain in composite panels at in gauges C and E was predicted (as a maximum deformation) for the different velocities which is shown in Figure 6. 19 and Figure 6. 20. The numerical deformations and experiment data were generally in good agreement. On the other hand, negative values in experimental test at the initial contact can be observed, which implies a vibration mode appeared in the panel during the acceleration phase due to the inertial effect of the panel weight, as shown in Figure 6. 21. The structural flexibility of the panel was very influential on this situation. The correlation between the experimental and numerical results could also be bettered acceptable by defining the acceleration phase in the numerical model. Moreover, the effect of the boundary conditions in the experimental setup had an effect on the test data compared with the numerical model.

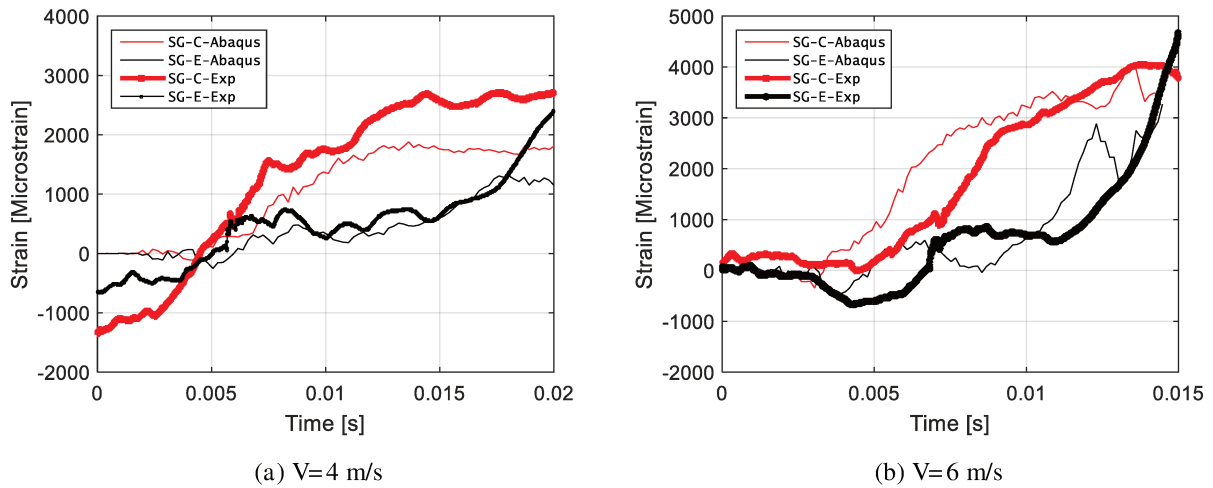


Figure 6. 19. Dynamic deformation for flexible panel (FP)

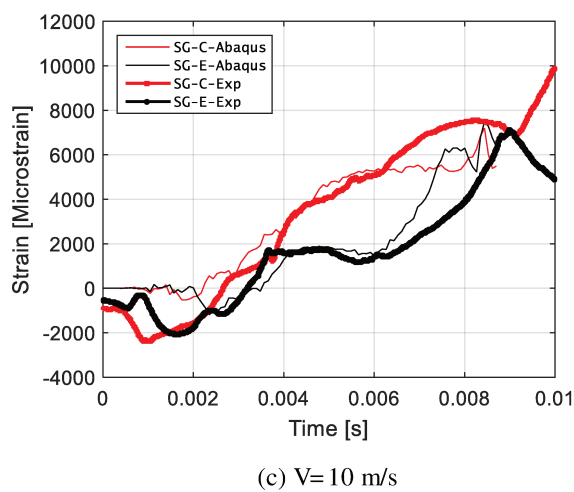
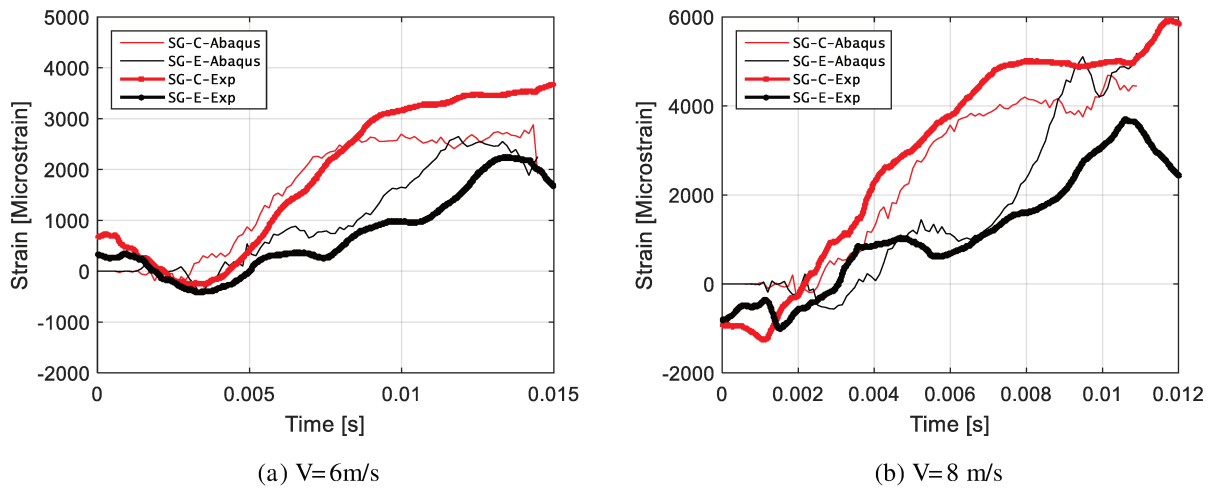


Figure 6. 20. Dynamic deformation for semi-flexible panel (SFP)

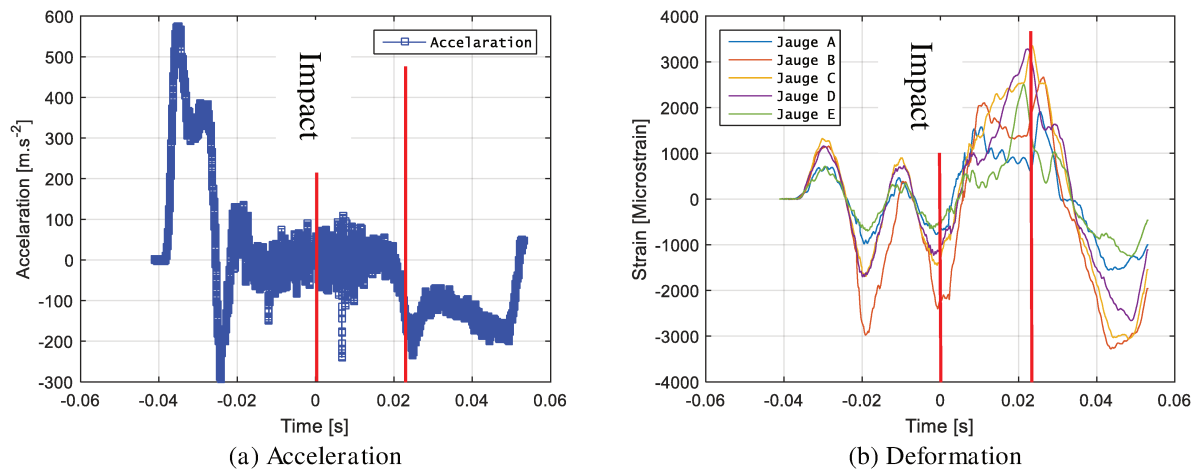


Figure 6. 21. Total signal

6.2.3 Damage assessment

In this section, the implementation of the intralaminar failure (VUMAT-subroutine) that was discussed in Chapter four was specified for the laminate composite. In the case of semi-flexible and flexible panels, numerical predictions indicated that the matrix damage initially occurred near the edges of the panel (keel and chine) due to high peak pressure. The snapshot of damage has presented in Figure 6. 22 and Figure 6. 23, respectively. However, damage increased relative to an increase of the impact velocity and the panel flexibility.

However, damage is raised as the results of changing in local deadrise angle and local impact velocity. These effects caused stress concentration in the centre of the panel and near the ends of the panel, Figure 6. 24.

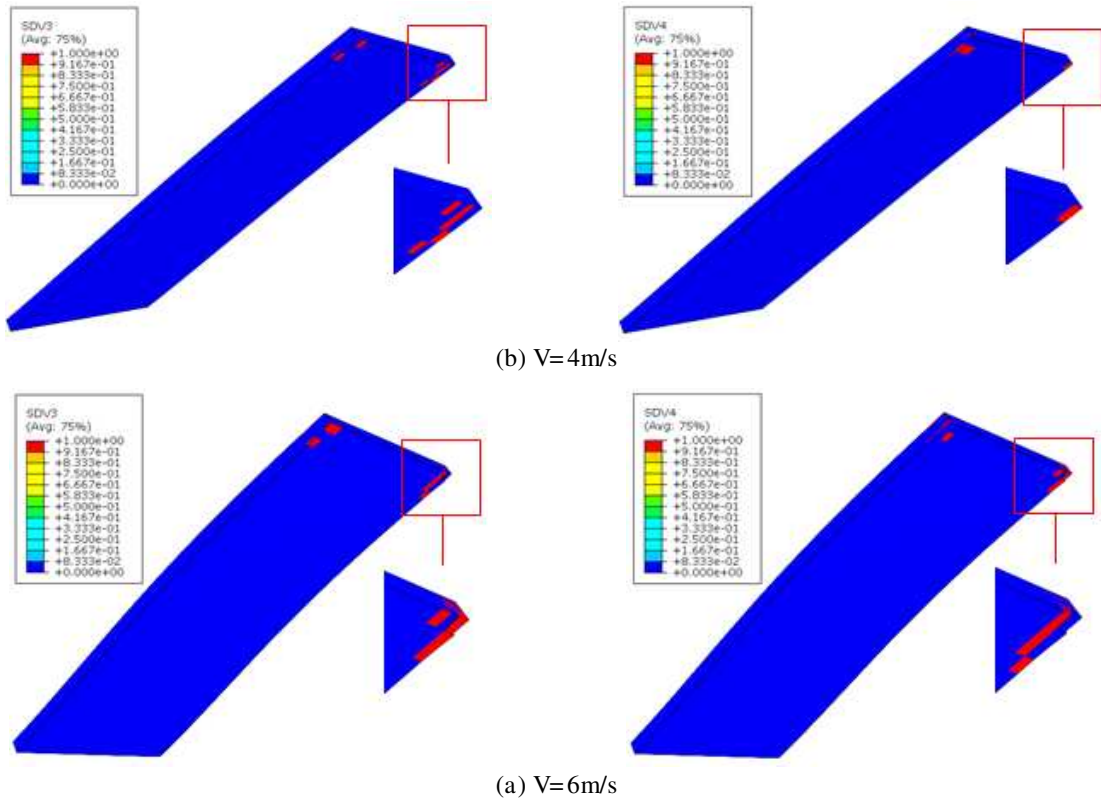


Figure 6. 22. Damage in the matrix tension and compression for semi-flexible laminate

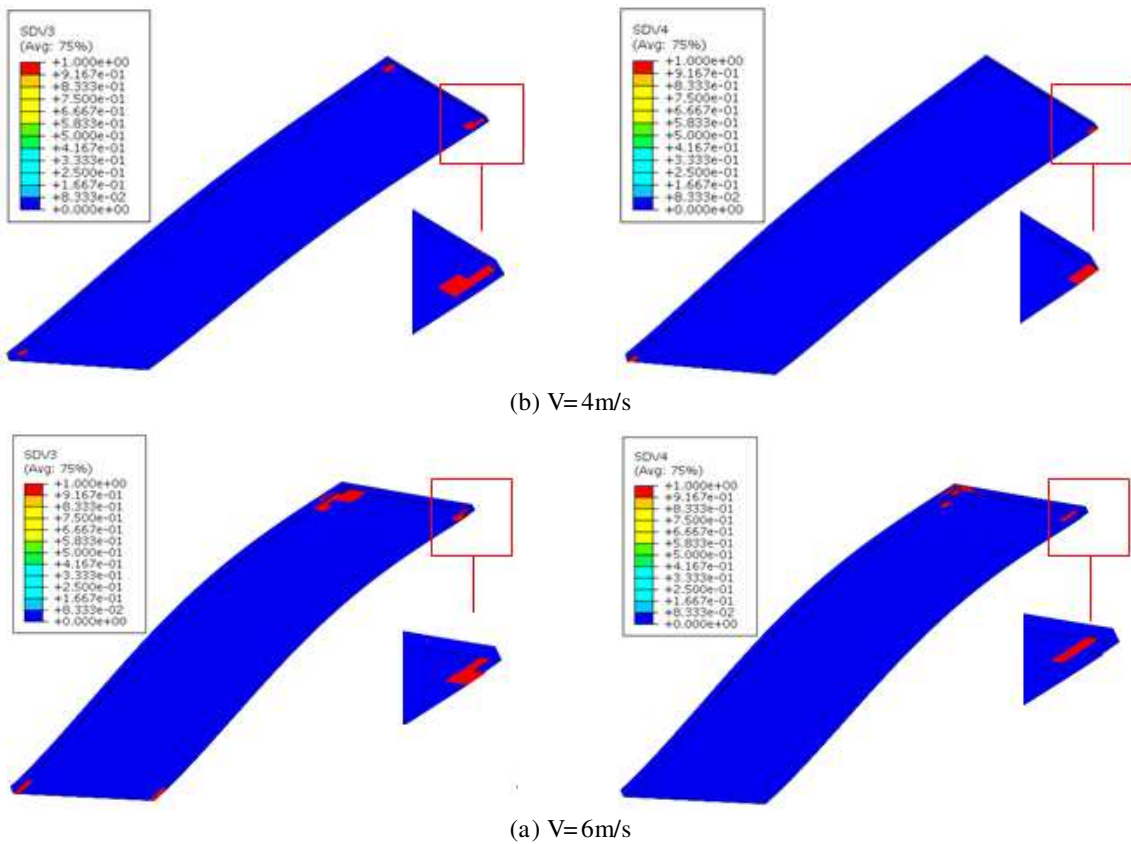


Figure 6. 23. Damage in the matrix tension and compression for flexible laminate

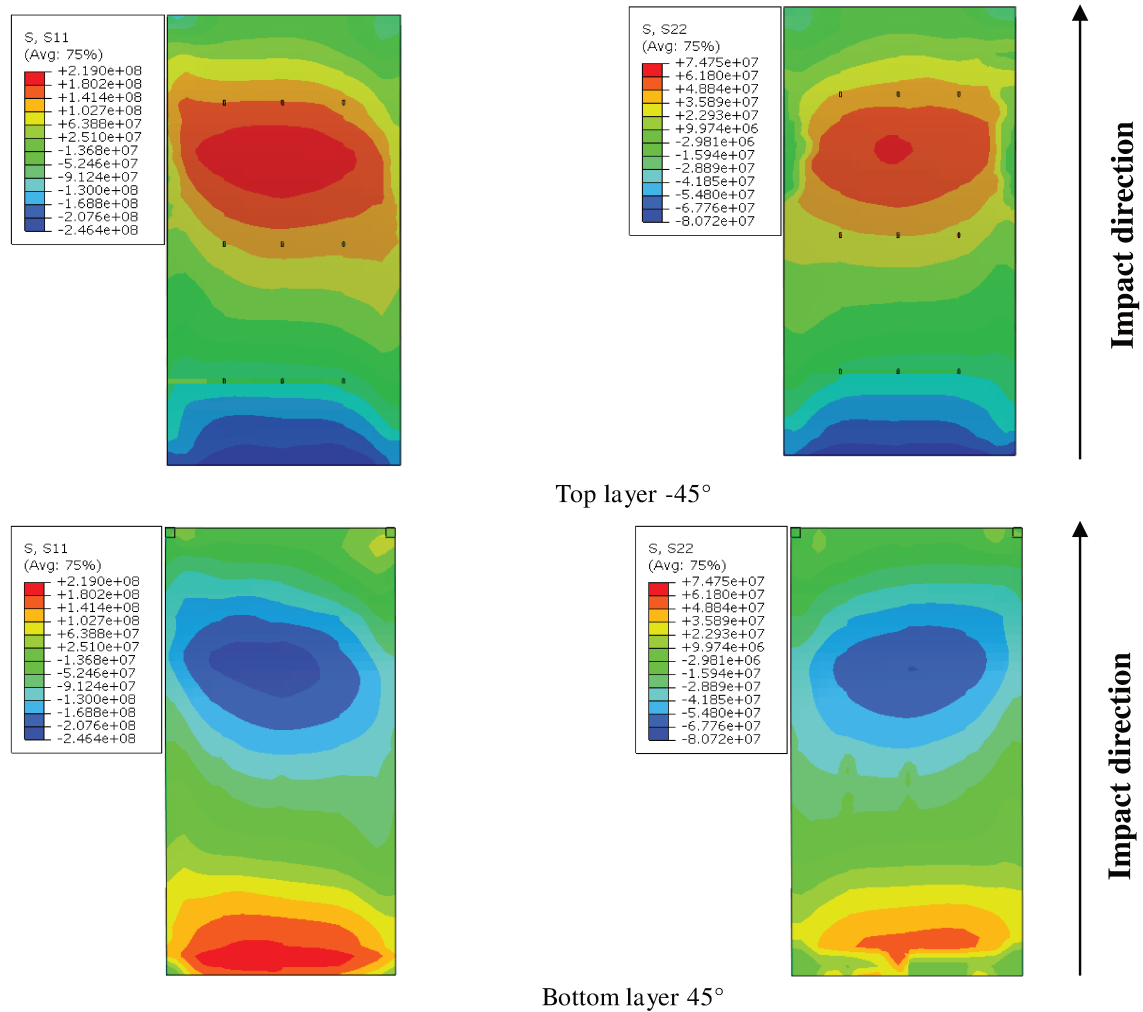


Figure 6. 24. Stress concentration distribution in semi-flexible panel, V=10m/s

On the other hand, matrix damage appears to be the first damage mode occurring in composite laminates under slamming impact loads, especially in the panel centre and panel ends, as illustrated in Figure 6. 25. This is happening when the allowable deflection of the panel exceeds 0.02 of the shortest panel span and the ultimate strain under single slamming impact ≈ 0.0035 [11, 12]. The matrix tensile damage intensifies in the top layers of the panel centre and the keel and chine locations due to a combination of the in-plan and out-of-plane loads. Therefore, with a repetitive slamming wave, matrix cracks develop and propagate in the direction of the fibre and along the delamination in the different laminate plies. These cracks can cause rupture of the fibres which leads to catastrophic failure.

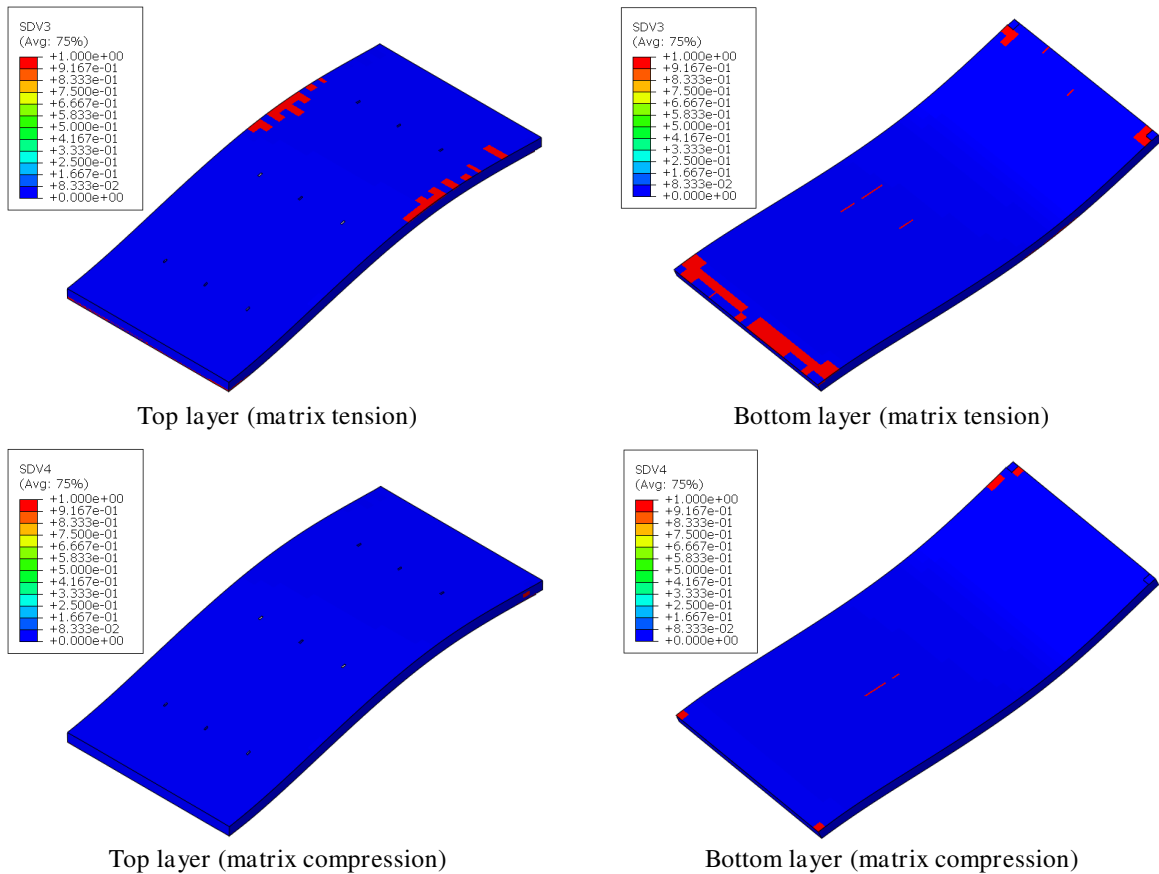


Figure 6. 25. Damage in semi-flexible panel, V=10m/s

Figure 6. 26 illustrates the variation in depth, or displacement of the impactor (composite panels), and the formation of the fluid jet in the water domain in the slamming test. It should be mentioned that the jet flow shows correct development and corresponds to slamming impact and non-surprising phenomena were observed.

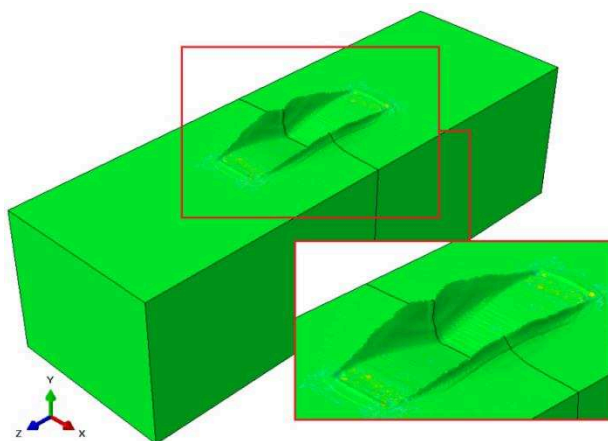


Figure 6. 26. Signature of the slamming problem: impacted zone by composite panels and formation of the water jet

Figure 6. 27 illustrates the damage history in different impact time. From these images, it appears that the damage directly related to the flexibility of composite panels. In most cases when the impact has occurred, at same time, the damage has been minimal for semi-flexible panels compared to the flexible panels (for example at $t=6.525$ ms). We also have note the formation of a pile-up region and water jet where the composite panel is completely submerged in water.

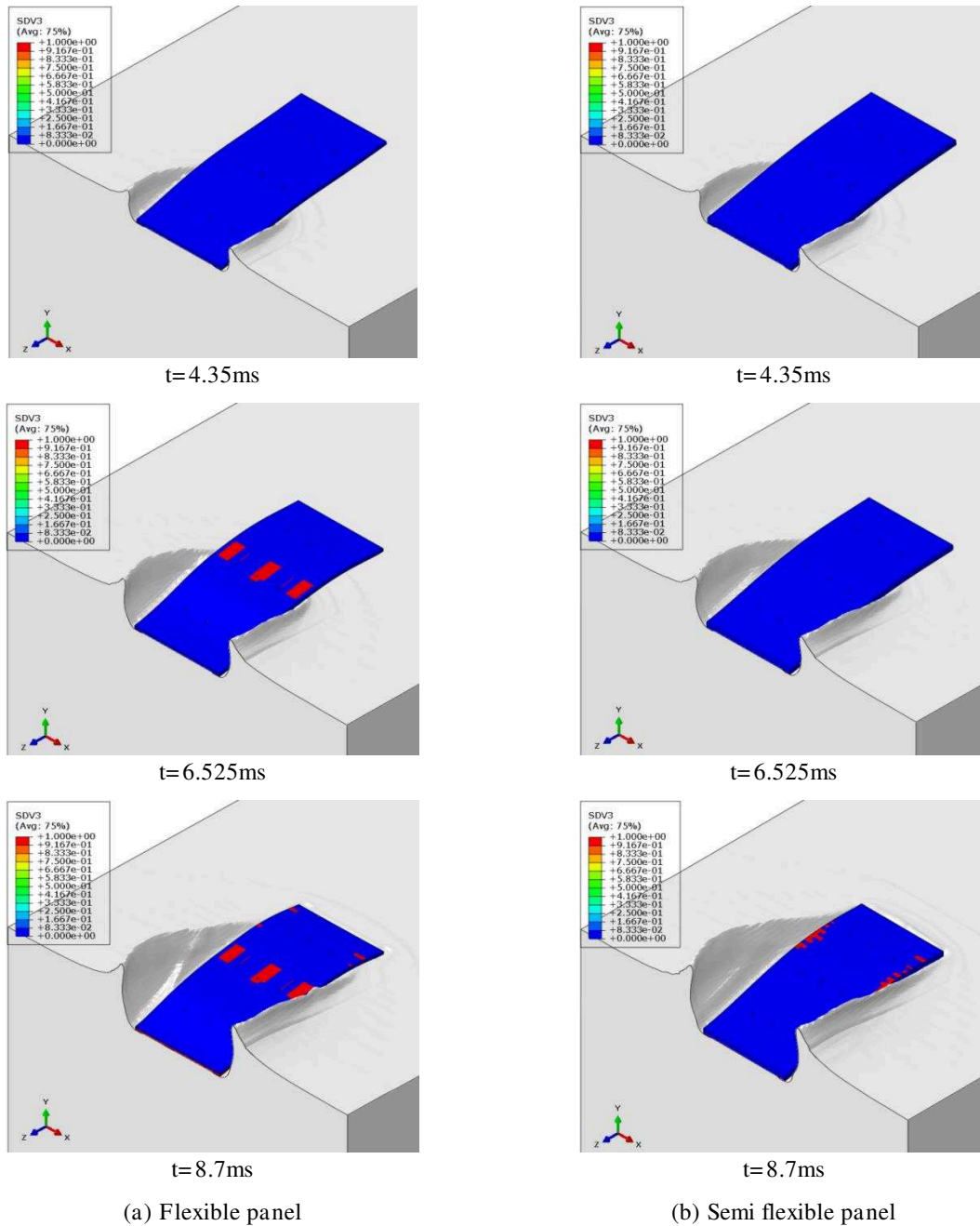


Figure 6. 27. The capture of damaged panels under slamming impact and formation of the fluid jet flow

6.3 Sandwich panel

6.3.1 Force response

The comparisons between experimental and numerical curves of the hydrodynamic force versus time have illustrated in Figure 6. 28 and Figure 6. 29. A good correlation between the experiment and numerical results in the elastic phase can be noted, with a small difference in the peak force. This can be attributed to the experiment impact velocity which is not really constant throughout impact duration compared with the numerical model in constant velocity. For an impact velocity of 10 m/s, the numerical results diverge from the experiment results, as a result of the structure damage due to shear force in the core PVC as the damage threshold velocity has exceeded. This damage mode is not included in the numerical model, therefore damage criteria must be implemented in the numerical model to achieve a good correlation with the experimental data, and this will be discussed in Section (6.3.3). The acceleration phase is also not taken into account. Indeed, this acceleration phase to achieve the desired velocity is accompanied by vibration of the structure and of the fixing system.

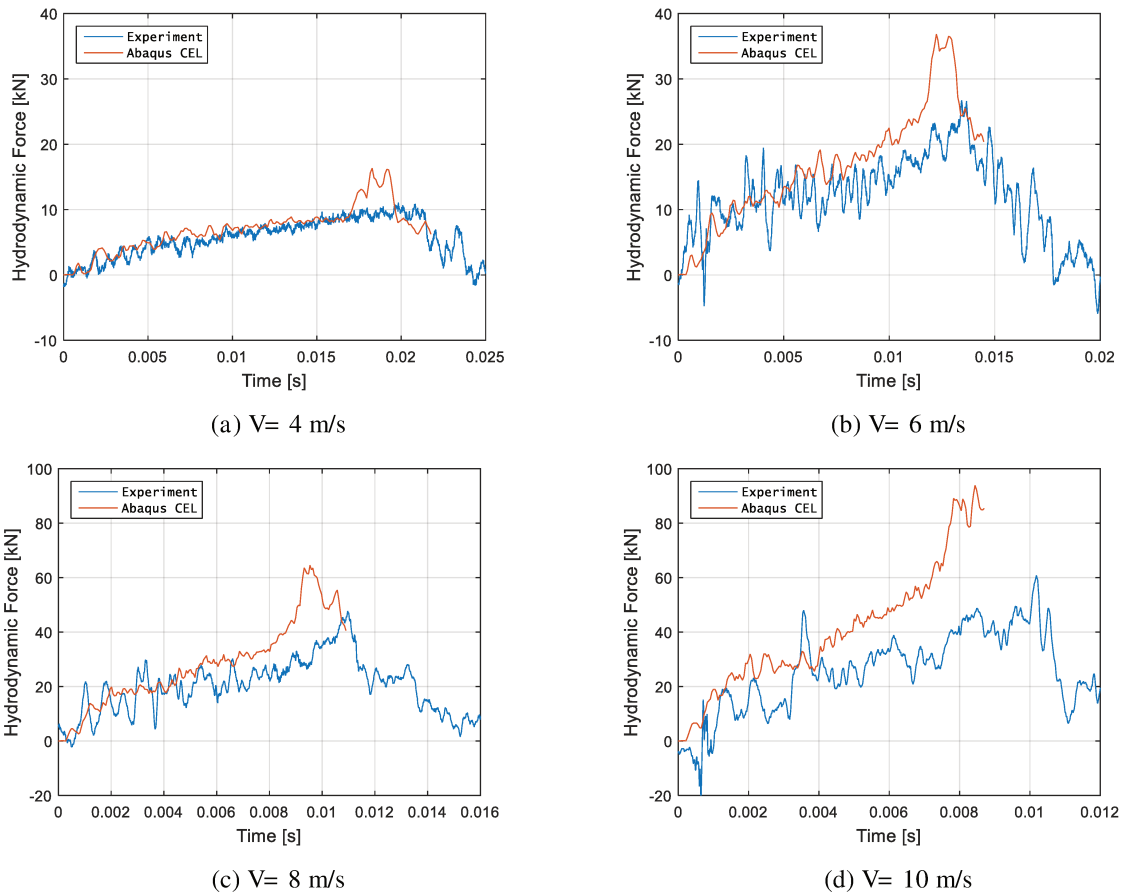


Figure 6. 28. Comparison of hydrodynamic force between numerical and experiment results, $t = 27 \text{ mm}$

For a thicker sandwich panel ($t= 37$ mm), it behaves like a rigid body for impact velocities lower than 10 m/s, and a small dynamic noise was noted in the hydrodynamic force especially in the elastic phase. The numerical results overpredict the load that found in the experimental results at impact velocity 10 m/s, which can be explained by structure damage due to shear force in the core and the debonding of the skin/core interface of the sandwich panel. This indicated that the velocity limit value exceeded the ultimate flexing capacity.

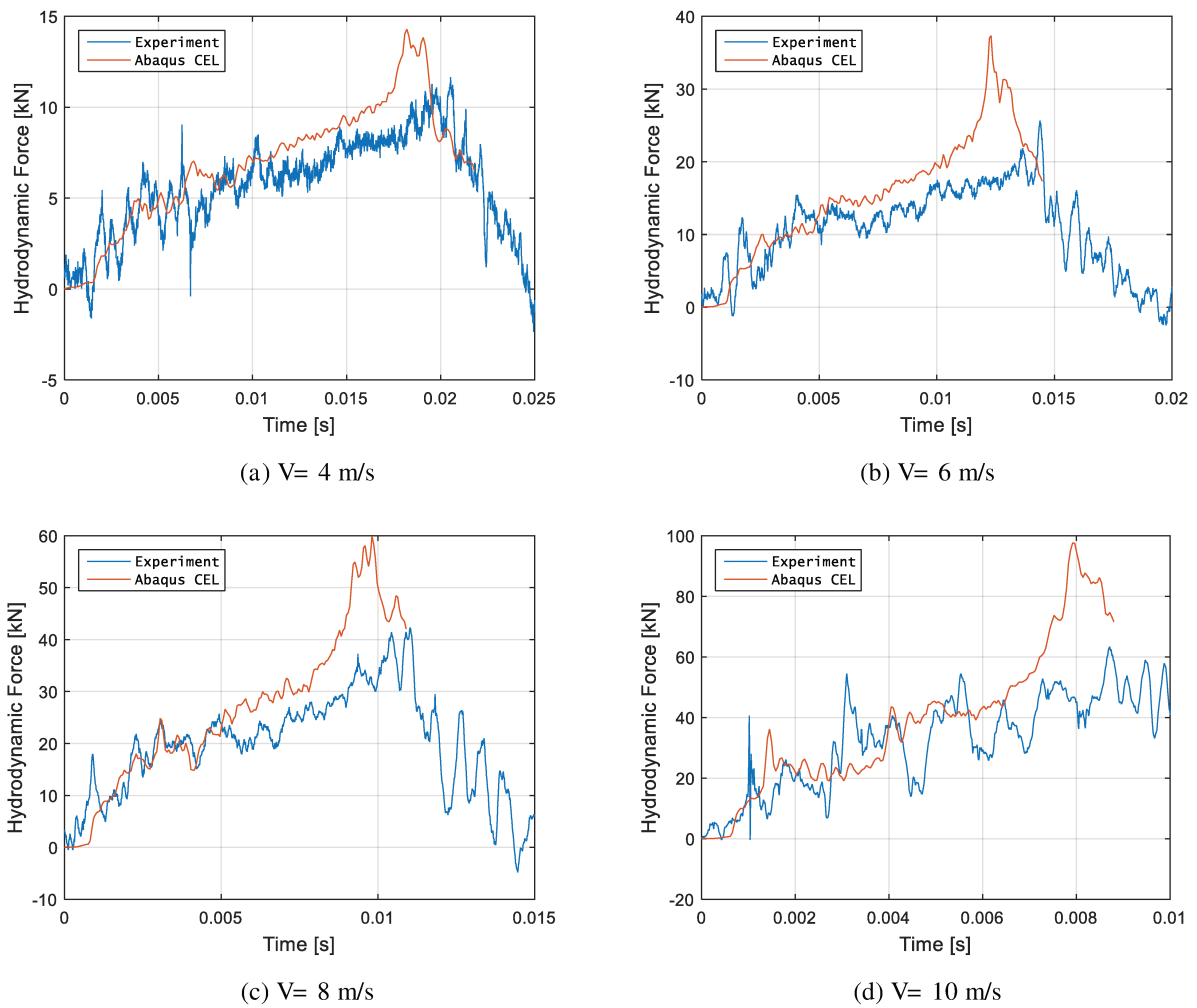


Figure 6. 29. Comparison of hydrodynamic force for sandwich panel, $t= 37$ mm

6.3.2 Deformation response

In general, the sandwich panel has less deformation than occurs in the laminated composite panels, as shown in Figure 6. 30 and Figure 6. 31. This comes from the fact that the sandwich

panel has a high in-plane and flexural stiffness. It should be noted that the sandwich panel gives more resistance in hydrodynamic force, a lower deformation response and is light weight compared with composite panels. These own advantages lead to the widespread use of these structures in marine applications.

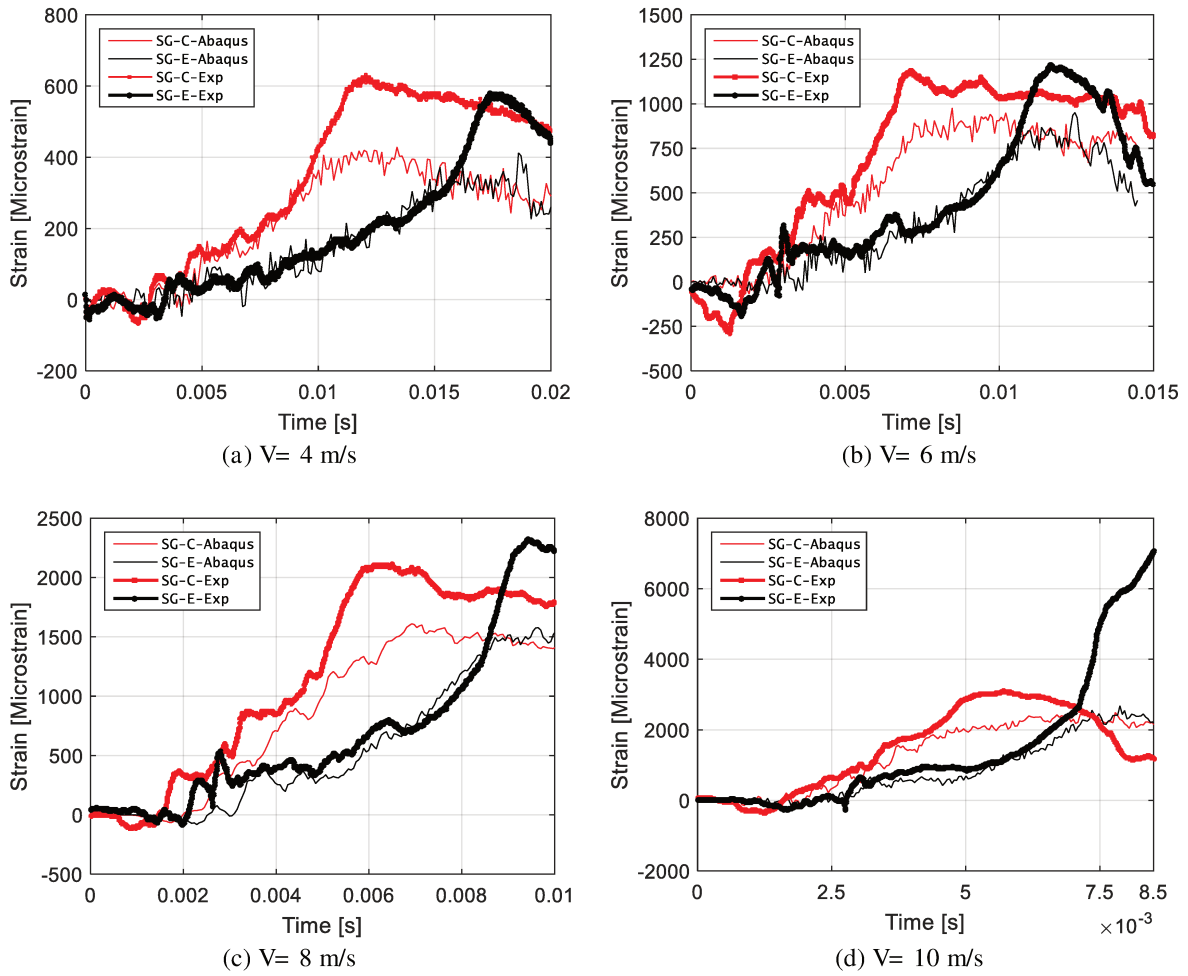


Figure 6. 30. Comparison of gauges deformation between numerical and experimental results, $t=27\text{mm}$

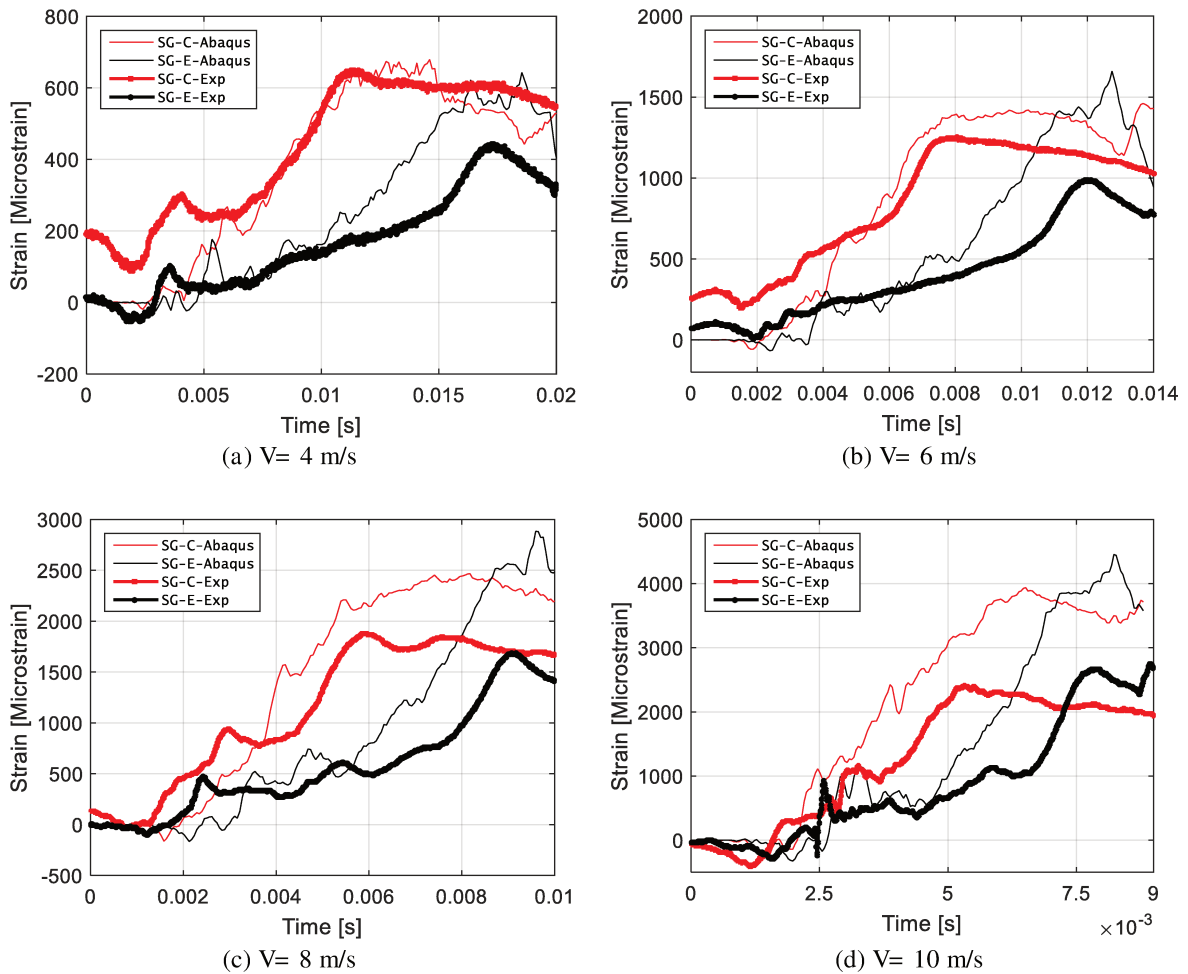
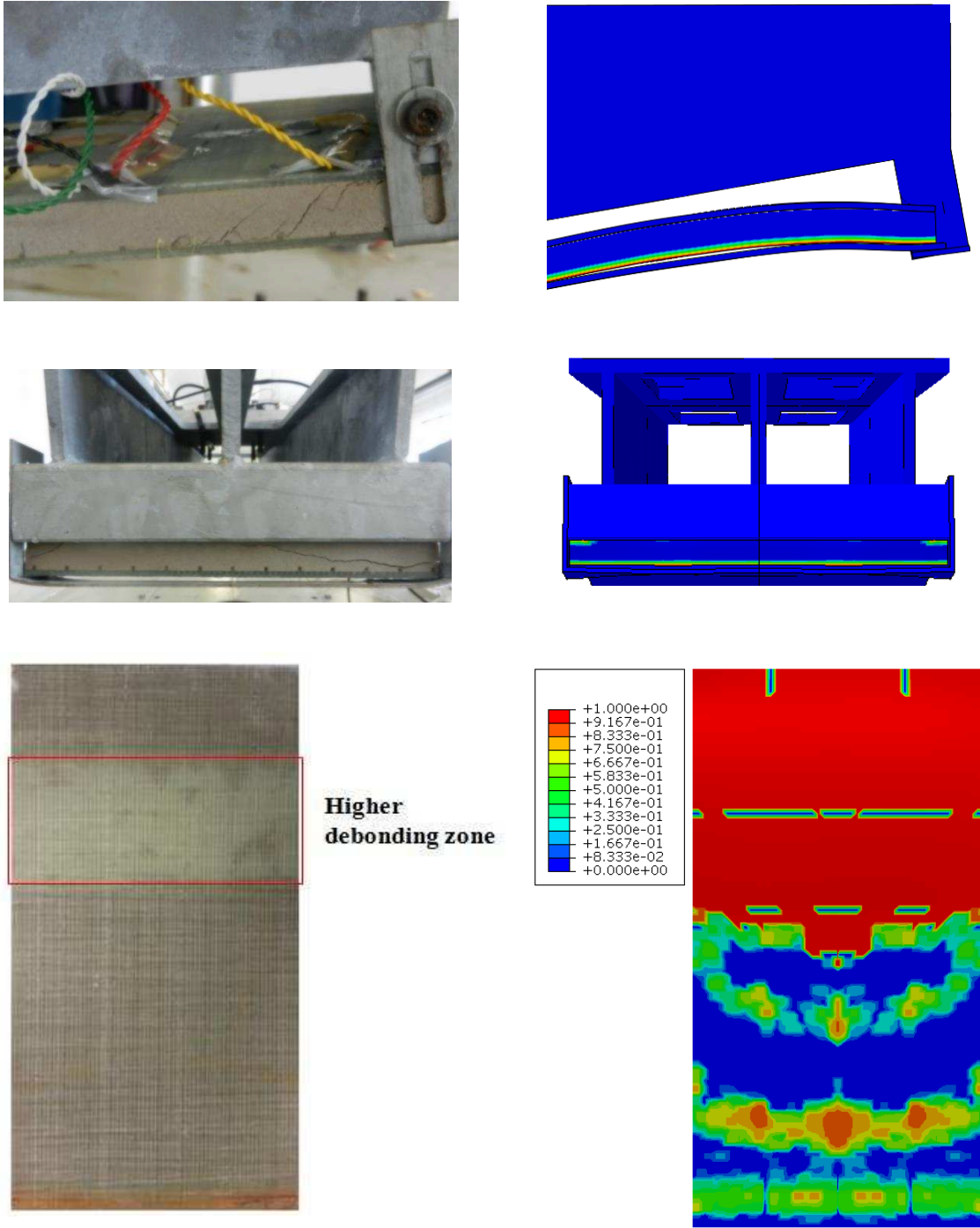


Figure 6. 31. Comparison of gauge deformation between numerical and experimental results, $t=37\text{mm}$

6.3.3 Damage comparison of sandwich panels

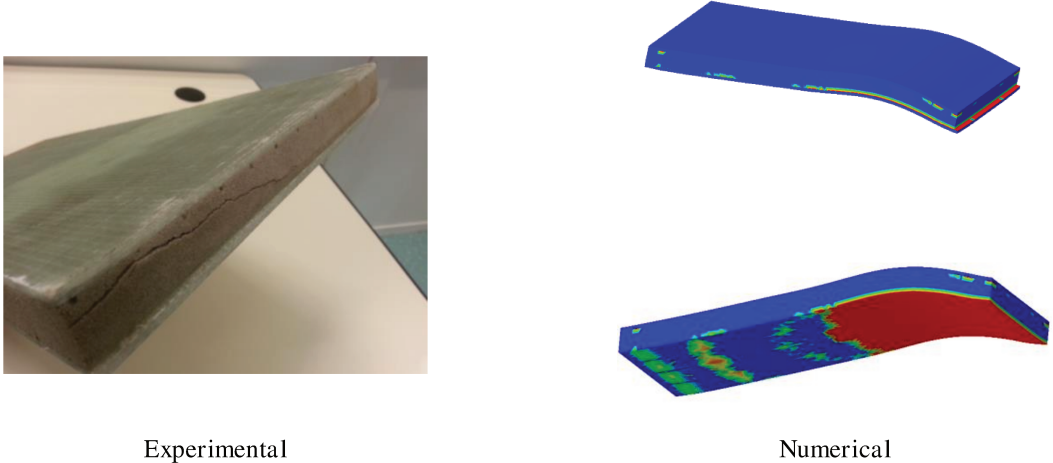
The failure modes in sandwich structures are defined by two main damages modes, namely: debonding between the skin/core and core shear. In the numerical model, cohesive zone model was implemented to predict the debonding of skin/core, Figure 6. 32. This is also obvious from the visual correlation between the numerical and experimental results of impacted panels, which gives a good vision of the dynamic behaviour and debonding failure of the skin/core interface. 3D snapshots of sandwich panels after testing are presented in Figure 6. 33. In this figure the debonding of the skin is observed. The failure starts with core shearing and debonding followed by total buckling and debonding of skin. In spite of that, the core shear damage was not integrated in the numerical model. For a good estimate of the damage in sandwich structures, failure criteria must be identified for the core shear stress.



(a) Experimental

(b) Numerical

Figure 6. 32. Comparison of damaged zone between numerical and experimental results, V=10 m/s



Experimental Numerical
 Figure 6. 33. Damage of core and debonding sandwich panels after test

In addition to the definition of the debonding skin-core failure and the intralaminar failure of skin laminate, a core shear failure was predicted based on the Christensen criteria (for low density cores) and integrated in the numerical model, which is defined by the interaction between the uniaxial and shear stress in a single mode as follows [13]:

$$\left(\frac{1}{\sigma_{11}^T} - \frac{1}{\sigma_{11}^C} \right) (\sigma_{11} + \sigma_{22} + \sigma_{33}) + \frac{1}{\sigma_{11}^T |\sigma_{11}^C|} (\sigma_{11} + \sigma_{22} + \sigma_{33})^2 - \frac{\sigma_{11} \sigma_{22}}{(\sigma_{12}^U)^2} - \frac{\sigma_{22} \sigma_{33}}{(\sigma_{23}^U)^2} \leq 1 \quad (6.4)$$

It can be noted that the effect of the out of the plane stress has added to the formula, which takes into consideration the three-dimensional effect that happens under dynamic impact. Figure 6. 34 shows a satisfactory agreement of the numerical results comparing with experimental data once the different failure modes were applied in the numerical model.

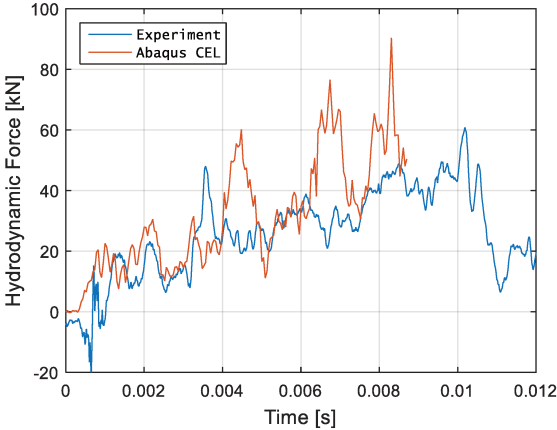


Figure 6. 34. Comparative hydrodynamic force between experimental and numerical results

Figure 6. 35 shows the damage in the sandwich panel due to the debonding and core shear in both experimental and numerical approaches. It demonstrates that prediction of the beginning and location of the core shear in the numerical model gives a good correlation with the experiment data. On other hand, the intralaminar damage in the skin occurs slight in the matrix tension and compression that has not influence on the panel response.

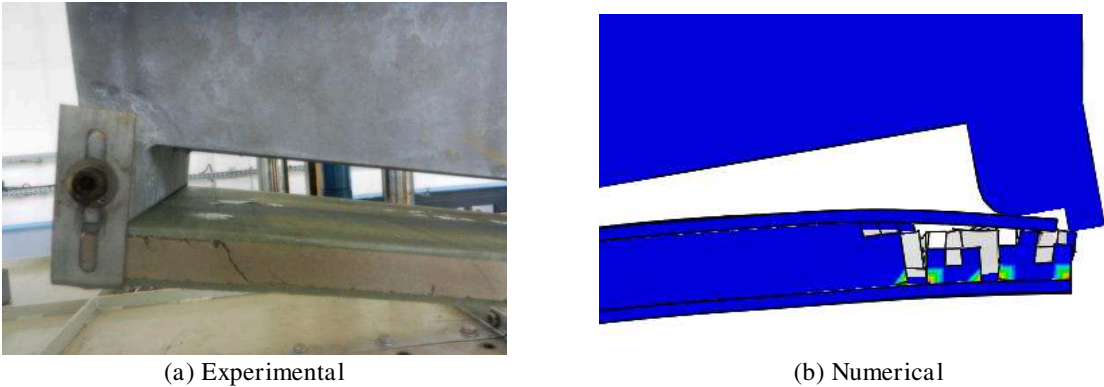


Figure 6. 35. Failure modes comparison of numerical vs. experimental (debonding and core shear) results

6.4 Discussion, non-dimensional slamming force

A Summary of the experimental tests and numerical results is depicted in Figure 6. 36, could be concluded that the present numerical model could be efficiently used to estimate the structure response subjected to the slamming impact. Table 6. 3 is summarises the experimental data and numerical results (hydrodynamic force and non-dimensional slamming force) for different panel stiffnesses and different impact velocities.

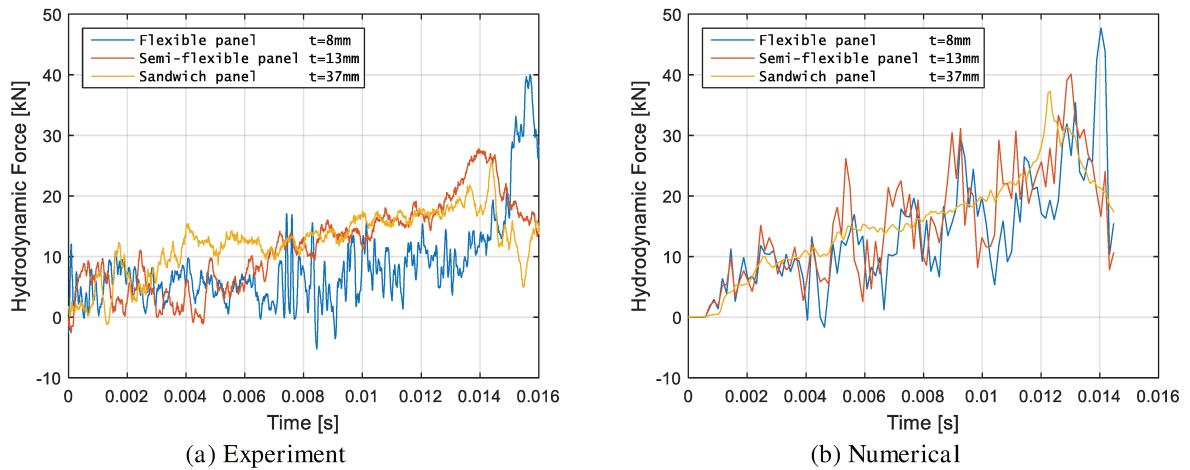


Figure 6. 36. Comparison of hydrodynamic force for different panel stiffness, $V=6$ m/s

The non-dimensional slamming force (C_s) for the wedge shape with constant velocity was calculated as follows:

$$C_s = \frac{F}{0.5 \rho V^2 \hat{A}} \quad (6.5)$$

($\hat{A} = 2W * Vt / \tan\beta$) is the projection of the panel area on the water surface. It should be noted that the experimental impact velocities were not really constant, therefore the mean velocity through the impact duration was used in this estimation.

The comparison of the non-slamming forces is mentioned in Figure 6. 37. The flexibility of the panel is an important factor in slamming loads as there is change in the local deadrise angle and the projection area of the panel on the water surface. Therefore, it can be observed that when the flexibility of the panel increases, the force coefficient value begins to deviate from that of more stiff panels.

This helps the ship designer to take this coefficient into consideration throughout the design phase. Actually, this coefficient differs in deformable structures from that in rigid structures, according to the Wagner ($f(\beta) = \frac{3\pi}{2}$) and von Kármán models($f(\beta) = \pi$) [5, 7].

V (m/s)	Specimens	Hydrodynamic force kN		Non dimensional slamming force Cs	
		Exp	Num	Exp	Num
4	Composite(FP) t=8mm	17.95	22.19	12.62	12.54
	Composite (SFP) t=13mm	-	-	-	-
	Sandwich panel t=27 mm	11,26	16.33	7.24	9.89
	Sandwich panel t=37 mm	11,04	14.29	6.08	8.65
6	Composite(FP) t=8mm	35.63	47.77	9.62	11.14
	Composite (SFP) t=13mm	29.78	40.12	8.60	7.48
	Sandwich panel t=27 mm	24.39	36.84	7.20	6.53
	Sandwich panel t=37 mm	25.34	37.33	6.57	6.73
8	Composite(FP) t=8mm	-	-	-	-
	Composite (SFP) t=13mm	64.95	64.94	9.21	8.69
	Sandwich panel t=27 mm	48.98	64.54	7.08	9.36
	Sandwich panel t=37 mm	43.37	59.93	7.11	8.42
10	Composite(FP) t=8mm	-	-	-	-
	Composite (SFP) t=13mm	130.53	108.3	10.87	8.78
	Sandwich panel t=27 mm	64.48	90.4	6.77	7.68
	Sandwich panel t=37 mm	64.26	97.61	6.17	8.71

Table 6. 3. Summary of experimental and numerical results

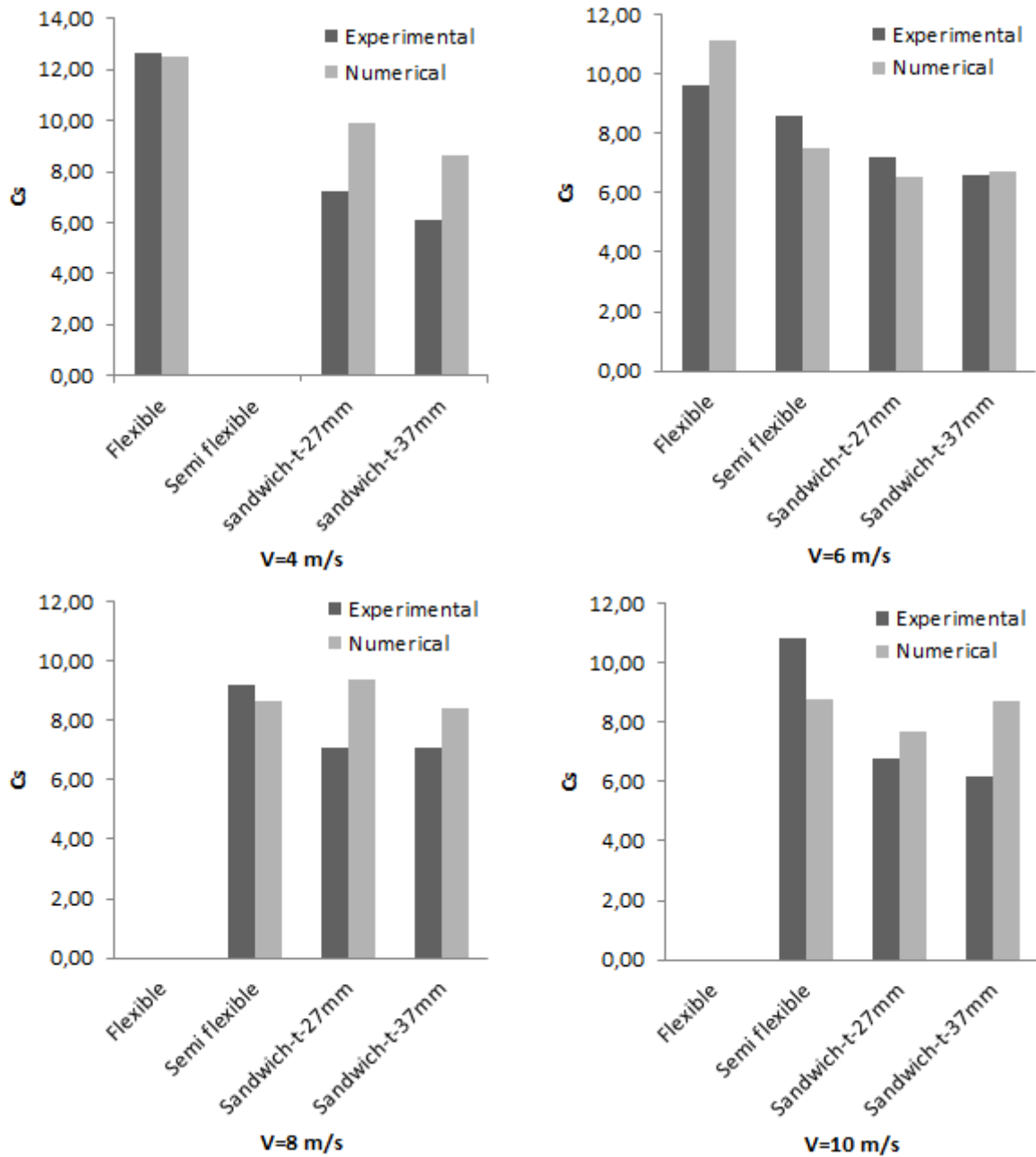


Figure 6. 37. Comparison of the non-dimensional slamming force ($\beta=10^\circ$) with different materials and velocities

6.5 Conclusions

In this chapter, the comparison between the experimental data and numerical results has been achieved. The hydrodynamic force and dynamic deformation responses were predicted numerically for both laminate and sandwich panels (with different stiffness) under constant velocity. The slamming model was constructed in three dimension scheme based on the Coupled Eulerian-Lagrangian Model (CEL) built-in the finite element code

(Abaqus/Explicit). The pressure distribution, deflection of the panel, local deadrise angle and the deformation of panels have been investigated as indicators to describe hydroelastic effects during the water-structure interaction. Thus, this assists ship designers for predicting global and local hydrodynamic loads. Different damage modes were incorporated in the numerical model using continuum damage mechanics (CDM) and fracture mechanics, including the intralaminar and debonding damage (skin/core interface). Two failure criteria (Hashin criteria for the laminate composite materials and Christensen criteria for the core in sandwich structure) were defined and integrated into the VUMAT subroutine to better estimate the failure mechanism. In addition, the cohesive zone model (CZM) was used to predict the debonding skin/core in sandwich panels and interlaminar damage in skin. The numerical model showed convincing results in judging experimental data but exhibited some differences in the time and the peak force. This was due to variations in the experimental velocity of the impact duration which was not constant as in the numerical model, also other possible damage mechanisms may be happen that are not integrated in the present numerical model. We believe that it is possible to improve the numerical results to be more satisfactory with the experimental data. This can be done by identifying the actual velocity profile in the numerical model, however, this increases computational time significantly.

References

- [1] R. Panciroli, "Hydrodynamic impact of deformable wedges," in *Dynamic Failure of Composite and Sandwich Structure*, New York, London, Springer Science, Business Media Dordrecht, 2013, pp. 1-45.
- [2] Owaisur Rahman Shah, M. Tarfaoui, "Effect of adhesive thickness on the Mode I and II strain energy release rates. Comparative study between different approaches for the calculation of Mode I & II SERR's," *Composites Part B: Engineering*, vol. 96, pp. 354-363, 1 July 2016.
- [3] I. Daniel, M. Isaac, "Influence of core properties on the failure of composite sandwich beams," *Journal of mechanics of materials and structures*, vol. 4, no. 7-8, pp. 1271-1286, 2009.
- [4] Owaisur Rahman Shah, M. Tarfaoui, "Determination of mode I & II strain energy release rates in composite foam core sandwiches. An experimental study of the composite foam core interfacial fracture resistance," *Composites Part B*, vol. 111, pp. 134-142, 2017.
- [5] H. Wagner, "Über stoss und gleitvorgänge an der oberfläch von flüssigkeiten," *Zeitschrift fuer Angewandte Mathematik und Mechanik*, vol. 12, pp. 193- 215, 1932.
- [6] DVN, "Hull Structure Design, Fiber Composite and Sandwich Constructions," in *Rule for Classification of High speed, Light Craft and Naval Surface Craft*, Part 3, Chapter 4, 2011.
- [7] T. Von Karman, "The impact of seaplane floats during landing," *NACA TN.*, 1929.
- [8] M. Battley, T. Allen, "Servo-hydraulic System for Controlled Velocity Water Impact of Marine Sandwich Panels," *Experimental Mechanics*, vol. 52, pp. 95-106, 2012.
- [9] E. Bozhevolnaya, O.T. Thomsen, "Structurally graded core junctions in sandwich beams: fatigue loading conditions," *Composite Structures*, vol. 70, pp. 12-23, 2005.

- [10] T.Allen, M. Battley, “Quantification of hydroelasticity in water impacts of flexible composite hull panels,” *Ocean Engineering*, vol. 100, pp. 117-125, 2015.
- [11] B. Shafiq, S. Charca, F. Just, “Repeated slamming of the foamcore sandwich composite panels on water,” in *ICCM17*, Edinburgh, UK, 27-31 July 2009.
- [12] S.Charca, B.Shafiq,, “Damage Assessment Due to Single Slamming of Foam Core Sandwich Composites,” *Journal of Sandwich Structures and Materials*, vol. 12, no. 1, pp. 97-112, August 2009.
- [13] R.M. Christensen, D.c.Freeman, S.J.DeTeresa , “Failure criteria for isotropic materials, applications to low-density types,” *International Journal of Solids and Structures*, vol. 39, pp. 973-982, 2002.

Conclusions and perspectives

Conclusions

The main objectives of this work are to study experimentally the response of deformable laminated and sandwich structures subjected to the water-entry problem, in addition to establishing an appropriate modelling and validation of the numerical approach for slamming impacts and composite behaviour. The thesis consists of two aspects to analysis the slamming phenomena which are fluid structure interaction and the structure response. In marine structural applications, the slamming phenomenon is considered critical impact load in the design requirements for both rigid and deformable structures. To this end, Chapter one gave a wide ranging state of art and assessment of the different approaches to aspects including analytical, numerical and experimental methods to predict these loads.

Numerical methods based on the Arbitrary Lagrangian Eulerian (ALE) and Coupled Eulerian Lagrangian (CEL) have adopted to simulate the fluid structure interaction in the case of the slamming impact. The main advantage of the latter technique is that it is appropriate for non-linear problems, where large deformations occur, and it can handle simultaneously the structure and fluid in a single computation. Although, the numerical results are in good agreement with the experimental data, this method also requires a high computation time to resolve the problem. In addition, good simulation results depend on the mesh density of the fluid domain. Therefore, the model parameters (Chapter two) must be selected carefully.

The slamming of the composite vessel with single and multi-repeating impacts cause a reduction in the material resistance which leads to the occurrence of effective damage and even catastrophic failure. Therefore, damage modelling based on the degradation of the material stiffness was constituted using the user material subroutine VUMAT implemented in explicit finite element code (Abaqus) for both the intralaminar and interlaminar damage of the laminate composite, and the debonding skin/core of sandwich panels based on the cohesive

Conclusions and perspectives

zone model (CZM). The damage model was validated in sequence procedures including the one element test, high impact velocity loading and slamming impacts. The one element was tested under tension and compression dynamic loading and varying fracture energies (fibre and matrix) were applied to evaluate the model and estimate the damage evolution. In the high impact velocity, the numerical results estimated correctly the damage initiation and gave accurate estimations for the damage evolution of the failure mechanisms for fibre and matrix when compare with experimental data. So, we can note that main damage modes happen in the composite laminates which are matrix cracks and delamination that propagates and develops quickly, especially in the matrix and through the thickness (out-of-plane) of the structure. To validate the application of the presented model to slamming impact simulations, we simulated the water entry problem of composite wedges which was performed in the previous experimental works. Subsequently, this investigation could help the ship designers to predict the damage tolerance and given appropriate safety factors to design requirements when using composite materials.

A series of experimental tests (Chapter five) were performed for different panel rigidities under various impact velocities to demonstrate the hydroelastic effects and the structural response including the hydrodynamic force and panel deformation. The main points of the test results could be summarized as follows:

1. The inertia effect was noted at the early stage of the impact event and its influence depends on the loading rate. Therefore, it more appears more frequently at a lower impact velocity, which has a longer wetting time than the first natural frequency of the dry structure.
2. Structure flexibility has an effect on the hydrodynamic loads due to the change in local deadrise angle and local velocity of the fluid flow. These effects can reduce or increase the slamming loads.
3. Under a presented boundary condition (full camped conditions), the most critical locations that induce high hydrodynamic pressure are usually in the centre and close to chine edge of the panel. Therefore, great attention must be paid to these locations during the design stage.

Conclusions and perspectives

4. More Flexible panels have a higher peak force and significant dynamic noise compared to higher stiffness panels. For this reason, flexible panels behave differently from the rigid bodies when impacting water.
5. Maximum force and deformation occur near the chines which are substantial enough to cause damage to the structure and leading to catastrophic failure. Consequently, repetition of the slamming impact leads to a reduction in the material stiffness properties.

In Chapter six, a numerical model gave a reasonable correlation between the experimental and numerical results in the elastic phase with a small difference in the peak force. This can be attributed to the experiment impact velocity, which is not really constant throughout the impact duration compared with the numerical model that maintains a constant velocity. The acceleration phase before the initial water/structure contact was also not taken into account. Indeed, the acceleration phase could be defined in the numerical model. However, the computational time would increase significantly.

In addition, the numerical deformation was slightly different from the experimental data in all velocities. This difference can be attributed to the boundary conditions effect as in the experimental tests and due to the panel vibrating before the initial impact contact. By incorporating different damage modes including the intralaminar and debonding interface skin/core damage (Hashin criteria for the laminate composite materials and Christensen criteria for the core in sandwich structure) using Continuum damage mechanics (CDM) and fracture mechanics, the magnitude and shape of the numerical results were compared well with experimental data. We can see that the main damage modes in the laminate composite panels are the matrix tension and compression in the centre and close to the chine edge. In contrast, the core shear and debonding interface dominated the damage modes in the sandwich panels. However, the prediction of the beginning and location of the core shear in the numerical model gave a good correlation with the experimental data.

Finally, it can be concluded that the present numerical model is capable of predicting the slamming event and the structural response. Therefore, it can be extended to simulate other forms of complex structures and implemented to include large-scale vessel structures to estimate the global and local effects of the slamming phenomenon.

Perspectives and future works

According to the above-mentioned summaries and in order to improve the results of this work, the following perspectives are recommended to be treated both slamming phenomenon and structural behaviour:

Future aspects of the slamming phenomenon

- Developing a numerical model that can predict the global response of the hull to the slamming impact rather than panels or local analysis. In addition, the strong coupling of the fluid structure interactions (as two separated computational domains for fluid and structure), and other numerical approaches may be needed to reduce the computational time for solving the problem. Some of the slamming impact results for our material structure were obtained using a smoothed particle method SPH, which is shown in Appendix (C).
- The influence of fluid compressibility and trapping air must be taken into account and integrate into the numerical model. These factors may cause a significant effect on the hydrodynamic loads, especially for high impact velocities and small deadrise angles.
- For more clarity of, the hydroelastic effect, pressure sensors can be useful in predicting of the pressure distribution (increases or decreases due to structural flexibility) along the interface between the structure and free water surface.
- The effect of the deadrise angle and the structural boundary conditions can play an important role in the hydrodynamic loads and the hydro-elastic effects. Therefore, experimental tests could be carried out for various deadrise angles and boundary conditions.

Future aspects of the structural behaviour

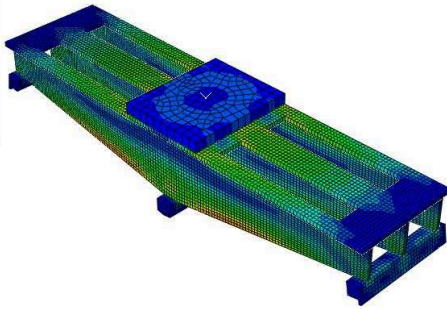
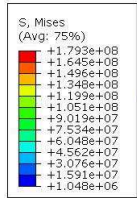
- Multiple slamming impacts need to be performed experimentally to estimate the post-structural strength and damage tolerance which would give a better indication of ship's service.

Conclusions and perspectives

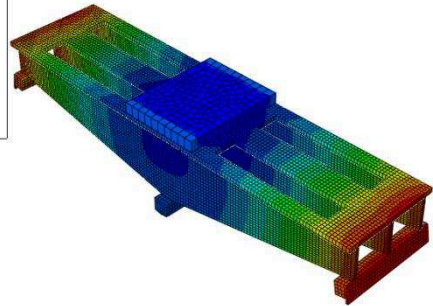
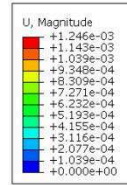
- To enhance the capability of the damage model in predicting the failure mechanism, multi-scale modelling could be improved the numerical damage model to deal with the microstructure scale.
- In addition to the above, new measurement techniques can be exploiting in experimental tests such as the Fibre Bragg Grating (FBG) that can measure deformation and detect internal as well as external damage in composite and sandwich panels in several locations.

Appendix A

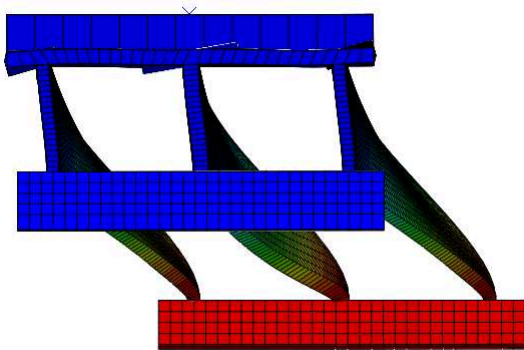
Natural frequency analysis of Fixture system and panels



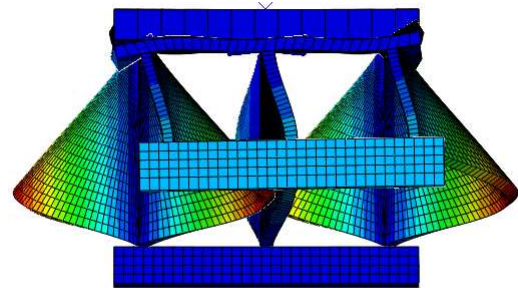
Von Mises Stress



Displacement

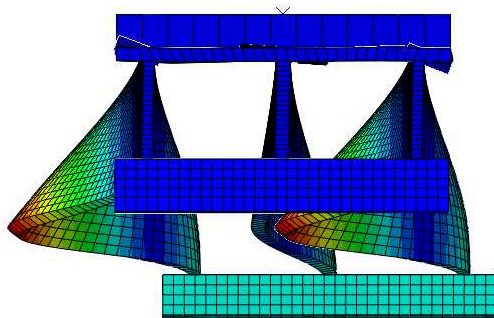


Mode 1

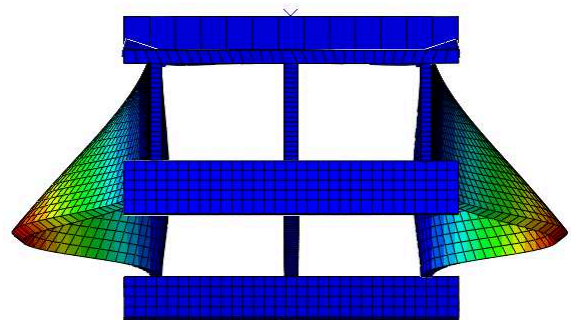


Mode 2

Frequency



Mode 1



Mode 2

Buckling

Figure A. 1. Fixture System with angle of 10°

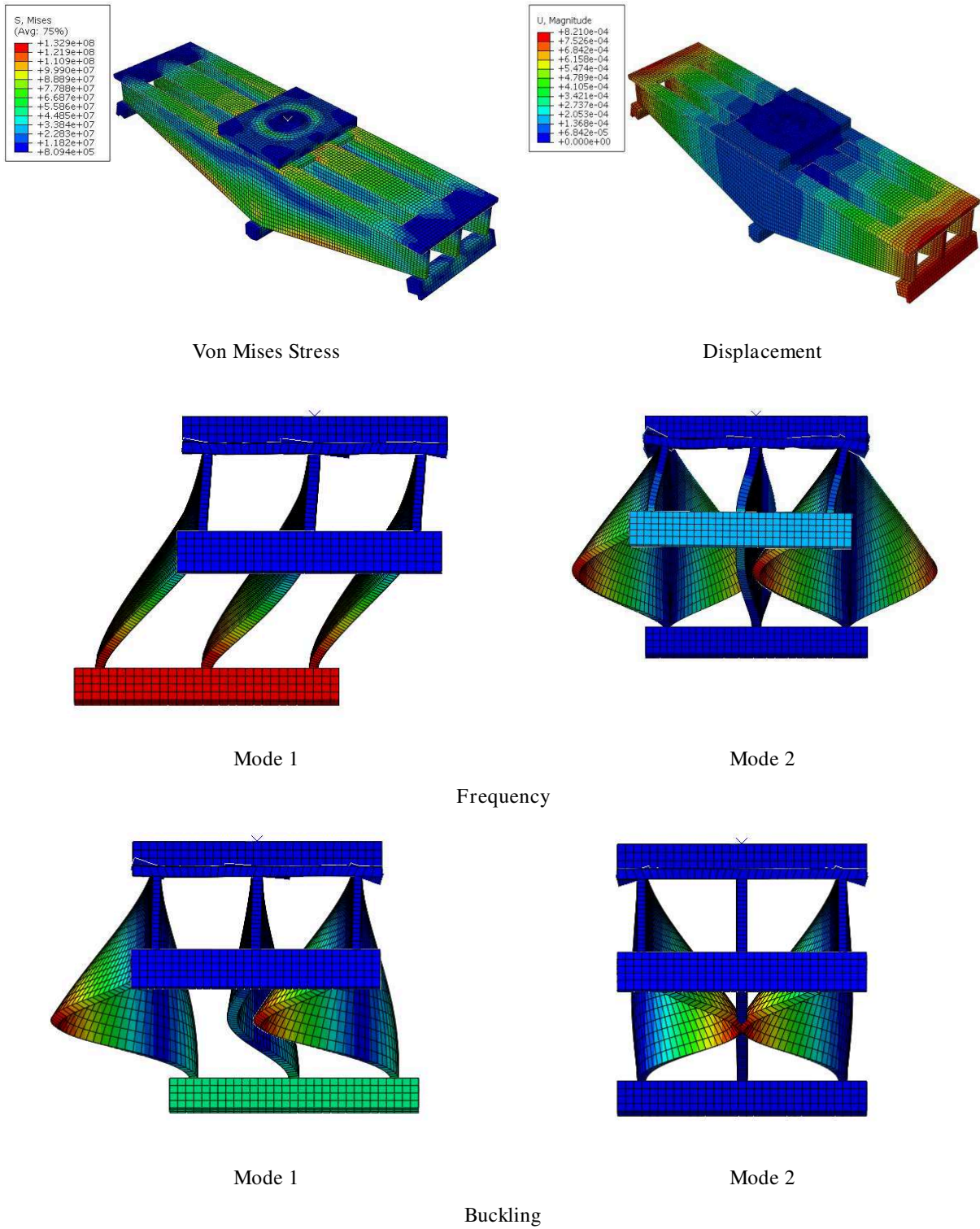


Figure A. 2. Fixture System with angle of 15°

System characteristics					4 MPa	4 MPa		
Deadrise angle	Max dis system (mm)	Max stress (MPa)	Frequency		Buckling		System mass (Kg)	Panel mass (Kg)
			Mode 1	Mode2	Mode 1	Mode 2		
10	1,2	179,3	33,146	48,034	3,6289	3,8396	48,45	6,58
15	0,8	132,9	23,298	42,95	4,0429	4,2446	52,67	6,58

Table A. 1. Fixture system analysis

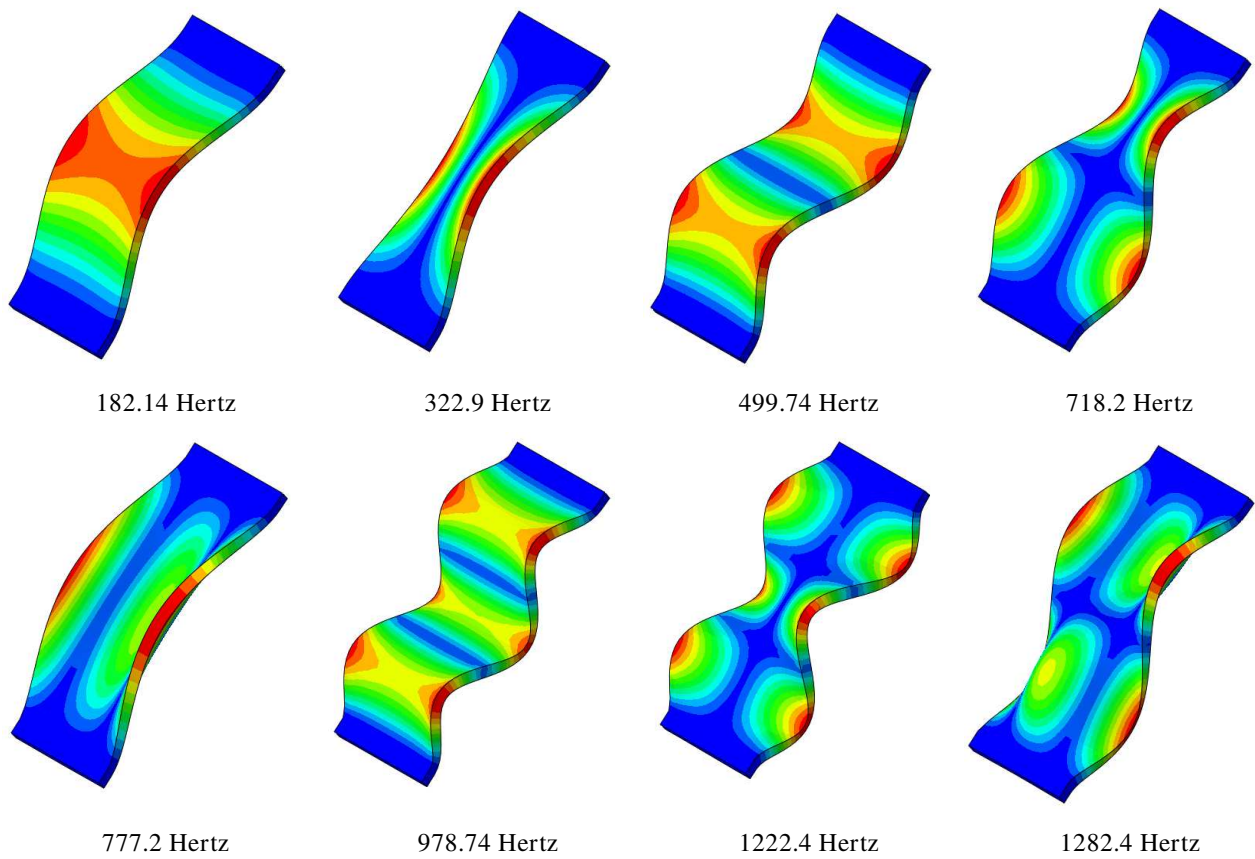


Figure A. 3. Natural frequency analysis of composite panel, thickness =13 mm

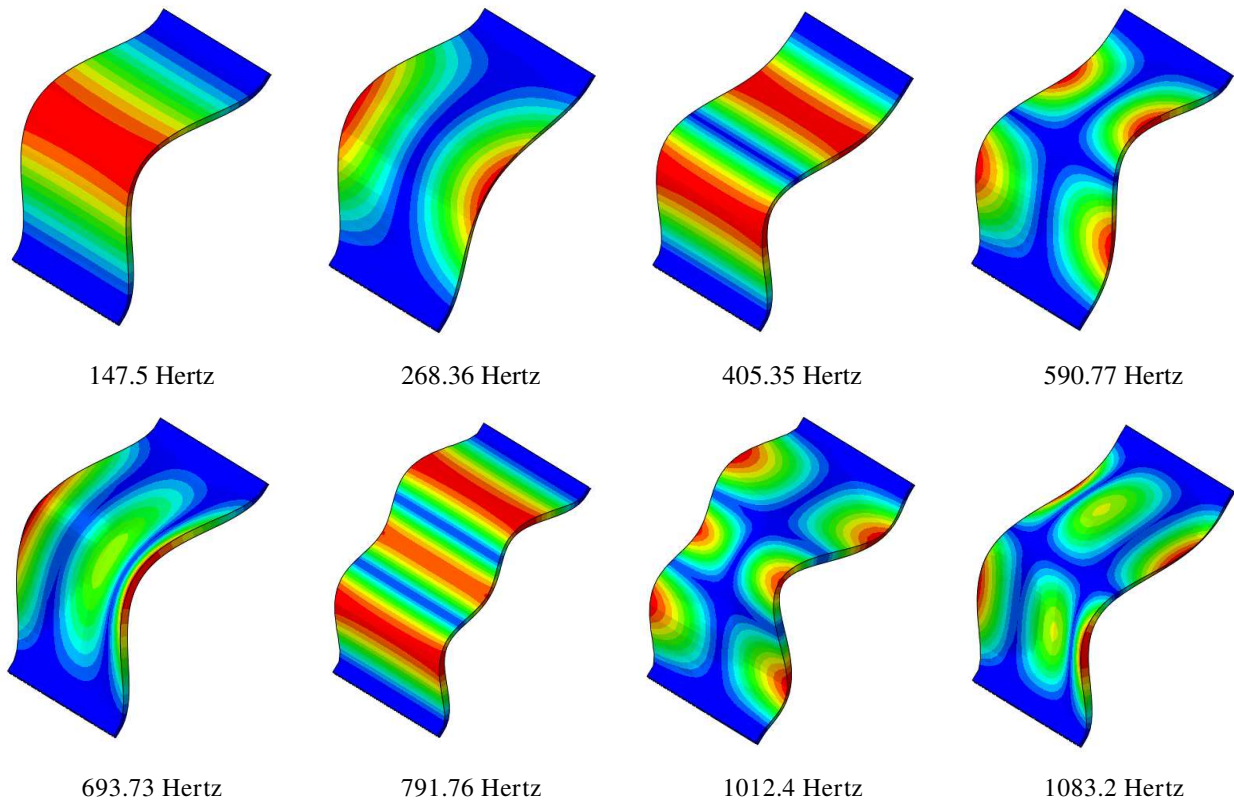


Figure A. 4. Natural frequency analysis of composite panel, thickness =8 mm

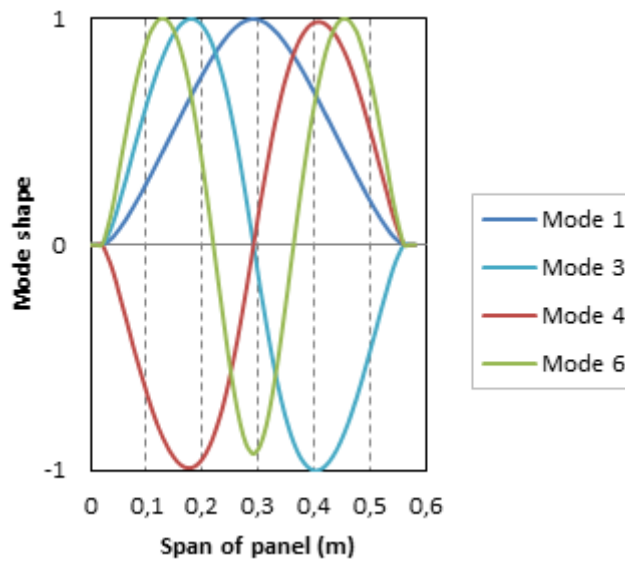


Figure A. 5. Mode shape of composite panel, thickness =8 mm

Appendix B

Manufacture and specifications of composite materials

The composite material panels were manufactured using the vacuum resin infusion process. Firstly, the preparation of layers to be fit the desired thickness and stacking sequence of the panel was achieved, Figure B. 1a. After that, the stacking is cutting to the final estimation dimensions (± 25 mm), Figure B. 1b. In the middle of the panel, the stacking was covered at the top side by using texture of the cloth which has capable to isolate the resin infusion tubes from the stacking layers, that easily to remove from the stacking when pulling the panel from the mold, Figure B. 1c. The resin infusion tubes were distributed in the configuration which allows injecting the resin in uniform manner and can improve resin flow at different locations of the stacking, as the resin will always travel in the path of least resistance.



(a) Stacking of composite layers



(b) Cutting of desired panel dimensions



(c)

Figure B. 1. Preparation of the stacking sequence and cut of panels

Once the dry materials are laid in place, the vacuum bag was constructed using plastic film and attaches tubing for the resin and vacuum lines, Figure B. 2. The vacuum is applied before the infusion of the resin, and then the resin was injected through the stacking composite. The duration of polymerization is more than 8 hours at room temperature after the resin injection was completed. After that, the vacuum bag and the breather cloth are released and the panels are removed from the mold. The stacking composite is cut to the desired size of the panel (500 x 250 mm).



(a) Vacuum bag before infusion



(b) Injection of the resin



(c) Removed the vacuum bag after polymerization



(d) Final composite panel before cutting

Figure B. 2. Vacuum bag and infusion of the resin

Manufacture of Sandwich panels

The same procedure for the manufacture of sandwich panels was carried out as that performed in laminated composite materials, Figure B. 3, but PVC foam core is closed to avoid the absorption of the resin by the core pores.



(a) Vacuum bag before infusion



(b) Injection of the resin



(c) Complete the injection of resin and polymerization



(d) Final sandwich panel before cutting

Figure B. 3. Manufacture of sandwich panels

Appendix C

Smooth Particle Hydrodynamic method SPH

The Smoothed particle hydrodynamic method is performed to simulate the slamming event. This offers alternative method to confirm the results of the coupled Eulerian Lagrangian approach (CEL) that was adopted in this work. The same numerical model of the CEL was used to represent the SPH model. However, the meshed elements of the fluid domain were replaced by particles.

The SPH method was based on the interpolation of the points [1]. That means that these points could be described by differential equations without any mesh. The Lagrangian derivative $\frac{d\rho}{dt}$ and $\frac{dv}{dt}$ for each points of the fluid is determined relative to the time integration. The quantities of the $\rho \nabla \cdot v$ and $\frac{\nabla P}{\rho}$ are determined for each point, thus the spatial derivatives are determined using the Kernel function between the point and the domain surrounding of the other points. Then each point has discrete quantities of ρ , P and v .

The integral interpolation for any function $f(r)$ can be defined as [2]:

$$f(r) = \int f(x) W(r - x, h) dx \quad (C. 1)$$

The gradient of any function can be written in the form:

$$\nabla f(r) = \int \nabla f(x) W(r - x) dx \quad (C. 2)$$

Where W is the Kernel function, h is the smooth length.

For the slamming event with free surface flow, the classical Navier-Stokes equations need to be solved. Assuming the fluid is non-viscous and the shear stress is neglected then the system reduces to the Euler equations as follows [2]:

$$\frac{dv}{dt} = g - \frac{\nabla P}{\rho} \quad (C. 3)$$

$$\frac{d\rho}{dt} = -\rho \nabla \cdot v \tag{C. 4}$$

Where g , ρ , P and v are the body forces, density of the fluid, pressure and velocity of the fluid respectively.

With interpolation of the points through the domain D, the particle can be introduced:

$$\int f(x) dx = \sum_i f_i w_i \tag{C. 5}$$

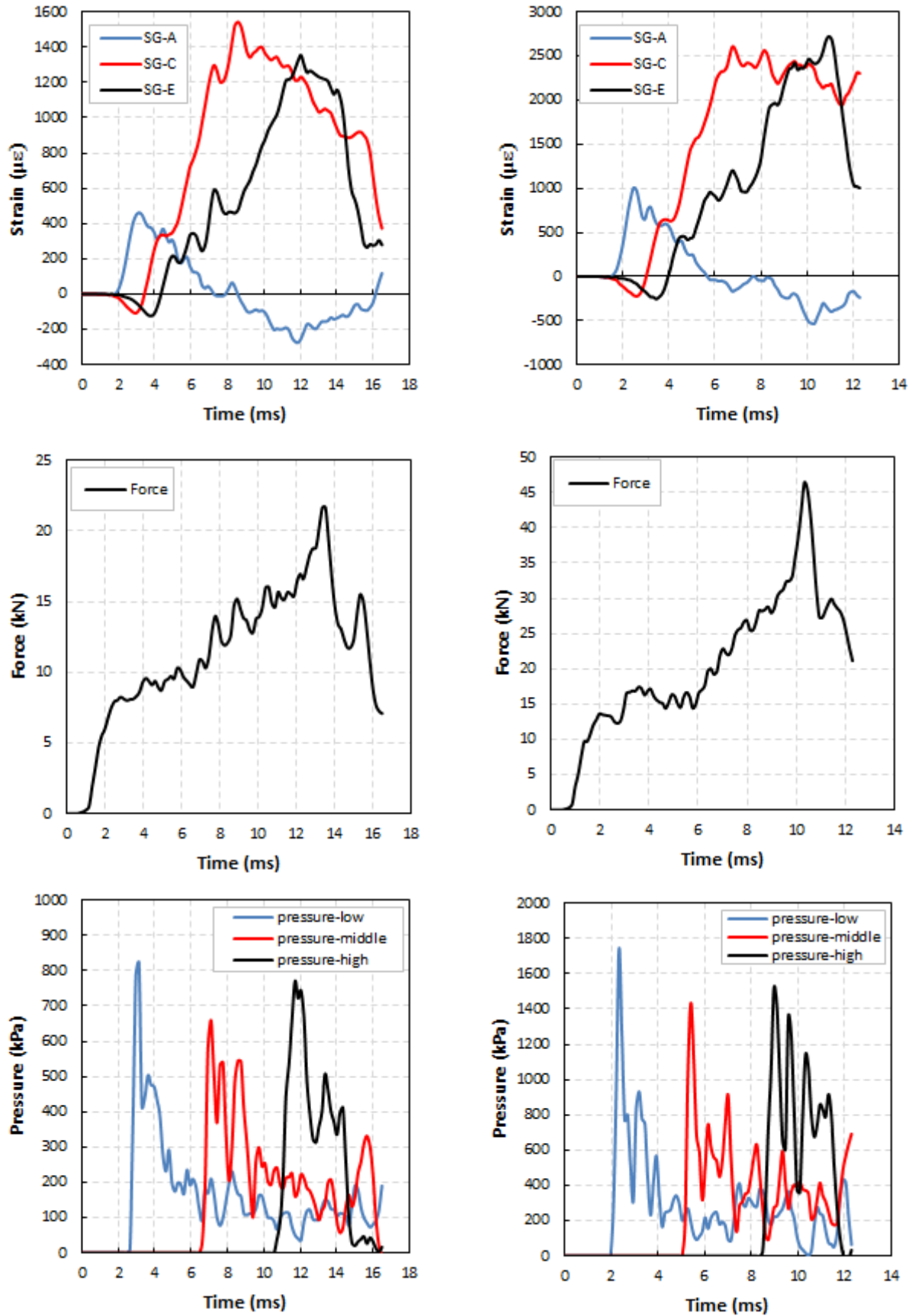
Where i represents each interpolation point with the domain D, w_i weight term and has the dimension of a volume.

Using the Lagrangian derivative and Euler equations, the formulation of the momentum equations can be written [2]:

$$\frac{dv}{dt} = g - \sum_j m_j \left(\frac{P_i}{\rho_i^2} + \frac{P_j}{\rho_j^2} \right) \nabla W(x_i - x_j, h) \tag{C. 6}$$

$$\frac{d\rho_i}{dt} = \sum_j m_j (v_i - v_j) \nabla W(x_i - x_j, h) \tag{C. 7}$$

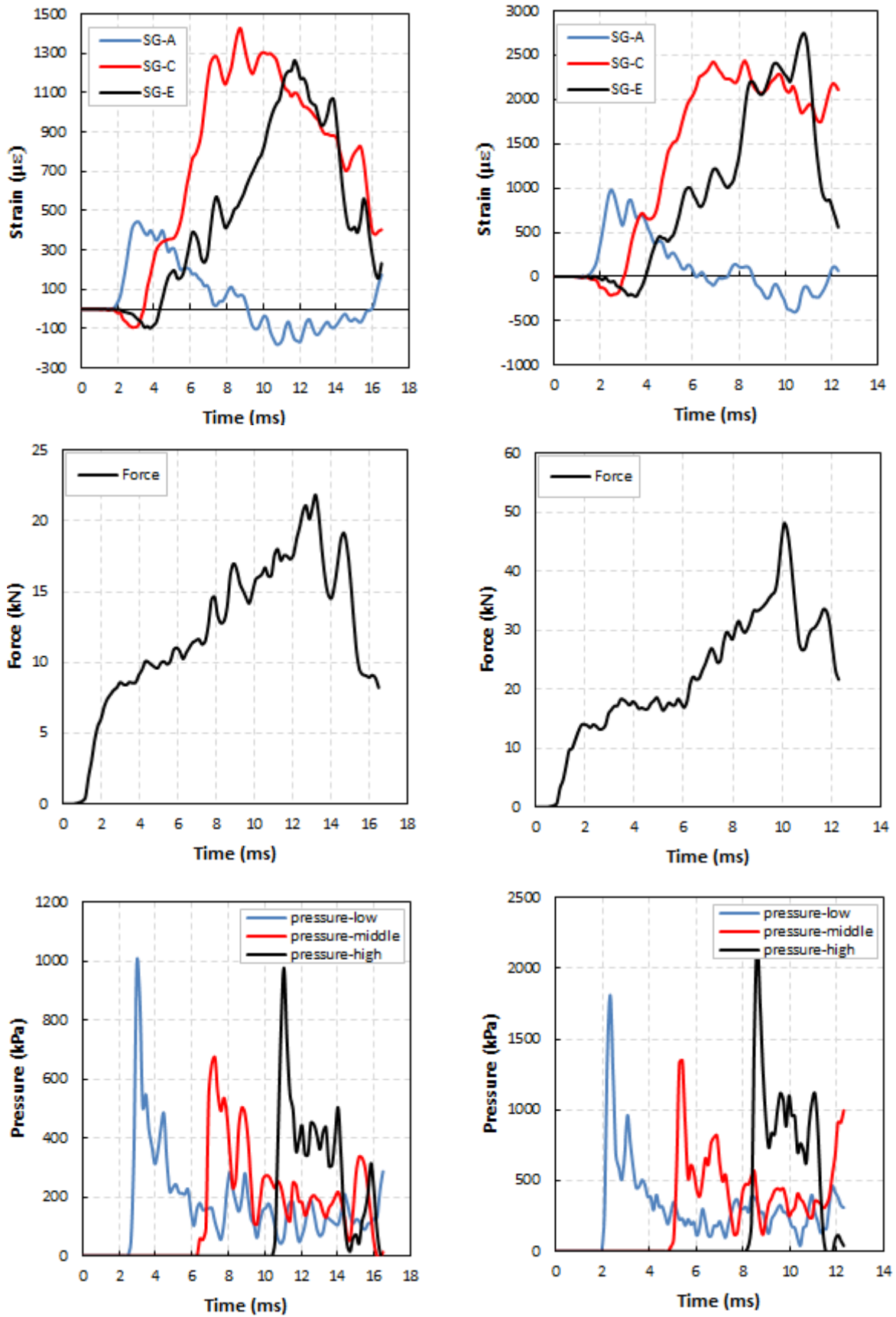
Some of the results obtained for sandwich panels subjected to the slamming impact in our cases, as shown in the figures below, which were implemented using a smoothed particle hydrodynamics (SPH) approach in the commercial code ABAQUS/Explicit.



(a) $V = 6 \text{ m/s}$

(b) $V = 8 \text{ m/s}$

Figure C. 1. Sandwich panel, $t = 27 \text{ mm}$



(a) $V = 6 \text{ m/s}$

(b) $V = 8 \text{ m/s}$

Figure C. 2. Sandwich panel, $t = 37 \text{ mm}$

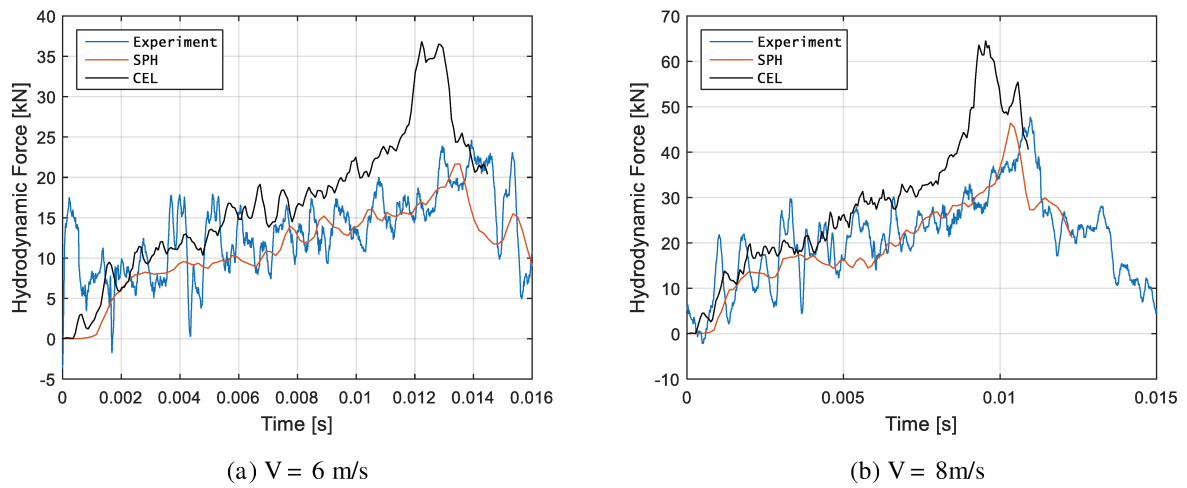


Figure C. 3. Comparison of hydrodynamic force for sandwich panel, $t= 27$ mm.

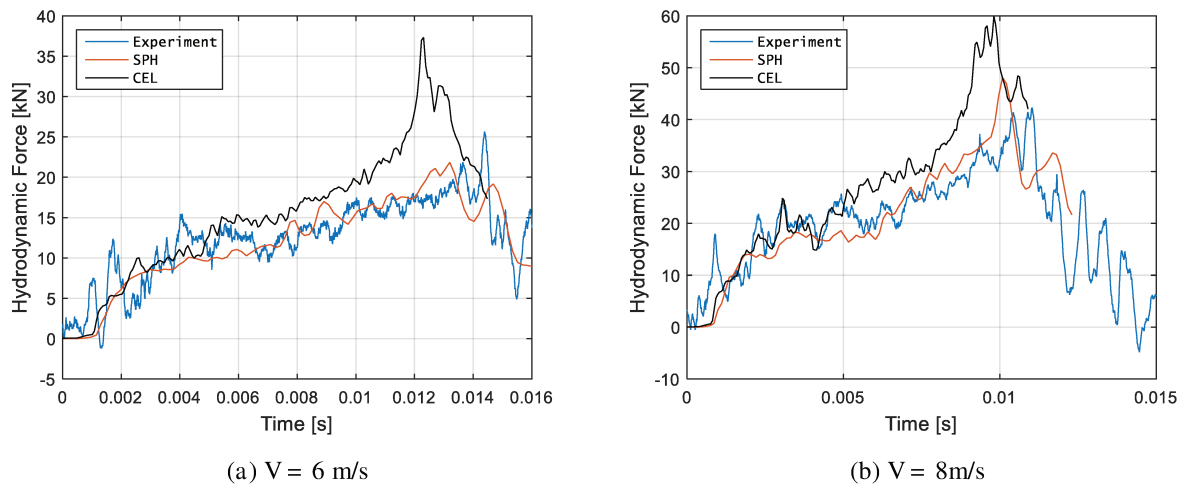


Figure C. 4. Comparison of hydrodynamic force for sandwich panel, $t= 37$ mm

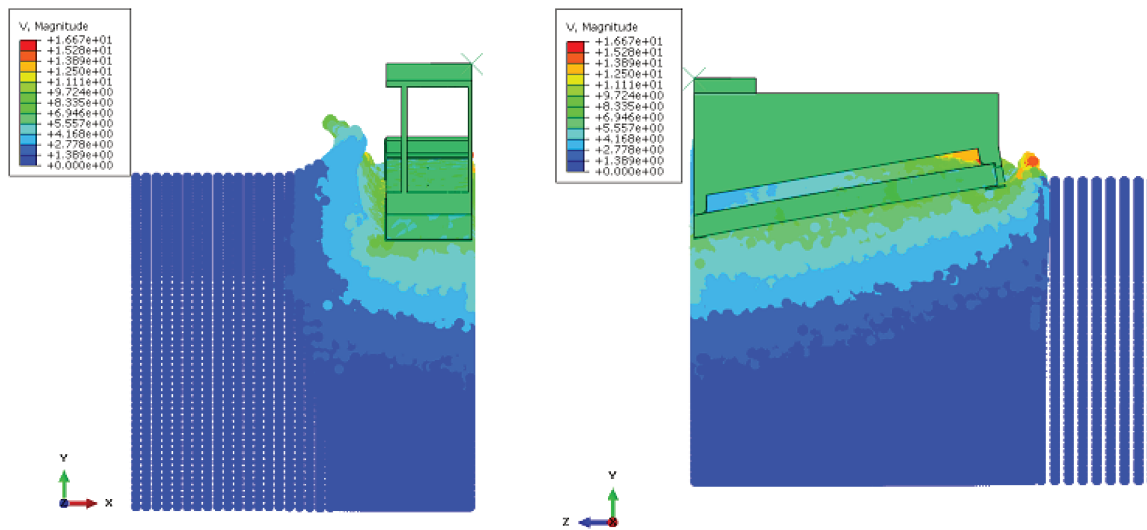


Figure C. 5. Water flow elevation for sandwich panel, $t= 37$ mm and $V=6$ m/s

References

[1] J.J. Monaghan, "Smoothed particle hydrodynamics," *Annu. Rev. Astron. Astrophys.*, vol. 30, pp. 543-574, 1992.

[2] G. Oger, M. Doring, B. Alessandrini, P. Ferrant, "Two-dimensional SPH simulations of wedge water entries," *Journal of Computational Physics*, vol. 213, pp. 803-822, 20

Design and Optimisation the Composite Material structures for Naval Applications: Effects of slamming

Abstract:

Generally, when marine vessels encounter the water surface on entry and subsequently re-enter the water at high speed (slamming), this can subject the bottom section of the vessels to both local and global effects and generate unwanted vibrations in the structure, especially over very short durations. In marine design, the vessel speed has become an important aspect for optimal structure. Therefore, design requirements have been optimized in relation to the structural weight. In other hand, the appearance of the composite structures in the last decades has encouraged the exploitation of these structures in major construction projects for lightweight marine and aerospace applications. This is due to the nature of their mechanical properties which shows a high stiffness-to-weight ratio. In contrast, the interaction between deformable structures and free water surface can be modified the fluid flow and changed the estimated hydrodynamic loads comparing with rigid body, due to appearance of hydroelastic effects. Moreover, these structures are always subject to different and complex damage mechanisms under dynamic loading. For these reasons, the flexibility and the damage failure modes in composite materials introduce additional complexity for predicting hydrodynamic loads when interactive with water. This considered a key challenge to use these materials in marine applications. Therefore, special attention must be taken in the design phase and the analysis of performances during lifetime use. The main contributions of this work are the experimental and numerical study of the dynamic behavior of composite panels and the quantification of the effect of the flexibility of these structures on the hydrodynamic loads and the resulting deformations. To study these effects, laminate composite and sandwich panels with two different rigidities and subjected to various impact velocities have been investigated experimentally using high speed shock machine with velocity control system. The dynamic resistance was analysed in terms of hydrodynamic loads, dynamic deformation and failure mechanisms for different impact velocities. The general analysis of experiment results were indicated that more flexible panel has a higher peak force as velocity increases compared with higher stiffness panels. On the other hand, the slamming model was implemented in Abaqus/Explicit software based on Coupled Eulerian Lagrangian model approach (CEL). In addition, different damage modes are developed and constructed using a user-defined material subroutine VUMAT and implemented in Finite element method, including the intralaminar damage, debonding in skin/core interface, and core shear to cover all possible damage modes throughout structures. The numerical model gave a good agreement results in judging with experimental data for prediction of the hydrodynamic force and panel deformation. Additionally, this study gives qualitative and quantitative data which provides clear guidance in design phase and the evolution of performances during lifetime of composite structures, for marine structure designers.

Keyword: Composite structures; Marine Application; Fluid-Structure Interaction; Slamming effect, Dynamic loading; Constant velocity; Experimental and numerical investigation; Structural response; Hydroelastic effects; Damage mechanisms.

Conception et Optimisation des Matériaux et Structures Composites pour des Applications Navales: Effets du tossage

Résumé:

L'interaction fluide-structure vise à étudier le contact entre un fluide et un solide. Ce phénomène est très présent lors de l'impact d'une vague sur une structure ou l'inverse. La réponse de la structure peut être fortement affectée par l'action du fluide. L'étude de ce type d'interaction est motivée par le fait que les phénomènes résultants sont parfois catastrophiques pour les structures composites ou constituent dans la majorité des cas un facteur dimensionnant important. Le fluide est caractérisé par son champ de vitesse et de pression. Il exerce des forces aérodynamiques ou hydrodynamiques sur l'interface de la structure qui subit des déformations sous leurs actions. Ces déformations peuvent affecter localement le champ de l'écoulement et donc les charges appliquées. Ce cycle des interactions entre le fluide et le solide est caractéristique du phénomène de slamming. Pour une conception optimale des structures marines, la vitesse du navire est devenue un paramètre important. Par conséquent, les exigences de conception ont été optimisées par rapport au poids structurel. D'autre part, l'apparition des structures composites au cours des dernières décennies a favorisé l'exploitation de ces matériaux dans les grands projets de construction pour les applications marines et aérospatiales. Ceci est dû à la nature de leurs propriétés mécaniques, car elles présentent un rapport rigidité / poids élevé. En revanche, l'interaction entre les structures déformables et la surface libre de l'eau peut affecter le flux du fluide en contact avec la structure ainsi que et les charges hydrodynamiques estimées par rapport au corps rigide, en raison de l'apparition des effets hydro-élastiques. En outre, ces structures sont toujours soumises à des mécanismes de dommages différents et complexes sous un chargement dynamique. Pour ces raisons, la flexibilité et les modes de défaillance dans les matériaux composites présentent une complexité supplémentaire pour prédire les charges hydrodynamiques lorsqu'il y a une interaction avec un fluide (l'eau). Ceci a présenté un défi majeur pour utiliser ces matériaux dans les applications maritimes. Par conséquent, une attention particulière doit être accordée dans la phase de conception et l'analyse des performances pendant l'utilisation à vie. Les principales contributions de ce travail sont l'étude expérimentale et numérique du comportement dynamique des panneaux composites et la quantification de l'effet de la flexibilité de ces panneaux composites sur les charges hydrodynamiques et les déformations résultantes. Pour étudier ces effets, des panneaux composites stratifiés et sandwichs avec deux rigidités différentes sont soumis à diverses vitesses d'impact à l'aide d'une machine de choc équipée d'un système de contrôle de la vitesse. La résistance dynamique a été analysée en termes de charges hydrodynamiques, de déformations dynamiques et de mécanismes de défaillance pour différentes vitesses d'impact. L'analyse des résultats expérimentaux a montré que l'effort maximal augmente avec l'augmentation de la flexibilité des panneaux. D'autre part, le modèle numérique de tossage a été implémenté dans le logiciel Abaqus / Explicit basé sur l'approche du modèle Couplé Euler Lagrange (CEL). En outre, différents modes de défaillance des matériaux composites ont été développés et implémentés à l'aide d'une subroutine « VUMAT » définie par l'utilisateur et mis en œuvre dans le code de calcul éléments finis. Pour couvrir tous les modes de défaillance possibles dans les structures composites, l'implémentation de l'endommagement comprend : la rupture intralaminar, la décohésion de l'interface peau / âme et le cisaillement de l'âme. La confrontation des résultats expérimentaux avec les modèles numériques sur la prédiction de la force hydrodynamique et de la déformation du panneau valide l'approche adoptée. En outre, cette étude fournit aux concepteurs de structures maritimes des données qualitatives et quantitatives qui donnent des conseils clairs sur la phase de conception et l'évolution des performances mécaniques des structures composites pendant leur durée de vie.

Mot-clé: Structures composites; Applications marines; Interaction fluide-structure; Effet du tossage; Chargement dynamique; Vitesse constante; Investigation expérimentale et numérique; Réponse structurelle; Effets hydro-élastiques ; Mécanismes d'endommagement.